

**EXPERIMENTAL INVESTIGATION AND ANALYSES OF
CONTINUOUS TYPE HYBRID
PHOTOELECTROCHEMICAL HYDROGEN
PRODUCTION SYSTEMS**

By

CANAN ACAR

A Thesis Submitted in Partial Fulfillment

of the Requirements for the degree of Doctor of Philosophy

in

Mechanical Engineering

University of Ontario Institute of Technology

Faculty of Engineering and Applied Science

Oshawa, Ontario, Canada

© Canan Acar, 2016

ABSTRACT

Hydrogen is a highly versatile energy carrier that may become one of the key pillars to support the future CO₂-free energy infrastructure. When used in fuel cells, H₂ is converted to water and it gives little or zero exhaust of greenhouse gases. For H₂ economy to succeed, it needs to be produced in a clean, sustainable, reliable, and feasible way.

The main objective of this study is to develop and investigate a continuous type hybrid photoelectrochemical-chloralkali H₂ production reactor that converts the by-products into useful industrial commodities (i.e., Cl₂ and NaOH). This system maximizes solar spectrum use by taking advantage of photocatalysis and PV/T. Furthermore, by using electrodes as electron donors to drive the photochemical reaction, the potential of pollutant emissions are minimized.

Four different processes are tested by using the present reactor: electrolysis, PEC, chloralkali, and PEC-chloralkali. During all processes, the present reactor is tested under four temperatures (20, 40, 60, and 80°C) and three inlet mass flow rates (0.25, 0.50, and 0.75 g/s). Furthermore, PEC-based processes are tested under two light settings (600 and 1200 W/m²). These results are compared to the thermodynamic model outputs. Parametric studies are run by varying the operating temperature (0°C–80°C), inlet mass flow rate (0.01 g/s–1 g/s), and environmental temperature (0°C–40°C).

The present experimental results show that PEC-chloralkali has the highest H₂ production rate compared to other processes at all temperatures and flow rates. Under 1200 W/m² irradiation, at 20°C and 0.75 g/s, Process 4 has a H₂ production rate of 3.48 mg/h. 27% and 26% are the highest energy and exergy efficiencies reached at 0.75 g/s inlet mass flow rate and 20°C operating temperature and under 600 W/m² irradiation.

A multi-objective optimization study is performed to find the decision variables for the highest possible production, efficiencies, and lowest possible exergy destruction, cost, and emissions. These parameters are 1°C operating temperature, 1.4 g/s inlet flow rate, 6 m² total photoactive area, and 0°C environmental temperature. And overall exergy efficiency is 30%, and H₂ production cost and emissions are 9.67 USD/kg H₂ and 7.39 kg CO₂/kg H₂.

ACKNOWLEDGEMENTS

The journey of my PhD studies and the process of writing this thesis have been nothing short of amazing. And it is the result of many experiences I have encountered at UOIT from dozens of remarkable individuals who I also wish to acknowledge.

First and foremost, I wish to thank my advisor, Prof. Dr. Ibrahim Dincer, the director of the UOIT Clean Energy Research Laboratory. He has always believed in me to reach my full potential since the day I met him in December 2011. Dr. Dincer has a great vision and clear mind and he has showed me what I could achieve. This PhD would not be possible without his guidance, patience, understanding, motivation, and support. His endless energy have always kept me going and made me feel excited to be a member of his team. I strongly believe that he has taught me not only to become a better researcher, but also a better human being in general. I hope to keep working with Dr. Dincer in the future and I know that I will always be proud to have my PhD under his supervision.

Besides my advisor, I would like to thank Dr. Calin Zamfirescu for helping me to build the experimental setup, his insightful comments, and for the challenging questions and great discussions which incited me to widen my research from various perspectives.

I also thank past and current members of Dr. Dincer's research group for the stimulating discussions, sleepless nights before deadlines, and for all the fun we have had in the last four years. It would be impossible for me to list all the names but my special thanks go to Dr. Hasan Ozcan for helping me to become a mechanical engineer since the beginning of my studies at UOIT. I would also like to thank not only my colleague, but also dear friend Janette Hogerwaard. It has been so much fun to know her during this journey. Yusuf Bicer and Farrukh Khalid deserve special thanks for being more than fellow team members. I am sure they all will accomplish great things in the future.

I am particularly lucky for having such great friends in my life. As the space is limited, I can only highlight a few of them here: first, Ekin Aslan, for always being there and having time for me, for the motivation, and for the laughs. And Ipek Akinci, who has always believed in me, always supported me, and always had a positive impact in my life. My dear high school friend Giray Ozil: his understanding, support, and great humor have

made this journey a lot more bearable. I also would like to mention Dr. Emre Karaoglan here, who has never let me have the PhD blues, for his endless joy, support, and great insight in many aspects of life (especially optimization part of this thesis).

Last but not the least, I would like to thank my family: Cennet, Recep, and Nihan for supporting me spiritually throughout writing this thesis and my life in general. Here, I also would like to add Ozgur Isik, the newest member to our family, for becoming a great brother to me. I am very lucky to have such great parents for raising me with a love of science and supporting me in all my pursuits. And a great sister who has turned out to be my best friend forever. As I am a person now, for what I have accomplished, and for anything I will ever achieve, I am eternally in debt to my family. Finally, I would like to mention two special people: my grandfather Hakki Acar and my uncle Mustafa Atsiz whom I lost during the pursuit of my PhD. This thesis is dedicated to both of them.

TABLE OF CONTENTS

ABSTRACT	i
ACKNOWLEDGEMENTS	ii
TABLE OF CONTENTS	iv
LIST OF FIGURES	xi
LIST OF TABLES	xx
NOMENCLATURE	xxii
CHAPTER 1: INTRODUCTION	1
1.1 Energy and Environmental Issues	1
1.2 Hydrogen Production Methods	5
1.3 Solar Hydrogen Production	9
1.4 Photoelectrochemical Hydrogen Production	11
1.5 Motivation and Objectives	13
1.5.1 Motivation	13
1.5.2 Objectives	14
1.6 Summary of Approach and Rationale	16
1.7 Thesis Outline	18
CHAPTER 2: LITERATURE REVIEW	19
2.1 Introduction	19
2.2 Photoelectrochemical Hydrogen Production	21
2.2.1 Reactor Design	24
2.2.2 Photoelectrodes	27
2.2.3 Membranes	28
2.2.4 System Hybridization	30
2.3 Overall System Analysis	32

2.4 System Integration	34
2.5 Main Gaps in the Literature	36
2.6 The Need for the Current Study	37
CHAPTER 3: BACKGROUND	38
3.1 Introduction	38
3.2 Photoelectrochemical Hydrogen Production	39
3.2.1 Principles of Photoelectrochemical Hydrogen Production	40
3.2.2 Energy and Quantum Efficiencies	45
3.2.3 System Requirements	48
3.2.4 Photoelectrochemical Hydrogen Production Experiments	51
CHAPTER 4: EXPERIMENTAL APPARATUS AND PROCEDURE	57
4.1 System Description	57
4.2 Experimental Setup	60
4.3 Electrolytes, Electrodes and Membrane	64
4.4 Instruments and Devices	68
4.5 Experimental Procedure	71
4.5.1 Process 1: Electrolysis Experiments	71
4.5.2 Process 2: Photoelectrochemical Experiments	73
4.5.3 Process 3: Chloralkali Experiments	74
4.5.3 Process 4: Photoelectrochemical-Chloralkali Experiments	74
4.6 Experimental Uncertainties	75
4.7 Development of Integrated System	77
CHAPTER 5: ANALYSES AND OPTIMIZATION	79
5.1 Basic Thermodynamic Concepts	79
5.2 Model Development	86

5.3 Efficiency Assessment	95
5.4 Integrated System Analysis.....	97
5.5 Exergoeconomic Analysis.....	101
5.6 Exergoenvironmental Analysis.....	106
5.7 Optimization Study	108
CHAPTER 6: RESULTS AND DISCUSSION.....	112
6.1 Process 1 – Electrolysis: Results and Discussion	112
6.1.1 Effect of Operating Temperature	113
a. Measured Current Results	113
b. Hydrogen Production Results	114
c. Energy Efficiency Results.....	114
d. Exergy Efficiency Results.....	115
e. Exergy Destruction Results.....	116
f. Optimum Operating Temperature Results.....	117
6.1.2 Effect of Inlet Mass Flow Rate	118
a. Measured Current Results	118
b. Hydrogen Production Results	119
c. Energy Efficiency Results.....	120
d. Exergy Efficiency Results.....	121
e. Exergy Destruction Results.....	122
f. Optimum Inlet Mass Flow Rate Results.....	122
6.1.3 Effect of Environmental Temperature	123
6.1.4 Coated Membrane Results	124
6.1.5 Uncertainty Analysis Results.....	124
6.1.6 Statistical Analysis Results	125

6.2 Process 2 – Photoelectrochemical: Results and Discussion.....	128
6.2.1 Effect of Operating Temperature	129
a. Measured Current Results	129
b. Hydrogen Production Results	130
c. Energy Efficiency Results.....	130
d. Exergy Efficiency Results.....	131
e. Exergy Destruction Results.....	132
f. Optimum Operating Temperature Results.....	133
6.2.2 Effect of Inlet Mass Flow Rate	134
a. Measured Current Results	134
b. Hydrogen Production Results	135
c. Energy Efficiency Results.....	136
d. Exergy Efficiency Results.....	137
e. Exergy Destruction Results.....	138
f. Optimum Inlet Mass Flow Rate Results.....	138
6.2.3 Effect of Environmental Temperature	139
6.2.4 Coated Membrane Results	140
6.2.5 Uncertainty Analysis Results.....	141
6.2.6 Statistical Analysis Results	141
6.3 Process 3 – Chloralkali: Results and Discussion	145
6.3.1 Effect of Operating Temperature	146
a. Measured Current Results	146
b. Hydrogen Production Results	146
c. Energy Efficiency Results.....	147
d. Exergy Efficiency Results.....	148

e. Exergy Destruction Results.....	149
f. Optimum Operating Temperature Results.....	150
6.3.2 Effect of Inlet Mass Flow Rate	151
a. Measured Current Results.....	151
b. Hydrogen Production Results	152
c. Energy Efficiency Results.....	152
d. Exergy Efficiency Results.....	153
e. Exergy Destruction Results.....	154
f. Optimum Inlet Mass Flow Rate Results.....	155
6.3.3 Effect of Environmental Temperature	155
6.3.4 Uncertainty Analysis Results.....	156
6.3.5 Statistical Analysis Results	156
6.4 Process 4 – Photoelectrochemical-Chloralkali: Results and Discussion	160
6.4.1 Effect of Operating Temperature	161
a. Measured Current Results	161
b. Hydrogen Production Results	162
c. Energy Efficiency Results.....	162
d. Exergy Efficiency Results.....	164
e. Exergy Destruction Results.....	165
f. Optimum Operating Temperature Results.....	165
6.4.2 Effect of Inlet Mass Flow Rate	166
a. Measured Current Results	166
b. Hydrogen Production Results	167
c. Energy Efficiency Results.....	168
d. Exergy Efficiency Results.....	169

e. Exergy Destruction Results.....	169
f. Optimum Inlet Mass Flow Rate Results.....	170
6.4.3 Effect of Environmental Temperature	171
6.4.4 Uncertainty Analysis Results.....	172
6.4.5 Statistical Analysis Results	172
6.5 Integrated System Results.....	177
6.5.1 Effect of Operating Temperature	177
a. Hydrogen and Chlorine Production Results.....	177
b. Electricity and Heat Production Results	178
c. Exergy Destruction Results.....	179
d. Energy and Exergy Efficiencies Results.....	179
6.5.2 Effect of Inlet Mass Flow Rate	181
a. Hydrogen and Chlorine Production Results.....	181
b. Electricity and Heat Production Results	182
c. Exergy Destruction Results.....	183
d. Energy and Exergy Efficiencies Results.....	183
6.5.3 Effect of Photoactive Area.....	184
a. Hydrogen and Chlorine Production Results.....	185
b. Electricity and Heat Production Results	186
c. Exergy Destruction Results.....	187
d. Energy and Exergy Efficiencies Results.....	187
6.5.4 Effect of Environmental Temperature	187
a. Electricity and Heat Production Results	188
b. Exergy Destruction Results.....	189
c. Energy and Exergy Efficiencies Results.....	190

6.5.5 Case Study Results.....	191
a. Case Study 1: Optimum Operating Temperature Results	191
b. Case Study 2: Optimum Inlet Mass Flow Rate Results	192
c. Case Study 3: Optimum Photoactive Area Results.....	192
d. Case Study 4: Optimum Environmental Temperature Results	193
e. Overall Comparison Results of the Case Studies.....	194
6.6 Exergoeconomic Analysis Results.....	195
6.7 Exergoenvironmental Analysis Results	199
6.8 Optimization Study Results	204
CHAPTER 7: CONCLUSIONS AND RECOMMENDATIONS	211
7.1 Conclusions.....	212
7.2 Recommendations.....	215
REFERENCES	216

LIST OF FIGURES

Figure 1.1 World’s fuel shares of (a) TPES, (b) total final consumption, (c) electricity generation, and (d) CO ₂ emissions in 2013 (other comprises geothermal, recovered heat, solar, wind, etc.) (data from [1]).	2
Figure 1.2 HCF, GF, and EIF of hydrogen and other fossil fuels [6].	4
Figure 1.3 Outline of selected hydrogen generation routes classified by primary energy source and manufacturing method (modified from [8]).	5
Figure 2.1 Illustrative representation of a sample open photocell (adapted from [76]).	25
Figure 2.2 Illustration of a sample ion-permeable membrane divided PEC cell (adapted from [79]).	26
Figure 2.3 Illustrative representation of a PEC cell separated by a glass frit (adapted from [80]).	27
Figure 3.1 Illustration of (a) a PEC reactor with a semiconductor based photoanode and a metal based cathode and (b) its energy diagram (adapted from [114]).	40
Figure 4.1 Process flow diagram of present experimental setup.	58
Figure 4.2 Summary of four types of processes tested during present experimental studies.	58
Figure 4.3 Present experimental setup (left), closer look at illuminated reactor (top right), and feed tanks with heater (bottom right).	59
Figure 4.4 Illustrative representation of hybrid reactor’s operation procedure (during Process 4).	61
Figure 4.5 Schematic illustration of interactions between present reactor and other experimental setup components.	62
Figure 4.6 Schematic illustration of hybrid reactor during Processes 3 and 4.	63
Figure 4.7 Present experimental setup during electrodeposition process.	68
Figure 4.8 Solar simulator illuminating the reactor at 1 Sun intensity.	69
Figure 4.9 Omega PSU505 potentiostat during an experimental run.	69
Figure 4.10 Multi-channel BT100-1L Peristaltic pump (a) and pump during an experimental run (b).	70
Figure 4.11 Electrolyte feed tanks with heaters (a), volumetric water displacement cylinder (b), and temperature/pH monitor (c).	71

Figure 4.12 Schematic description of present experimental procedure.	72
Figure 4.13 Schematic description of experimental runs during electrolysis (Process 1).	73
Figure 4.14 Schematic description of experimental runs during PEC (Process 2).	74
Figure 4.15 Schematic description of experimental runs during chloralkali (Process 3). 75	
Figure 4.16 Schematic description of experimental runs during PEC-chloralkali (Process 4).	76
Figure 4.17 Conceptual block diagram of integrated system for solar H ₂ , Cl ₂ , electricity, and heat production.	78
Figure 5.1 Schematic of continuous type hybrid reactor used in Processes 1, 2, 3 and 4.80	
Figure 5.2 Exergoenvironmental analysis methodology (modified from [199]).	107
Figure 6.1 Effect of operating temperature on current measurement results (Process 1).	113
Figure 6.2 Effect of operating temperature on H ₂ production with comparison of experimental and model outputs (Process 1).	114
Figure 6.3 Effect of operating temperature on energy efficiency with comparison of experimental and model outputs (Process 1) – (i) cooling, (ii) heating.	115
Figure 6.4 Effect of operating temperature on exergy efficiency with comparison of experimental and model outputs (Process 1) – (i) cooling, (ii) heating.	116
Figure 6.5 Effect of operating temperature on exergy destruction –model outputs (Process 1) – (i) cooling, (ii) heating.	117
Figure 6.6 Normalized rankings of H ₂ production, efficiencies, and exergy destruction at different operating temperatures (Process 1).	118
Figure 6.7 Effect of inlet mass flow rate on current measurements (Process 1).	119
Figure 6.8 Effect of inlet mass flow rate on H ₂ production with comparison of experimental and model outputs (Process 1).	120
Figure 6.9 Effect of inlet mass flow rate on energy efficiency with comparison of experimental and model outputs (Process 1).	120
Figure 6.10 Effect of inlet mass flow rate on exergy efficiency with comparison of experimental and model outputs (Process 1).	121

Figure 6.11 Effect of inlet mass flow rate on exergy destruction –model outputs (Process 1).	122
Figure 6.12 Normalized rankings of H ₂ production, efficiencies, and exergy destruction at different inlet mass flow rates (Process 1).	123
Figure 6.13 Effect of environmental temperature on exergy destruction and efficiencies (Process 1) – (i) heating, (ii) cooling.	123
Figure 6.14 Effect of membrane coating on current measurements at different applied potentials.	124
Figure 6.15 Results of (a) DOE model, (b) operating temperature leverage plot, and (c) inlet mass flow rate leverage plot of Process 1 experimental current measurements.	125
Figure 6.16 Results of (a) DOE model, (b) operating temperature leverage plot, and (c) inlet mass flow rate leverage plot of Process 1 experimental hydrogen production results.	126
Figure 6.17 Results of (a) DOE model, (b) operating temperature leverage plot, and (c) inlet mass flow rate leverage plot of Process 1 experimental energy efficiency results.	127
Figure 6.18 Results of (a) DOE model, (b) operating temperature leverage plot, and (c) inlet mass flow rate leverage plot of Process 1 experimental exergy efficiency results.	128
Figure 6.19 Effect of operating temperature on current measurement results (Process 2).	129
Figure 6.20 Effect of operating temperature on H ₂ production with comparison of experimental and model outputs (Process 2).	130
Figure 6.21 Effect of operating temperature on energy efficiency with comparison of experimental and model outputs (Process 2) – (i) cooling, (ii) heating.	131
Figure 6.22 Effect of operating temperature on exergy efficiency with comparison of experimental and model outputs (Process 2) – (i) cooling, (ii) heating.	132
Figure 6.23 Effect of operating temperature on exergy destruction–model outputs (Process 2) – (i) cooling, (ii) heating.	133
Figure 6.24 Average normalized rankings of H ₂ production, efficiencies, and exergy destruction at different operating temperatures (Process 2).	134
Figure 6.25 Effect of inlet mass flow rate on current measurements (Process 2).	135

Figure 6.26 Effect of inlet mass flow rate on H ₂ production with comparison of experimental and model outputs (Process 2).	135
Figure 6.27 Effect of inlet mass flow rate on energy efficiency with comparison of experimental and model outputs (Process 2).	136
Figure 6.28 Effect of inlet mass flow rate on exergy efficiency with comparison of experimental and model outputs (Process 2).	137
Figure 6.29 Effect of inlet mass flow rate on exergy destruction –model outputs (Process 2).	138
Figure 6.30 Average normalized rankings of H ₂ production, efficiencies, and exergy destruction at different inlet mass flow rates (Process 2).	139
Figure 6.31 Effect of environmental temperature on exergy destruction and efficiencies under 600 W/m ² irradiation (Process 2) – (i) heating, (ii) cooling.	139
Figure 6.32 Effect of environmental temperature on exergy destruction and efficiencies under 1200 W/m ² irradiation (Process 2) – (i) heating, (ii) cooling.	140
Figure 6.33 Effect of membrane coating on current measurements at different applied potentials under 1200 W/m ² irradiation.	141
Figure 6.34 Results of (a) DOE model, (b) operating temperature leverage plot, (c) inlet mass flow rate leverage plot, and (d) irradiation level leverage plot of Process 2 experimental current measurements.	142
Figure 6.35 Results of (a) DOE model, (b) operating temperature leverage plot, (c) inlet mass flow rate leverage plot, and (d) irradiation level leverage plot of Process 2 experimental hydrogen production results.	143
Figure 6.36 Results of (a) DOE model, (b) operating temperature leverage plot, (c) inlet mass flow rate leverage plot, and (d) irradiation level leverage plot of Process 2 experimental energy efficiency results.	144
Figure 6.37 Results of (a) DOE model, (b) operating temperature leverage plot, (c) inlet mass flow rate leverage plot, and (d) irradiation level leverage plot of Process 2 experimental exergy efficiency results.	145
Figure 6.38 Effect of operating temperature on current measurement results (Process 3).	146

Figure 6.39 Effect of operating temperature on H ₂ production with comparison of experimental and model outputs (Process 3).	147
Figure 6.40 Effect of the operating temperature on energy efficiency with comparison of experimental and model outputs (Process 3) – (i) cooling, (ii) heating.	148
Figure 6.41 Effect of operating temperature on exergy efficiency with comparison of experimental and model outputs (Process 3) – (i) cooling, (ii) heating.	149
Figure 6.42 Effect of operating temperature on exergy destruction – model outputs (Process 3).	150
Figure 6.43 Normalized rankings of H ₂ production, efficiencies, and exergy destruction at different operating temperatures (Process 3).	150
Figure 6.44 Effect of inlet mass flow rate on current measurement results (Process 3).	151
Figure 6.45 Effect of inlet mass flow rate on H ₂ production with comparison of experimental and model outputs (Process 3).	152
Figure 6.46 Effect of inlet mass flow rate on energy efficiency with comparison of experimental and model outputs (Process 3).	153
Figure 6.47 Effect of inlet mass flow rate on exergy efficiency with comparison of experimental and model outputs (Process 3).	154
Figure 6.48 Effect of inlet mass flow rate on exergy destruction –model outputs (Process 3).	154
Figure 6.49 Normalized rankings of H ₂ production, efficiencies, and exergy destruction at different inlet mass flow rates (Process 3).	155
Figure 6.50 Effect of environmental temperature on exergy destruction and efficiencies (Process 3) – (i) heating, (ii) cooling.	156
Figure 6.51 Results of (a) DOE model, (b) operating temperature leverage plot, and (c) inlet mass flow rate leverage plot of Process 3 experimental current measurements.	157
Figure 6.52 Results of (a) DOE model, (b) operating temperature leverage plot, and (c) inlet mass flow rate leverage plot of Process 3 experimental hydrogen production results.	158
Figure 6.53 Results of (a) DOE model, (b) operating temperature leverage plot, and (c) inlet mass flow rate leverage plot of Process 3 experimental energy efficiency results.	159

Figure 6.54 Results of (a) DOE model, (b) operating temperature leverage plot, and (c) inlet mass flow rate leverage plot of Process 3 experimental exergy efficiency results.	160
Figure 6.55 Effect of operating temperature on the current measurement results (Process 4).	161
Figure 6.56 Effect of operating temperature on H ₂ production with comparison of experimental and model outputs (Process 4).	162
Figure 6.57 Effect of operating temperature on energy efficiency with comparison of experimental and model outputs (Process 4) – (i) cooling, (ii) heating.	163
Figure 6.58 Effect of operating temperature on exergy efficiency with comparison of experimental and model outputs (Process 4) – (i) cooling, (ii) heating.	164
Figure 6.59 Effect of operating temperature on exergy destruction –model outputs (Process 4).	165
Figure 6.60 Average normalized rankings of H ₂ production, efficiencies, and exergy destruction at different operating temperatures (Process 4).	166
Figure 6.61 Effect of inlet mass flow rate on measured current (Process 4).	167
Figure 6.62 Effect of inlet mass flow rate on H ₂ production with comparison of experimental and model outputs (Process 4).	167
Figure 6.63 Effect of inlet mass flow rate on energy efficiency with comparison of experimental and model outputs (Process 4).	168
Figure 6.64 Effect of inlet mass flow rate on exergy efficiency with comparison of experimental and model outputs (Process 4).	169
Figure 6.65 Effect of inlet mass flow rate on exergy destruction –model outputs (Process 4).	170
Figure 6.66 Average normalized rankings of H ₂ production, efficiencies, and exergy destruction at different inlet mass flow rates (Process 4).	170
Figure 6.67 Effect of environmental temperature on exergy destruction and efficiencies under 600 W/m ² irradiation (Process 4) – (i) heating, (ii) cooling.	171
Figure 6.68 Effect of environmental temperature on exergy destruction and efficiencies under 1200 W/m ² irradiation (Process 4) – (i) heating, (ii) cooling.	172

Figure 6.69 Results of (a) DOE model, (b) operating temperature leverage plot, (c) inlet mass flow rate leverage plot, and (d) irradiation level leverage plot of Process 4 experimental current measurements.....	173
Figure 6.70 Results of (a) DOE model, (b) operating temperature leverage plot, (c) inlet mass flow rate leverage plot, and (d) irradiation level leverage plot of Process 4 experimental hydrogen production results.....	174
Figure 6.71 Results of (a) DOE model, (b) operating temperature leverage plot, (c) inlet mass flow rate leverage plot, and (d) irradiation level leverage plot of Process 4 experimental energy efficiency results.	175
Figure 6.72 Results of (a) DOE model, (b) operating temperature leverage plot, (c) inlet mass flow rate leverage plot, and (d) irradiation level leverage plot of Process 4 experimental exergy efficiency results.	176
Figure 6.73 Effect of operating temperature on (a) H ₂ and (b) Cl ₂ production of integrated system.	178
Figure 6.74 Effect of operating temperature on electricity and heat production of integrated system.	179
Figure 6.75 Effects of: (a) operating temperature, (b) inlet flow rate, (c) photoactive area, and (d) environmental temperature on exergy destruction of integrated system– (i) heating, (ii) cooling.....	180
Figure 6.76 Effect of operating temperature on (a) energy and (b) exergy efficiencies of integrated system.	181
Figure 6.77 Effect of inlet mass flow rate on (a) H ₂ and (b) Cl ₂ production rate of integrated system.	182
Figure 6.78 Effect of inlet mass flow rate on electricity and heat production of integrated system.	183
Figure 6.79 Effect of inlet mass flow rate on (a) energy and (b) exergy efficiencies of integrated system.	184
Figure 6.80 Effect of photoactive area on (a) H ₂ and (b) Cl ₂ production rate of integrated system.	185
Figure 6.81 Effect of photoactive area on electricity and heat production of integrated system.	186

Figure 6.82 Effect of photoactive area on (a) energy and (b) exergy efficiencies of integrated system.	188
Figure 6.83 Effect of environmental temperature on electricity and heat production of integrated system – (i) heating, (ii) cooling.	189
Figure 6.84 Effect of environmental temperature on (a) energy and (b) exergy efficiencies of integrated system.	190
Figure 6.85 Operating temperature based normalized rankings of selected performance criteria of integrated system.	191
Figure 6.86 Inlet mass flow rate based normalized rankings of selected performance criteria of integrated system.	192
Figure 6.87 Photoactive area based normalized rankings of selected performance criteria of integrated system.	193
Figure 6.88 Environmental temperature based normalized rankings of selected performance criteria of integrated system.	193
Figure 6.89 Overall performance comparison of case studies based on normalized rankings of selected performance criteria of integrated system.	195
Figure 6.90 Effect of operating temperature on H ₂ and Cl ₂ production costs of integrated system.	196
Figure 6.91 Effect of inlet mass flow rate on H ₂ and Cl ₂ production costs of integrated system.	197
Figure 6.92 Effect of photoactive area on H ₂ and Cl ₂ production costs of integrated system.	197
Figure 6.93 Effect of environmental temperature on H ₂ and Cl ₂ production costs of integrated system.	198
Figure 6.94 Overall performance and cost comparison of case studies based on normalized rankings.	199
Figure 6.95 Effect of operating temperature on CO ₂ emissions of integrated system. ...	200
Figure 6.96 Effect of inlet mass flow rate on CO ₂ emissions of integrated system.	201
Figure 6.97 Effect of total photoactive area on CO ₂ emissions of integrated system. ...	202
Figure 6.98 Overall performance, cost, and emissions comparison of case studies based on normalized rankings.	203

Figure 6.99 H ₂ and Cl ₂ production comparison of selected case studies used in optimization study.....	206
Figure 6.100 Heat and electricity production comparison of case studies used in optimization study.....	206
Figure 6.101 Energy and exergy efficiencies comparison of case studies used in optimization study.....	207
Figure 6.102 Cost and emissions comparison of selected case studies used in optimization study.....	207
Figure 6.103 Overall performance, cost, and emissions comparison of optimization case studies based on normalized rankings.....	208
Figure 6.104 Energy and exergy efficiencies of present hybrid system compared to available data in literature.....	209
Figure 6.105 Cost and emissions of present hybrid system compared to the available data in literature.....	210

LIST OF TABLES

Table 1.1 HHV and LHV of hydrogen and common fossil fuels at 25°C and 1 atm.....	3
Table 1.2 Classification of selected hydrogen manufacturing approaches.	6
Table 1.3 Summary of worldwide power production capabilities of sustainable energy resources.	8
Table 1.4 An outline of solar hydrogen generation approaches.....	10
Table 3.1 Charge carrier mobility data of selected semiconductors at 298 K.....	44
Table 3.2 Electrical conductivities for selected electrolytes and their resultant resistances and voltage drops at a current density of 5 mA/cm ²	55
Table 4.1 Pressure, temperature, pH sensor characteristics.	64
Table 4.2 Solubility, reactivity/corrosivity, and price comparison of Cl ⁻ /OH ⁻ salt pairs.	64
Table 4.3 Selected technical properties of some commercially available membranes.	66
Table 4.4 Relative errors and accuracy related to measurement devices.....	77
Table 5.1 Stream definitions of experimental setup during various processes.....	81
Table 5.2 Definitions and mass flow rates of hybrid reactor system (Processes 1 and 2).	88
Table 5.3 Summary of stream mass flow rates and concentrations of hybrid reactor (Processes 3 and 4).....	90
Table 5.4 Minimum theoretical required potentials of anode and cathode half reactions (Processes 1 and 2).....	96
Table 5.5 Minimum theoretical required potentials of anode and cathode half reactions (Processes 3 and 4).....	96
Table 5.6 Stream descriptions and associated mass, energy, exergy, and exergy flow rates of integrated system.	98
Table 5.7 Summary of energy, entropy, and exergy flow rates of Streams 4–7.	100
Table 5.8 Summary of energy and exergy efficiencies of integrated system.....	100
Table 6.1 Summary of uncertainties during the Process 1 experimental runs.	124
Table 6.2 Summary of uncertainties during Process 2 experimental runs.	141
Table 6.3 Summary of uncertainties during Process 3 experimental runs.	156
Table 6.4 Summary of uncertainties during Process 4 experimental runs.	172
Table 6.5 Performance comparison of selected case studies.....	194

Table 6.6 Performance and cost comparison of selected case studies.	199
Table 6.7 Performance, cost, and emissions comparison of selected case studies.....	203
Table 6.8 Description of selected case studies used in optimization study.....	205
Table 6.9 Overall performance, cost, and emissions comparison of selected case studies used in optimization study.	208

NOMENCLATURE

A	Area (m ²)
c	Cost per unit exergy (\$/GJ)
\dot{C}	Cost rate (\$/s)
E	Energy (kJ)
\dot{E}	Energy rate (kW)
E ^o	Open circuit voltage (V)
ex	Specific exergy (kJ/kg)
Ex	Exergy (kJ)
$\dot{E}x$	Exergy rate (kW)
f	Exergoeconomic factor
F	Faraday constant (9.6485 x 10 ⁴ C/mol)
g	Gravitational acceleration (9.80665 m/s ²)
G	Gibbs free energy (kJ)
\dot{G}	Gibbs free energy rate (kW)
h	Specific enthalpy (kJ/kg)
H	Enthalpy (kJ)
i	Current density (A/m ²)
I	Irradiance (W/m ²)
i _o	Current density (A/m ²)
K	Electrical conductivity (ohm ⁻¹ -m ⁻¹)
m	Mass (kg)
\dot{m}	Mass flow rate (kg/s)
M	Molality (mol/L)
MW	Molar mass (kg/kmol)
n	Number of moles (mol or kmol)
\dot{n}	Molar flow rate (kmol/s)
P	Pressure (kPa)
Q	Heat (kJ)
\dot{Q}	Heat transfer rate (kW)

R	Universal gas constant (8.314 kJ/kmol-K)
s	Specific entropy (kJ/kg-K)
S	Entropy (kJ/K)
\dot{S}	Entropy rate (kW/K)
t	Time (s)
T	Temperature (°C or K)
v	Velocity (m/s)
V	Voltage (V)
W	Work (kJ)
\dot{W}	Work transfer rate (kW)
x	Mass fraction
y	Mole fraction
z	Altitude (m)
\dot{Z}	Cost of owning and operating the system (\$/s)

Greek Symbols

α	Portion of the solar light used by the photocatalyst (photocathode)
γ	Activity coefficient
Δ	Change
η	Energy efficiency
λ	Wavelength (nm)
ρ	Density (kg/m ³)
ψ	Exergy efficiency

Subscript and Superscripts

A	Anode
C	Cathode
ch	Chemical
cv	Control volume
dest	Destruction
e	Electron
en	Energy

ex	Exergy
g	Band gap
gen	Generation
in	Inlet stream
ke	Kinetic
mix	Mixture
out	Outlet stream
pe	Potential
ph	Physical or Photo
s	Salt (NaCl or NaOH)
sat	Saturated
sol	Solution
r	Reactor
PV	Photovoltaic
°	Standard state
0	Reference state

Acronyms

APCE	Absorbed Photon-to-Current Conversion Efficiency
CEM	Cation Exchange Membrane
CERL	Clean Energy Research Laboratory
DOE	Design of Experiments
ED	Electron Donor
EES	Engineering Equation Solver
EIF	Environmental Impact Factor
FTO	Fluorine doped Tin Oxide
GF	Greenization Factor
GHG	Greenhouse Gas
HCF	Hydrogen Content Factor
HER	Hydrogen Evolution Reaction
HHV	Higher Heating Value
IPCE	Incident Photon-to-Current Conversion Efficiency

IR	Infrared
LCA	Life Cycle Assessment
LHV	Lower Heating Value
MEA	Membrane Electrode Assembly
MPEA	Membrane Photoelectrode Assembly
NHE	Normalized Hydrogen Electrode
OCP	Over Current Protection
OD	Optical Density
OER	Oxygen Evolution Reaction
OP	Over Potential
OVP	Overvoltage Protection
PE	Photoelectrode
PEC	Photoelectrochemical
PL	Photoluminescence
PSU	Power Supply Unit
PV	Photovoltaic
PV/T	Photovoltaic thermal
RCD	Relative Cost Difference
SPECO	Specific Exergy Costing
SS	Sum of Squares
STH	Solar-to-Hydrogen
TPES	Total Primary Energy Supply
UOIT	University of Ontario Institute of Technology
UV	Ultraviolet

CHAPTER 1: INTRODUCTION

1.1 Energy and Environmental Issues

One of the most important challenges of the twenty-first century is keeping up with the growing worldwide energy needs due to increasing population and rising standards of living. In 2013, 9,301 Mtoe energy was consumed by approximately seven billion people worldwide. By 2050, these numbers are expected to go up to 20,000 Mtoe and nine billion, respectively [1]. Figure 1.1 exhibits the global fuel shares of total primary energy supply (TPES), total final consumption, electricity production, and the resulting CO₂ emissions.

From Figure 1.1, it can be seen that 81% of the global energy supply is met by fossil fuels. Nevertheless, as a consequence of their limited supply and nonhomogeneous distribution, fossil fuels are not anticipated to keep pace with the growing energy demand. Even in the case of permanent demand, based on the current fuel exhaustion levels, oil is expected to be completely used up in less than 80 years [1]. This number can go up to 160 years for natural gas and 400 years for coal [1]. Along with that, while fossil fuel reserves are becoming less reachable as the easily-accessible ones are exhausted, the fossil fuel prices continue rising. The International Energy Agency states that the utilization of easy-to-reach oil has hit its highest point in 2006 [1]. The increasing trend in oil prices is expected to continue with almost no possibility of reaching pre-2000 oil prices.

In conjunction with financial matters, GHG (mainly CO₂) emissions as a consequence of fossil fuel consumption, and their influence on global warming, have been causing significant worries. Atmospheric CO₂ concentration was around 280 ppm in the beginning of industrial revolution and have been increasing by around 2 ppm/year since then. As of May 2011, this amount has reached 394 ppm. The International Panel on Climate Change (IPCC) has announced that beyond 450 ppm, atmospheric CO₂ concentration can potentially cause a temperature rise higher than 2°C, which could possibly harm the whole ecosystem permanently. Taking the existing level and estimated yearly growth of CO₂ emissions into account, 450 ppm can be reached in under 30 years, if no preventative measures are undertaken in next to no time [2, 3]. Given that fossil fuel consumption is the reason of the 99% of the CO₂ emissions (Figure 1.1), change over to a

non-fossil fuel energy source may possibly significantly decrease the CO₂- associated emissions and their unfavourable influence on global warming.

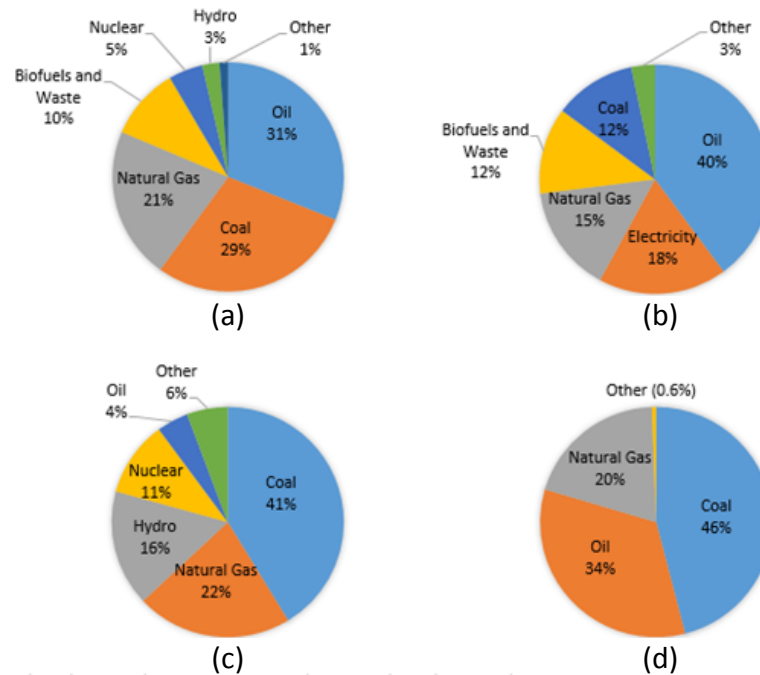


Figure 1.1 World's fuel shares of (a) TPES, (b) total final consumption, (c) electricity generation, and (d) CO₂ emissions in 2013 (other comprises geothermal, recovered heat, solar, wind, etc.) (data from [1]).

Meeting the significantly escalating global energy requirements with no or minimal environmental damage and fossil fuel dependence can only be accomplished by employing clean energy systems. These systems can present substantial environmental, energetic, financial, and societal advantages. To be considered actually sustainable, an energy system ought to meet these conditions: (i) insignificant or zero undesirable environmental or societal influence; (ii) negligible or no natural source exhaustion; (iii) capable of meeting the present and forthcoming population's energy requirements; (iv) reliable, affordable, and effective fashion; (v) air, land, and water safety; (vi) minor or zero net GHG emissions; and (vii) well-being at present with no burden to prospect generations [4].

Decreasing the dependency on fossil fuels and reducing potentially harmful emissions could be accomplished by using clean, vast, and sustainable energy sources. As a result of their low or zero end-use emissions and frequently reloaded sources, renewable energies (e.g., geothermal heat, sunlight, wind, waves, etc.) are respected as sustainable

replacements to fossil fuels. However, their discontinuous and inconsistent characteristics cause the requirement for effective storing methods. Renewable energies can be stored in chemical (i.e., hydrogen) or electrical energy form. Electricity is generally exploited as an energy storing option and it is heavily used on a daily basis. Hydrogen has been obtaining growing amount of consideration as a result of its favourable characteristics as an energy transporter. To confirm sustainable advancement and tackle economic and environmental issues, both electricity and hydrogen ought to be produced from renewable energy resources.

Hydrogen is an essential energy carrier for the following reasons: (i) it possesses good energy exchange effectiveness; (ii) it could be generated from water with zero emissions; (iii) it is plentiful; (iv) it could be stored in various arrangements (e.g., gaseous, liquid, or with metal hydrides); (v) it could be transferred across extended distances with minimal loss; (vi) it could be transformed into additional energy forms in more methods than every other fuel; (vii) it contains greater HHV and LHV than the majority of the traditional fossil fuels (Table 1.1); (viii) if it is generated from renewable energies and water, its manufacture, storing, transport and finale usage do not damage the environment. However, the majority of the hydrogen production methods are not well-established, causing elevated production cost and/or low efficiencies.

Table 1.1 HHV and LHV of hydrogen and common fossil fuels at 25°C and 1 atm.

Fuel	HHV (kJ/g)	LHV (kJ/g)
Hydrogen	141.9	119.9
Methane	55.5	50.0
Gasoline	47.5	44.5
Diesel	44.8	42.5
Methanol	20.0	18.1

Source: [5]

Unlike hydrogen, electricity is not suitable to store energy for extended periods of time. As mentioned earlier, hydrogen is a chemical fuel and it can be stored and transported by using the existing infrastructures. Electricity, on the other hand, has transient a nature. Therefore, the existing chemical energy storage and transport infrastructures cannot be employed for electricity. An additional drawback of electricity is the transmission losses due to the electrical resistance of system constituents. Because of its clear advantages over

electricity, hydrogen has turned out to be an alternative solution to energy supply, storage, and transport.

Here, we go further to compare hydrogen with other conventional fuels in terms of Environmental Impact Factor (*EIF*), Greenization Factor (*GF*) and Hydrogen Content Factor (*HCF*) to emphasize the importance of hydrogen as a unique energy storage option, through the following equations:

$$EIF = \frac{\text{kg } CO_2 \text{ product of combustion reaction}}{\text{kg fuel}} \quad (1.1)$$

$$GF = \frac{EIF_{max} - EIF}{EIF_{max}} \quad (1.2)$$

$$HCF = \frac{\text{kg of } H_2 \text{ in the fuel}}{\text{kg fuel}} \quad (1.3)$$

where EIF_{max} is the maximum value of EIF among the evaluated options. In this specific case with 3.6, coal is selected as the EIF_{max} .

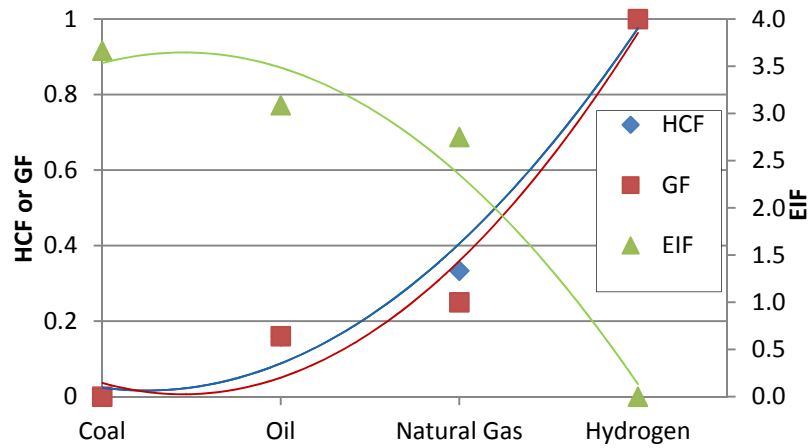


Figure 1.2 HCF, GF, and EIF of hydrogen and other fossil fuels [6].

As can be seen in Figure 1.2, with increasing HCF , the energy sources become greener (increasing GF) and the EIF decreases. This is a clear advantage of hydrogen in terms of reducing carbon-related emissions. In order to take full advantage of hydrogen, it needs to be manufactured from clean or renewable sources in reliable, affordable, and carbon-free ways [7].

1.2 Hydrogen Production Methods

Amongst the existing hydrogen generation alternatives, fossil fuel based ones are presently the most heavily used ones to manufacture hydrogen. On the other hand, switching to hydrogen economy necessitates it to be generated from clean or renewable and vast resources with the intention of building a sustainable energy system. In this section, various hydrogen production technologies are summarized. Figure 1.3 shows an outline of selected hydrogen generation techniques and Table 1.2 briefly describes each method along with their driving energies and material resources.

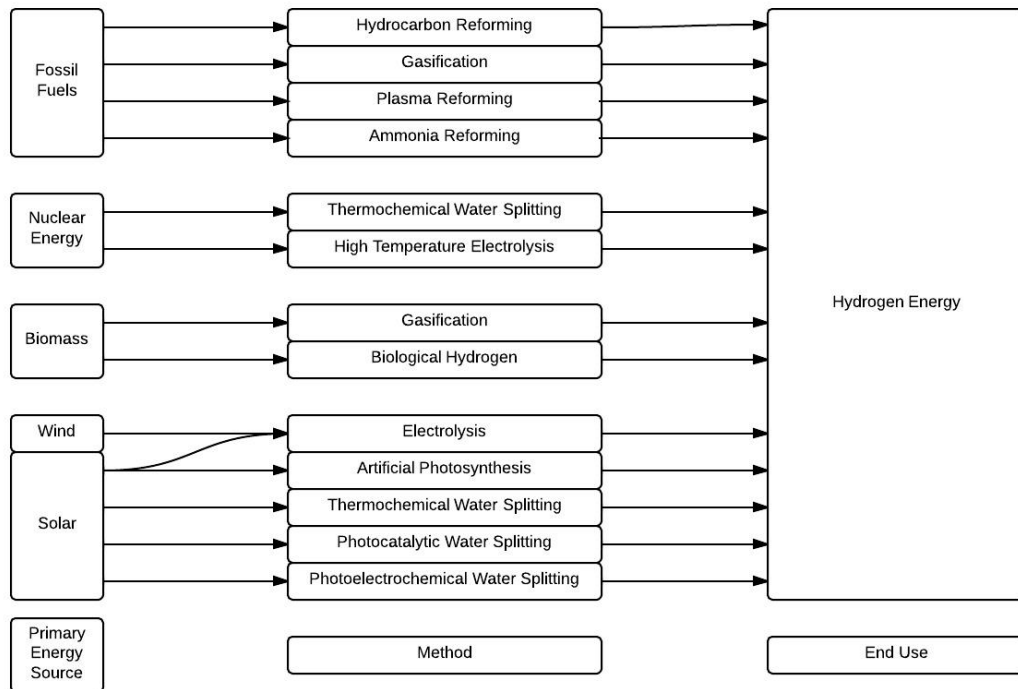


Figure 1.3 Outline of selected hydrogen generation routes classified by primary energy source and manufacturing method (modified from [8]).

Hydrogen from Fossil Fuels: Hydrogen can be manufactured from fossil fuels by using numerous production techniques, such as ammonia, hydrocarbon, and plasma reforming and gasification. Steam (in most cases natural gas) reforming, coal gasification, and partial oxidation are the most commonly exploited fossil fuel based hydrogen manufacturing approaches among the ones listed in Figure 1.3. Fossil fuel based hydrogen fabrication methods are currently being developed, established, and prepared to be commercialized;

and with these technologies, substantially uncontaminated hydrogen can be generated at moderately cheaper prices relative to the methods listed in Figure 1.3 and Table 1.2.

Table 1.2 Classification of selected hydrogen manufacturing approaches.

Hydrogen generation technique	Primary energy source		Material resources	Brief description
Electrolysis	Electrical energy		Water	Water decomposition into O ₂ and H ₂ by passing a direct current.
Thermochemical processes	Thermal energy	Thermochemical water splitting	Water	Chemical reactions are conducted cyclically with overall result of water molecule splitting.
		Biomass gasification	Biomass	Biomass converted to syngas and H ₂
PV-electrolysis	Photonic energy		Water	PV panels generate electricity to drive electrolyser.
Photocatalysis				Complex homogeneous catalysts or molecular devices with photo-initiated electrons collection are used to generate H ₂ from water.
PEC				A hybrid cell is used to generate PV electricity which drives the water electrolysis process.
High temperature electrolysis	Electrical + Thermal energy		Water	Thermal source and electrical power to split water in solid oxide cells.
Coal gasification			Fossil fuels	Coal is converted to syngas, then H ₂ extracted and CO ₂ separated/sequestered.
Fossil fuel reforming			Fossil fuels	Fossil fuels are converted to H ₂ with CO ₂ capture and sequestration.
Photoelectrolysis	Electrical + Photonic energy		Water	Photoelectrodes + external source of electricity.
Artificial photosynthesis	Photonic + biochemical energy		Biomass, water	Chemically engineered molecules and associated systems to mimic photosynthesis and generate H ₂ .

Source: [5]

For that reason, more than 95% of the worldwide hydrogen production is currently met by different fossil fuel feedstocks [9]. However, fossil fuel based hydrogen manufacturing approaches emit GHG (mainly CO₂); and in many circumstances, emission capture and storage systems reduce system effectiveness and escalate production costs. An additional drawback of these techniques is that they still depend on non-renewable and geographically restricted energy resources: fossil fuels, which challenge the sustainability of hydrogen economy [10].

Hydrogen from Nuclear: Hydrogen can be generated via thermochemical water-splitting cycles which function at temperatures around 500°C or higher by nuclear reactors [11]. Higher reaction rates and greater effectiveness could be accomplished at elevated temperatures. Until now, over 100 different high temperature water-dissociation thermochemical reactions have been studied [12]. Decreasing the temperature requirements to reach high effectiveness is a critical task for thermochemical cycles [13]. Thermochemical cycles necessitate specific reactors that are fabricated via chemically inactive distinctive materials equipped to resist high temperatures and corrosion [14]. Acquiring these distinctive materials in a cost-effective manner is an additional noteworthy challenge of thermochemical cycles. Nevertheless, thermochemical cycles demonstrate favourable performances to be respected as prospective techniques to generate hydrogen [15]. High temperature electrolysis has a capability to deliver high electricity-to-hydrogen conversion effectiveness of about 80% under pressure. Nonetheless, this amount cannot be attained when the total effectiveness is considered, as a result of low effectiveness of nuclear power plants (about 33%) [16]. Building reactors that work at higher exit temperatures is a potential approach to resolve the low effectiveness setback. For example, the 20% effectiveness at 350°C escalates to approximately 50% at 950°C [17].

Hydrogen from Biomass: Hydrogen can be generated via various kinds of biomass; for instance, forestry, industrial, living organism, and municipal waste, and crops. Biochemical, gasification, and thermochemical methods are generally utilized to generate hydrogen from biomass. Amongst the existing biomass based hydrogen generation paths, gasification is currently the viable alternative while simulated photosynthesis is the most favourable one. The chemical processes involved in biomass based hydrogen generation are quite comparable to those of fossil fuel based ones. Biomass is reflected as an abundant renewable resource (participating to 12% of the worldwide energy supply), and could possibly decrease CO₂ emissions, on condition that the CO₂ emissions are absorbed back by the biomass itself in the course of photosynthesis [18].

Hydrogen from Wind Energy: Using the electricity produced through wind turbines for electrolysis demonstrates a high possibility amongst renewable resources for generating emissions-free hydrogen, particularly for distributed systems. One of the challenges of this

method is the cost of wind turbines and electrolysers. Optimization of turbine-electrolyser-storage system is an additional challenge for producing hydrogen from wind energy [6].

Hydrogen from Solar Energy: Solar hydrogen generation could be achieved by means of various methods, such as artificial photosynthesis, PV-electrolysis, and photoelectrolysis, and thermochemical, photocatalytic and PEC water dissociation. Every method possesses particular benefits and drawbacks. When affordability, dependability, and environmental influence are taken into consideration, PEC hydrogen generation technique appears to be a favourable option amongst the existing solar hydrogen paths [19].

There is noteworthy volume of studies in the literature on hydrogen based systems with an objective of generating hydrogen effectively in an affordable and reliable manner with lowest environmental damage. The approaches stated to this point could be employed alone, or in conjunction with additional options with the intention of reaching this objective. Fossil fuel based hydrogen is not regarded as sustainable; however, these techniques could be utilized while the renewable hydrogen generation methods are getting more technologically advanced [20]. Table 1.3 evaluates the projected worldwide power production capacities of biomass, nuclear, solar, and wind energies.

Table 1.3 Summary of worldwide power production capabilities of sustainable energy resources.

Energy Source	Power (TW)	Remarks
Hydro	1.5	Necessitates damming of more than 70% of the existing rivers, may seriously impact the downriver and neighbouring environment as well as fish movement.
Wind	4	10–15% of worldwide technical capacity for on- and off-shore systems, probable influence on wildlife movement, unfavourable visual and sound impact.
Biomass	10	Needs 10% of Earth’s land to be covered with switch grass, might cause certain biodiversity damage and water contamination problems.
Nuclear	10	Involves building of a 1-GW peak power plant every 35 h for the following 40 years. Limited uranium sources indicate requirement for fast breeder or thorium reactors. The nuclear waste management is a debateable subject.
Solar	20	Necessitates 0.16% of the Earth’s surface to be covered with 10% effective solar cells. Cost and efficiency issues should be tackled.

Source: [21]

Table 1.3 demonstrates that compared to biomass, hydro, nuclear, and wind; solar energy is the single renewable energy resource that can supply 20 TW power generation. Moreover, solar energy does not cause as unfavourable consequences on the environment as the other options on Table 1.3. 0.16% of the Earth’s surface is around 816,000 km²,

which is equivalent to the total land area of Turkey and Greece, combined [24]. Consequently, covering an area of this magnitude with 10% effective solar cells is a vastly difficult mission. With the intention of tackling this subject, an effective solar-to-hydrogen path ought to be established with lowest environmental influence and improved hydrogen generation yields and rates.

The most appropriate hydrogen generation method selection depends on numerous internal and external system features given that every technique has both benefits and drawbacks. Resource accessibility, affordability and reliability, geographic position, population and climate, and compatibility with the current infrastructure are some of the criteria to bear in mind when selecting the most advantageous hydrogen generation path. Fossil fuels are estimated to meet a 25–30 TW energy utilization for at least a few centuries [21]; consequently, they are anticipated to be utilized as the principal hydrogen resource while the required infrastructure is being developed to generate hydrogen from renewables in TW level [22, 23].

1.3 Solar Hydrogen Production

Solar energy, by means of a renewable and abundant source, could become a probable sustainable resolution to the growing global energy demand. Approximately 30 minutes of solar irradiation reaching to the Earth's surface comprises as much energy as the worldwide annual energy consumption [25]. An additional benefit of solar energy is its comparatively small gradual system expansion price relative to traditional fuels [26].

Despite its many advantages discussed in Section 1.2, solar energy possesses an intermittent character; day/night cycles and hazy days greatly influence the quantity of solar energy gets reaching to the Earth's surface. For that reason, solar energy necessities to be stored in an altered fashion with the intention of providing a constant energy supply. As a chemical fuel, hydrogen appears to be a favourable storage material due to its high energy storing capability and easiness of transportation [27].

Given that water is a reliable and easily manageable resource of hydrogen, water dissociation is a favourable path for solar to hydrogen energy transformation. A visible light photon has a minimum and maximum energy of 1 eV and 3 eV (or 100 kJ/mol and

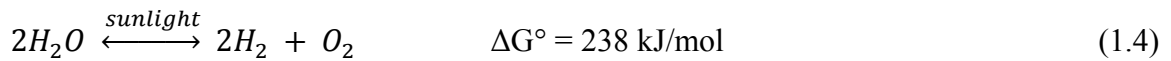
300 kJ/mol), respectively, which is sufficiently adequate to generate hydrogen through water dissociation [24]. A variety of the available paths for solar hydrogen generation are briefly described in Table 1.4. More information on these methods can be found from van de Krol and Grätzel [24] and Chen et al. [28].

Table 1.4 An outline of solar hydrogen generation approaches.

Solar H ₂ Production Systems	Type	Processes	Process Description	End Products
PV	Low Temperature	Electrolysis	Water electrolysis	H ₂ , O ₂
Photocatalytic		Photocatalysis	Water photocatalysis	H ₂ , O ₂
PEC		Photoelectrolysis	Water photoelectrolysis	H ₂ , O ₂
Photobiological		Photobiolysis	Plant and algal photosynthesis	H ₂
Concentrated Solar Thermal	High Temperature	Thermolysis	Thermal dissociation of water	H ₂ , O ₂
		Thermochemical Cycles	Thermochemical cycles using metal oxides	H ₂ , O ₂
		Gasification	Steam–gasification of coal and other solid carbonaceous materials	H ₂ , CO ₂
		Cracking	Thermal decomposition of natural gas (NG), oil, and other hydrocarbons	H ₂ , C
		Steam Reforming	Steam reforming of NG, oil, and other hydrocarbons	H ₂ , CO ₂
		Electrolysis	Water electrolysis via high temperature and solar thermal electricity generation	H ₂ , O ₂

Source: [29]

The solar water splitting reaction can be written as follows:



This study focuses on electrolysis, photoelectrolysis, photocatalysis, and PEC. One of the reasons for selecting these methods among the ones listed in Table 1.4 is to minimize safety issues, lower system energy necessities, and enhance system control through selecting low temperature processes rather than the high temperature approaches. Additionally, by lowering temperature constraints, large scale solar concentrators are no longer required, the system could function in environmental conditions, and consequently, the hybrid structure could operate greatly in small scales and in areas that are geographically inaccessible by the grid as well. Correspondingly, by utilizing chloralkali

method together with the designated solar hydrogen generation approaches, it is intended to transform by-products to commercially practical merchandises, and consequently, increase system effectiveness. The hybrid structure is developed in a way that product gases are accumulated with no requirement of post-separation.

1.4 Photoelectrochemical Hydrogen Production

PEC-based hydrogen generation is one of the most favourable technologies which could possibly deliver a clean, affordable, and reliable energy carrier by taking advantage of the ~120,000 TW of irradiation that continuously reaches the Earth's surface [25].

PEC based hydrogen generation theory has been considered for years since the original experiment in 1972 by Fujishima and Honda [30]. In 2014, Luo et al. [31] have confirmed a PEC solar-to-hydrogen exchange effectiveness of 12.3%, emphasizing the abundant possibility for a PEC technology that merges the solar energy collecting and water electrolysis in a stand-alone mechanism. Fundamentally, once a PEC semiconductor apparatus with the appropriate set of characteristics is submerged in an aqueous electrolyte and exposed to sunlight, the photon energy is transformed to electrochemical energy, that could dissociate water into hydrogen and oxygen. As a result, discontinuous solar energy is transformed into a characteristically more storable energy form.

PEC water dissociation is an effective yet complicated procedure. In order to direct it to happen effectively and sustainably, a number of strategic conditions need to be sustained concurrently: (i) the semiconductor structure should produce adequate voltage with the introduction of incoming photon energy to dissociate water, (ii) the overall band gap needs to be small enough to absorb a substantial percentage of the solar spectrum, (iii) the band edge potentials at the surfaces has to cover the hydrogen and oxygen redox potentials, (iv) the structure should display long-standing robustness against corrosion in aqueous electrolytes, and lastly, (v) the charge transportation from the semiconductor surface to the electrolyte has to be efficient to reduce energy losses because of the kinetic overpotential and it should be selective for the hydrogen evolution reaction (HER) and oxygen evolution reaction (OER). Currently, no affordable substances and/or systems satisfy all of these requirements for feasible hydrogen generation. Despite the fact that

research and development is continuing to encounter substances with appropriate attributes that address these conditions, improvements in material science and interfacial electrochemistry are still required [28].

Numerous published books [24, 28, 32] and review articles [33-35] consist of outstanding analyses of the essential theories of PEC. Within PEC structures, arriving photons ($h\nu$) produce electrons (e^-) and holes (h^+). The photogenerated electrons and holes are disconnected afterwards and pass through the semiconductor in reverse ways. The holes power the OER at the surface of the semiconductor working electrode. At the same time, the electrons are transported to the surface of the counter electrode to run the HER. Minimum possible voltage required to dissociate water (ΔE°) is 1.23 V.

Along with the thermodynamic prerequisite, there are overpotentials related to powering the hydrogen evolution reaction (OP_{HER}) and oxygen evolution reaction (OP_{OER}) at the solid-liquid interface. Decreasing these overpotentials by means of the advances in effective catalysis intended for both of the half-reactions is a fundamental measure to develop greatly effectual water dissociation designs [28].

Second law of thermodynamics related losses through the photogenerated electrons and holes should be taken into account as well [26, 27, 36]. The actual powering force for water dissociation is presented as photovoltage (V_{ph}). As a consequence of the losses happening due to several reasons, such as spontaneous emission, partial light absorbing, and electron-hole recombination [36], V_{ph} is always less than the band gap of the semiconductor. Additional circumstances for example non-ideal band assembly configuration could further decrease accessible photovoltage.

Semiconductor substance band gap has a significant influence on PEC solar-to-hydrogen (STH) transformation effectiveness. It is essential to put emphasis on the fact that only band gap is not adequate to estimate the PEC water dissociation competence. If the photovoltage generated via the semiconductor is not sufficient to overcome thermodynamic obstacles and overpotential losses, water dissociation does not take place, and STH efficiency cannot be distinguished.

In spite of the challenges, there are promising paths for accomplishing the essential objective of affordable, reliable, emission-free, and efficient PEC hydrogen generation. For

sustained advancement in tackling the most significant outstanding technical and financial obstacles, commonly acknowledged criteria in the classification and reporting of PEC constituents and apparatuses are required. This is fundamental to allow scientists from diverse backgrounds to describe their findings in means which permit direct assessments. It is estimated that wide-reaching implementation of consistent approaches for distinguishing, recording and inspecting PEC constituents would cause more precise and trustworthy data. This will also accelerate the policymaking procedure for ordering research sources in the direction of the most favourable paths. Quantifying technical obstacles and bottlenecks throughout consistent approaches would essentially demonstrate to be important in forming research concentration fields and innovative directions to tackle these challenges. A comprehensive and widely-accepted understanding of the constituents and systems for PEC hydrogen generation would unquestionably assist research and development, and improve the subject in the direction of developing mechanisms to address all of the PEC prerequisites.

As research and development advances, the improvement of a complete set of standard procedures would turn out to be gradually significant to the research community. These procedures can provide regulation to satisfactory and undesirable exercises in the representation of PEC constituents as well as the measurement and reporting of efficiencies and the stability of such devices. It is anticipated that the approaches pronounced in this study will be advanced and extended in upcoming works.

1.5 Motivation and Objectives

In this section, motives behind this study are introduced and objectives which are set to be achieved during the course of this research are listed.

1.5.1 Motivation

Among available renewable energy options, sunlight is the only resource with sufficient abundance to replace most or all of our current fossil energy use. However, existing PV and solar thermal technologies cannot be scaled infinitely due to the temporal and geographic intermittency of sunlight. Therefore, efficient and inexpensive methods for

storage of solar energy in a dense medium are needed in order to greatly increase the utilization of solar energy as a primary resource. Despite their vast amount of potential advantages, the viability of PEC-based hydrogen production systems at different scales is still unclear. The lack of satisfactory solar hydrogen production systems which are environmentally benign, low cost, efficient, and safe is one of the main problems for the transition to a solar energy based hydrogen economy.

The underlying motivation of this work is the potential for combining PEC with chloralkali process in a hybrid reactor to improve the solar spectrum utilization and hydrogen production yield as well as converting the by-products into commercially valuable commodities. For this purpose, a system consisting of a photoactive ion selective membrane to carry out PEC process combined with chloralkali is developed as a method for solar fuel generation.

1.5.2 Objectives

The specific objectives of this thesis study are given as follows:

1. To develop the continuous type hybrid PEC-chloralkali reactor for each of the process types:
 - a. Electrolysis: In the absence of sunlight, the reactor works as an electrolyzer. The inputs are saturated NaCl solution, H₂O, and electricity. NaCl and NaOH solutions are used as anolyte and catholyte, respectively. H₂ and Cl₂ gases, and NaOH solution are main outputs of the system. The system operates continuously with the anode and cathode separated by a selective cation exchange membrane.
 - b. PEC process: In a PEC, cell current and voltage are simultaneously produced upon absorption of solar light by one or more of the electrodes. The inputs and outputs of PEC are the same as photoelectrolysis. However, in PEC process, H₂ is produced via both photoelectrolysis and photocatalysis.
2. To design electrolysis and PEC experimental studies:
 - a. To select the suitable materials research for each system component, such as Cu₂O coated membrane electrode assembly (MEA) instead of two separate electrodes and an ion selective membrane.

- b. To select the primary variables to investigate production yields and system performance and method of monitoring and control to direct experiments. These variables are applied potential, solar simulator's irradiation level, temperature, inlet flow rate, and H₂ production via volumetric displacement cylinder.
 - c. To determine the operating conditions for each process type by defining input parameters to be varied (temperature, inlet flow rate, and irradiation level), control parameters to be monitored (temperature, applied voltage, current generation), and output parameters to be measured (H₂ production via volumetric displacement cylinder).
3. To conduct various experimental studies on each process type based on different parameters and environmental conditions to investigate the effect of key variables on product yields and system performance:
 - a. Electrolysis: Investigate the effect of anolyte and catholyte flow rates and operating temperature. In this case, the system is tested at four different operating temperatures (20, 40, 60, and 80°C) and three different flow rates (0.25, 0.50, and 0.75 g/s). By measuring pH of outlet streams, quality and pressure of the gases leaving the anode and the cathode, ensure the electrolysis and chloralkali reactions are proceeding in a controlled environment and examine how each parameter affects the H₂ production rate and energy requirements and losses within the system.
 - b. PEC process: Study the effect of light intensity, operating temperature, and anolyte and catholyte flow rates. In order to determine the catalytic activity of the photocathode, compare the H₂ production yields with electrolysis experiments. In this case, the system is tested at two different irradiation levels (600 and 1200 W/m²), four different temperatures (20, 40, 60, and 80°C) and three different flow rates (0.25, 0.50, and 0.75 g/s).
4. To perform comprehensive energy and exergy analyses for electrolysis and PEC experiments:
 - a. To carry out mass, energy, entropy, and exergy balance equations for all components and use the Engineering Equation Solver (EES) software to solve the balance equations.

- b. To perform electrochemical modeling to investigate the relationship between production yields and applied voltage, incident solar irradiation, and/or any potential voltage drops.
 - c. To compare the results of the balance equations and electrochemical model calculations with experimental outputs, and highlight any inconsistencies and their significance.
 - d. To calculate the energy and exergy efficiencies of the system, conduct parametric studies by altering key parameters affecting the system within an acceptable range, and perform exergy analysis to investigate the potential challenges on the system.
 - e. To determine the exergy destruction with their magnitudes and identify the effects of different parameters, such as irradiation level, inlet flow rate, and environmental and operating temperatures on rate of exergy destruction.
 - f. To conduct exergoeconomic and exergoenvironmental analyses of the system in order to relate exergy with cost and environmental impact.
5. To utilize a multi-objective optimization technique on the system parameters (i.e., operating temperature, inlet flow rate, photoactive area, and environmental temperature) with respect to (i) exergy analysis to improve the system efficiency, (ii) exergoeconomic analysis to reduce the associated cost, and (iii) exergoenvironmental analysis to reduce the environmental impact.
6. To apply optimized operating parameters on the system to improve system performance by increasing H₂ production yields, efficiencies, and minimizing losses.

1.6 Summary of Approach and Rationale

In this thesis, a comprehensive investigation of the hybrid PEC-chloralkali reactor and its integrated system is developed and various assessments are performed by using various tools of thermodynamics, thermochemistry and economics, and by conducting experimental research on the hybrid reactor.

Initially, the hybrid PEC-chloralkali reactor is simulated by using the EES software in order to decide the key operating parameters, such as anolyte and catholyte flow rates and required voltages. Two different processes are experimentally investigated in this

study: electrolysis and chloralkali. Both operation types are tested under three different light irradiation levels (no light, low intensity, and high intensity) using similar operating parameters, such as inlet flow rates, temperatures, and voltages. During the experimental studies, three different inlet flow rates (0.25, 0.50, and 0.75 g/s) and four different operating temperatures (20, 40, 60, and 80°C) are used to investigate H₂ production rates and efficiencies of different operation types. A MATLAB code is also adapted to determine uncertainty of the experimental results. Experimental H₂ production and efficiency results are compared to the EES model outputs for all cases to evaluate how well the models agree with the actual experimental results.

Further investigation is conducted by scaling up the system simulated in EES software. Scaled up reactor model is then integrated into a multi-generation system which consists of a solar splitter which sends the solar irradiation up to wavelength of 400 nm directly to the reactor. Rest of the incoming solar energy is sent to a PV panel in order to generate the electricity to back up the reactor. Excess electricity is stored and considered as another useful product. PV panel is cooled down in order to increase the operating performance and minimize any losses related to heating up. This recovered heat is sent to the reactor when operating at temperatures higher than the environmental temperature. Excess heat is stored and considered as another useful output.

The integrated system is analyzed by using thermodynamic tools (mass, energy, entropy, and exergy) by considering all components. The performance results of the integrated system is then evaluated and compared to existing electrolysis, chloralkali, PV-electrolysis, and PEC systems. The exergoeconomic and exergoenvironmental analyses of the final design are conducted based on the state point information from thermodynamic analysis, and a comparison is made with electrolysis, PV-electrolysis, and PEC in terms of efficiency, environmental impact, and economics. A multi-objective optimization study of the final design is also conducted by considering system cost, environmental impact, and efficiency as objective functions to be enhanced.

A thermodynamic assessment of the integrated system is performed to provide a better view of H₂ production performance of the system. Several parametric studies are conducted to optimize system efficiencies by considering several system and

environmental parameters. These parameters are operating temperature, inlet flow rate, environmental temperature, and photoactive area.

1.7 Thesis Outline

This thesis contains seven chapters. A comprehensive introduction and background on energy and environmental issues and selected H₂ production methods, and motivation and objectives of the thesis are provided in Chapter 1. Chapter 2 focuses on literature review on PEC, including reactor design, electrode selection, membranes and MEA, and system hybridization. Detailed background on PEC water splitting is given in Chapter 3. Chapter 4 represents the present experimental apparatus and procedure. In this chapter, both integrated system and hybrid PEC-chloralkali reactor is introduced and the present experimental reactor setup along with auxiliary components are explained. The present experimental procedure, evaluation of uncertainties, and details of system integration are also provided in Chapter 4. Detailed thermodynamic analyses and optimization of the hybrid reactor and its integrated system are represented in Chapter 5. Chapter 6 provides results as well as their comprehensive comparison by providing deep information on main and detailed findings from this research. And finally, conclusions and recommendations are provided in Chapter 7.

CHAPTER 2: LITERATURE REVIEW

2.1 Introduction

In the literature, there are several studies focusing on how hydrogen can be one of the most effective solutions playing a significant role in providing better environment and sustainability. Among the possible hydrogen production methods studied in the literature, natural gas steam reforming is the most commonly used process, resulting heavy GHG emissions. Around 50% of the global hydrogen demand is met by natural gas steam reforming, 30% from oil reforming, 18% from coal gasification, 3.9% from water electrolysis, and 0.1% from other sources [4]. In order to remove the adverse effects of fossil fuel utilization on the environment and human health, hydrogen should be produced from clean and abundant sources with environmentally benign methods.

Dincer [5] has categorized hydrogen generation methods, based on various criteria, such as elemental and material source, energy sources used, operating conditions, targeted applications, etc. “Green hydrogen” concept has been introduced for hydrogen production options and discussed them accordingly based on the systems and applications.

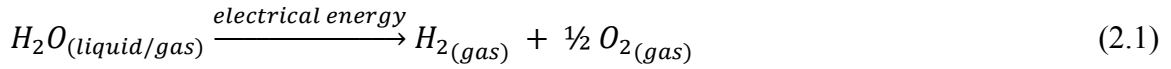
Dincer and Rosen [37] have used thermodynamics and life cycle assessment (LCA) to investigate various hydrogen production and fuel cell options based on their sustainability features. They have investigated sustainability and efficiency of these systems by using second law of thermodynamics, namely exergy.

Dincer and Zamfirescu [20] have technically reviewed and grouped a number of sustainable hydrogen generation methods based on their energy and material resources. They have classified these several resources, ranging from natural sources to wastes and from conventional resources to clean energy resources.

Since the Sun and water considered as sustainable sources, solar based water dissociation is an attractive process of hydrogen production. Therefore, many studies have discussed the potential benefits of these sources for sustainable development [38, 39].

As a simple and efficient method of splitting water into hydrogen and oxygen, electrolysis has been extensively studied in the literature since the beginning of the 1800s [40]. Electrolyzers can produce hydrogen in both batch and large scales, and they are

currently used to meet about 4% of global hydrogen demand [41]. The net reaction during electrolysis can be written as:



Since the first modern energy crisis in 1973, there has been ongoing effort to reduce the energy requirements of electrolysis [42]. Introduction of solar electricity via PV panels, and the possibility of its electrolysis applications (electrochemical, photolysis, and PEC applications) received a lot of attention from the scientific community [43].

On the other hand, using photocatalysis is another promising option for clean solar hydrogen production, being potentially applicable for large and small scale hydrogen generators [44]. Photocatalysis provide reasonable solar-to-H₂ efficiency, low process cost with reasonable but cheap catalysts selection, and is able to separate H₂ and O₂ evolution during reaction. They are small reactor systems meeting the requirements for residential applications can be mass produced, thus providing a huge market potential [21, 27].

This approach has been employed by many scientists for clean and sustainable hydrogen production especially after Fujishima and Honda's study [30] on PEC-based water splitting using TiO₂ as photocatalysis. Since then the reaction has been studied extensively by many researchers. In 2013, Kamat and Bisquert [45] have reviewed some past studies on photoreactions generating hydrogen. Also, various photocatalytic systems for hydrogen production have been reviewed by Acar et al. [19] and Zamfirescu et al. [46].

PEC-based hydrogen production can be a cost effective way to produce hydrogen. However, the main concern of PEC process is increasing the efficiency and stability of the photoactive materials [47, 48] to achieve the required efficiency target of 10% to be viable for commercialization [44, 49]. At the moment, stable photoelectrode materials are mostly based on metal oxides which have low efficiency [50, 51], while some materials which provide required efficiency to be commercialized are based on multi-junction conventional semiconductor with short life time [52, 53].

This chapter focuses on literature review on PEC-based hydrogen production including reactor design, electrodes, membranes and MEA, system hybridization, overall

system analysis, and system integration. In the end, main gaps in the literature are identified and the need for the current study is explained.

2.2 Photoelectrochemical Hydrogen Production

The simplest system for exploring the idea of visible light water splitting is a PEC system [54] since it avoids potential difficulties as a result of the unwanted H_2 – O_2 recombination by dividing anode and cathode. Because the potential of electrons in trap states below the conduction band is not sufficiently negative to reduce water, a bias voltage (330 mV) must be applied for water splitting to occur. The low quantum efficiencies of PEC systems could be tackled by an enhanced design at molecular level [54].

Liao et al. [55] have detected that in a PEC, the photocatalyst is deposited as a thin film on an electrode to develop a photoanode or photocathode to accomplish the water-dissociation reaction in electrolyte solution. Still, an exterior circuit is necessitated to regulate the photogenerated electron flow from the photoanode to a cathode, where hydrogen is generated. As water is dissociated to generate hydrogen, oxygen is produced at the anode at the same time. The photogenerated electron reacts with the proton at the cathode section, generating hydrogen.

There are many kinds of PEC-based hydrogen production systems and photosensitive semiconductors investigated and reported in the literature. The most promising option so far is TiO_2 . In addition to TiO_2 , numerous other semiconductors have been investigated, such as, $BiVO_4$, Fe_2O_3 , WO_3 , and ZnO . Metal nitrides and phosphides (e.g., GaP and Ta_3N_5), metal oxy-nitrides (e.g., $TaON$), and n- and p-type silicon (Si) have also been considered in the available literature.

A completely integrated arrangement of nanoscale photoelectrodes manufactured from inorganic nanowires designed for direct solar water dissociation has been explained by Liu et al. [56]. The artificial photosynthetic structure consists of two semiconductor light absorbers with large surface area, an interfacial layer for charge transportation, and spatially disconnected co-catalysts to accelerate the water reduction and oxidation. In the presence of modelled sunlight, a 12% solar-to-hydrogen transformation effectiveness is accomplished, which is similar to that of natural photosynthesis. A prototypical “Z-

scheme” structure with two light absorbing substances has been selected in their investigation to determine the competency of an integrated nanostructure to use solar energy to dissociate water [57]. Earth abundant and stable semiconductors, Si and TiO₂, have been preferred as the H₂-producing photocathode and O₂-producing photoanode, respectively. With illumination, photoexcited electron–hole couples are produced in Si and TiO₂, which absorb different sections of the solar spectrum. The photogenerated electrons in the Si nanowires are transferred to the surface and reduce protons to produce H₂. In the meantime, the photogenerated holes in the TiO₂ nanowires oxidize water to generate O₂. The holes from Si and electrons from TiO₂ are combined again at the ohmic connection, accomplishing the dispatch of the “Z-scheme” [57], comparable to that of natural photosynthesis.

Recently, a molecular water oxidation Ru catalyst has been manufactured and immobilized simultaneously with a molecular photosensitizer [Ru(bpy)₂(4,4-(PO₃H₂)₂bpy)]Br₂ on nanostructured TiO₂ molecules placed on conducting fluorine doped tin oxide (FTO) glass, establishing a photoactive anode (TiO₂) [58]. By employing TiO₂ in place of the working electrode in a three-electrode PEC, visible light powered water dissociation has been effectively established in an aqueous phosphate buffer solution, with O₂ and H₂ bubbles generated from the working and the counter electrodes, respectively. A high photocurrent density of more than 1.7 mA/cm² has been accomplished.

Lai and Sreekantan [59] have discovered that combining WO₃ with TiO₂ can enable enhanced charge division and effective visible light reaction. Georgieva et al. [60] have described the bi-component WO₃ and TiO₂ to demonstrate increased UV photocatalytic and photoelectrocatalytic action for the reason that of their valence and conduction band energy diagrams support electron injection from the conduction band of TiO₂ to that of WO₃ and hole transfer between valence bands in the reverse direction. This could decrease electron–hole recombination in both semiconductors. Thuy et al. [61] have presented that, integrating ZnSe with TiO₂ not only effectively decreases the recombination between photogenerated electrons and holes but also improves the absorption of solar energy. The low band gap of ZnSe accomplishes light absorption in broader spectrum range.

The application of inorganic dyes on TiO₂ surface has appealed remarkable concentration as a sensitization technique for visible-light powered PEC-based water dissociation. Meshram et al. [62] have observed that methylene blue (MB) dye interacted unsuccessfully with CuO as a photocatalyst but reacted in a different way under solar irradiation. Furthermore, they have observed that the degree of MB dye deprivation has not been the same for assorted crystal structures of the CuO photocatalyst. Le et al. [63] have applied Rh B dye on the surface of Co/TiO₂ substances and determined an effective visible absorbance edge band in the range of 450–600 nm and a marginally reduced band gap of 2.58 eV in comparison to Co/TiO₂ (2.75 eV) and TiO₂ (3.21 eV), along with enhanced photocatalytic water dissociation results performance outcomes.

The structure of TiO₂ also has significant impact on the effectiveness of photocatalysis for H₂ generation [64]. Hosseini and Momeni [65] have observed that the Pt-NP/TNT electrodes effectively generated a high current density for methanol electro-oxidation practices. Dong et al. [66] have shown that TiO₂ nanowire arrays have demonstrated improved PEC characteristics compared to those of casually positioned TiO₂ nanowires due to their smaller grain boundaries, directional electron transportation and improved light-processing competency. This innovative form of TiO₂ nanowire photocatalyst has a great potential. Chang et al. [67] have demonstrated that unoccupied crystal-like TiO₂ nano-fibers could bring improved photocatalytic activity in comparison to analogous solid TiO₂ nano-fibers. In another study, Petronella et al. [68] have confirmed that TiO₂ nanorods are more efficient photocatalysts compared to industrial TiO₂ P25 Degussa. Xiao et al. [69] have ascertained that the UV-diffuse reflectance spectra of all the N,S-Co-doped TiO₂ nanobelts investigated significantly broaden the absorption edge into the visible light section and demonstrate outstanding photocatalytic effectiveness in comparison to industrial Degussa P25.

Contrary to unattached photocatalysts, heterojunction semiconductors show enhanced performances for electron–hole separation and they could decrease the energy loss due to electron–hole recombination, which results improved photocatalytic activity. Jang et al. [70] have demonstrated that PV and PEC with junction semiconductors indicate significantly enhanced activities in comparison to designs containing single

semiconductors. They have established that the photoactivity of a system is enhanced as the photocatalyst's manufacture get more complex and sophisticated.

Rabbani et al. [71] have coupled PEC with chloralkali and tested the system in batch type operation. Acar and Dincer [72] have enhanced the studies on PEC and chloralkali in a continuous type hybrid system. Acar et al. [73] have coupled this hybrid system with a desalination unit, enhancing the products into H₂, Cl₂, NaOH, and fresh water.

2.2.1 Reactor Design

For PEC-based water dissociation, the photoreactor consists of some key components, such as electrodes, semiconductor based photoelectrodes, electrolytes, etc. This configuration is frequently called as a photocell. A number of review papers on photoreactors and/or photocells for PEC have been published in the last couple of years [33, 74]. Specifically, Minggu et al. [33] have methodically reviewed the main points of the PEC reactor vessels, from the operating procedures to the feasible arrangements, and they have also reported possible large-scale hydrogen generation experiments.

The earliest PEC-based water dissociation possibility has been pointed out by Fujishima and Honda [30], as discussed earlier. Their PEC system basically consists of a photoanode made from n-type TiO₂ and Pt counter-electrode.

Since Fujishima and Honda's ground-breaking study, remarkable assessments have been performed with the intention of developing PEC cells with enhanced effectiveness, from simple systems to state-of-the-art structures. Comparable to photoreactor of slurry-based water dissociation, the physical structure has an important effect on the overall efficiency. Here, PEC cells are explained in two different groups: (i) open photocells and (ii) photocells with gas separation and collection.

Open photocells

The very elementary structure of an open photocell (Figure 2.1) has three types of electrodes, namely (i) working electrode, (ii) counter electrode, and (iii) reference electrode. Generally, these electrodes are submerged in the electrolyte in an open container and the potential of the working electrode is regulated through a potentiostat. This photocell

structure is also known as three-electrode arrangement, and is perhaps the most frequently utilized alternative in small-scale experiments [75-77].

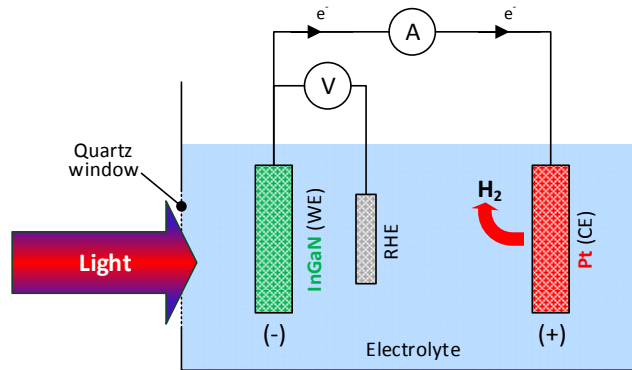


Figure 2.1 Illustrative representation of a sample open photocell (adapted from [76]).

Maeda et al. [78] have exploited SrNbO_2N as the working electrode, and Pt wire as the counter electrode, and Ag/AgCl reference electrode. Their electrolyte has been Na_2SO_4 solution (pH=6). Gas evaluation is investigated through gas chromatography technique. The photocell container could be manufactured from quartz or Pyrex glass and its shape may range from square to semi-round or round with the intention of enhanced utilization of incoming light irradiation [78]. The distance between electrodes is quite significant and consequently scholars are continuously seeking for new designs to maintain this distance stable throughout PEC experiments. For this purpose, a number of researchers have established PEC cells with stationary docks for each and every electrode.

Photocells with gas separation and collection

Considering that both H_2 and O_2 gases are produced during the PEC-based water dissociation procedure, gas separation is absolutely important bearing in mind the gas collection and safety hazard issues. Until now, numerous PEC designs with gas separation properties have been designed, developed, and tested.

Ion-permeable membrane divided PEC cells

A possible method to collect product gases separately is to position an ion-permitting membrane between the anode and cathode (Figure 2.2). Alternatively, anode and cathode

could be built connected by the membrane. The membrane permits ion interchange amongst the two partitions of the photoreactor. It also helps to collect the gases separately.

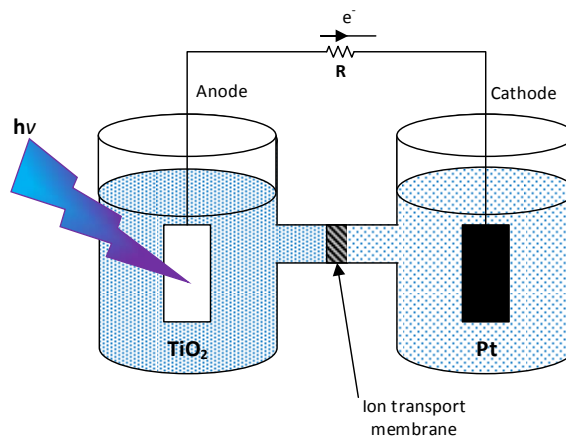


Figure 2.2 Illustration of a sample ion-permeable membrane divided PEC cell (adapted from [79]).

In a photoreactor designed by Ida et al. [79], the TiO_2 photoanode and the CaFe_2O_4 photocathode have been positioned in two quartz cells, and connected through a Nafion 117 film. Both of the quartz cells have been irradiated by using an Xe lamp. Nafion is frequently utilized as the ion-permitting membrane. However, Minggu et al. [33] have demonstrated that Nafion or other positive-ion interchange membranes are not suitable for cation-consisting electrolytes. In these systems, positive ions (e.g., Na^+) substitute H^+ in the membrane and delay the proton transfer across the membrane. In these situations, different separators could be utilized to substitute cation exchange membranes (CEM).

PEC cells with different separators

In addition to ion-permitting membranes, different separators could be utilized to separate the H_2 - and the O_2 -production; for instance, glass frit diaphragms, asbestos diaphragms, and others. Glass frit has the benefit of chemical, mechanical, and thermal robustness, and therefore is a suitable selection (Figure 2.3).

Asbestos based diaphragm is another type utilized in alkaline electrolyzers because of its advantageous hydrophilicity and capacity to block reverse-diffusion of OH^- . However, asbestos diaphragm usage is restricted due to its swelling characteristics and chemical instability in case of high electric current [80].

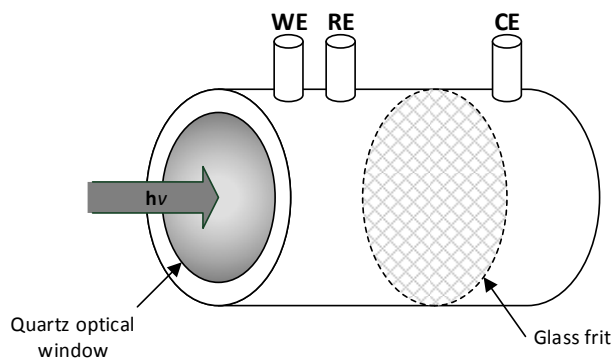


Figure 2.3 Illustrative representation of a PEC cell separated by a glass frit (adapted from [80]).

PEC cells with quartz window

Manufacturing a PEC reactor entirely from quartz or Pyrex glass is quite costly. Therefore, building a PEC reactor using more affordable substances is preferred. A possible approach for accomplishing this goal is to assemble a reactor using less costly substances but introducing a quartz window where the photons could enter to the reactor and activate the photoelectrode. The PEC reactors could be built by using glass, Perspex, Teflon, etc., and the quartz window can be stabilized through nuts and bolts with O-rings or gaskets.

2.2.2 Photoelectrodes

Photoelectrodes are commonly manufactured by depositing a thin sheet of semiconductor substances on top of the substrate through a conducting top surface. The substrate can be see-through conducting glass, such as fluorine-doped tin oxide (FTO) [77, 78, 81, 82] or a metal piece [75]. Semiconductor substances could be deposited basically by doctor blading technique [83]. New methods have been established to manufacture photoelectrodes with enhanced qualities in which the morphology and other characteristics of the semiconductor substances could be accurately monitored and regulated, involving anodization [80], radio frequency (RF) magnetron sputtering [84], hydrothermal growth method [77], electrophoretic deposition [75], atomic layer deposition [82], etc. A photoelectrode with improved qualities can be manufactured through enhanced ohmic contact treating and appropriate insulation [33, 85]. Following the semiconductor deposition on photoelectrode surface, an empty part of the substrate is frequently retained undeposited. The aim here is

to attach a copper wire to the photoelectrode with silver glue. Epoxy resin could be utilized to shield the photoelectrode excluding the photoactive part. And a glass tube is sufficient enough to protect the copper wire [33].

Photoelectrodes could be manufactured from a specific type of semiconductor alone or together with various types of semiconductor layers or even from homogeneous hybrid substances. For instance, semiconductors with various band gaps could be deposited onto a single substrate layer-by-layer, and as a result permit the photoelectrode to absorb a broader section of solar spectrum. Several semiconductor layers could as well be deposited on top of each other to shield the unstable semiconductors inside [82].

Acar and Dincer [86] have evaluated CdS, TiO₂, CdSe, WO₃, Fe₂O₃, and CuO/Cu₂O based photoelectrodes prepared by various coating methods as chemical vapor deposition, electrochemical deposition, electrodeposition, sol-gel, spin coating, and spray pyrolysis. They have carried out comparative performance evaluations for PEC-based hydrogen production. The photocurrent generation and voltage/light requirements of the selected photoelectrodes have been compared to evaluate the impact of material and method selection on PEC-based hydrogen generation. Their results have showed that among selected photoelectrode coating materials, CdS based photoelectrodes generate the highest photocurrent (3715.58 mA/cm²), followed by CdSe (2963.43 mA/cm²), CuO/Cu₂O (1873.33 mA/cm²), TiO₂ (1500.60 mA/cm²), WO₃ (1435.28 mA/cm²), and Fe₂O₃ (443.3 mA/cm²). Average photocurrent densities of selected coating methods have showed that photocathodes processed by spin coating produce the highest photocurrent (2343.57 mA/cm²), followed by electrochemical deposition (1623.36 mA/cm²), electrodeposition (1359.77 mA/cm²), spray pyrolysis (1217.50 mA/cm²), chemical vapor deposition (619.44 mA/cm²), and sol-gel (335.06 mA/cm²).

2.2.3 Membranes

A large amount of the photocatalytic membrane reactors (PMRs) investigated for H₂ production through water dissociation imitate the Z-scheme structure utilized by green plants during natural photosynthesis. Z-scheme fundamentally consists of a twofold photocatalyst structure intended for water oxidation (causing O₂ production) and for water

reduction (resulting H₂ generation). Additionally, a redox couple is utilized to regenerate the catalyst transferring the electrons amongst the two partitions of the reactor. A membrane is necessitated to separate the solutions with the H₂- and the O₂-photocatalyst and shuffling electrons through the electron redox moderator. Most commonly, a Nafion membrane which is tailored to permit the ions exchange, is utilized [35].

Nafion is a copolymer of tetrafluoroethylene and perfluoro(4-methyl-3,6-dioxo-7-octene-1-sulfonyl-fluoride). Nafion polymer is a thermoplastic balm which could be manufactured in various forms for instance beads, films, and tubes. The perfluorinated structure of the copolymer provides chemical and thermal stability which is hardly ever attainable in nonfluorinated polymers. The suspended sulfonyl fluoride assemblies are chemically altered to sulfonic acid resulting an ionic functionality. For instance, by straightforward soaking in an acidic solution, the film can be loaded with H⁺ ions [35].

The unique functional properties of Nafion polymer have permitted a comprehensive variety of functions. Many efforts have been performed to integrate semiconductor nanoparticles in a Nafion film. Deposition of Pt metal on one side of the film is an approach which is utilized to convert H⁺ into H₂ [35].

Seger et al. [47] have reported a TiO₂-Nafion-Pt integrated membrane structure with methanol as sacrificial agent and UV light illumination, without any applied voltage. TiO₂ photocatalyst has supported the methanol oxidation whilst H⁺ ions are transferred to the Pt particle surface through the Nafion membrane simultaneously. H⁺ ions have been converted to a H₂ at a production rate of 69 mL/h-cm².

An innovative double-cell where the Z-scheme benefits and the H-type reactor integrated, has been established by Lo et al. [87]. In their reactor, WO₃ and Pt/SrTiO₃:Rh powders have been utilized to produce O₂ and H₂, respectively. A CEM is used in between the two half-cells of the reactor, permitted the transmit of both protons and Fe(II)/Fe(III) ions in solution. In a different work, H₂ and O₂ have been generated by employing Pt/SrTiO₃:Rh and BiVO₄ by Yu et al. [88] in a dual reactor with a Nafion membrane.

Recently, an innovative membrane photosystem has been proposed by Tsydenov et al. [89] established on a porous polymeric membrane improved with Pt and TiO₂ to allow H₂ generation from ethanol dehydrogenation. A polytetrafluoroethylene filter adjusted with

polypropylene, thanks to its good chemical and physical stability during light irradiation, has been utilized in collaboration.

In another study, two-layer photoelectrode development has been examined by Liao et al. [90] intended for visible light water dissociation into H₂ and O₂. The photocatalyst, consisting in a layer of WO₃ and a layer of TiO₂ deposited on a Pt treated foil, has been examined in an H-type reactor and in photovoltammetry experimentations, presenting promising catalytic characteristics upon visible light irradiation. Photocatalytic tests have been conducted through UV and visible light demonstrating an improved performance in comparison to that of the TiO₂ electrode.

Moreover, Marschall et al. [91] have developed a membrane structure with dual chambers intended for uncontaminated H₂ and O₂ generation. In their system, membrane separated and simultaneously strengthened a carbon coated Degussa TiO₂-P25 photoanode and a Pt cathode. Sacrificial agents have not been utilized in their setup. Numerous membrane kinds, such as commercial Nafion, FKE (Fumatech) membranes, custom developed sulfonated polyethersulfone (sPES) flat sheet, and sPES/mesoporous-Si-MCM-41-nanoparticles [92] have been experimented in the photocatalytic system.

2.2.4 System Hybridization

Since it is not possible to directly store or constantly supply solar energy, the transformation of solar energy to a form of energy that can be stored has essential significance. In order to use low energy density solar flux as efficiently as possible, entire solar spectrum ought to be utilized effectually, and the effectiveness of each stage of the energy transformation process must be enhanced. An additional substitute for hydrogen generation via solar energy without consuming supplementary chemicals is a hybrid system. First hybrid system combining photochemical, thermochemical, and electrochemical reactions has been demonstrated in late 1970s [93].

Abdin et al. [94] have investigated hydrogen production, storage and conversion to electricity in integrated hybrid energy systems. In their study, the need for and state of the art in modelling such systems have also been briefly addressed. They have concluded that because of the commercial availability of its components, the hybrid system in which solar

electricity is used to electrolyse water and a fuel cell to consume stored hydrogen to produce electricity is the most promising hybrid energy system.

There is increasing interest in the use of solar–hydrogen hybrid energy systems for power supply in remote areas or other standalone applications. The attractions of such systems are zero GHG emissions, complete stand-alone operation over extended periods of time and low maintenance. The use of hydrogen for energy storage rather than batteries potentially allows season-to-season storage of energy and hence a smaller solar collector area with no need for a back-up diesel generator [95].

Belmili et al. [96] have studied the feasibility of a hybrid wind–PV power system to meet the load requirements for off-grid electrification and developed a strategy to optimise the size of the energy generation and storage subsystems. Their results have showed that the more reliable solution was that in which 80% of the load to be covered by PV and the other 20% by the wind turbines.

In another study, Baniasadi et al. [97] have developed and analyzed a novel hybrid structure for hydrogen generation through solar energy. They have hybridized a photocatalytic system through an exterior electrical supply, employment of a light powered proton pump, and effective photosensitizers. They have used energy and exergy methods to investigate their system's performance and compared the results with other existing water splitting methods. Their results have showed that hybridization resulted a satisfactory enhancement in the photochemical activity with nearly 30% escalation in effectiveness. In comparison to traditional electrolysis, solar powered approaches are moderately inadequate, and these systems require additional efforts aimed at commercialization goals. Low quantum efficiency of existing photocatalysts is a critical challenge to be tackled with the intention of decreasing energy and exergy destructions and losses.

A photocatalytic reactor triggered by solar energy and UV–visible light sources in continuous operation and actual process circumstances has been investigated for scale-up targets by Baniasadi et al [98]. They have used an assembly of a hybridized photocatalysis reactor that utilizes the light energy from both the Sun and a lamp, in conjunction with electrodes to substitute sacrificial electron donors that consume photogenerated holes or transfer charge to a metallic active center of catalyst that leads to hydrogen evolution. They

have utilized UV–visible lamps inside a sunlight concentrator to support the photoreactions during night or cloudy periods.

Zamfirescu et al. [99, 100] have provided useful data for planning and performing experiments with a specially designed photoreactor and also for various photoreaction applications, such as water splitting in continuous flow photoreactors, hybrid photocatalysis systems, or copper-chlorine compounds disproportionation using photonic radiation.

Hybrid structures, more specifically, the ones incorporate photocatalysis reactors and PV arrays have similarly been considered lately. A photochemical-PV hybrid structure that produces hydrogen and oxygen from water in different partitions has been demonstrated in a new study by Huang et al. [101]. It seems that photocatalysis could be employed by utilization of the UV radiation energy for water disinfection while the intermediate portion of solar spectrum is utilized to produce electricity for pumping purposes and to supply heating. A small scale model, which accomplishes these tasks, has been effectively built and confirmed by Fuentes et al. [102].

2.3 Overall System Analysis

Overall hybrid PEC-based hydrogen production system necessitates a wide-ranging investigation to incorporate each and every one of the countless characteristics of photo-induced hydrogen generation process. This analysis should cover topics starting from the irradiation area to kinetic reactions to charge transfer kinetics and diffusion. It requires experimental and mathematical approaches to collect sufficient information for a comprehensive scheme of water dissociation that is efficient, economically justifiably, and scalable for high quantity production.

Baniasadi et al. [103] have investigated the properties and performance of a comprehensive dual-cell water dissociation structure with photocatalytic hydrogen and electrocatalytic oxygen generation. For each cell, a variety of considerations influence the system efficiency. The consequential impact ought to be taken into account in an engineering design. The intra-molecular charge transfer and ionic diffusion in hydrogen

generating reactor are directly influenced by light irradiation, and photocatalyst concentration.

Analysis of a photochemical water dissociation system using a proton exchange membrane has been conducted by Zamfirescu et al. [26]. In their study, equations for adsorbed radiation, volume ratio of reactors, and proton exchange membrane area have clearly been stated and explained along with their key values. The authors have also defined overall system efficiency equation.

Zamfirescu and Dincer [104] have conducted a comprehensive overall system analysis of an integrated system for solar hydrogen production. In their study, equations for entropy constant for a single photon; energy, entropy, and exergy rates of solar irradiation; spectral reflectance; and optical loss factor have been explicitly stated and explained. The authors have evaluated energy, exergy, and entropy rates of each inlet/outlet stream of every component of the overall system. They also have provided energy and exergy efficiencies of each component along with corresponding equations as well as the improvement factors.

Rabbani et al. [105] have performed electrochemical modeling and analysis of a hybrid PEC-chloralkali reactor for hydrogen production. They have used electrochemical analysis to find the overall potential in the hybrid reactor. They have investigated the effects of current density, electrode distance, reactor operating temperature, and electrolyte concentration on reactor performance. In a different study, same authors [71] have conducted energy and exergy assessment to evaluate overall efficiencies of the hybrid PEC-chloralkali reactor. The authors have used various operating criteria and ranked the desirability of each scenario in terms of energy and exergy efficiencies.

Later, Acar and Dincer [72] have modified the hybrid reactor developed by Rabbani et al. [71, 105] for continuous type of operation. They have thermodynamically analyzed this hybrid system based on an electrochemical model. The authors have stated that their hybrid system photoelectrochemically dissociates water and conducts chloralkali electrolysis simultaneously. Their setup has reported to have a possibility to generate hydrogen in an efficient, reliable, and affordable manner and in an environmentally friendly technique by getting the most out of the exploited solar spectrum and transforming the by-

products into beneficial industrial commodities. Additionally, by utilizing electrodes as electron donors to power photochemical hydrogen generation, their hybrid reactor has minimalized possible contaminant releases. The products of the hybrid reactor have been listed as H₂, Cl₂ and NaOH, all of them are desirable commercial goods.

A scale-up analysis of a dual-cell photo reactor based on a kinetic and radiation model and mass balance of reactants has been presented by Baniyadi et al. [106]. Exergoeconomic analysis of photocatalytic water splitting plants with different production capacities has also been performed to provide detailed information on the economic aspects of the engineered overall hydrogen production process.

An overview of new hydrogen production methods under development at UOIT's Clean Energy Research Laboratory (CERL) using electricity, thermolysis, electrolysis, hydrolysis and photochemical methods have been presented by Dincer and Naterer [107]. The authors have provided descriptions, analysis methods, and sample results of the novel hybrid hydrogen production methods in a detailed manner.

2.4 System Integration

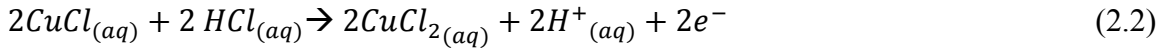
According to Dincer and Zamfirescu [108], it seems that the significant influence on the accomplishment of scaled up solar hydrogen generation is the synergistic incorporation of crucial technologies and additional valued commodities production and at the same time maintaining the system simplicity. For the reason that more than one products are obtained, the economic feasibility of the system is improved and the necessity of considerably enhanced hydrogen generation effectiveness turns out to be less rigorous. Hybrid systems that incorporate photochemical reactors for hydrogen generation with single-gap PV-electrolyzes might be an alternate opportunity to develop affordable solar energy systems.

One of the integrated hydrogen systems which uses solar energy as a primary source of energy has been installed in February 2007 and still working on the campus of Pamukkale University Denizli, Turkey [109]. Both passive and active solar heating systems are employed in a residential building. The goal of this project has been to design a unique, integrated system for the building, using only solar energy to meet all energy needs –with

no inputs from fossil based energy sources – and to provide an environmentally benign design and operation.

In their study, Zamfirescu et al. [110] have developed and thermodynamically analyzed a new conceptual design of a photochemical cell for copper chloride disproportionation and hydrogen generation. Their cell have coupled the protons that are:

(i). produced in copper disproportionation:



(ii). consumed in the photocatalytic water reduction process:



The configuration of an optical splitter system for concentrated solar radiation has been suggested and its benefits for system integration have been investigated.

Integration of a photocatalytic reactor with PV-electrolysis has been conducted by Zamfirescu et al. [27]. Their model have showed that, once incorporated with PV-electrolysis, the system's yearly hydrogen generation is 6.4 kg H₂/m² of solar accumulator. An additional twofold reactor scheme supported by a dye sensitized solar cell which incorporates photocatalysis and PEC methods for improving the amount of hydrogen production has been reported by Zamfirescu et al. [110]. In their system, the solar energy consumption factor has been enriched with incorporation of various light absorbing procedures through an attached solar thermal collector that also produces hot water by utilizing the infrared photons.

A comprehensive analysis has been conducted by Baniyadi et al. [111] to investigate the thermodynamic and electrochemical performance of an oxygen evolving reactor integrated with a catalytic hydrogen production reactor. An electrochemical model has been developed by the authors to quantify the over-potential requirements of the OER under various conditions. A transient phenomenological model for ion transfer in the OER has been provided in their study. The model has developed a better understanding of the

ion transfer phenomena occurring in a complete system and how it contributes to electrochemical cell performance.

Zamfirescu and Dincer [104] have designed and investigated an innovative integrated system which incorporates photocatalysis, PV, thermal engine, and chemical energy storing for enhanced solar energy utilization through energy and exergy approaches. Their system have generated hydrogen and sulfur from sulfurous waters particularly discharged from chemical and petrochemical processes. They have divided solar spectrum into three regions by utilizing optical structures covered with certain dielectric coatings: (i) the high energy spectrum, containing photons with wavelengths smaller than 500 nm, is utilized to produce hydrogen from water photolysis, (ii) the middle energy spectrum covering wavelengths between 500 and 800 nm is employed to produce electricity with PV and (iii) the low energy spectrum of photons with wavelengths longer than 800 nm is exploited to produce electricity with a thermally driven Rankine engine (RE).

Acar et al. [73] have integrated the hybrid PEC-chloralkali reactor initially designed by Rabbani et al. [71, 105] and modified by Acar and Dincer [72] into a desalination system. Their overall integrated system have consisted of several subsystems, such as light harvesting, desalination, and hybrid PEC-chloralkali. Light harvesting subsystem has heliostat field, hot mirror spectral splitter, upper/middle spectral splitter, lower spectrum absorption, and PV arrays. In their study, the authors have summarized mass, energy, entropy, and exergy balance equations for each and every component. Every stream's energy, entropy, and exergy content have been stated in [73]. In addition, the authors have conducted an economic analysis of the integrated system.

2.5 Main Gaps in the Literature

PEC-based hydrogen production has been studied actively by many researchers as it is a promising step towards reliable, affordable, and carbon-free energy systems. There are many studies in the literature investigating the effect of various novel photocatalysts, membranes, reactor designs, and electrolytes. There are also a few studies in the literature focusing on the integration of PEC systems into stand-alone hydrogen production systems.

It is also stated in the literature that, existing photoactive materials can only use a certain portion of solar spectrum, which has not been reported to exceed 20% in the literature. Despite the fact that there is significant amount of research going on in the field of photocatalyst fabrication – aiming to harness a larger portion of the spectrum, solar splitting has only been studied by a few number of researchers.

Solar splitting has a potential to support clean energy systems to reach maximum possible efficiencies. In the literature, this idea is gaining some momentum, but there is still a lot of potential and gaps in the literature to be filled. Hybrid PEC-chloralkali reactors show a great potential in terms of efficiency maximization and conversion of by-products into useful industrial commodities. A batch scale hybrid reactor has been designed, built and tested by Rabbani et al. [71, 105]. However, there is lack of design, system analysis, and experimental performance investigation on continuous type hybrid PEC reactors.

2.6 The Need for the Current Study

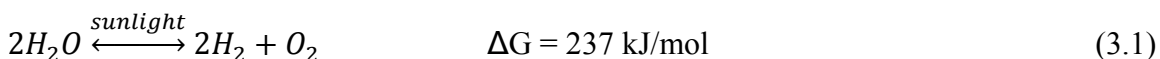
As mentioned in earlier sections, PEC-based hydrogen production has many advantages. However, there are several challenges associated with photoactive materials. For most of the photoactive materials, it is not possible to acquire stability, efficiency, appropriate band gap, and conduction and valance band locations simultaneously. For PEC-based hydrogen production to become more advantageous, a photoactive material should have these properties. In addition, a PEC system should use low cost and abundant materials. Currently, there has been no proven photoactive material in the literature meeting all of these criteria.

Additionally, within the available literature, there has not been any reported information on integrated hybrid PEC-chloralkali reactor combined with PV/T to provide H₂, Cl₂, electricity, and heat simultaneously. There has been also no study performed to investigate cost and environmental impact of such integrated multi-generation system. The aim of this study is to integrate PEC-based hydrogen production with chloralkali process and a PV/T system to minimize system losses by recovering all useful energy for the end user. This system is also suitable for scale up.

CHAPTER 3: BACKGROUND

3.1 Introduction

Based on the considerations discussed in earlier chapters, transformation of solar energy to hydrogen seems to be a desirable path. Water is an accessible and sustainable material resource for hydrogen generation. A rough calculation shows that about 5.6×10^{13} L of water is required to meet the projected annual global energy demand in 2035 (7.6×10^{20} J [1]) in the hydrogen form. This matches up to 0.02% of the yearly rain fall, or 0.000003% of the quantity of water in the world's oceans [24]. The water dissociation reaction can be expressed as



PEC-based hydrogen production has several advantages compared to possible solar hydrogen production methods as briefly summarized in Chapter 1. One of the key benefits of PEC-based H_2 production is that H_2 and O_2 are generated at different parts of the reactor. As a result, crucial safety issues are avoided and uncomplicated product gas separation is achieved without suffering from a serious energy loss due to post-separation. Another improvement is that this method could be accomplished at low temperatures, i.e., room temperature. As a result, there is no large-scale solar concentrator requirement. Large scale solar concentrators limit a system's operation to big central locations in sunny areas of the world. Last but not least, an additional benefit is that a PEC-based water splitting system can be assembled completely with no need of organic substances. As a result, PEC systems have a considerable amount of robustness and resilience in electrochemical solutions which is challenging to accomplish with organic or biological structures [112].

PEC-based hydrogen production provides two possible benefits compared to PV-electrolysis. The primary improvement is based on the information that existing electrolyzers necessitate reactor potentials of about 1.9 V with the intention of reaching their optimum functioning current densities of around 1 A/cm^2 . Since the thermodynamically necessary voltage for water dissociation is 1.23 V, this fact yields a highest threshold of 65% on the complete energy transformation effectiveness [31]. On the contrary, the current density at a semiconductor photoelectrode submerged in water is

considerably lower (maximum of 10–20 mA/cm²) and consequently the necessary overpotential is significantly reduced. The following improvement is that a PEC structure could be assembled as a stand-alone, monolithic design. As a result, less packing constituents (e.g., frame, glass, connections, etc.) might result considerable cost effectiveness. Projected prices of hydrogen generation via PV-electrolysis is more than 8 USD/kg, which is a lot higher than the 2–4 USD/kg objective fixed by the U.S. Department of Energy for upcoming hydrogen generation systems. PEC-based water dissociation might provide a path in the direction of hydrogen production prices around 3–5 USD/kg, which is reasonable compared to available energy resources [24].

3.2 Photoelectrochemical Hydrogen Production

A PEC reactor essentially contains one or two photoelectrodes (i.e., photoanode and photocathode). In a PEC, at least one electrode is a semiconductor. The photonic energy is absorbed by the photoelectrode(s) in a PEC. PV cells and PEC semiconductor electrode have analogous operating mechanisms. In both systems, electron-hole pairs are produced by the photons with energies higher than the band gap of the photoactive surface. Such electron-hole pairs are used to either reduce or oxidize water. PEC can use solar spectrum more efficiently compared to photocatalysis and PV-electrolysis since it combines water electrolysis and photocatalysis in one single element. Since PECs do not have the need of additional power supplies, they are more compact, which is one of the major advantages of these systems [113].

Semiconductor photoelectrode is an essential constituent of PEC systems. An efficient photoelectrode accomplishes four missions at the same time: (i) photonic energy captivation; (ii) charge separation; (iii) charge transportation; and (iv) H₂ or O₂ generation on its surface. Furthermore, the photoelectrode should be robust and corrosion-resistant in electrolyte medium, affordable, reliable, and pollutant free. There is no semiconducting material proven to meet these challenging requirements. As a result, the composite materials are used as photoelectrodes because of their advantages. These composite materials consist of various different substances to perform different duties to meet a broad range of PEC water splitting criteria [114].

Metal oxides have some advantages as semiconducting electrodes in PEC systems. The major benefit of metal oxides is their low price and outstanding robustness against (photo)corrosion in electrolytic mediums – it should be noted that their stability is influenced by the type of metal oxide and solution pH. Most important drawbacks of metal oxide-based photoelectrodes can be listed as their low photonic energy capture and weak charge transportation characteristics. For this reason, in order to address the main drawbacks of metal oxide based photoelectrodes; mesoporous materials, guest–host nanostructures, tandem junctions, and plasmonics are used in the literature. There is also ongoing research on the development of new composite metal oxide photoelectrodes [115].

3.2.1 Principles of Photoelectrochemical Hydrogen Production

PEC Reactor

Figure 3.1 presents the schematic illustration of charge separation in a PEC reactor with a semiconductor based photoanode and a metal based counter electrode.

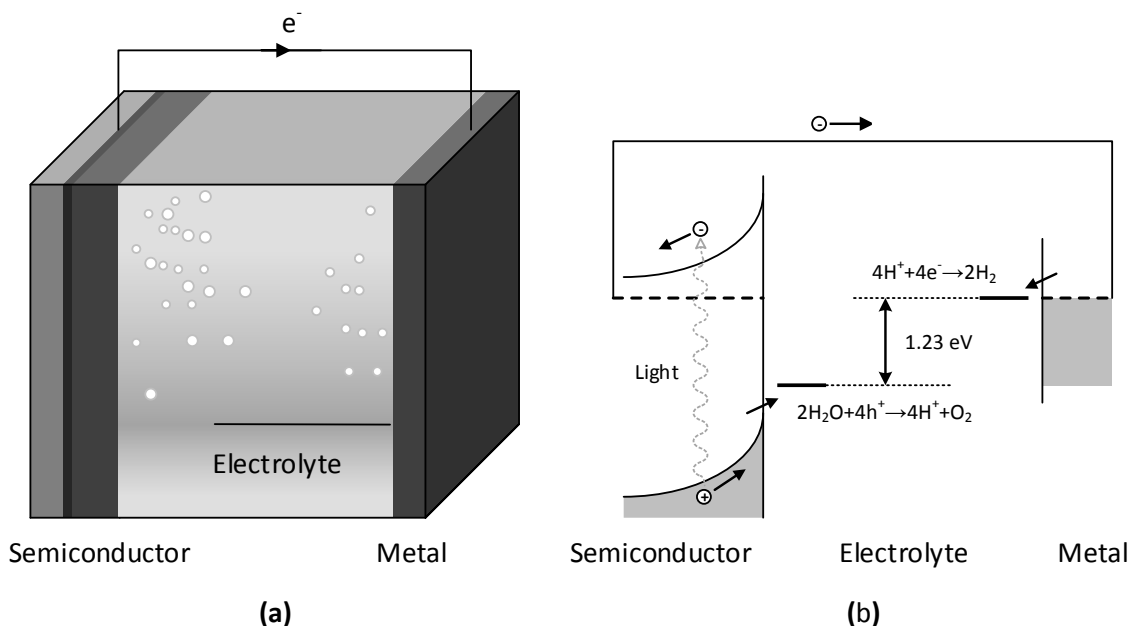


Figure 3.1 Illustration of (a) a PEC reactor with a semiconductor based photoanode and a metal based cathode and (b) its energy diagram (adapted from [114]).

The key constituent of the PEC reactor is the semiconductor, since it transforms incoming photonic energy to electron–hole pairs. The semiconducting photoelectrode’s

electric field separates the electrons and holes upon light irradiation. The photogenerated electrons are sent to the conductive rear contact, and are transferred to the metal counter-electrode through an exterior cable. H^+ ions are reduced to form H_2 gas at the surface of the metal counter electrode. It should be noted that in case a photocathode is used, this reduction would occur at the photoactive semiconductor's surface. The photogenerated holes are transferred to the semiconductor surface. Here, they oxidize water to generate O_2 gas. In an alkaline electrolyte, the reduction and oxidation reactions are:



In an acidic medium, the OH^- ions in Equations (3.2) and (3.3) are neutralized by H^+ ions, and the resulting net reactions are:



The Gibbs free energy change of the overall water splitting reaction is calculated from the following equation:

$$\Delta G = -nF\Delta E \quad (3.6)$$

Here, n is the number of moles of electrons evolved, F is the Faraday's constant, and ΔE stands for electrochemical cell voltage. At standard temperature (298 K) and molar concentrations (1 mol/L, 1 bar), the electrochemical reactor potential ΔE of -1.229 V relates to a Gibbs free energy change of $+237$ kJ/mol H_2 . Consequently, since the Gibbs free energy change is positive, the water splitting reaction is not spontaneous. However, this does not mean that all photocatalytic reactions are nonspontaneous. For instance, Gibbs free energy change of photodegradation of organic pollutants is negative, as a result, this reaction is spontaneous.

Semiconductor Photoelectrode Substances

Effective visible light capturing and charge transportation are two of the fundamental prerequisites for an efficient semiconductor photoelectrode substance. It is generally – although not all the time – straightforward and easy to find out these characteristics of a

particular material experimentally. Without a doubt, this methodology turns out to be impractical if it is required to investigate a whole category of potential photoelectrode substances. For these situations, a more productive method could be to determine the electronic arrangement of a base substance, and utilize this information to evaluate how the composite characteristics change, for instance, composition. The methodology to determine and assess complete structural characteristics of semiconductor photoelectrodes for efficient water splitting is still being developed and there is no generally accepted standard procedure. However, the necessary computing power and software are already accessible, and the amount of electronic structure computations described in the literature, even by experimental working groups, is increasing quickly. However, with the intention of using these materials to calculate particular photoelectrode characteristics, it is required to comprehend how chemical bonds amongst the atoms influence the electronic structure.

In the majority of traditional semiconductors, for example Si and Ge, covalent bonds are dominating. For instance, in Si, the outside 3s and 3p orbitals come together to establish hybrid sp^3 orbitals. Neighboring sp^3 orbitals co-operate to set up bonding and antibonding arrangements which produce the valence and conduction bands of the substance, respectively [116].

The bonding in metal oxide semiconductors is especially different in nature. Since oxygen has a lot higher electronegativity compared to existing metals, the valence electrons are either fully or partially transmitted from the oxygen to the metal ion. For that reason, the bonding characteristics of metal oxides is extremely polar or sometimes even ionic. A qualitative band representation can be made by forming a molecular orbital (MO) diagram from the individual atomic energy levels [30, 117].

It should be noted that such a “local” approach is completely unsuitable for covalent semiconductors for example Si, because in Si, electrons are entirely delocalized throughout the substance. The local feature of the energy bands in metal oxides occasionally causes confusing understandings. For instance, “free” electrons in TiO_2 are every so often differentiated from Ti^{3+} types. Despite the fact that this kind of dissimilarity could be reasonable at the material surface, where the electronic structure is deformed because of a

disorder of the lattice symmetry, it is not observable in the bulk in which the conduction band is mostly consisted of Ti 3d orbitals.

Despite the fact that it seems complex, the electronic band structure can straightforwardly provide various significant understandings for photoelectrode substances. The first feature is the optical alteration characteristics. If the peak position in the valence band is situated at the same k-vector as the lowermost position of the conduction band, the optical conversion does not necessitate the crystal momentum to be altered. On the other hand, indirect conversions do demand a modification in crystal momentum. Since photons carry very little momentum, indirect transitions require absorption or emission of a phonon (i.e., a lattice vibration) and are much less likely to occur. As a consequence, the absorption coefficient of indirect semiconductors is much smaller than that of direct semiconductors – the difference can be two orders of magnitude. This is why direct semiconductors, such as amorphous Si or $\text{CuIn}_x\text{Ga}_{1-x}\text{Se}_2$ (CIGS) can absorb all incident light in just a few micrometers, whereas crystalline (indirect) Si solar cells typically have a thickness of about 300 μm .

Bandgap of a substance may be calculated based on the absorption coefficient versus wavelength measurements. If the lowest part of the conduction band and the highest part of the valence band are presumed to possess a parabolic profile, the absorption coefficient α (m^{-1}) can be calculated based on the following equation:

$$\alpha = \frac{A(h\nu - E_g)^m}{h\nu} \quad (3.7)$$

where A is a constant and m is based on optical conversion characteristics: if the substance has a direct bandgap, $m = 1/2$, and if the substance has indirect bandgap, $m = 2$. Equation (3.7) shows that extrapolation of $(\alpha h\nu)^{1/2}$ versus $h\nu$ plot provides the indirect bandgap. And on the other hand, extrapolation of $(\alpha h\nu)^2$ versus $h\nu$ presents the direct bandgap of the substance. Both of these plots are named as ‘‘Tauc plot’’ [118] and are generally utilized in the photoelectrochemistry and photocatalysis literature.

An additional understanding which might be acquired based on the electronic band structure is the charge carriers’ movement. Charge carriers’ mobility depends on the thickness of the conduction and valence bands. For Si, these bands are moderately wide,

covering over 10 eV. This is because of the extensive overlay of the sp^3 orbitals on neighboring atoms. Supplementary overlay amongst atomic wave functions causes wider bands and more straightforward transportation of free charge carriers throughout the substance. Broad bands that are heavily bent generally mean high charge carrier mobility. A high mobility is particularly necessary in photoelectrodes with indirect bandgap. This is due to the fact that these substances necessitate a large width to captivate all the incoming photonic energy. This represents that photogenerated electrons and holes have to pass through longer distances to access the interface.

Table 3.1 presents a summary of the charge carrier mobility of selected semiconductors at 298 K. One possible cause of the small charge carrier mobility of transition metal oxides is their moderately contracted 3d orbitals. As a result, they have fewer overlay with neighboring atoms compared to the s- and p-orbitals. It is also possible to evaluate this phenomena from electrostatic point of view. The electrostatic contact of a free electron with the adjacent cations causes a local lattice alteration. This alteration complements the electron as it travels throughout the lattice, and this is named a polaron. In cases where the interaction is significantly resilient, the polaron may even be confined in a specific lattice site. After that, the electron may only travel by heat triggered bouncing, and this mobility is considerably small. Related reflections can be used in “free” holes in the valence band, these can produce polarons throughout electrostatic interface with the neighboring oxygen ions. Charge transportation through polarons is assumed to have a significant impact in, e.g., hematite ($\alpha\text{-Fe}_2\text{O}_3$).

Table 3.1 Charge carrier mobility data of selected semiconductors at 298 K.

Material	Mobility ($\text{cm}^2/\text{V/s}$)		References
	Electrons	Holes	
Si	1,500	450	[119]
GaAs	8,500	400	[119, 120]
CdS	340	50	[119, 120]
ZnO	200	180	[119, 120]
TiO ₂ (anatase)		0.002 ⁽¹⁾	[121, 122]
WO ₃	10		[123]
$\alpha\text{-Fe}_2\text{O}_3$	0.1 ⁽²⁾	0.2 ⁽³⁾	[124]
Cu ₂ O		90	[125]

(1) Theoretical estimate

(2) At 1,200 K

(3) At 1,400 K

Semiconductors for feasible functions are generally doped, essentially with the goal to enhance their electrical conductivity. In metal oxide based photoelectrodes, shallow electron donors and acceptors are nearly constantly required due to their small intrinsic charge carrier mobility. Some examples of electron donor-type dopants are Ti^{4+} on a Fe^{3+} base in Fe_2O_3 , or phosphorus in Si. The additional valence electron brought by the electron donor atom is lightly connected to the electron donor nucleus, and might be excited to the conduction band. In conduction band, electron donor enhances the conductivity. On the other hand, holes in electron acceptor-type dopants can be excited to the valence band. Because a hole means a missing electron, it is possible to imagine this as an electron being excited from the valence band into the energy level of the acceptor substance.

A selection of dopants can improve the optical captivation of broad bandgap semiconductors [126], enhance the charge carrier diffusion distance [127, 128], or increase the catalytic activity at semiconductor interface [129]. Additional dopants undesirably impact the properties, for instance, by presenting mid-gap bulk or surface states which become recombination sites [130, 131].

In addition the dopants, native point defects also generally occur in the substance. Some examples are surface vacancies, interstitials, or substituents. These defects might have a comparable impact on the optical, electrical, and catalytic characteristics as dopants. They are made by intrinsic defect-chemical reactions, or by an alteration in the lattice stoichiometry as a result of an exchange of, e.g., O_2 with the gas phase. Because virtually every single defect affects the efficiency of the substance in one manner or another, the capability to comprehend and estimate the connection among dopants and defect concentrations is of utmost significance for fabricating effective photoelectrodes.

3.2.2 Energy and Quantum Efficiencies

PEC reactors performance is evaluated by various criteria. Among them, energy efficiency is one of the most commonly used one. If every photogenerated electron and hole are assumed to be utilized in the water dissociation reaction, the following equation can be used to calculate the overall solar-to-hydrogen efficiency (η_{STH}) as

$$\eta_{STH} = \frac{W_{out} - W_{in}}{i} = \frac{j_{photo}(V_{redox} - V_{bias})}{i} \quad (3.8)$$

Here, \dot{I} is the power input, which is solar irradiation, \dot{W}_{out} and \dot{W}_{in} are electrical power output and input, respectively. V_{redox} is typically accepted to be 1.23 V (at around 298 K). This amount is water dissociation reaction's Gibbs free energy change which is 237 kJ/mol. On the other hand, the enthalpy change of water splitting reaction, which is 286 kJ/mol, is occasionally utilized. This gives a redox potential of 1.48 V. The potential calculated based on the enthalpy change is applicable in cases where the generated hydrogen is planned to be burned in a combustion chamber. While the potential calculated based on the Gibbs free energy change is more suitable in cases where the hydrogen is transformed into electricity in a fuel cell [132]. In cases where the intended utilization of product hydrogen is not known, it is most likely more suitable to take the Gibbs free energy change as basis as it gives lower efficiencies. When AM1.5G solar irradiation ($\dot{I}=1,000 \text{ W/m}^2$) is used and no bias is applied ($V_{bias}=0 \text{ V}$), overall solar-to-hydrogen efficiency can possibly be calculated straight from the photocurrent (j_{photo}):

$$\eta_{STH} = 1.23 \times j_{photo} \quad (3.9)$$

where unit of η_{STH} is % and j_{photo} is mA/cm². Hence, a photocurrent of around 8 mA/cm² is necessitated to accomplish the 10% overall solar-to-hydrogen efficiency objective for financially sustainable PEC reactors.

It should be emphasized that V_{bias} in Equation (3.8) denotes the definite potential difference amongst the working and counter electrodes. This potential difference can be indirectly determined by using a three-electrode measurement technique. In this method, the working electrode potential is measured comparatively with respect to the reference electrode potential. Since this method commonly causes some mistakes, it would be better to avoid using the three-electrode measurement technique if possible.

Measuring the quantity of hydrogen production by mass spectrometry and/or gas chromatography is a more direct technique to evaluate the solar-to-hydrogen efficiency [133, 134]. Water displacement in an inverted burette is another way to verify the amount of production. With this method, the solar-to-hydrogen (STH) efficiency is calculated by

$$\eta_{STH} = \frac{\dot{n}_{H_2} G_{f,H_2}^{\circ}}{\dot{I}} \quad (3.10)$$

where \dot{n}_{H_2} is the hydrogen generation rate at the irradiated surface (mol/s/m²) and G_{f,H_2}° is the Gibbs free energy change of hydrogen production (237 kJ/mol).

When reporting STH efficiencies, the following assumptions are made (i) the reaction is stoichiometric (H₂:O₂ molar ratio is 2:1); (ii) there are no side reactions happening as a result of additional chemicals, such as electrolytes, electron donors, and/or acceptors and (iii) the irradiation source is stated appropriately and it sufficiently agrees with the AM1.5G spectrum in concentration and spectral distribution [135].

In cases where efficiency restraining criteria are being identified, it is an advantageous approach to use the quantum efficiency as a function of wavelength. External quantum efficiency is defined as the ratio of the incoming photons which are transformed to electrons to the external circuit current measurement. This term is called the incident photon-to-current conversion efficiency (IPCE), which is calculated as

$$IPCE(\lambda) = \frac{hc}{e} \left(\frac{j_{photo}(\lambda)}{\lambda I(\lambda)} \right) \quad (3.11)$$

In the literature, there are IPCE values reported to be higher than 80% for the photo-oxidation of water, for instance, for WO₃ [136] and for TiO₂ under UV irradiation [137]. An additional beneficial efficiency indicator is the absorbed photon-to-current conversion efficiency (APCE). Compared to the IPCE, the APCE accounts for the reflection losses as well. APCE is frequently mentioned as the internal quantum efficiency, and it is calculated based on the IPCE, which is shown in the following equation:

$$APCE(\lambda) = \frac{IPCE(\lambda)}{A(\lambda)} = \frac{IPCE(\lambda)}{1-R-T} \quad (3.12)$$

Here, A , R , and T are the optical absorption, reflection, and transmission, respectively. The optical absorption (A) should not to be mistaken as the absorbance or optical density (OD). OD is specified by:

$$OD = -\text{Log} \left(\frac{T}{1-R} \right) = \frac{\alpha L}{2.303} \quad (3.13)$$

where α is the absorption coefficient and L is the substrate thickness. APCE should be used in cases where it is aimed to estimate electron-hole recombination inside the semiconductor. The IPCE is more applicable to utilize when evaluating conversion

efficiencies of overall devices and systems. In some special cases, the IPCE is evaluated in monochromatic illumination to estimate the photocurrent in real solar light:

$$J_{solar} = \int (IPCE(\lambda) \times \Phi(\lambda) \times e) d\lambda \quad (3.14)$$

In this equation, J_{solar} is the overall solar photocurrent in A/m² and $\Phi(\lambda)$ is the photon flux of solar irradiation in photons/m²/s. The photon flux might be determined based on the tabulated solar irradiation data, $E(\lambda)$, via [135]

$$\Phi(\lambda) = \frac{E(\lambda)}{hc/\lambda} \quad (3.15)$$

An important underlying assumption for Equation (3.14) is that there is generally a direct connection amongst the monochromatic photocurrent density and the light intensity, however, there are exceptions. A super-linear photocurrent escalation with increasing light intensity is occasionally detected for nanostructured substances having above average concentrations of moderately narrow surface or interface traps. In such cases, these interface traps firstly require to be filled up before the charge carriers could make it to the electrolyte or the rear contact [138]. On the other hand, slow charge transportation or charge transference through the substrate interface could cause a build-up of free charge carriers at or close to the interface. As a result, amount of recombination proliferates and this will cause a sublinear intensification of the photocurrent with light intensity.

3.2.3 System Requirements

Some of the prerequisites for effective water dissociating photoanode and/or photocathode substances could be listed as [139]

- Reliable light captivation (visible light is preferred)
- Good chemical stability, robustness, and corrosivity resistance in the dark and under irradiation
- Suitable band edge locations which include both the water reduction and oxidation potentials
- Effective charge transportation within the semiconductor
- Reduced overpotentials for water reduction/oxidation
- Abundancy, reliability, and affordability

A semiconducting substance's bandgap determines in which part of the solar spectrum it can convert incoming photonic energy to electrons and holes. The smallest bandgap necessary to dissociate water is 1.23 eV. However, the thermodynamic losses of about 0.3–0.4 eV should also be taken into account when determining the minimum bandgap [140]. In addition to the thermodynamic losses, overpotentials around 0.4–0.6 eV should be considered as well. These overpotentials are necessitated at different locations within the system to support adequately fast reaction kinetics [141]. Consequently, the bandgap has to be no less than 1.9 eV, which resembles to a light captivation starting at 650 nm. Under 400 nm the sunlight intensity decreases promptly, resulting a greater boundary of 3.1 eV on the bandgap. For this reason, the optimal bandgap width ought to be anywhere among 1.9 and 3.1 eV, and this range is in the visible portion of the solar spectrum. In a comprehensive analysis, Murphy et al. [141] have recommended an optimal bandgap of 2.03 eV, resulting a solar-to-hydrogen efficiency of 16.8%.

Chemical stability, robustness, and corrosivity resistance requirements severely limit the effectiveness of numerous photoactive substances. A lot of the non-oxide semiconductors either dissolve or produce a narrow oxide coating which inhibits charge transferral through the semiconductor/electrolyte boundary. Oxide semiconductors are more stable; however, they might be disposed to anodic or cathodic decomposition. The common tendency is that the stability against (photo)corrosion enhances as the bandgap becomes wider. Even though this trend disagrees with the efficient visible light captivation, an appropriate bandgap for efficient water splitting and decent chemical stability are not automatically directly affected from each other. However, it is also possible to claim that a small bandgap generally comes with a high valence band energy, and that could actually cause less chemical stability within the substance.

There are a limited number of semiconductors with suitable band edge locations which include both the water oxidation and reduction potentials. The semiconductors with suitable band edge locations either have a very large bandgaps (e.g., SrTiO₃, SiC) or are not stable in electrolytic solutions (Cu₂O, CdS). Band edges of non-oxide semiconductors are generally in better agreement with the water reduction side, and in the meantime, oxide semiconductors' band edges support water oxidation reaction.

The fourth prerequisite, which is effective charge transportation, is accomplished in various substances (such as TiO_2 , WO_3) with no problem. However, in some materials, low charge transfer rates is among one of the major reasons of low overall solar-to-hydrogen transformation effectiveness. A remarkably significant case for how low charge transportation affects overall solar-to-hydrogen efficiency is $\alpha\text{-Fe}_2\text{O}_3$. Electronic band structure, and intrinsic and extrinsic charge transportation elements of the substances provides significant indications in connection with the charge carrier mobility. Extensive overlay of metal 3d orbitals commonly results great electron mobility. And on the other hand, the overlay of O-2p orbitals influences the hole mobility in the majority of the metal oxides. The extrinsic factors, specifically shallow electron donors and/or acceptors and recombination centers, are have much more significant impact on a material's photocatalytic activity. [139].

For n-type semiconductors, the reduced overpotentials for water reduction/oxidation suggests that hole transferral through the semiconductor/electrolyte boundary ought to have appropriately high speeds so as to match with the anodic decomposition reaction rate. More commonly, interfacial charge transferral has to be sufficiently quick to prevent the charge carrier build-up at the semiconductor/electrolyte interface. Charge carrier accumulation could possibly reduce the electric field strength and could cause an associated escalation in electron-hole recombination. In order to enhance charge transfer kinetics, substances with active catalytic surfaces could be used. The following are some examples of efficient O_2 generation catalysts which are namely RuO_2 [140], IrO_x [142], and Co-based compounds [143]. On the other hand, Pt, Rh [144], Cr-Rh, RuO_2 , or NiO_x [133] are generally utilized as H_2 production catalysts.

At the present time, there is no existing photoactive semiconductor substance which can meet all of the criteria discussed above. There are four major trade-offs when selecting a photoactive semiconductor:

- Bandgap versus stability
- Photon absorption versus charge transportation
- Electron-hole recombination versus catalysis
- Performance versus cost

The bandgap versus stability trade-off has been discussed previously in this section. The second trade-off is particularly significant for semiconductors that have low absorption coefficients, for example, metal oxides with indirect bandgaps. Majority of the electron–hole pairs are generated distantly from the surface of these materials. These charge carriers recombine before arriving to semiconductor/electrolyte boundary. The third trade-off indicates that the catalytically active surface locations tend to behave as effective recombination sites for electronic charge carriers. Furthermore, particular co-catalysts for H₂ or O₂ generation might increase the reverse-reaction with H₂ and O₂ to produce water. Pt is a very well-known example to this case. This situation can create some issues when designing reactors in which the product gas cross-over is not possible to be prevented. Interestingly, NiO is an effective H₂ generation catalyst and when NiO is used, the H₂ and O₂ reverse reaction does not appear to happen [133]. The fourth and last trade-off indicates the most important reason for the attention to cheaper metal oxides. The economic feasibility of novel and advanced multi-junction structures is questionable [49].

3.2.4 Photoelectrochemical Hydrogen Production Experiments

Despite of the promising technical advancements, PEC-based water dissociation remains to stay as a majorly experimental subject. One of the main reasons of this is the fact that most of the photoelectrode characteristics are evaluated by elements that are either challenging to regulate or not very well comprehended yet. And as a result, it is complicated to estimate the effect of photoactive materials' characteristics on their solar hydrogen production effectiveness. Presence of particular defects, for example, dislocations or impurities can be used as an example here. It is generally not possible to prevent these defects, particularly in cases where low-temperature and low-cost fabrication techniques are utilized. A significant phase in the development process of a photoelectrode is for that reason to methodically optimize the production procedure so as to accomplish greatest possible photoactivity. Some optimization considerations for photoelectrode production can be listed as deposition temperature, substance cleaning process, additional materials employed to optimize the boiling point, surface tension, solution water content or viscosity, postdeposition heat treatments to enhance the crystallinity, dipping the synthesized photoelectrodes in a precursor solution to improve inter-particle contacts, etc.

A generally used way to evaluate the optimum photoactivity is the photocurrent density in 1 Sun irradiation which is accepted to be $1,000 \text{ W/m}^2$. In order to assess the photocurrent for various photoactive substances, two requirements must be met. The major criteria is that the recorded data exhibit the photoactive materials' characteristics, in spite of the challenges or restrictions caused by the measurement device. For instance, mass transportation restrictions could be prevented by thorough designing of the electrochemical reactor. Resistance losses and pH variabilities can be eliminated or minimized by selecting appropriate electrolytes. For a meaningful assessment of performance results described by various laboratories and research institutions in the literature, second principle should be taken into consideration. This criterion states that the measurements have to be conducted in precisely identical circumstances. Even though it seems insignificant, there are numerous performance statements in the literature that do not fulfill this requirement. This might be because of the lack of appropriate devices (especially standardized light sources). In addition, there is absent material in most studies where the authors relate their findings. In order to prevent this situation, it is important to state the substrate area and thickness, the intensity and type of light source, the electrolyte composition, concentration, and pH, the reactor design, and counter electrode area, and the applied potential.

Along with performance assessments, numerous PEC experimentations are intended to recognize rate-determining stages or to identify specific substance characteristics. Electron donor or acceptor densities and the flat band potential are examples of substance characteristics that can be estimated by electrochemical impedance measurements. The difficulty with these measurements is that they always produce data; however, it could be challenging – and occasionally even impracticable – to interpret the measured data to the anticipated substance characteristics. Cautiously conducted control experimentations and a decent fundamental knowledge of the measurement devices – especially the potentiostat and the frequency response analyzer (FRA) – are necessary in order to obtain more meaningful data.

More material on PEC experiments and measurement devices is accessible; however, this information is generally scattered throughout numerous scientific journal articles, books, and technical notes. Furthermore, a large number of beneficial procedures

and techniques are transferred by interactions among associates or between supervisors and students, and therefore cannot be located in the literature.

The major characteristic that differentiates the PEC reactor from a typical electrochemical one is the existence of an optically translucent screen. Through that screen, the photoactive material can be irradiated. Because standard glass has a light cut-off below wavelengths of ~ 350 nm, fused silica (amorphous SiO_2) is more generally employed as a screen substance in PEC reactors. UV-grade fused silica is translucent in the complete spectrum from UV to near-IR with a transmission above 90% between 200 nm and 2.2 mm. UV-grade fused silica presents outstanding chemical stability in both acidic and alkaline aqueous suspensions (with the exception of in HF) and the material is moderately inexpensive. Most of the PEC reactors are commercially accessible, quite robust (even though they are almost completely made from glass), and not hard to employ including the electrode integration process. Unfortunately, PEC reactors also have several drawbacks. Since they are made from glass, the reactor might be relatively big and, meaning large amount of electrolyte (>100 mL) requirement. Then they become unreasonable when testing large numbers of photoelectrodes. Furthermore, the distance between the working and counter electrodes generally surpasses 5 cm and might increase the resistance losses at high current densities. One practical problem is photoelectrode mounting: since the substrate is completely submerged in the electrolyte, it requires to be partly covered with, e.g., epoxy resin to prevent any direct contact between the electrolyte and the conducting rear-contact and/or the linking cable. An additional way is to employ membrane photoelectrode assemblies (MPEA).

The electrolyte in an electrochemical reactor contains a solvent where the active materials to be reduced or oxidized are dissolved. For PEC-based water dissociation, the solvent and the active materials are H_2O . Since fresh water is not conductive enough, supportive ions need be included to make sure that the anticipated current flow could be accomplished. The supportive electrolyte concentration ought to be appropriately sufficient to prevent high losses throughout the electrolyte. These Ohmic losses should be balanced by amplifying the applied bias potential, which negatively influences the overall effectiveness of the photoelectrode. The voltage drop equation is written as

$$V_{loss} = I \times R_E \quad (3.16)$$

Here, I is the total current traveling between the working and counter electrodes, and R_E is the electrolyte resistance. The electrolyte resistance is calculated based on the electrolyte conductivity, κ , and the cell constant, K_{cell} , which is given by

$$R_E = \frac{K_{cell}}{\kappa} \quad (3.17)$$

For the simple PEC reactor geometry, the cell constant is calculated based on the distance between the electrodes (L) divided by the electrode area (A),

$$K_{cell} = \frac{L}{A} \quad (3.18)$$

The cell constant is influenced by the reactor geometry, and could be calculated from an impedance measurement of R_E by utilizing a standard electrolyte solution with well-known conductivity.

The electrolyte conductivity is strongly affected by the type of dissolved ions and their concentrations. It is essential to comprehend that the relationship between the conductivity and the concentration is generally not direct. This is because of either incomplete dissociation of the anions and cations (i.e., weak electrolytes) and/or ion-solvent interactions. Deviances from linearity might also happen at concentrations over 1 mM, and could definitely have an important impact on practical dissociation purposes. At significantly high concentrations (above 1 M), ion-pair founding might cause conductivity decrease with increasing concentration.

Table 3.2 provides a summary of the conductivities of various electrolytes generally utilized in PEC reactor assessment studies. In order to provide an approximate indication of the Ohmic losses, Table 3.2 also shows the voltage drop throughout the electrolyte for a current density of 5 mA/cm². Noticeably, minimum concentrations of 0.5 M are needed to keep Ohmic losses at a tolerable point.

In practice, H₂SO₄ and HCl solutions with concentrations between 0.5 M and 1 M are generally employed as acidic electrolytes for most of the metal oxides, such as WO₃ or TiO₂ [59]. In addition, for WO₃, NaCl has been utilized to imitate saline mediums [145].

Table 3.2 Electrical conductivities for selected electrolytes and their resultant resistances and voltage drops at a current density of 5 mA/cm².

Reference electrode	Concentration	κ	R_E	V_{loss} at 5 mA/cm ²	T	Ionic species	Limiting ionic conductivity
	M	$\Omega^{-1}\text{m}^{-1}$	Ω	mV	(°C)	(in H ₂ O)	$10^{-4} \text{ m}^2/\Omega\text{-m}$
KOH	1.0	20.1	5.0	25	20	H ⁺ , OH ⁻ , K ⁺	349.8
	0.5	10.7	9.3	47	18		73.5
	0.1	2.26	44	221	18		50.1
NaOH	0.5	8.6	12	58	18	Na ⁺ , OH ⁻	197
NaCl	5.0	21.4	4.7	23	18	Na ⁺ , Cl ⁻	76.4
	1.0	7.44	13	67	18		162
	0.5	3.8	26	132	18		
	0.1	1.07	93	467	18		
H ₂ SO ₄	3.5	73.9	1.4	7	18	H ⁺ , SO ₄ ²⁻	
	1.0	36.6	2.7	14	18		
K ₂ SO ₄	0.5	6.2	16	81	20	K ⁺ , SO ₄ ²⁻	
Distilled water	-	10 ⁻³ -10 ⁻⁴	10 ⁵ -10 ⁶	∞	20	-	
Millipore water	-	5.5-10 ⁻⁶	18-10 ⁶	∞	25	-	

Source: [24]

For photoelectrodes with neutral or alkaline solution requirements, for example α -Fe₂O₃ [146], KOH, or NaOH solutions with concentrations between 0.5 M and 1 M are generally employed. Various metal oxides are just stable in moderately neutral mediums. A common example is BiVO₄, that is only stable between pH 3 and 11 and it is generally investigated in aqueous solutions of 0.5 M Na₂SO₄ or K₂SO₄ [147]. To prevent localized pH variations in electrolytes – which could influence the flat band potential – additional pH buffer solution in the electrolyte should be considered. An appropriate selection is the commonly acknowledged phosphate buffer KH₂PO₄/K₂HPO₄, which results a pH of 6.86 at 25°C after adding 0.025 M of each species to the electrolyte [148].

In order to effectively eliminate the generated H₂ and O₂ gases from the electrolyte, the electrolyte can be constantly purged with an inert gas for instance N₂ or Ar. Purging with inert gases eliminates the reverse-reaction of dissolved H₂ and O₂ to produce water, and it also keeps the redox potentials constant during the testing period. Uninterrupted purging throughout the electrolyte should be averted if the inert gas bubbles disturb the incoming irradiation route and cause too much fluctuation on the photocurrent signal.

When this interference and fluctuation are not possible to be avoided, the electrolyte can be purged completely for at least 20 minutes before running the PEC experiment, and hang the purge tube above the electrolyte to produce a layer of inert gas over it. Mixing the electrolyte with a magnetic stir bar significantly improves the purging effectiveness and makes fast elimination of any dissolved O₂ possible. Mixing is generally not needed to tackle mass transport restrictions in the electrolyte due to high ionic concentrations, and is frequently not preferred to avoid measurement inconsistencies.

CHAPTER 4: EXPERIMENTAL APPARATUS AND PROCEDURE

The present experimental setup has a hybrid dual half-cell reactor with a CEM used for four different processes which are electrolysis, chloralkali, PEC, and PEC-chloralkali based H₂ production. During electrolysis and PEC processes, O₂ and H₂ gases leave the anode and cathode, respectively. During chloralkali and PEC-chloralkali processes, Cl₂ gas leaves the reactor from the anode. Gaseous H₂ and NaOH solution are produced in the cathode.

4.1 System Description

Figure 4.1 presents the process flow diagram of the present experimental setup. This setup is used for four different processes (Figure 4.2), namely:

- Process 1: Electrolysis – conducted under no light irradiation and H₂O is used as electrolyte. It is tested at three different flow rates and four different temperatures.
- Process 2: PEC – tested under 600 and 1,200 W/m² irradiation levels. H₂O is used as electrolyte. Three different flow rates and four different temperatures are investigated.
- Process 3: Chloralkali – conducted under no light irradiation and NaCl and NaOH solutions are used as anolyte and catholyte, respectively. It is tested at three different flow rates and four different operating temperatures.
- Process 4: PEC-chloralkali – conducted under 600 and 1,200 W/m² irradiation levels and NaCl and NaOH solutions are used as anolyte and catholyte, respectively. It is tested at three different flow rates and four different temperatures.

From Figure 4.1, it can be seen that the present experimental setup has eight main components, namely (I) reactor; (II) electrolyte feed tanks; (III) electrolyte dump tanks; (IV) peristaltic pumps; (V) water displacement cylinder; (VI) heaters; (VII) potentiostat; and (VIII) solar simulator. In all cases, where specified, additional (a) and (b) terms are used for anolyte and catholyte, respectively. It should be noted that during electrolysis and chloralkali (Processes 1 and 3), no irradiation needed, therefore solar simulator is not used.

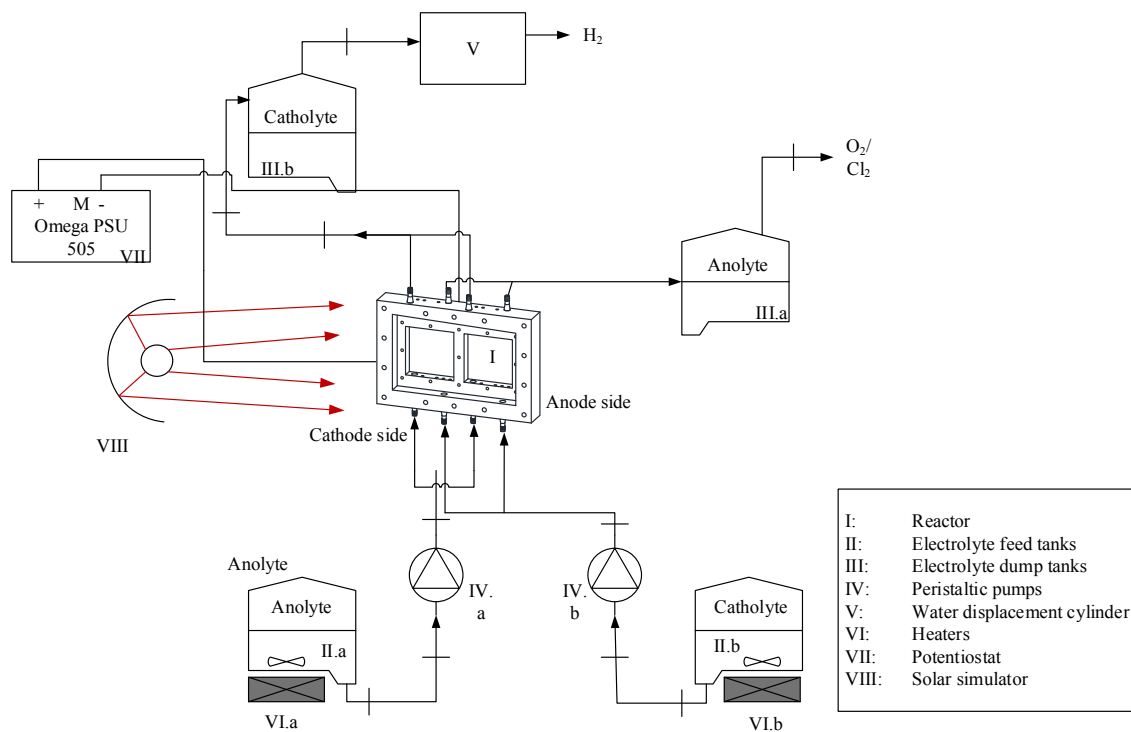


Figure 4.1 Process flow diagram of present experimental setup.

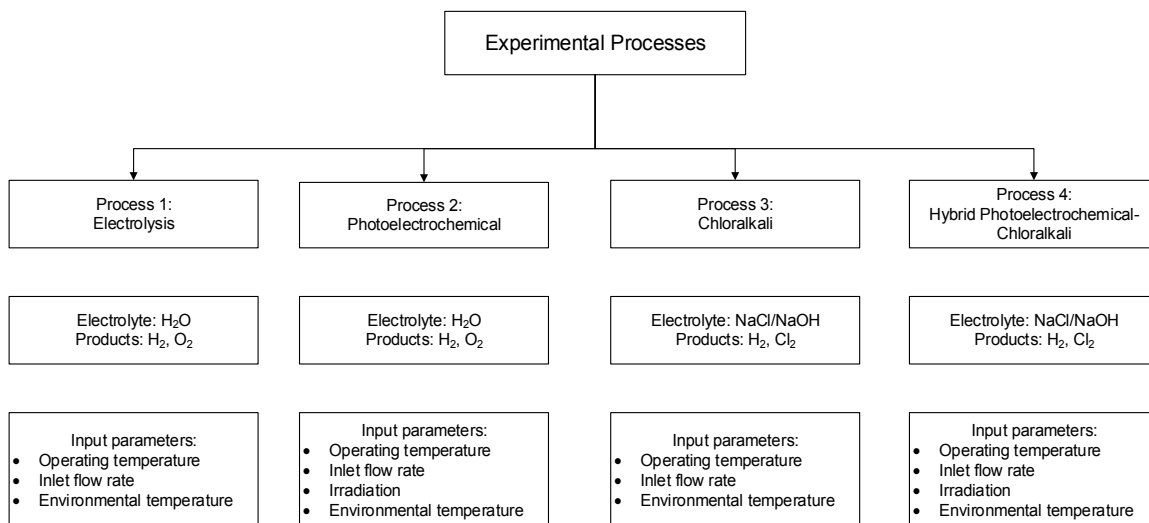


Figure 4.2 Summary of four types of processes tested during present experimental studies.

All four processes shown in Figure 4.2 use the same process flow diagram (Figure 4.1) with minor differences. For instance, in Processes 1 and 2, anolyte and catholyte feed and dump only include H₂O. In Processes 3 and 4, anolyte feed is saturated NaCl solution

while catholyte feed is H_2O . In all processes, H_2 gas leaves the catholyte dump tank (III.b). However, the gas leaves the anolyte tank (III.a) is different in Processes 1 and 2 (O_2) and Processes 3 and 4 (Cl_2). Anolyte and catholyte dump in Processes 3 are depleted NaCl and NaOH solutions, respectively. The process flows as the anolyte and catholyte feeds are prepared in (II.a and II.b) before entering to the reactor (I), for instance, during operations at higher temperatures, these tanks are heated via (VI.a and IV.b). The feed flow rates are monitored and controlled by peristaltic pumps (IV.a and IV.b). Anolyte and catholyte outlet streams, called dump, are sent to dump tanks (III.a and III.b). In all processes the H_2 gas leaving (III.b) is collected and measured by volumetric water displacement technique. The gas product from (III.a), either O_2 or Cl_2 , is not measured and released towards the vent. Solar simulator (VIII) is used in Processes 3 and 4. Potentiostat (VII) is used in all processes to provide the external power need of the reactor and to measure the current.

Figure 4.3 shows the present experimental setup tested at UOIT's CERL during operation under irradiance from the solar simulator. A closer look at the illuminated reactor and feed tanks as well as the heaters is also provided in Figure 4.3.

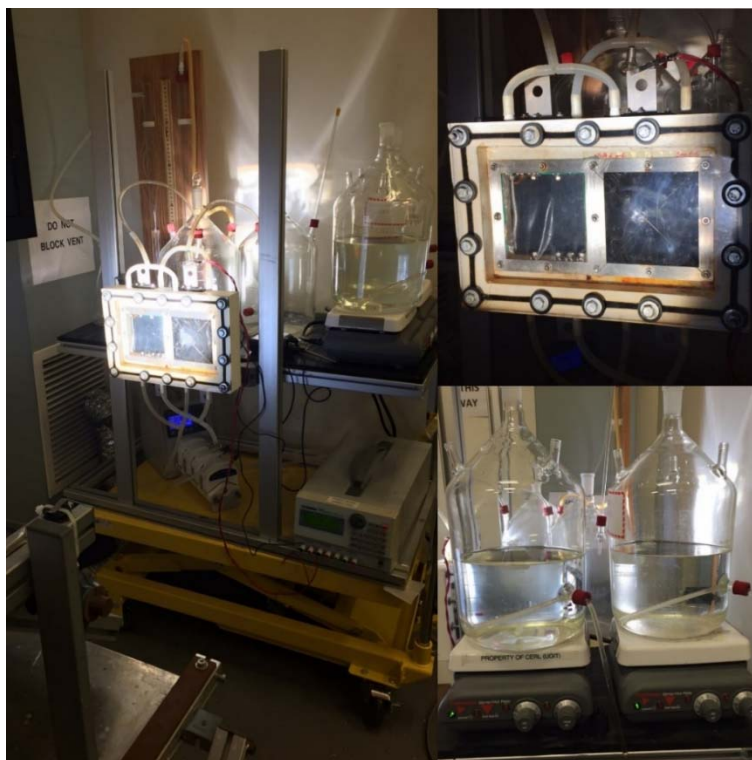


Figure 4.3 Present experimental setup (left), closer look at illuminated reactor (top right), and feed tanks with heater (bottom right).

4.2 Experimental Setup

The core element of the present experimental setup is the hybrid reactor. The reactor gets the most out of solar spectrum by combining the solar energy absorbing characteristics of the photocathode and PV/T together. The portion of the solar spectrum that cannot be utilized by the photocatalyst is directed to PV/T via a solar spectral splitter in which the produced electricity supports the electricity input to the reactor. The electrodes are also employed as electron donors/acceptors for photocatalytic H₂ generation, minimizing the requirement for supplementary chemical substances (e.g., sacrificial donors), consequently decreasing the potential waste product discharges. The hybrid reactor can be exploited for a variety of reactions:

- When there is no sufficient light (i.e., night time, cloudy days, etc.) the hybrid reactor uses electricity to produce O₂ or Cl₂ and H₂ gases. Water and chloralkali electrolyses happen in Processes 1 and 3, respectively.
- When there is sufficient light, the hybrid reactor exploits photoelectrolysis and photocatalysis simultaneously to produce H₂. The electrodes are employed to dissociate water electrochemically. In addition, the photocathode is utilized to split water photocatalytically. In Process 2, PEC reaction generates H₂ and O₂ gases. In Process 4, PEC-chloralkali produces H₂ and Cl₂ gases and NaOH solution.

The hybrid reactor's operation procedure for Process 4 is explained in Figure 4.4. The overall system collects and concentrates the incoming solar light irradiation and splits the solar spectrum to make best use of the harvested solar energy. The fraction of solar energy directed to PV/T is utilized to support the required electricity to generate Cl₂, H₂ and NaOH through electrolysis. The portion led to PEC reactor is directly processed by the photocathode to produce H₂ gas and NaOH. In Process 2, solar spectrum is similarly split, and higher energy portion is sent to the reactor, while the rest is sent to the PV/T. The only difference is that in Process 2, there is no chloralkali, so the products are H₂ and O₂ gases only. In Processes 1 and 3, all of the solar spectrum is sent to the PV/T to run PV-electrolysis or PV-chloralkali. In all cases, the heat recovered by cooling down the PV/T to maintain a certain level of solar-to-electricity conversion efficiency can be sent to the reactor to operate at temperatures higher than the environmental temperature.

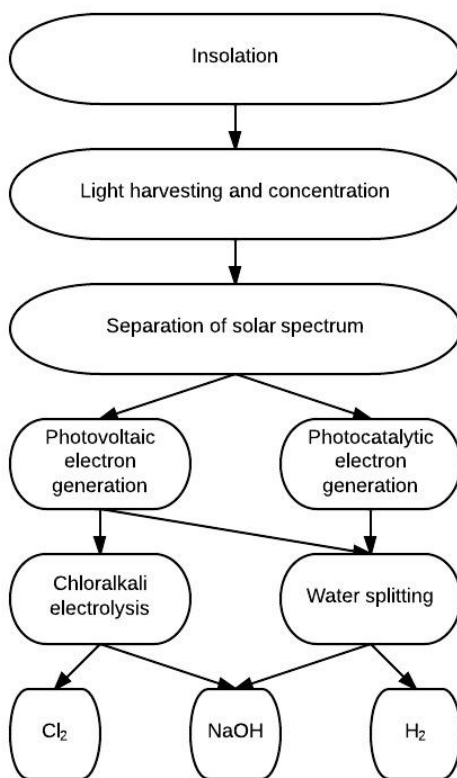


Figure 4.4 Illustrative representation of hybrid reactor's operation procedure (during Process 4).

During the course of the experiments, a constant volume reactor is used to keep the control volume constant. The reactor is connected to a set of monitoring and data acquisition components and an external energy supply to simulate the power generated by the PV/T. The operational energy requirements (i.e., pumps, data acquisition, sensors, etc.) are met by electricity. Electricity is also used to provide for electrolysis and chloralkali (Processes 1 and 3) and support PEC process (Processes 2 and 4). In addition, during Processes 2 and 4, (PEC and PEC-chloralkali), the reactor is illuminated by the solar simulator. Monitoring, controlling, and analyzing of operating parameters, input and output are conducted by pH and temperature sensors, voltage and current readings, and gas analyzers. A magnetic stirrer/heater is used to provide uniform temperature distribution inside the reactor. For each inlet stream, a feedback heater is used to keep the inlet streams at the desired operating temperature. The interactions between the present reactor and other

experimental setup components are presented in Figure 4.5. Anode and cathode are divided by a CEM. The reactor uses a MEA which is referred as MPEA.

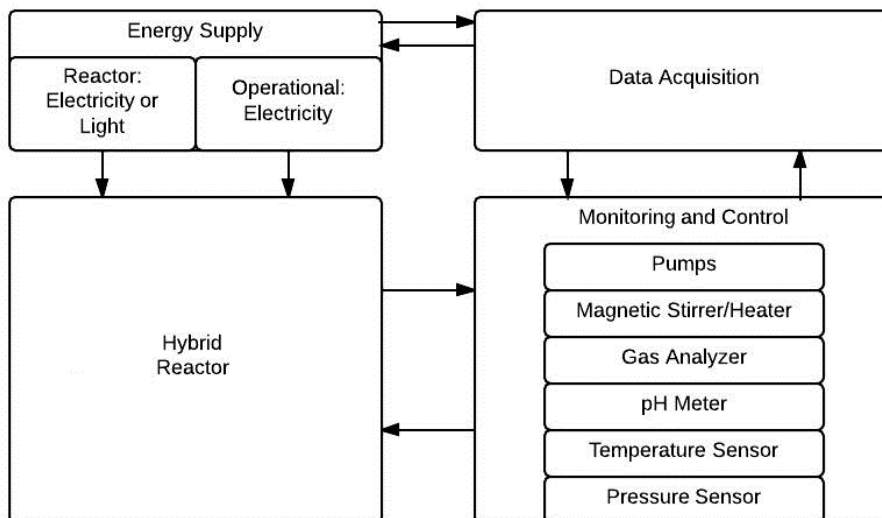


Figure 4.5 Schematic illustration of interactions between present reactor and other experimental setup components.

The hybrid reactor is the key component of the present experimental setup. The reactor has an MPEA which is consisted of an anode, a CEM, and a photocathode. Figure 4.6 shows the schematic illustration of the hybrid reactor for Processes 3 and 4, including the inlet and outlet streams. Streams 1, 2, 4, and 5 are in liquid state and 3 and 6 are in gas state. In addition to separating the product gases, the membrane neutralizes the OH^- ions in the cathode division by selectively facilitating the transport of the positive ions of the Cl^- salt from the anode to cathode section. Process 3 proceeds very similarly to Process 4, with the exception of lack of light. In Processes 1 and 2, H_2O is used in Streams 1, 2, 4, and 5 and H^+ ion passes through the membrane from the anode to cathode partition. The reactor has optically translucent windows to permit the irradiation of the photocathode throughout the PEC and PEC-chloralkali processes (Processes 2 and 4). The anode and cathode reactions during Processes 1 and 2 are given in Equations (4.1) and (4.2) as



And the reactions during Processes 3 and 4 are given in Equations (4.3) and (4.4).

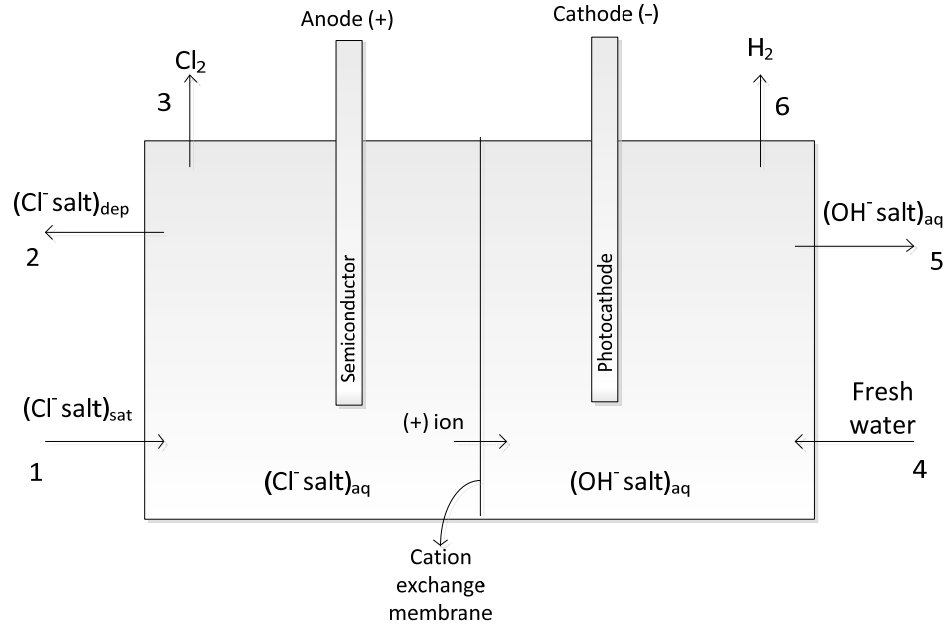
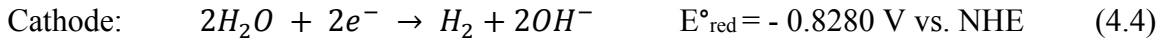


Figure 4.6 Schematic illustration of hybrid reactor during Processes 3 and 4.

The experiments are performed by using distilled water from Turbo Water and Omega PSU505 as a power supply. PSU505 has 3 programmable outputs; its total output power from all three channels is 120W. PSU505 also provides OVP (overvoltage protection) and OCP (over current protection). PSU505 has an average response time of 50 ms, and it is highly efficient and remains stable during source and load fluctuations. Voltage–current measurements are used to acquire the sign, density, and the onset potential of the current as well as energy and exergy efficiencies as a function of the applied potential. A multi-channel peristaltic pump from Longer Instruments, BT100-1L, is used to validate, monitor and control the inlet and outlet flow rates of both the anode and cathode. BT100-1L can support flow rates between 0.002 – 480 mL/min and allows each channel to have a different flow rate, making it possible to change each inlet/outlet flow rate independently. Table 4.1 shows the range, resolution and response time characteristics of the pressure, temperature, and pH sensors.

Table 4.1 Pressure, temperature, pH sensor characteristics.

Sensor	Range	Resolution	Response Time
Pressure	Up to 210 kPa	0.05 kPa	100 μ s
Temperature	-20°C–115°C	0.07°C	4s (to 90% of full reading in water)
pH	0–14	0.01	1s

4.3 Electrolytes, Electrodes and Membrane

Due to its poorly conductive nature, electrolytes are needed to support ions to ensure the desired current rates to split water. These electrolytes can either be reduced or oxidized, depending on the compartment they are used in (anode or cathode).

Ohmic losses (voltage drops) across the reactor due to the internal resistance can become a major issue during electrolysis, chloralkali, PEC, and PEC-chloralkali processes. These losses increase the applied potential requirements, which eventually reduce the system efficiency, and hence, lower system performance. This issue can be addressed by the proper selection of electrolytes. Table 4.2 presents the solubility, reactivity/corrosivity, and price comparison of Cl⁻/OH⁻ salt pairs.

Table 4.2 Solubility, reactivity/corrosivity, and price comparison of Cl⁻/OH⁻ salt pairs.

Electrolyte	Solubility (M)	Reactivity	Price (\$/g)	Issues
LiCl	12.9		6.2	Expensive
LiOH	5.3		0.4	
BeCl ₂	1.9		56.6	Expensive Commercially not available
Be(OH) ₂				
NaCl	6.1		0.1	No specific issues (selected electrolyte pair)
NaOH	27.8		0.9	
MgCl ₂	5.7		0.3	Poor solubility
Mg(OH) ₂	0.0			
KCl	4.6		10.62	Expensive
KOH	21.6	Corrosive	0.8	
CaCl ₂	6.7	Reacts violently with water	0.1	Poor solubility
Ca(OH) ₂	0.0		0.2	
RbCl	7.5		32.8	Expensive
RbOH	9.8		10.2	
SrCl ₂	3.4		14.9	Expensive Commercially not available
Sr(OH) ₂	0.1			
CsCl	11.1		2.17	Expensive
CsOH	20.0		2.84	
BaCl ₂	1.7		15.82	Expensive Commercially not available
Ba(OH) ₂	0.2			

For comparison purposes, in Processes 1 and 2, only H₂O is used to produce H₂ within the absence and presence of light. In Processes 3 and 4, the hybrid reactor produces H₂ in the cathode department, causing an OH⁻ accumulation while the anode produces Cl₂. The electrolytes considered to be used in this study are Cl⁻ and OH⁻ based salts to maintain Cl₂ production and OH⁻ neutralization in anode and cathode, respectively. Based on the solubility, reactivity/corrosivity, and price comparison of Cl⁻/OH⁻ salt pairs (Table 4.2), NaCl and NaOH are used as electrolytes in anode and cathode, respectively.

Depending on the operating conditions, during each experimental run, H₂ and Cl₂ gases can dissolve in catholyte and anolyte solutions. These dissolved gases could change redox potentials or they could cause back-reactions. Therefore, after each experiment, it is necessary to remove these product gases from electrolytes by purging them with inert gases (e.g., N₂). Purging efficiency can be increased by using a magnetic stirrer, which keeps both the anolyte and catholyte homogeneous and minimizes mass transport related restrictions. However, in cases where the ionic concentrations are high, stirring might not be necessary.

With the selection of the electrolytes, the overall reaction becomes:



During oxidation and reduction reactions, electron acceptors and donors are needed to be provided steadily as they are used up. Replacement and renewal of these materials are critical research and development challenges. In this study, a hybrid reactor uses an external power source (electricity generated via PV/T) and two electrodes immersed in two different electrolyte solutions to supply and transfer electrons in two compartments. The electrode in cathode department is a photocathode, which drives photochemical H₂ production reaction, besides transferring electrons. The electrodes should have high electrochemical and photochemical activities to avoid performance limitations. Good stability and small over potential for H₂/Cl₂ evolution are other performance criteria for electrolytes. In order to provide homogeneous current densities, electrodes should be placed symmetrically. Ion exchange capacity, thickness, area resistance, and permselectivity of some CEM are listed in Table 4.3.

With the help of their electrically charged functional sites, ion exchange membranes selectively to separate ions: a positively charged membrane (anion-exchange) only allows anions to pass through while a negatively charged membrane (cation-exchange) only allows cations to pass through. This membrane property is called permselectivity, which is customizable based on different system requirements [149]. In this study, the anode and cathode are separated by a cation-exchange membrane. The membrane selectively permits the transfer of either H^+ (in Processes 1 and 2) or Na^+ ions (in Processes 2 and 4) produced during O_2 (Processes 1 and 2) or Cl_2 (Processes 3 and 4) evolution at the anode into the cathode chamber where neutralization of OH^- ions occurs. And as a result, H_2O (Processes 1 and 2) or $NaOH$ solution (Processes 3 and 4) is produced.

Table 4.3 Selected technical properties of some commercially available membranes.

Membrane	Ion-exchange Capacity (meq/g)	Thickness (mm)	Resistance ($\Omega\text{ cm}^2$)	Permselectivity (%)
<i>Asahi Glass Co. Ltd., Japan</i>				
CMV	2.4	0.15	2.9	95
HJC	1.8	0.83	2.0 – 2.8	92
<i>CSMCRI, India</i>				
IPC	1.4	0.14 – 0.16	1.5 – 2.0	97
HGC	0.67 – 0.77	0.22 – 0.25	4.0 – 6.0	87
<i>DuPont Co., USA</i>				
Nafion 117	0.9	0.2	1.5	97
Nafion 901	1.1	0.4	3.8	96
<i>FuMA-Tech GmbH, Germany</i>				
FKB	0.9 – 1.0	0.08 – 0.1	< 4	> 98
FKE	> 1	0.05 – 0.07	< 3	> 98
FKL	> 1	0.11 – 0.12	< 4	> 92
FKS	> 1	0.11 – 0.13	< 8	> 96
<i>Ionics Inc., USA</i>				
61CZL38	2.6	0.63	9	95
CMI-7000	1.5 – 1.8	0.2 – 0.7	8.0 – 12.0	94
<i>RAI Research Corp., USA</i>				
R-5010-H	0.9	0.24	8.0 – 12.0	95
R-1010	1.2	0.1	0.2 – 0.4	86
<i>Tokuyama Soda Co. Ltd., Japan</i>				
CMX	1.5 – 1.8	0.14 – 0.20	1.8 – 3.8	97
CMS	2	0.15	1.5 – 2.5	95

In this study, H_2 screener MEA with an active area of 100 cm^2 is purchased from Alfa Aesar. The MEA, which is about 0.4 cm thickness, has a nominal Pt loading of 0.4 mg/cm^2 on both anode and cathode sides. The membrane is composed of 50 wt. % non-woven carbon fibers, 35 wt. % perfluorosulfonic acid (PFSA)/membrane, 5 wt. %

polytetrafluoroethylene (PTFE), 5 wt. % carbon (black), 5 wt. % catalyst (finely divided Pt on C).

In order to develop the MPEA mentioned earlier in this chapter, the cathode side of this membrane is electrodeposited with Cu_2O . Cu_2O is considered as one of the most promising photosensitive materials for PEC water splitting because of its low toxicity, abundance, low environmental damage and simple production process. Cu_2O is a p-type semiconductor with a direct band gap of 2.0 eV [150]. It can absorb solar radiation in the range of 300–600 nm, covering about 50% of the photons of the solar spectrum. Cu_2O is considered as a promising candidate photocathode in a PEC cell, because the conduction band edge of Cu_2O (ca. -1.35 V vs. Ag/AgCl at pH=7) is sufficiently more negative than the reduction potential of water (ca. -0.61 V vs. Ag/AgCl at pH=7) [151]. Therefore, Cu_2O is in principle capable of decomposing water into H_2 as a photocathode.

Cu_2O can be synthesized by various methods, such as sputtering [152, 153], chemical vapor deposition [154], thermal oxidation [155], chemical bath deposition [156], and electrodeposition [157–159]. The electrodeposition technique has attracted special interest for the preparation of Cu_2O thin films in recent years. It has two major advantages, namely its simplicity and the low growth temperature, leading to low cost processes and a large number of industrial applications. Electrodeposition allows stoichiometry, thickness, and microstructure control of the films by adjusting the deposition parameters.

Cu_2O films are electrodeposited in a three-electrode configuration in galvanostatic mode based on the procedure described in [160]. In the electrodeposition setup, working electrode is the MEA described above, counter electrode is a Pt wire wrapped around graphene, and reference electrode is Ag/AgCl. Cu_2O is electrodeposited by reduction of an alkaline aqueous solution of cupric lactate. The electrolytic bath contained 0.4 M copper (II) sulfate and 3 M lactic acid as chelating agent to stabilize Cu^{2+} ions by complexing. The bath temperature is set to room temperature (about 20°C). The pH of the bath is adjusted to 11 by adding KOH solution. The electrodeposition process is shown in Figure 4.7.

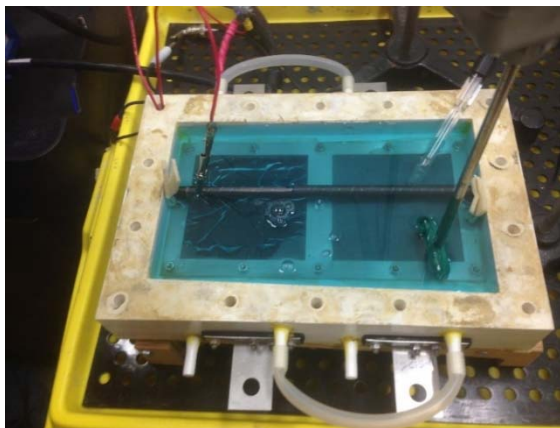


Figure 4.7 Present experimental setup during electrodeposition process.

4.4 Instruments and Devices

In addition to the reactor explained above, a solar simulator (VIII), potentiostat (VII), peristaltic pump (IV), temperature and pH sensor, volumetric water displacement cylinder (V), four glass vessels (two for feed and two for dump electrolytes, II and III), and two hot plates (VI) are used in the present experimental setup.

OAI's Trisol™, TSS 208, with an active illumination area of 208 x 208 mm is used as solar simulator. The simulator used evolved homogenous beam optics that consist of patented glazed mirrors, filters, and a beam homogeneity integrator. OAI's solar simulator claims to deliver substantially precise, collimated rays with elongated operating lengths. OAI solar simulator is licensed to ASTM E927-05, IEC 60904-9 2007, and JIS C 8912 criteria for Class AAA operation (Spectral Match 400–1100nm wavelength in 100nm bandwidth increases, Non-Uniformity, and Temporal Instability). The simulator has spectral match patented filters for working analysis of dye sensitized cells, organic PV, concentrated PV, and multi-junction GaAs based solar cells. The simulator filter is devised to mimic the Air Mass 1.5 Global (AM1.5G). The ray concentration can be fine-tuned from 0.6 to 1.2 Suns. The simulator has a standard configuration with adjustable power mode, steady power, or stable light intensity processes. An adjustable power source permits the ray intensity array to be from 0 Suns to 1.2 Suns. During the constant intensity operation, lamp power routinely fine-tunes to preserve a constant Sun intensity while lamp power begins to decay with time. Figure 4.8 shows the solar simulator illuminating the reactor.



Figure 4.8 Solar simulator illuminating the reactor at 1 Sun intensity.

The cathode of the reactor is exposed directly to photonic radiation which is assisted electrically by means of a potentiostat (VII). A potentiostat is a device which applies a potential across a pair of electrodes and simultaneously measures the current which flows through a solution of an anolyte. Figure 4.9 shows the potentiostat used in this study.



Figure 4.9 Omega PSU505 potentiostat during an experimental run.

The potentiostat used for this research is the Omega PSU505 Programmable DC Power Supply which has three channels. Channel 1 and 2 have a maximum current of 3 A and a maximum voltage of 30 Volts (maximum output power of 90 W). Channel 3 has a maximum current of 5 A and a maximum voltage of 15 Volts (maximum output power of 30 W). In this study, Channel 1 is used to support the reactor.

Figure 4.10 shows the peristaltic pump in operation. A multi-channel peristaltic pump from Longer Instruments, BT100-1L, is used to validate, monitor, and control inlet and outlet flow rates of both the anode and cathode.

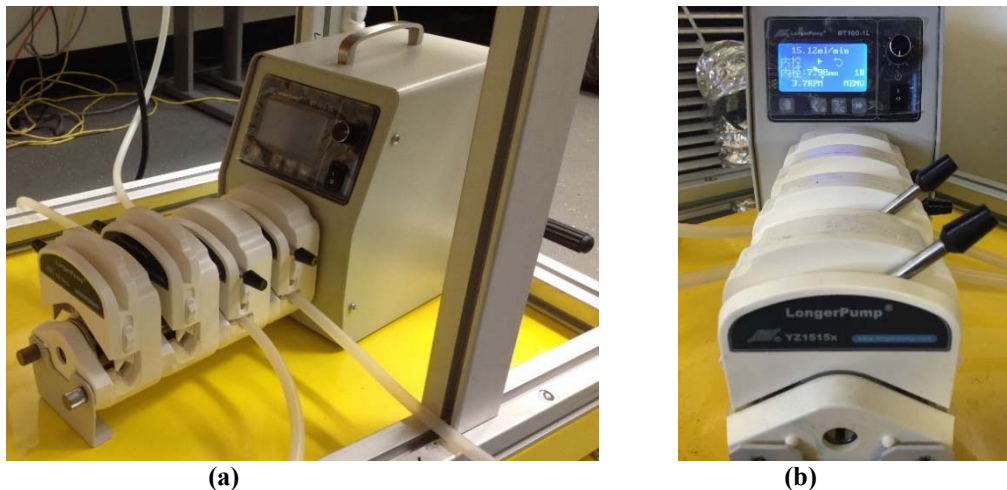


Figure 4.10 Multi-channel BT100-1L Peristaltic pump (a) and pump during an experimental run (b).

BT100-1L can support flow rates between 0.002–480 mL/min and it allows each channel to have a different flow rate, making it possible to change each inlet/outlet flow rates independently. The speed can be adjusted manually or automatically through external control. It also has the advantage of store the running parameters automatically which makes it fairly easy to operate.

The electrolyte feed tanks with heaters and volumetric water displacement cylinder are shown in Figure 4.11. The heaters (Corning Stirrer/Hot Plate) are used to heat the two inlet streams, when the experiment is required to run at temperatures higher than the atmospheric temperature. Omega PHH-103 is used to monitor the temperature and pH of electrolyte feed and dump tanks. In addition, a magnetic stir bars are used in feed tanks to keep the anolyte and catholyte solutions as homogenous as possible. Electrolyte feed and dump tanks are custom-made by ProScience GlassShop Division with a capacity of 6000 mL. Chemglass screw thread connectors with caps and sealing rings.

In all processes, experimental runs are conducted at atmospheric pressure at various temperatures. The amount of H₂ produced during each experimental run is measured by using the volumetric water displacement cylinder shown in Figure 4.11. The cylinder has

a 2 cm radius. Ideal gas law is used to calculate number of moles of H_2 production in all processes at all operating temperatures.

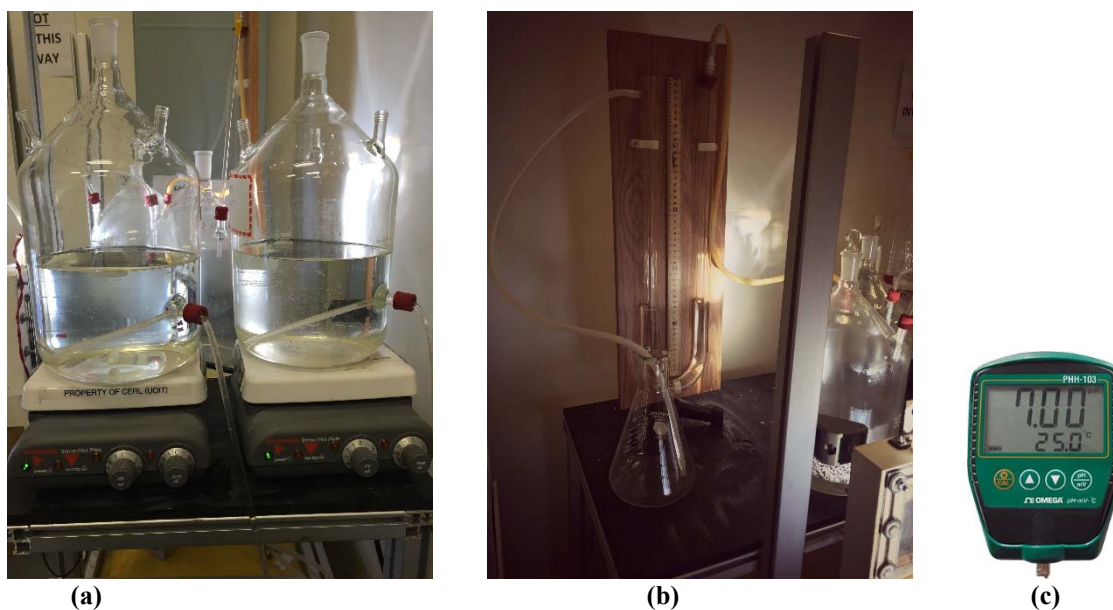


Figure 4.11 Electrolyte feed tanks with heaters (a), volumetric water displacement cylinder (b), and temperature/pH monitor (c).

4.5 Experimental Procedure

During the initial phases of the experimental planning (Figure 4.12), the following issues are identified, addressed, and determined: (i) primary variables to be investigated, (ii) type of control to be exerted on the experiment, (iii) ranges of primary variables, (iv) instrumentation accuracy, and (v) safety precautions. Figure 4.12 describes the general procedure followed throughout the experimental runs. The experimental procedure is developed and utilized, based on some sources available in the literature [161, 162]. The types of experiments performed in this study are: (i) Process 1: electrolysis, (ii) Process 2: PEC, (iii) Process 3: chloralkali, and (iv) Process 4: PEC-chloralkali.

4.5.1 Process 1: Electrolysis Experiments

As it can be seen from Figure 4.12, electrolysis experiments start with checking the proper operation of the system components including potentiostat, heaters, water displacement cylinder, temperature sensor, peristaltic pump, and electrolyte feed and dump tanks. Any

sign of improper operation is calibrated and fixed before starting the experimental run. Distilled water is used as anolyte and catholyte in electrolysis experiments. Following the electrolyte preparation, cell voltage and temperature are set to desired operating values.

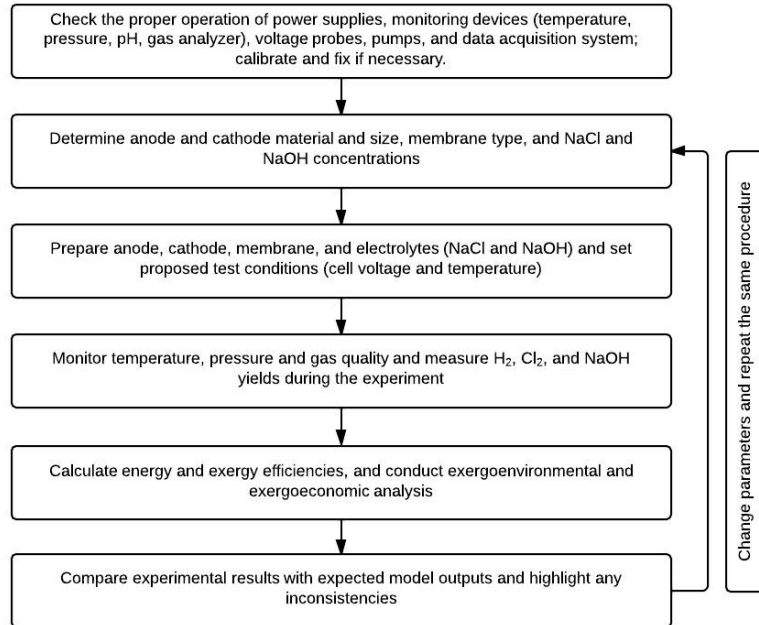


Figure 4.12 Schematic description of present experimental procedure.

During the experimental runs, temperature, electrolyte inlet flow rates, applied voltage and resulting current, and the water level at the displacement cylinder (as well as the level in feed and dump tanks) are monitored and H₂ yield is calculated. Once the experimental run is completed, energetic and exergetic performances are evaluated from the amount of H₂ produced and energy/exergy input. The results are compared with the expected model outputs and any inconsistencies are highlighted and investigated. The same test is run again to check repeatability. Once the consistency and repeatability are verified, the same procedure is repeated with different parameters. The following parameters are investigated during the electrolysis experiments (Figure 4.13):

- i. Electrolyte inlet flow rates: 0.25, 0.50, and 0.75 g/s
- ii. Operating temperature: 20, 40, 60, and 80°C

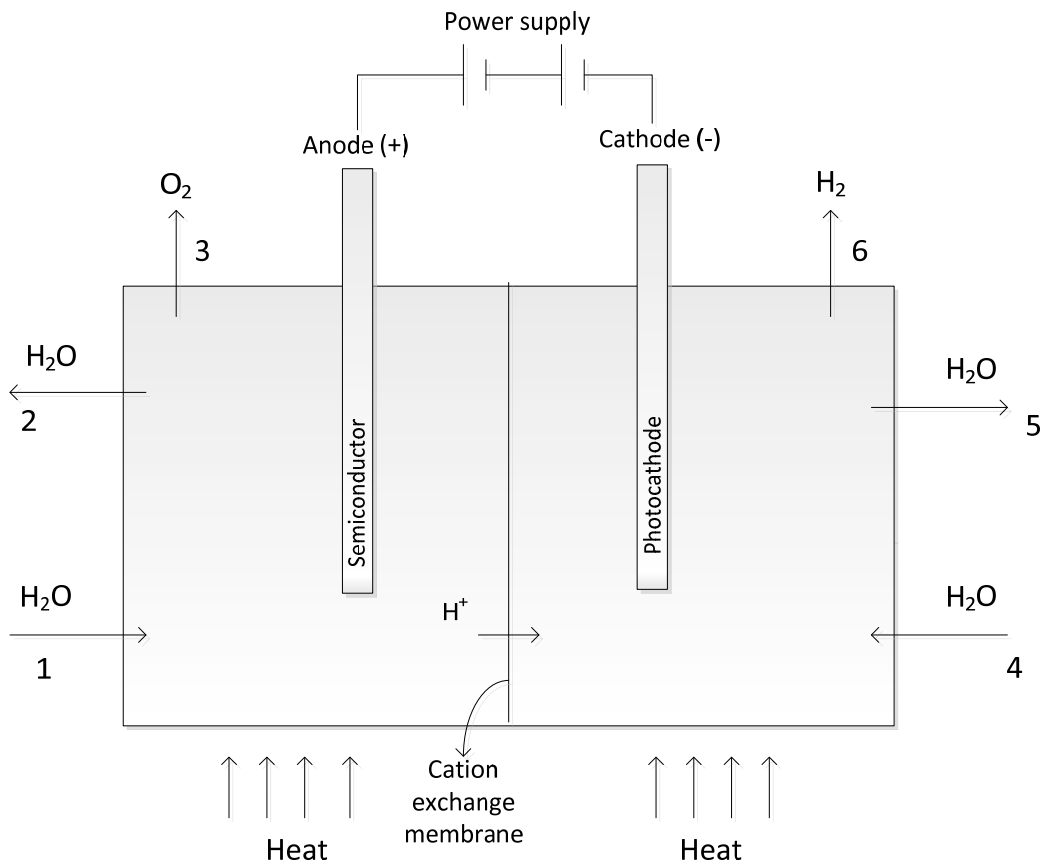


Figure 4.13 Schematic description of experimental runs during electrolysis (Process 1).

In electrolysis experiments, H_2O enters the anode where it is dissociated to H^+ and O_2 (Equation 4.1). H^+ ions pass through the CEM and H_2 is produced in the cathode (Equation 4.2).

4.5.2 Process 2: Photoelectrochemical Experiments

Process 2 is very similar to Process 1, therefore same procedure is followed and same equations apply to Process 2 as well. In addition to the two parameters mentioned in Process 1, in Process 2, two different light intensities of 600 W/m^2 (0.6 Suns) and 1200 W/m^2 (1.2 Suns) are tested to measure light response of the MPEA and the effect of light intensity on the amount of H_2 production and system efficiencies. Figure 4.14 shows the schematic representation of the PEC experiment.

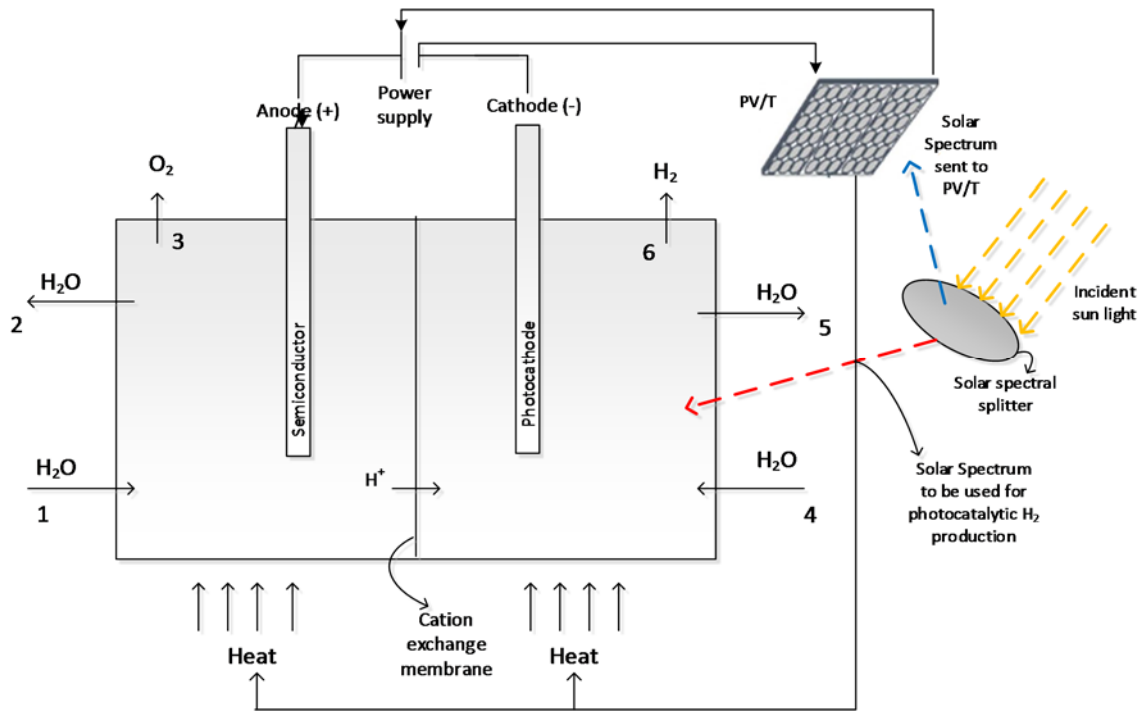


Figure 4.14 Schematic description of experimental runs during PEC (Process 2).

4.5.3 Process 3: Chloralkali Experiments

Process 3 is also similar to Process 1, therefore the same experimental procedure is followed. However, in Process 3, NaCl is used as anolyte, and NaOH is used as catholyte. The product gas H₂ leaves the cathode with NaOH solution and Cl₂ leaves the anode with NaCl solution. The anode and cathode reactions of Process 3 are given in Equations (4.3) and (4.4). The parameters used in Process 3 are the same as Process 1, for comparison purposes. Figure 4.15 shows the schematic of the PEC experiment.

4.5.3 Process 4: Photoelectrochemical-Chloralkali Experiments

The procedure for PEC-chloralkali experiments (Figure 4.16) is also similar to the electrolysis, PEC, and chloralkali. Equations (4.3) and (4.4) give the reactions taking place in anode and cathode, respectively. The experimental parameters varied during the present experiments are operating temperature, electrolyte flow rate, and illumination density, which are the same as Process 2 for comparison purposes.

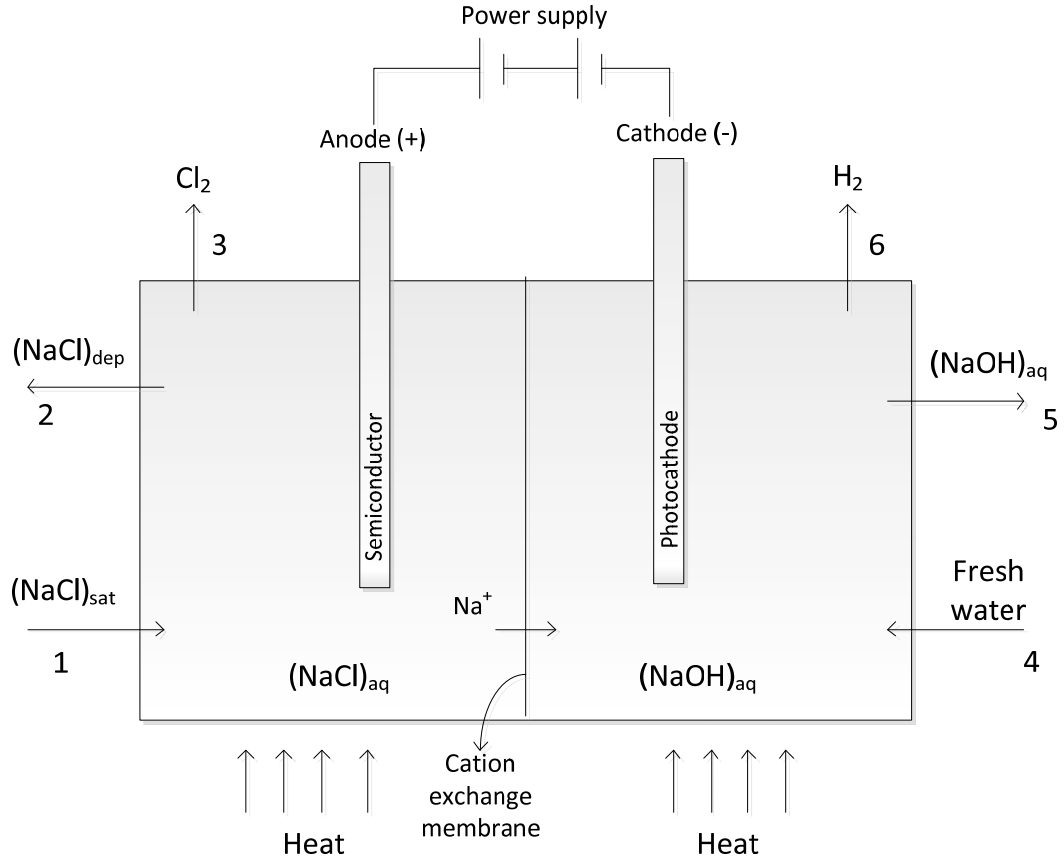


Figure 4.15 Schematic description of experimental runs during chloralkali (Process 3).

Like electrolysis and photoelectrolysis experiments, in a PEC process (Figure 4.16), saturated NaCl solution enters the anode where NaCl dissociated to Na^+ and Cl^- , and Cl^- is oxidized to Cl_2 . The Na^+ ions pass through the CEM where it is used to neutralize OH^- , producing NaOH, H_2 is also produced in the cathode. In this case, the simulator is used as the source of solar energy.

4.6 Experimental Uncertainties

Uncertainty analysis of an experiment is crucial to determine the effect of device accuracies, and their bias and precision errors [163]. Calculation of the experimental uncertainty is based on the bias and precision errors of the measurement devices and it is defined as follows:

$$U_i = (B_i^2 + P_i^2)^{0.5} \quad (4.6)$$

Here, B stands for bias error and P stand for precision error.

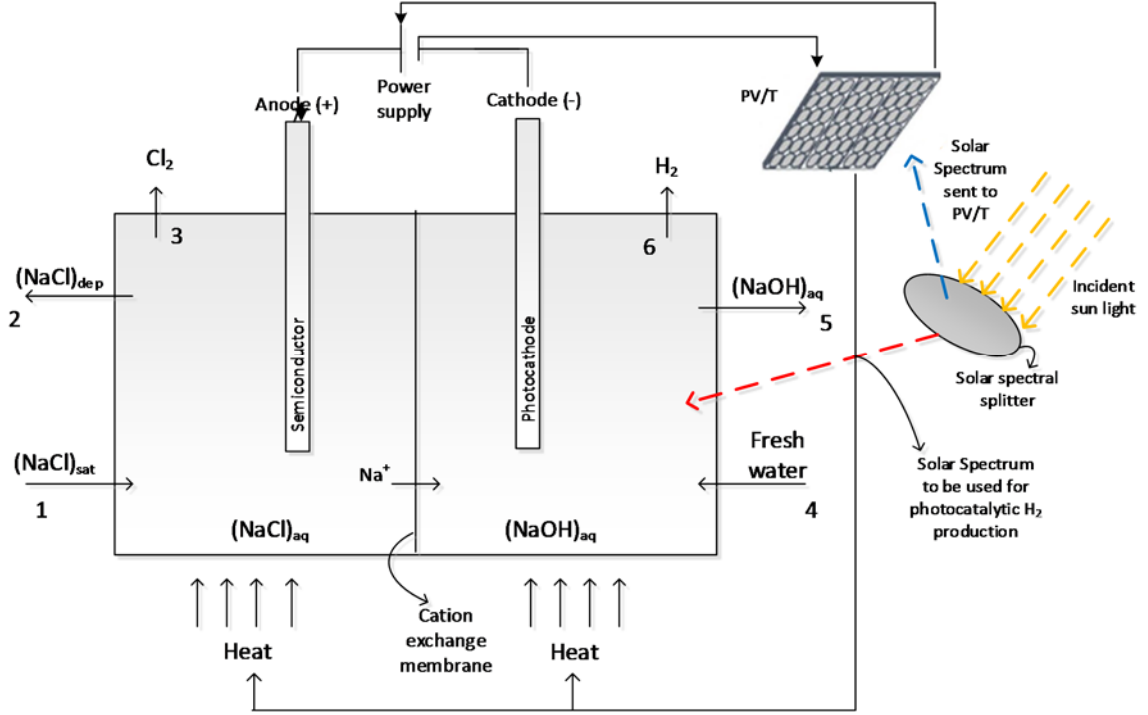


Figure 4.16 Schematic description of experimental runs during PEC-chloralkali (Process 4).

Table 4.4 represents the bias and precision errors of all devices affecting the measurements in the experiments. Bias error is the average difference between the estimator and the true value. Precision error is the standard deviation of the estimator. Bias and precision errors are calculated based on the partial derivatives of the varying parameters and corresponding device errors. The varied parameters in the experiments are operating temperature, electrolyte flow rate, and irradiation level. The corresponding equations for uncertainty in the amount of current generation are written as follows:

$$B_i^2 = \left(\frac{\partial i}{\partial T}\right)^2 B_T^2 + \left(\frac{\partial i}{\partial F}\right)^2 B_F^2 + \left(\frac{\partial i}{\partial I}\right)^2 B_I^2 \quad (4.7)$$

$$P_i^2 = \left(\frac{\partial i}{\partial T}\right)^2 P_T^2 + \left(\frac{\partial i}{\partial F}\right)^2 P_F^2 + \left(\frac{\partial i}{\partial I}\right)^2 P_I^2 \quad (4.8)$$

where T , F , and I , stand for temperature, flow rate, and irradiation level, respectively. Also, the equations for uncertainty in the amount of H_2 production are written as

$$B_{H_2}^2 = \left(\frac{\partial H_2}{\partial T}\right)^2 B_T^2 + \left(\frac{\partial H_2}{\partial F}\right)^2 B_F^2 + \left(\frac{\partial H_2}{\partial I}\right)^2 B_I^2 \quad (4.9)$$

$$P_{H_2}^2 = \left(\frac{\partial H_2}{\partial T}\right)^2 P_T^2 + \left(\frac{\partial H_2}{\partial F}\right)^2 P_F^2 + \left(\frac{\partial H_2}{\partial I}\right)^2 P_I^2 \quad (4.10)$$

Similarly, the uncertainty in the energy efficiency (η) can be determined by the following equations:

$$B_\eta^2 = \left(\frac{\partial \eta}{\partial T}\right)^2 B_T^2 + \left(\frac{\partial \eta}{\partial F}\right)^2 B_F^2 + \left(\frac{\partial \eta}{\partial I}\right)^2 B_I^2 \quad (4.11)$$

$$P_\eta^2 = \left(\frac{\partial \eta}{\partial T}\right)^2 P_T^2 + \left(\frac{\partial \eta}{\partial F}\right)^2 P_F^2 + \left(\frac{\partial \eta}{\partial I}\right)^2 P_I^2 \quad (4.12)$$

The exergy efficiency (ψ) can be calculated correspondingly as

$$B_\psi^2 = \left(\frac{\partial \psi}{\partial T}\right)^2 B_T^2 + \left(\frac{\partial \psi}{\partial F}\right)^2 B_F^2 + \left(\frac{\partial \psi}{\partial I}\right)^2 B_I^2 \quad (4.13)$$

$$P_\psi^2 = \left(\frac{\partial \psi}{\partial T}\right)^2 P_T^2 + \left(\frac{\partial \psi}{\partial F}\right)^2 P_F^2 + \left(\frac{\partial \psi}{\partial I}\right)^2 P_I^2 \quad (4.14)$$

The partial derivatives of the variables are calculated from a correlated equation obtained from the experimental results which is a function of all variables. A code is modified in order to determine uncertainty of the experiments, using MATLAB software [164].

Table 4.4 Relative errors and accuracy related to measurement devices.

Variable	Device	Accuracy	Range	Reference value	Relative bias error	Relative precision error
Irradiation, I	Trisol Solar Simulator TSS-208	± 20.28 W/m ²	600-1200 W/m ²	1200 W/m ²	0.0169	0.0001
Flow rate, F	LongerPump BT100-1L YZ1515X	± 0.01 mL/min	Up to 380 mL/min	60 mL/min	0.0002	0.0006
Temperature, T	Omega PHH-103A	$\pm 0.02^\circ\text{C}$	Up to 1250°C	400°C	0.0001	0.0006
Voltage, V	Omega PSU-505	± 0.00725 V	0 to 15 V	2.5 V	0.0029	0.0005
Current, i	Omega PSU-505	± 0.0045 A	0 to 5 A	1 A	0.0045	0.0005

4.7 Development of Integrated System

A block illustration of the integrated system is shown in Figure 4.17 which describes the large scale conceptual system. The solar irradiation (Stream 1) is sent to the solar spectral splitter (Unit I). Here, photons with wavelengths up to 400 nm is sent directly to the hybrid

reactor (Unit III). Rest of the spectrum (Stream 2) is sent to the PV/T (Unit II) where the produced electricity (Stream 4) is sent to support Unit III. Excess electricity (Stream 5) is served as a product of the integrated multi-generation system. In order to minimize any efficiency losses, PV/T is cooled down and the recovered heat is used to heat up Unit III (Stream 6) when operating at temperatures higher than the environmental temperature. Stream 7 is the heat product, which is recovered from the PV/T and not used by Unit III.

Comprehensive energy and exergy analyses are conducted on the integrated system. In addition, exergoenvironmental and exergoeconomic analyses are performed. This provides substantial information about the performance, efficiency, cost, and emissions during the operation of the integrated system. All balance equations is written for all system components to eventually form a closed algebraic system. The solution of the system leads to the determination of the exergy destructions for each component, the exergy corresponding to produced H_2 , Cl_2 , electricity, and heat production. In addition, a multi-objective optimization study is utilized to determine the optimum key operating parameters resulting highest system efficiency and lowest environmental impact and cost possible

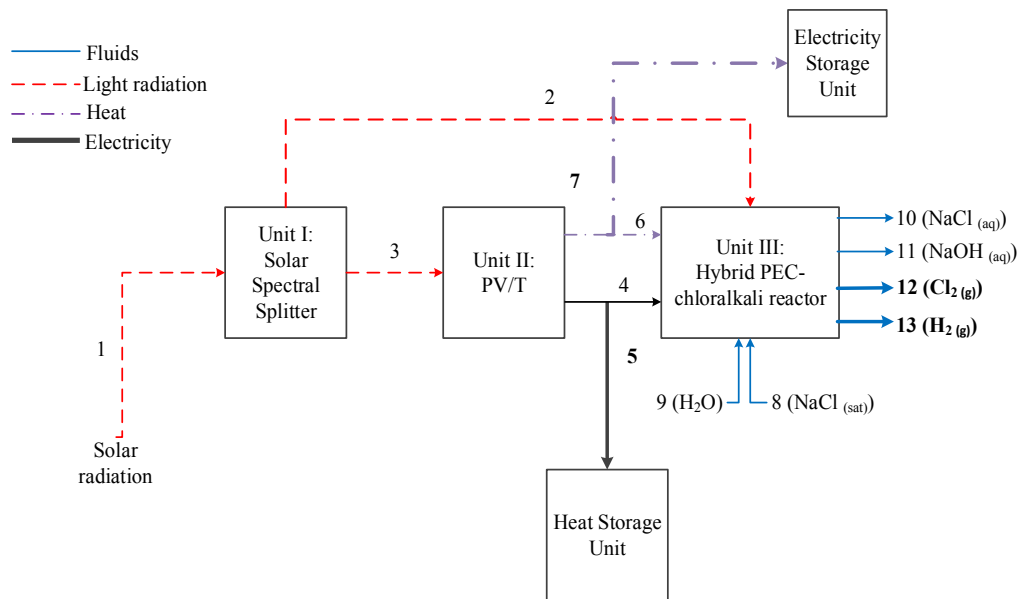


Figure 4.17 Conceptual block diagram of integrated system for solar H_2 , Cl_2 , electricity, and heat production.

CHAPTER 5: ANALYSES AND OPTIMIZATION

Thermodynamic performance of the hybrid reactor and the integrated multi-generation system are examined by conducting quantitative energy and exergy analyses. An economic evaluation of the integrated system is performed based on the exergoeconomic analysis. An exergoenvironmental investigation is employed to assess the potential environmental impact of the integrated system. In this chapter, the assumptions, basic concepts, procedure, and equations used to evaluate system performance are described and explained. Throughout this study, the following assumptions are utilized:

- Environmental temperature (T_0) and pressure (P_0) are 20°C and 1 atm, respectively.
- All streams and components are at operating temperature and pressure at all times.
- All processes take place in steady-state and steady-flow.
- All processes proceed to completion.
- Changes in potential and kinetic energies are negligible.
- Change in the control volumes (reactor and integrated system units) is disregarded.
- H₂, O₂, and Cl₂ gases are presumed to be ideal.
- The heat losses to environment are neglected.
- The auxiliary components are assumed to be well insulated and capable of conducting electricity with no loss.
- The spectral splitting system is evaluated from the procedure reported by Zamfirescu and Dincer [104].

For the integrated multi-generation system, a hypothetical location is chosen where sufficient solar irradiation exists, which is presumed to be 1 kW/m² with AM1.5G solar spectrum [165]. Number of annual operational sunlight hours is taken as 2000 h [104].

5.1 Basic Thermodynamic Concepts

In this section, overall mass, energy, entropy and exergy balance equations are listed and modified based on the assumptions and operating conditions of the hybrid reactor and integrated multi-generation system. The heat and work input/output, entropy generation, and exergy destruction rates, and energetic and exergetic effectiveness are evaluated from these balance equations.

Mass Balance Equation (MBE):

General conservation of mass in a control volume for any system can be written in its most general arrangement as

$$\frac{dm_{cv}}{dt} = \sum \dot{m}_{in} - \sum \dot{m}_{out} \quad (5.1)$$

where m and \dot{m} are the mass and mass flow rate, and the subscripts “ cv ”, “ in ” and “ out ” specify the control volume and the inlet and outlet of the control volume, respectively.

In the course of steady-state steady-flow operation, Equation (5.1) becomes:

$$\sum \dot{m}_{in} = \sum \dot{m}_{out} \quad (5.2)$$

Figure 5.1 shows the schematic of the experimental setup used during the experimental testing of Processes 1, 2, 3, and 4, which are explained in the previous chapter. Table 5.1 summarizes what each stream is composed of during each process.

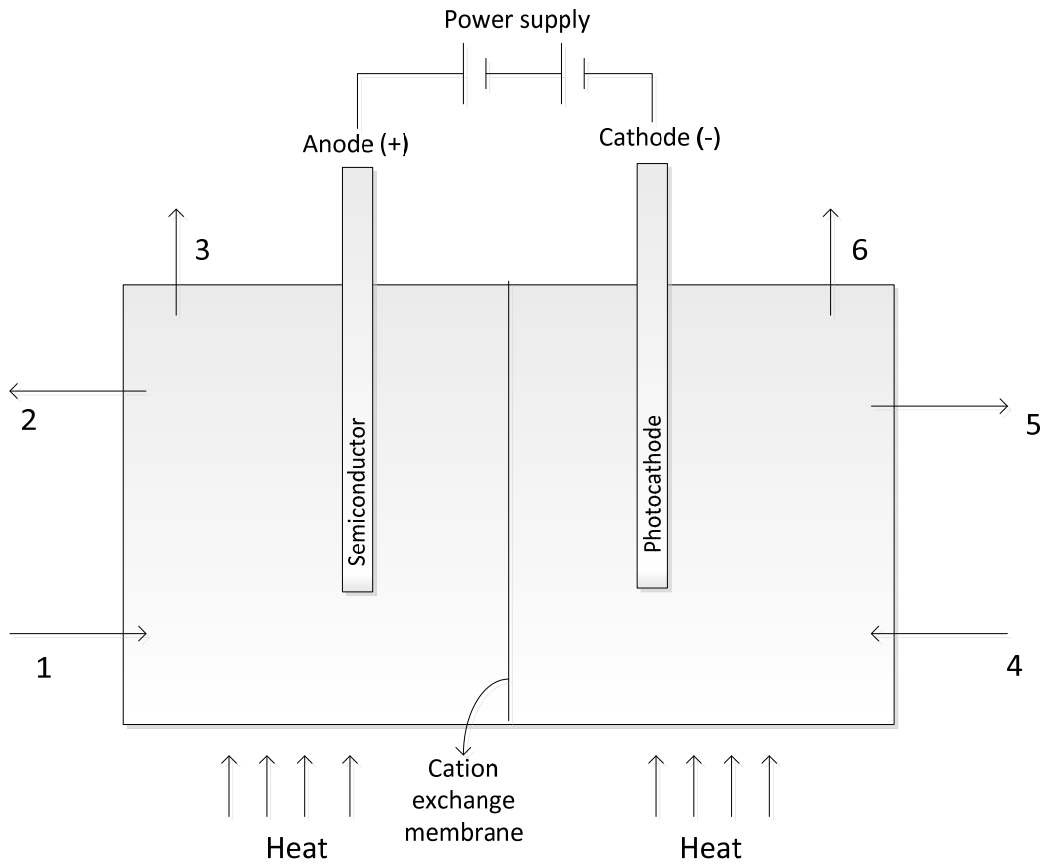


Figure 5.1 Schematic of continuous type hybrid reactor used in Processes 1, 2, 3 and 4.

Table 5.1 Stream definitions of experimental setup during various processes.

Stream	Processes 1 and 2	Processes 3 and 4
1	Fresh water inlet	Saturated NaCl solution inlet
2	Fresh water outlet	Depleted NaCl solution outlet
3	O ₂ gas outlet	Cl ₂ gas outlet
4	Fresh water inlet	Fresh water inlet
5	Fresh water outlet	NaOH solution outlet
6	H ₂ gas outlet	H ₂ gas outlet

The steady-state steady-flow mass balance equation (MBE) of the hybrid reactor in continuous operation (Figure 5.1) is:

$$\dot{m}_1 + \dot{m}_4 = \dot{m}_2 + \dot{m}_3 + \dot{m}_5 + \dot{m}_6 \quad (5.3)$$

Energy Balance Equation (EBE):

Conservation of energy equation in a control volume can be formulated from the first law of thermodynamics which states:

$$E_2 - E_1 = \delta Q - \delta W \quad (5.4)$$

where heat and work interactions between the control volume and its surroundings are represented by Q and W , respectively. Initial and final states are denoted by subscripts 1 and 2. E can be any form of energy (potential, kinetic, and/or flow) that a system could have at a given state. The general transient type energy balance equation is [166]:

$$\frac{dE_{cv}}{dt} = \dot{Q}_{cv} - \dot{W}_{cv} + \sum \dot{m}_{in} \left(h + \frac{V^2}{2} + gz \right)_{in} - \sum \dot{m}_{out} \left(h + \frac{V^2}{2} + gz \right)_{out} \quad (5.5)$$

where \dot{Q} and \dot{W} are the rates of heat and electricity flows inside the control volume, respectively. And h , V , z and g represent the specific enthalpy, velocity, altitude, and gravitational acceleration, respectively. Equation (5.5) can be modified by the steady-state steady-flow process assumption, and if the potential and kinetic energy differences are neglected, the energy balance can be rewritten as [167]

$$\sum \dot{m}_{in} h_{in} + \dot{Q}_{in} + \dot{W}_{in} = \sum \dot{m}_{out} h_{out} + \dot{Q}_{out} + \dot{W}_{out} \quad (5.6)$$

The continuous type hybrid reactor used in this study (schematically shown in Figure 5.1) has no work or heat output, and by considering the stream numbers, the steady-state steady-flow energy balance equation (EBE) can be written as

$$\dot{m}_1 h_1 + \dot{m}_4 h_4 + \dot{W}_{in} + \dot{Q}_{in} = \dot{m}_2 h_2 + \dot{m}_3 h_3 + \dot{m}_5 h_5 + \dot{m}_6 h_6 \quad (5.7)$$

where h_{1-6} denotes the specific enthalpies of the related streams, and \dot{W}_{in} indicates the overall electricity supply to the reactor. The \dot{Q}_{in} in Equation (5.7) denotes the heat requirement to retain the operating temperature above environmental temperature, when needed. Note that \dot{Q}_{in} is zero if the reactions proceed at room temperature.

Throughout electrolysis and chloralkali (Processes 1 and 3), the work input is electricity, while in PEC and PEC-chloralkali (Processes 2 and 4) the work input is solar energy. These processes' work input are evaluated based on the following equations:

$$\text{Processes 1 and 3:} \quad \dot{W}_{in} = \dot{W}_{electricity} = V \times i \quad (5.8)$$

$$\text{Processes 2 and 4:} \quad \dot{W}_{in} = \eta_{PV}(1 - \alpha) \dot{I} A_{PV} + \alpha \dot{I} A_{photocathode} \quad (5.9)$$

where V is volts (V), i is current in amps, η_{PV} and A_{PV} are the efficiency and area of PV/T, respectively, \dot{I} is the solar irradiation per unit area, $A_{photocathode}$ is the photocathode area, and α is the fraction of solar spectrum employed by photocathode for PEC-based H₂ generation.

In Processes 3 and 4, temperature (T) and concentration (x) dependent specific enthalpy (h) equation of a NaCl solution can be written as [168]

$$h = A + B T + C T^2 + D T^3 + E T^4 \quad (5.10a)$$

Between 0 and 300°C, A, B, C, D, and E can be defined as [168]

$$A = 0.5 + 37.8 x - 368.2 x^2 - 652.9 x^3 + 2890 x^4 \quad (5.10b)$$

$$B = 4.145 - 4.973 x + 4.482 x^2 + 18.31 x^3 - 46.41 x^4 \quad (5.10c)$$

$$C = 0.0007 - 0.0059 x + 0.0854 x^2 - 0.4951 x^3 + 0.8255 x^4 \quad (5.10d)$$

$$D = (-0.0048 + 0.0639 x - 0.714 x^2 + 3.273 x^3 - 4.85 x^4) \times 10^{-3} \quad (5.10e)$$

$$E = (0.0202 - 0.2432 x + 2.054 x^2 - 8.211 x^3 + 11.43 x^4) \times 10^{-6} \quad (5.10f)$$

Entropy Balance Equation (EnBE):

Using the second law of thermodynamics, the entropy balance equation can be written as

$$\frac{dS_{cv}}{dt} = \sum \dot{m}_{in} s_{in} - \sum \dot{m}_{out} s_{out} + \sum \frac{\dot{Q}_{cv}}{T_0} + \dot{S}_{gen} \quad (5.11)$$

where s stands for specific entropy and \dot{S}_{gen} is the rate of entropy generation. Unlike energy, entropy is not conserved; it is generated during a process due to system irreversibilities. Thus, the amount of entropy leaving the control volume exceeds the input entropy due to entropy generation associated with irreversibilities. During the steady-state steady-flow operation, Equation (5.11) becomes:

$$\sum \dot{m}_{in} s_{in} + \sum \frac{\dot{Q}_{cv}}{T_0} + \dot{S}_{gen} = \sum \dot{m}_{out} s_{out} \quad (5.12)$$

For the continuous type hybrid reactor shown in Figure 5.1, the steady-state steady-flow entropy balance equation (EnBE) can be written as

$$\dot{m}_1 s_1 + \dot{m}_4 s_4 + \frac{\dot{Q}_{in}}{T_0} + \dot{S}_{gen} = \dot{m}_2 s_2 + \dot{m}_3 s_3 + \dot{m}_5 s_5 + \dot{m}_6 s_6 \quad (5.13)$$

where s_{1-6} signifies the specific entropies of the associated streams and \dot{S}_{gen} is the rate of entropy generation in the system. T_0 is the environmental temperature.

In Processes 3 and 4, specific entropy (s) of a NaCl solution is a function of its temperature (T) and concentration (x) which can be expressed as [168]:

$$s = A + B T + C T^2 + D T^3 + E T^4 \quad (5.14a)$$

Between 0 and 150°C, A, B, C, D, and E can be defined as [168]

$$A = 0.0012 + 2.854 x - 8.677 x^2 + 23.77 x^3 - 30.94 x^4 \quad (5.14b)$$

$$B = 0.0154 - 0.0244 x + 0.0686 x^2 - 0.1232 x^3 + 0.0616 x^4 \quad (5.14c)$$

$$C = (-0.0295 + 0.1551 x - 0.9586 x^2 + 2.541 x^3 - 2.078 x^4) \times 10^{-3} \quad (5.14d)$$

$$D = (0.0738 - 0.9527 x + 6.969 x^2 - 21.37 x^3 + 20.94 x^4) \times 10^{-6} \quad (5.14e)$$

$$E = (-0.0982 + 2.104 x - 16.89 x^2 + 56.06 x^3 - 58.71 x^4) \times 10^{-9} \quad (5.14f)$$

Exergy Balance Equation (ExBE):

Exergy can be defined as the maximum work that can be extracted from a system interacting with its reference environment [169]. The reason for investigating exergy in addition to energy is to perform a quantitative evaluation of imperfection causes and indicate possible process improvements from thermodynamics point of view, taking economic analysis into account as well [170]. Similar to entropy, exergy is exempt from

the conservation law. Exergy balance is a statement of law of energy degradation as it describes the irretrievable loss of exergy due to process irreversibilities [171]. Exergy balance equation for system components in the general form can be described as follows:

$$\frac{dEx_{cv}}{dt} = \sum \dot{E}x_Q - \sum \dot{E}x_w + \sum \dot{E}x_{in} - \sum \dot{E}x_{out} - \dot{E}x_{dest} \quad (5.15)$$

where $\dot{E}x_Q$, $\dot{E}x_w$, and $\dot{E}x_{flow}$ represent the exergy transfer rates associated with heat, boundary or shaft work, and flow stream, respectively. Exergy destruction rate indicates the system irreversibility and it is shown in the equation as $\dot{E}x_{dest}$.

The steady-state steady-flow exergy balance equation can be written as [172]

$$\sum \dot{m}_{in} ex_{in} + \sum \dot{E}x_{Q_{in}} + \sum \dot{E}x_{W_{in}} = \sum \dot{m}_{out} ex_{out} + \sum \dot{E}x_{Q_{out}} + \sum \dot{E}x_{W_{out}} + \dot{E}x_{dest} \quad (5.16)$$

Exergy of Heat Transfer: When there is heat transfer involved in a system with a rate of \dot{Q} in a control volume at an operating temperature of T , the highest conversion rate from thermal energy to desired work, which states the thermal exergy flow, is calculated as [172]

$$\dot{E}x_Q = \dot{Q} \left(1 - \frac{T_0}{T}\right) \quad (5.17)$$

where $\left(1 - \frac{T_0}{T}\right)$ is the dimensionless exergetic temperature, sometimes referred as Carnot efficiency working between the surrounding temperature at T_0 and the system (i.e., operating) temperature T .

Exergy of Work: From the simple definition, the work equivalent of a given form or energy is a measure of its exergy [171], it can be stated that the exergy transfer with shaft or boundary work equals to work and the exergy transfer rate can be specified as well by the power or the work transfer rate. The following equation shows the exergy transfer rate associated with work considering the change of the volume as well:

$$\dot{E}x_w = \dot{W}_{cv} + P_0 \frac{dV_{cv}}{dt} \quad (5.18)$$

where P_0 is the environmental (or dead state) pressure. If the control volume is assumed to be constant, then the exergy transfer rate becomes:

$$\dot{E}x_w = \dot{W}_{cv} \quad (5.19)$$

Exergy of Flow: Exergy of a flow of a particular substance could be expressed as the maximum quantity of work that can be obtained when the flow is taken away from its original state to the environmental state throughout a process of interactions with its environment [171]. Exergy transfer by the stream through any system component can be expressed in terms of the specific flow exergy as follows:

$$\sum \dot{E}x_{flow} = \sum (\dot{m}_i ex_i) \quad (5.20)$$

Exergy related to a stream flow is consisted of four major elements: physical (ex^{ph}), chemical (ex^{ch}), kinetic (ex^{ke}) and potential (ex^{pe}) [172]. Thus, specific flow exergy is stated as

$$ex_{flow} = ex^{ph} + ex^{ch} + ex^{ke} + ex^{pe} \quad (5.21)$$

The flow associated specific exergy of a component (i) can be stated as:

$$ex_i = ex_i^{ph} + ex_i^{ch} + ex_i^{ke} + ex_i^{pe} = (h - h_0)_i - T_0(s - s_0)_i + ex_i^{ch} + \frac{v_i^2}{2} + gz_i \quad (5.22)$$

The kinetic and potential components of exergy appear in the previous equation are assumed to be negligible during the course of this study as the changes in velocities and within the system components are insignificant compared to the contributions of other terms. In that case, Equation (5.22) becomes:

$$ex_i = ex_i^{ph} + ex_i^{ch} + ex_i^{ke} + ex_i^{pe} = (h - h_0)_i - T_0(s - s_0)_i + ex_i^{ch} \quad (5.23)$$

The physical exergy portion of the flow exergy is affected by physical processes including thermal interactions with the environment to bring the flow from its original state to the environmental state which is at a temperature and pressure T_0 and P_0 , respectively. Specific physical exergy components are defined as

$$ex^{ph} = (h - h_0) - T_0(s - s_0) \quad (5.24)$$

where h and h_0 are specific enthalpies, and s and s_0 are the specific entropies at the original and the reference environment states, respectively.

The chemical exergy is the portion of the flow exergy that is caused by processes involving heat transfer and exchange of substances with the environment to bring the

substance to the dead state [171]. The chemical exergy of an ideal gas mixture can be evaluated from [172]:

$$ex_{mix}^{ch} = \sum y_i ex_i^{ch} + RT_0 \sum y_i \ln y_i \quad (5.25)$$

where y_i is the mole fraction of the component i in the gas mixture.

Combining Equations (5.16) to (5.25) yields

$$\sum \dot{m}_{in} (ex_{in}^{ph} + ex_{in}^{ch}) + \dot{Q}_{in} \left(1 - \frac{T_0}{T}\right) + \dot{W}_{in} = \sum \dot{m}_{out} (ex_{out}^{ph} + ex_{out}^{ch}) + \dot{E}x_{dest} \quad (5.26)$$

Rate of Exergy Destruction: Amount of exergy exiting the control volume must be less than the exergy input due to exergy destruction within the process/system. Exergy destruction rate, which is denoted as $\dot{E}x_{dest}$ in the general exergy balance equation, is directly related to the rate of entropy generation within the control volume:

$$\dot{E}x_{dest} = T_0 \dot{S}_{gen} \quad (5.27)$$

Exergy analysis acknowledges that energy cannot be created or destroyed but it can be degraded in quality, eventually reaching a complete equilibrium with the surroundings and hence of no further use for performing tasks [169]. For the continuous type hybrid reactor shown in Figure 5.1, the steady-state steady-flow exergy balance equation (ExBE) is formed as

$$\dot{m}_1 ex_1 + \dot{m}_4 ex_4 + \dot{W}_{in} + \dot{Q}_{in} \left(1 - \frac{T_0}{T}\right) = \dot{m}_2 ex_2 + \dot{m}_3 ex_3 + \dot{m}_5 ex_5 + \dot{m}_6 ex_6 + \dot{E}x_{dest} \quad (5.28)$$

where ex_{1-6} stands for the specific exergies of the related streams and \dot{W}_{in} denotes the total work input to the system. T_0 and T are the environmental and operating temperatures, respectively. Note that when T_0 is equal to T , there is no heat input, therefore, the exergy balance equation does not have the heat component when the operating and environmental temperatures are equal.

5.2 Model Development

Minimizing sum of squares (SS) is a usual approach in model development [173]:

$$SS^2 = \sum_{Data} [experiments - model]^2 \quad (5.29)$$

where “experiment” refers to an experimental measurement of a variable (e.g., production rate, efficiency, etc.). The “model” refers to predictions of the same variable evaluated by the model. An optimization method then should be used to fine-tune the parameter values in order to minimize the SS^2 . However, there is always some residual error which is a root mean error that combines experimental and fitting error. The root mean error is a reasonable estimate of experimental error. The introduction of additional constants would reduce the root mean error but it might also cause over-fitting.

Mass Flow Rates in Processes 1 and 2

For the continuous type hybrid reactor shown in Figure 5.1, the steady-state steady-flow mass balance equation (MBE) is provided in Equation (5.3). In this equation, \dot{m}_1 denotes the mass flow rate of H₂O entering the anode (kg/s), \dot{m}_2 and \dot{m}_3 symbolize the mass flow rate of H₂O and O₂ gas leaving the anode, respectively (kg/s). \dot{m}_4 stands for the mass flow rate of H₂O entering the cathode (kg/s), \dot{m}_5 and \dot{m}_6 symbolize the mass flow rate of H₂O and H₂ gas leaving the cathode (kg/s), respectively. By considering anode and cathode half reactions presented in Equations (4.1) and (4.2) and molar masses of H₂O, H₂O, and O₂, the following equation is derived:

$$\frac{\dot{m}_1 - \dot{m}_2}{18} = 2 \times \frac{\dot{m}_3}{16} = \frac{\dot{m}_6}{2} \quad (5.30)$$

And the mass flow rate of H₂O in Streams 4 and 5 are assumed to be related to the mass flow rate of H₂O entering the anode (Stream 1) as

$$\dot{m}_1 = \dot{m}_4 = \dot{m}_5 = \dot{m} \quad (5.31)$$

From Equation (5.30), the relationship between mass flow rates of Streams 1, 2, 3, and 6 can be written as

$$\dot{m}_2 = \dot{m}_1 - 9 \times \dot{m}_6 \quad (5.32)$$

$$\dot{m}_3 = 8 \times \dot{m}_6 \quad (5.33)$$

It should be noted that under steady-state steady-flow operation, H⁺ and OH⁻ ions are assumed to not get accumulated in the system. The mass flow rate relationships stated in Equations (5.30)–(5.33) are summarized in Table 5.2.

Table 5.2 Definitions and mass flow rates of hybrid reactor system (Processes 1 and 2).

Stream	Definition	Mass Flow Rate (kg/s)
1	Fresh water inlet	\dot{m}_1 : input, known
2	Fresh water outlet	$\dot{m}_2 = \dot{m}_1 - 9 \times \dot{m}_6$
3	O ₂ gas outlet	$\dot{m}_3 = 8 \times \dot{m}_6$
4	Fresh water inlet	$\dot{m}_4 = \dot{m}_1$:
5	Fresh water outlet	$\dot{m}_5 = \dot{m}_1$
6	H ₂ gas outlet	\dot{m}_6 : measured

Mass Flow Rates in Processes 3 and 4

For the continuous type hybrid reactor shown in Figure 5.1, the steady-state steady-flow mass balance equation (MBE) is written in Equation (5.3). Here, \dot{m}_1 denotes the mass flow rate of saturated NaCl entering the anode (kg/s), \dot{m}_2 and \dot{m}_3 symbolize the mass flow rate (kg/s) of depleted NaCl solution and Cl₂ gas leaving the anode, respectively. \dot{m}_4 stands for the mass flow rate (kg/s) of H₂O entering the cathode, \dot{m}_5 and \dot{m}_6 symbolize the mass flow rate of NaOH solution and H₂ gas leaving the cathode (kg/s), respectively. The mass flow rate equations are derived by considering anode and cathode half reactions presented in Equations (4.3) and (4.4) and molar masses of H₂O, NaCl, NaOH, H₂, and O₂. The mass flow rate of NaCl entering the anode is defined as

$$\dot{m}_{s1} = \dot{m}_1 x_{s1} \quad (5.34)$$

where x_{s1} is the mass fraction of NaCl in Stream 1 (the saturated NaCl inlet to the system). And the mass flow rate of H₂O entering the anode is:

$$\dot{m}_{w1} = \dot{m}_1 - \dot{m}_1 x_{s1} = \dot{m}_1(1 - x_{s1}) \quad (5.35)$$

Similarly, the mass flow rate of NaCl leaving the anode is:

$$\dot{m}_{s2} = \dot{m}_2 x_{s2} \quad (5.36)$$

where x_{s2} is the mass fraction of NaCl in Stream 2 (the depleted NaCl outlet of the system). And the mass flow rate of H₂O leaving the anode is:

$$\dot{m}_{w2} = \dot{m}_2 - \dot{m}_2 x_{s2} = \dot{m}_2(1 - x_{s2}) \quad (5.37)$$

The rate of NaCl consumption in the anode is:

$$\dot{m}_{s,consumption} = \dot{m}_{s1} - \dot{m}_{s2} = \dot{m}_1 x_{s1} - \dot{m}_2 x_{s2} \quad (5.38)$$

$$\dot{n}_{s,consumption} = \frac{\dot{m}_{s1} - \dot{m}_{s2}}{58.44} = \frac{\dot{m}_1 x_{s1} - \dot{m}_2 x_{s2}}{58.44} \quad (5.39)$$

where $\dot{m}_{s,consumption}$ (kg/s) and $\dot{n}_{s,consumption}$ (kmol/s) are the mass and molar consumption rates of NaCl in the anode taking the molar weight of NaCl as 58.44 kg/kmol. Using the steady-state steady-flow process, the following arrangements can be done:

- Cl⁻ ions do not get accumulated in the system. The molecular weight of Cl₂ is taken to be 70.91 kg/kmol. \dot{n}_3 and \dot{m}_3 represent the molar (kmol/s) and mass (kg/s) flow rates of Stream 3, which is the gaseous product Cl₂ leaving the anode:

$$\dot{n}_3 = \frac{\dot{n}_{s,consumption}}{2} = \frac{\dot{m}_{s1} - \dot{m}_{s2}}{116.88} = \frac{\dot{m}_1 x_{s1} - \dot{m}_2 x_{s2}}{116.88} \quad (5.40)$$

$$\dot{m}_3 = MW_{Cl_2} \dot{n}_3 = 35.45 \dot{n}_{s,consumption} = \frac{\dot{m}_{s1} - \dot{m}_{s2}}{1.64} = \frac{\dot{m}_1 x_{s1} - \dot{m}_2 x_{s2}}{1.64} \quad (5.41)$$

- Na⁺ ions do not get accumulated in the system. The Na⁺ ions from the consumed NaCl leave the system in only one Stream, 5. The molecular weight of NaOH is taken to be 40 kg/kmol. x_{s5} represents the mass fraction of NaOH in Stream 5 which is the product. NaOH solution leaving the cathode:

$$\dot{n}_{NaOH} = \frac{\dot{m}_{NaOH}}{MW_{NaOH}} = \frac{x_{s5} \dot{m}_5}{40} = \dot{n}_{s,consumption} = \frac{\dot{m}_1 x_{s1} - \dot{m}_2 x_{s2}}{58.44} \quad (5.42)$$

$$\dot{m}_5 = \frac{\dot{m}_1 x_{s1} - \dot{m}_2 x_{s2}}{1.46 x_{s5}} \quad (5.43)$$

- The H₂O in Streams 1 and 2 do not get electrolyzed. Therefore, in steady-state steady-flow operation, the amount of H₂O entering the anode in Stream 1 is equal to the one leaving in Stream 2, which leads to:

$$\dot{m}_{w1} = \dot{m}_{w2} = \dot{m}_1(1 - x_{s1}) = \dot{m}_2(1 - x_{s2}) \quad (5.44)$$

$$\dot{m}_2 = \frac{\dot{m}_1(1 - x_{s1})}{(1 - x_{s2})} \quad (5.45)$$

The molar flow rates expressed in Equations (5.39) and (5.42) also follow the overall reaction stoichiometry, which is: $2 \text{NaCl} + 2 \text{H}_2\text{O} \rightarrow \text{Cl}_2 + \text{H}_2 + 2 \text{NaOH}$. Based on the same stoichiometry, it can be seen that the molar rate of formation of Cl₂ (\dot{n}_3) and H₂

(\dot{n}_6) are equal. Using this information along with the molecular weight of H₂ (2.02 kg/kmol) leads to:

$$\dot{n}_6 = \frac{\dot{m}_1 x_{s1} - \dot{m}_2 x_{s2}}{116.88} \quad (5.46)$$

$$\dot{m}_6 = \frac{\dot{m}_1 x_{s1} - \dot{m}_2 x_{s2}}{57.86} \quad (5.47)$$

The mass flow rate relationships stated in Equations (5.34)–(5.47) are summarized in Table 5.3

Table 5.3 Summary of stream mass flow rates and concentrations of hybrid reactor (Processes 3 and 4).

Stream	Definition	Mass Flow Rate (kg/s)	Concentration (kg solute/kg solution)
1	Saturated NaCl solution inlet	\dot{m}_1 : input, known	x_{s1} : saturated solution, known
2	NaCl solution outlet	$\dot{m}_2 = \frac{(1-x_{s1})}{(1-x_{s2})} \dot{m}_1$	x_{s2}
3	Cl ₂ gas outlet	$\dot{m}_3 = 0.61 \frac{(x_{s1}-x_{s2})}{(1-x_{s2})} \dot{m}_1$	N/A
4	Fresh water inlet	$\dot{m}_4 = \frac{0.68-0.35 x_{s5}}{x_{s5}} \frac{(x_{s1}-x_{s2})}{(1-x_{s2})} \dot{m}_1$	N/A
5	NaOH solution outlet	$\dot{m}_5 = \frac{0.68}{x_{s5}} \frac{(x_{s1}-x_{s2})}{(1-x_{s2})} \dot{m}_1$	x_{s5}
6	H ₂ gas outlet	$\dot{m}_6 = 0.02 \frac{(x_{s1}-x_{s2})}{(1-x_{s2})} \dot{m}_1$	N/A

The solubility of NaCl in H₂O is dependent on temperature; therefore, x_{s1} can be estimated from [168]:

$$x_{s1} = x_{sat} = 0.2628 + 62.75 \times 10^{-6} \times T + 1.084 \times 10^{-6} \times T^2 \quad (5.48)$$

Electrochemical Model of Chloralkali (for Processes 3 and 4)

For a constant temperature and pressure electrochemical process, minimum required input work is equal to the change in Gibbs free energy. According to Faraday's law, the voltage required for a reversible electrochemical process can be expressed as [174]:

$$V_{rev} = \frac{\Delta G(T)}{n_e F} \quad (5.49)$$

where n_e is the number of electrons transferred per electrolyzed molecule and F is Faraday's constant which is equal to 96,485.3415 C/mol. It should be noted that the required voltage V is always larger than the reversible voltage, V_{rev} , because of the irreversibilities in the system. Electrochemical modeling is employed to calculate the potential requirement by

taking into account the decomposition voltage and ohmic losses across various reactor components. Jalali et al. [175] have discussed electrochemical modeling of a membrane based on a dual chloralkali cell in an electrolysis process. For the system shown in Figure 5.1, the general voltage balance within the hybrid reactor becomes:

$$V = E^\circ + V_A + V_{sol,a} + V_{CEM} + V_{sol,c} + V_C \quad (5.50)$$

where E° represents the open circuit cell voltage (i.e., sometimes identified as decomposition voltage), V_A denotes the voltage decrease through the anode, $V_{sol,a}$ indicates the voltage drop over anolyte (i.e., voltage decline in NaCl solution), V_{CEM} signifies the voltage decline through the CEM, $V_{sol,c}$ shows the voltage reduction over catholyte (i.e., voltage decay in NaOH solution) and V_C symbolises the voltage drop through the cathode. In anode, Cl^- is oxidized to Cl_2 and applying Nernst principle to the chemical reaction given in Equation (4.3) provides the following [175]:

$$E^\circ_A = E^\circ_{Cl^-/Cl_2} + \frac{RT}{nF} \ln \left(\frac{P_{Cl_2}}{(\gamma_{Cl^-})^2} \right) \quad (5.51)$$

where R is the universal gas constant, 8.3145 J/K-mol. T represents the operating temperature in K, n represents the number of electrons used to oxidize the Cl^- ions (in this case, $n=2$). P_{Cl_2} and γ_{Cl^-} are the partial pressure of Cl_2 gas and activity coefficient of Cl^- ion. $E^\circ_{Cl^-/Cl_2}$ is the standard electrode potential of chlorine (V), has previously been discussed in a variety of early studies [176–181]. Moussallem et al. [182] have reported the standard chlorine potential as a function of temperature ranging from 25°C to 80°C as

$$E^\circ_{Cl^-/Cl_2} = 1.47252 + (5.82271 \times 10^{-4}) T - (2.90055 \times 10^{-6}) T^2 \quad (5.52a)$$

Shock et al. [181] have also described the standard chlorine electrode potential as

$$E^\circ_{Cl^-/Cl_2} = 1.48467 + (3.958492 \times 10^{-4}) T - (2.750639 \times 10^{-6}) T^2 \quad (5.52b)$$

The differentiation between the standard chlorine electrode potential calculated from Equations (5.52a) and (5.52b) is 0.05V. In the cathode, H_2O is reduced into H_2 and OH^- ions and applying principle to the chemical reaction given in Equation (4.4) provides the following [175]:

$$E^\circ_C = E^\circ_{H_2O/H_2+OH^-} + 2.303 \frac{RT}{nF} \ln \left(\frac{P_{H_2}}{(\gamma_{OH^-})^2} \right) \quad (5.53)$$

where n represents the number of electrons used to oxidize the Cl^- ions (in this case, $n = 2$). P_{H_2} and γ_{OH^-} are the partial pressure of H_2 gas and activity coefficient of OH^- ion, respectively. $E^\circ_{\text{H}_2\text{O}/\text{H}_2+\text{OH}^-}$ is the standard electrode potential of hydrogen, typically accepted as 0.8280 V. The Nernst equation for the complete reaction stated in Equation (4.5) is written as [175]:

$$E^\circ_{\text{overall}} = -2.18 + 0.0004272 T + \frac{8.314 T \ln \beta}{96500} \quad (5.54)$$

where β is dependent upon partial pressures of H_2 and Cl_2 in the gas phase in addition to the activity coefficients of NaCl (γ_{NaCl}) and NaOH (γ_{NaOH}) which is written as

$$\beta = \frac{\gamma_{\text{NaCl}}(P_{\text{Cl}_2})^{1/2} (P_{\text{H}_2})^{1/2}}{\gamma_{\text{NaOH}}} \quad (5.55)$$

The activity coefficient of NaCl (γ_{NaCl}) changes with respect to its molar concentration, M (mol/L), which can be evaluated as [175]

$$\gamma_{\text{NaCl}} = 0.63 \exp(0.028 M_{\text{NaCl}}) \quad 1.2 \leq M_{\text{NaCl}} < 2 \quad (5.56)$$

$$\gamma_{\text{NaCl}} = 0.575 \exp(0.07 M_{\text{NaCl}}) \quad 2 \leq M_{\text{NaCl}} < 3.5 \quad (5.57)$$

$$\gamma_{\text{NaCl}} = 0.5 \exp(0.112 M_{\text{NaCl}}) \quad 3.5 \leq M_{\text{NaCl}} < 6 \quad (5.58)$$

The activity coefficient of NaOH (γ_{NaOH}) depends on its molar concentration, M (mol/L), which can be evaluated as [175]

$$\log \gamma_{\text{NaOH}} = -\frac{U\sqrt{M_{\text{NaOH}}}}{1 + \sqrt{2} M_{\text{NaOH}}} + B M_{\text{NaOH}} + C M_{\text{NaOH}}^2 + D M_{\text{NaOH}}^3 + E M_{\text{NaOH}}^4 M_{\text{NaOH}} < 12 \quad (5.59)$$

$$B = 0.0065 + 0.0016 T - 1.8 \times 10^{-5} T^2 \quad (5.60)$$

$$C = 0.014 - 0.0005 T + 5.6 \times 10^{-6} T^2 \quad (5.61)$$

$$D = 0.0006 + 5 \times 10^{-5} T - 6.48 \times 10^{-7} T^2 \quad (5.62)$$

$$E = 5.96 \times 10^{-6} - 1.81 \times 10^{-6} T + 2.4 \times 10^{-8} T^2 \quad (5.63)$$

$$U = 0.00087 T + 0.486 \quad 25^\circ\text{C} \leq T \leq 40^\circ\text{C} \quad (5.64)$$

$$U = 0.00144 T + 0.46 \quad 40^\circ\text{C} \leq T \leq 100^\circ\text{C} \quad (5.65)$$

$$\log \gamma_{NaOH} = a + b M_{NaOH} + c M_{NaOH}^2 \quad M_{NaOH} \geq 12 \quad (5.66)$$

$$a = -0.327 + 0.0031 T - 3.29 \times 10^{-5} T^2 \quad (5.67)$$

$$b = 0.0988 - 0.00059 T \quad (5.68)$$

$$c = -2.14 \times 10^{-6} - 3.93 \times 10^{-7} T + 0.53 \times 10^{-8} T^2 \quad (5.69)$$

The voltage drop across the anode is calculated as

$$V_A = c_A \log \left(\frac{i}{i_{0,a}} \right) \quad (5.70)$$

where c_A is the constant determined experimentally and $i_{0,a}$ represents the exchange current density. Both c_A and $i_{0,a}$ depend on the reaction characteristics (in this study, Cl_2 evolution reaction takes place in the anode, this information is used together with the operational specifications of the MPEA). $i_{0,a}$ also depends on the anode material and temperature (e.g., graphite electrode at $90^\circ C$, $i_0 = 0.0125$). When a dimensionally stable anode is selected, the voltage decrease for the Cl_2 production reaction is determined from the following equation:

$$V_A = 0.0277 \log \left(\frac{i}{i_0} \right) \quad (5.71)$$

The voltage drop across the anolyte solution, $V_{sol,a}$ can be determined from:

$$V_{sol,a} = \frac{i \times d_{AM}}{K_{NaCl}} \quad (5.72)$$

where i represents the current density, d_{AM} is the distance between the anode and CEM, K_{NaCl} represents the electrical conductivity of the NaCl solution. The electrical conductivity of the NaCl solution is a function of both its concentration and operating temperature and can be estimated as

$$K_{NaCl} = \left(1.1 - (0.33 \sqrt{\Omega_{NaCl}}) \right) (\lambda_{NaCl} \Omega_{NaCl}) \quad (5.73)$$

where λ_{NaCl} is a temperature dependent variable and Ω_{NaCl} depends on the concentration and density levels of the NaCl solution:

$$\lambda_{NaCl} = 5.67 + 0.229 T \quad (5.74)$$

$$\Omega_{NaCl} = \frac{M_{NaCl} \rho_{NaCl}}{1000 + (58.5 M_{NaCl})} \quad (5.75)$$

where ρ_{NaCl} represents the density of the NaCl solution (kg/m³) which is calculated from:

$$\rho_{NaCl} = A + B T + C T^2 + D T^3 + E T^4 \quad 0^\circ\text{C} \leq T \leq 300^\circ\text{C} \quad (5.76)$$

$$A = (1.001 + 0.7666x - 0.0149x^2 + 0.2663x^3 + 0.8845x^4) \quad (5.77)$$

$$B = -0.0214 - 3.496x + 10.02x^2 - 6.56x^3 - 31.37x^4 \quad (5.78)$$

$$C = (-5.263 + 39.87x - 176.2x^2 + 363.5x^3 - 7.784x^4) \times 10^{-3} \quad (5.79)$$

$$D = (15.42 - 167x + 980.7x^2 - 2573x^3 + 876.6x^4) \times 10^{-6} \quad (5.80)$$

$$E = (-0.0276 + 0.2978x - 2.017x^2 + 6.345x^3 - 3.914x^4) \times 10^{-6} \quad (5.81)$$

The voltage drop across the cation exchange member is:

$$V_{CEM} = \left(\frac{i \sigma_{CEM}}{K_{CEM}} \right) \quad (5.82)$$

where i represents the current density, σ_{CEM} signifies the membrane thickness and K_{CEM} denotes the electrical conductivity of the membrane which depends on such factors including the membrane's chemical composition, ionic form, operating temperature, pH of the solutions that the membrane is in interaction with, and the permeability of the membrane. Electrical conductivity of the membrane is commonly assessed and given by its manufacturer.

The voltage drop across the catholyte solution, $V_{sol,c}$ can be determined from:

$$V_{sol,c} = \frac{i \times d_{CM}}{K_{NaOH}} \quad (5.83)$$

where i represents the current density, d_{CM} is the distance between the cathode and CEM, K_{NaOH} represents the electrical conductivity of the NaOH. The electrical conductivity of NaOH is a function of its concentration and operating temperature and can be estimated as

$$K_{NaOH} = K_{NaOH,100^\circ\text{C}} \left(\frac{T}{373} \right)^S \exp \left(-\frac{E^*}{R} \left(\frac{1}{T} - \frac{1}{373} \right) \right) \quad (5.84)$$

$$\frac{E^*}{R} = 4456.5 + ((\Omega_{NaOH} - 2)(5109.5 - 4456.5)) \quad 2 \leq \Omega_{NaOH} < 3 \quad (5.85)$$

$$\frac{E^*}{R} = 5409.6 + ((\Omega_{NaOH} - 3)(4706.5 - 5109.8)) \quad 3 \leq \Omega_{NaOH} < 4 \quad (5.86)$$

$$\frac{E^*}{R} = 535.2\Omega_{NaOH} + 2617.8 \quad 4 \leq \Omega_{NaOH} < 7 \quad (5.87)$$

$$\frac{E^*}{R} = 967.5\Omega_{NaOH} + 548.2 \quad 7 \leq \Omega_{NaOH} < 16 \quad (5.88)$$

$$s = -9.6 + ((\Omega_{NaOH} - 2)(11.3 - 9.9)) \quad 2 \leq \Omega_{NaOH} < 3 \quad (5.89)$$

$$s = -11.3 + ((\Omega_{NaOH} - 3)(11.3 - 10)) \quad 3 \leq \Omega_{NaOH} < 4 \quad (5.90)$$

$$s = -1.06\Omega_{NaOH} - 5.8 \quad 4 \leq \Omega_{NaOH} < 7 \quad (5.91)$$

$$s = -2.44\Omega_{NaOH} + 5.3 \quad 7 \leq \Omega_{NaOH} < 16 \quad (5.92)$$

where $K_{NaOH,100^\circ C}$ represents the electrical conductivity of the aqueous NaOH at 100°C, and depends on the concentration of the NaOH in the aqueous solution which is estimated as

$$K_{NaOH,100^\circ C} = 2.6 + 40.9 \Omega_{NaOH} - 5.03 \Omega_{NaOH}^2 + 0.13 \Omega_{NaOH}^3 \quad 2 \leq \Omega_{NaOH} < 7 \quad (5.93)$$

$$K_{NaOH,100^\circ C} = 140.9 \quad 7 \leq \Omega_{NaOH} < 9 \quad (5.94)$$

$$K_{NaOH,100^\circ C} = 156 - 1.5 \Omega_{NaOH} \quad 9 \leq \Omega_{NaOH} < 16 \quad (5.95)$$

where Ω_{NaOH} depends on the concentration and density levels of the NaOH solution:

$$\Omega_{NaOH} = \frac{M_{NaOH}\rho_{NaOH}}{1000 + (40 M_{NaCl})} \quad (5.96)$$

The voltage drop across the cathode is calculated as:

$$V_C = c_c \log\left(\frac{i}{i_{0,c}}\right) \quad (5.97)$$

where c_c is the constant determined experimentally, $i_{0,c}$ represents the exchange current density. Both c_c and $i_{0,c}$ are dependent upon the nature of the reaction. $i_{0,c}$ also depends on the cathode material and temperature (i.e., for steel, $i_{0,c} = 0.0656$).

5.3 Efficiency Assessment

The present energy and exergy analyses are conducted to assess the thermodynamic performance of the PEC-chloralkali process. Estimating the theoretical energy requirement of the process is the first step of the analysis. The total theoretical energy demand of the system is calculated by:

$$\Delta H = \Delta G + T\Delta S \quad (5.98)$$

where ΔG and $T\Delta S$ represent the net change in Gibbs free energy (and its equivalent to the electrical demand) and thermal energy demand (J/mol), respectively. The enthalpy and entropy values of H_2O , H_2 , Cl_2 and $NaOH$ are available in EES, but for $NaCl$, correlations based on curve fitting of the data presented by Sparrow [168] are used.

The minimum theoretical electrical potential for the anode and cathode reactions of the hybrid reactor for Processes 1, 2, 3, and 4 are given in Tables 5.4 and 5.5. It is important to note that theoretical energy requirement neglects any potential losses; therefore, it is always less than the actual energy demand.

Table 5.4 Minimum theoretical required potentials of anode and cathode half reactions (Processes 1 and 2).

Electrode	Reaction	Minimum Required Potential (V)
Anode	$2H_2O \rightarrow 4H^+ + O_2 + 4e^-$	1.229
Cathode	$4H^+ + 4e^- \rightarrow 2H_2$	-
Overall	$2H_2O \rightarrow 2H_2 + O_2$	1.229

Table 5.5 Minimum theoretical required potentials of anode and cathode half reactions (Processes 3 and 4).

Electrode	Reaction	Minimum Required Potential (V)
Anode	$2Cl^- \rightarrow Cl_2 + 2e^-$	1.3578
Cathode	$2H_2O + 2e^- \rightarrow H_2 + 2OH^-$	0.8280
Overall	$2H_2O + 2NaCl \rightarrow H_2 + Cl_2 + 2NaOH$	2.1858

Energy Efficiency Assessment

As the measure of energy related effectiveness, energy efficiency of a process or system is defined as the ratio of useful output of the system to the energy input to the system.

$$\eta = \frac{\Sigma \text{useful output energy}}{\Sigma \text{input energy}} = 1 - \frac{\Sigma \text{energy loss}}{\Sigma \text{input energy}} \quad (5.99)$$

The energy efficiency of Processes 1 and 2 are defined as

$$\eta = \frac{\dot{m}_6 \text{HHV}_{H_2}}{\dot{W}_{in}} \quad (5.100)$$

Here, HHV is the higher heating value of H_2 and \dot{W}_{in} is defined in Equations 5.8–5.10. The stream numbers are indicated in Figure 5.1.

For Processes 3 and 4, the energy efficiency can be evaluated in two distinct approaches. In the first approach, H₂ is respected as the only preferred product whereas in the second way Cl₂ and NaOH are counted as beneficial products together with the H₂. Subsequently, the energy efficiency equations for the first and second cases become:

$$\eta_1 = \frac{\dot{m}_6 HHV_{H_2}}{\dot{W}_{in} + \dot{m}_1 h_1 + \dot{m}_4 h_4} \quad (5.101)$$

$$\eta_2 = \frac{\dot{m}_6 HHV_{H_2} + \dot{m}_3 h_3 + \dot{m}_5 h_5}{\dot{W}_{in} + \dot{m}_1 h_1 + \dot{m}_4 h_4} \quad (5.102)$$

Exergy Efficiency Assessment

Based on the second law of thermodynamics, exergy efficiency is defined based on the exergy content of the system inputs and outputs, which gives a better insight of system performance. Exergy efficiency concept differentiates irreversibilities from losses, this provides information about the potential system improvements by decreasing the losses.

$$\psi = \frac{\sum \text{useful output exergy}}{\sum \text{input exergy}} = 1 - \frac{\sum \text{exergy loss}}{\sum \text{input exergy}} \quad (5.103)$$

The exergy efficiency of Processes 1 and 2 are defined as

$$\psi = \frac{\dot{m}_6 ex_6}{\dot{W}_{in}} \quad (5.104)$$

The exergy efficiency of Processes 3 and 4 can be evaluated in two approaches. In the first approach, H₂ is taken to be the only preferred product whereas in the second efficiency, Cl₂ and NaOH are also both respected as functional yields along with the H₂. Consequently, the exergy efficiency equations for first and second case become:

$$\Psi_1 = \frac{\dot{m}_6 ex_6}{\dot{W}_{in} + \dot{m}_1 ex_1 + \dot{m}_4 ex_4} \quad (5.105)$$

$$\Psi_2 = \frac{\dot{m}_6 ex_6 + \dot{m}_3 ex_3 + \dot{m}_5 ex_5}{\dot{W}_{in} + \dot{m}_1 ex_1 + \dot{m}_4 ex_4} \quad (5.106)$$

5.4 Integrated System Analysis

The integrated multi-generation system, as presented in Figure 4.16, has three major components, namely (I) solar spectral splitter, (II) PV/T, and (III) hybrid reactor. There are 13 streams which are explained in detail in Table 5.6

Table 5.6 Stream descriptions and associated mass, energy, exergy, and exergy flow rates of integrated system.

Stream	Description	Mass flow rate (\dot{m})	Energy rate (\dot{E})	Entropy rate (\dot{S})	Exergy rate ($\dot{E}x$)
1	Incoming solar irradiance	-	\dot{E}_1	\dot{S}_1	$\dot{E}x_1$
2	Higher spectrum of the solar irradiance sent to the reactor	-	\dot{E}_2	\dot{S}_2	$\dot{E}x_2$
3	Lower spectrum of the solar irradiance sent to the PV/T	-	\dot{E}_3	\dot{S}_3	$\dot{E}x_3$
4	Electricity output of PV/T sent to the reactor	-	\dot{E}_4	\dot{S}_4	$\dot{E}x_4$
5	Excess electricity output of PV/T considered as the system output	-	\dot{E}_5	\dot{S}_5	$\dot{E}x_5$
6	Heat recovered from PV/T sent to the reactor	-	\dot{E}_6	\dot{S}_6	$\dot{E}x_6$
7	Excess heat recovered from PV/T considered as the system output	-	\dot{E}_7	\dot{S}_7	$\dot{E}x_7$
8	Saturated NaCl solution input to the reactor	\dot{m}_8	\dot{E}_8	\dot{S}_8	$\dot{E}x_8$
9	Water input to the reactor	\dot{m}_9	\dot{E}_9	\dot{S}_9	$\dot{E}x_9$
10	Depleted NaCl solution output of the reactor	\dot{m}_{10}	\dot{E}_{10}	\dot{S}_{10}	$\dot{E}x_{10}$
11	NaOH solution output of the reactor	\dot{m}_{11}	\dot{E}_{11}	\dot{S}_{11}	$\dot{E}x_{11}$
12	Cl ₂ gas output of the reactor	\dot{m}_{12}	\dot{E}_{12}	\dot{S}_{12}	$\dot{E}x_{12}$
13	H ₂ gas output of the reactor	\dot{m}_{13}	\dot{E}_{13}	\dot{S}_{13}	$\dot{E}x_{13}$

Unit I: Solar Spectral Splitter

Solar spectral splitter is the first unit that processes the incoming solar irradiation (\dot{E}_1) enters where it is divided into higher (\dot{E}_2) and lower spectrum (\dot{E}_3).

There is no mass flow involved in Unit I, therefore, there are 3 balance equations. It should be noted that energy, entropy, and exergy flow rates of Streams 1–3 are calculated based on the procedure described by Zamfirescu and Dincer [104].

The energy balance equation of Unit I is:

$$\dot{E}_1 = \dot{E}_2 + \dot{E}_3 \quad (5.107)$$

The energy flow rates of Streams 1, 2, and 3 are calculated as

$$\dot{E}_1 = A_s \int_0^\infty i_\lambda d\lambda \quad (5.108)$$

$$\dot{E}_2 = A_r \int_0^{500} i_\lambda d\lambda \quad (5.109)$$

$$\dot{E}_3 = A_p \int_{500}^{\infty} \dot{I}_\lambda d\lambda \quad (5.110)$$

where A_s , A_r , and A_p are the active areas of the solar splitter, hybrid reactor, and the PV/T. \dot{I}_λ is the spectral irradiance of direct normal radiation and λ is the wavelength in nm.

The entropy balance equation of Unit I can be written as

$$\dot{S}_1 + \dot{S}_{gen} = \dot{S}_2 + \dot{S}_3 \quad (5.111)$$

The entropy flow rates of Streams 1, 2, and 3 are calculated as

$$\dot{S}_i = \frac{\dot{E}_i}{T_i} \quad (5.112)$$

where i can be Stream 1, 2, or 3 and T_i is the temperature of the associated stream.

The exergy balance equation of Unit I can be written as

$$\dot{E}x_1 = \dot{E}x_2 + \dot{E}x_3 + \dot{E}x_{dest} \quad (5.113)$$

The exergy flow rates of Streams 1, 2, and 3 are calculated as

$$\dot{E}x_i = \dot{E}_i \left(1 - \frac{T_0}{T_i} \right) \quad (5.114)$$

where i can be Stream 1, 2, or 3 and T_i is the temperature of the associated stream.

Unit II: PV/T

Lower spectrum irradiation (\dot{E}_3) enters the PV/T where it is converted to electricity (\dot{E}_4 and \dot{E}_5). In order to keep the PV/T as efficient as possible, heat is recovered (\dot{E}_6 and \dot{E}_7) during operation in order to prevent the PV/T from overheating. Streams 4 and 6 (\dot{E}_4 and \dot{E}_6) are sent to the reactor and Streams 5 and 7 are the excess electricity and heat which are served as useful products.

Similar to Unit I, there is no mass flow involved in Unit II, therefore, there are 3 balance equations. The energy, entropy, and exergy balance equations of Unit II are:

$$\dot{E}_3 = \dot{E}_4 + \dot{E}_5 + \dot{E}_6 + \dot{E}_7 \quad (5.115)$$

$$\dot{S}_3 + \dot{S}_{gen} = \dot{S}_4 + \dot{S}_5 + \dot{S}_6 + \dot{S}_7 \quad (5.116)$$

$$\dot{E}x_3 = \dot{E}x_4 + \dot{E}x_5 + \dot{E}x_6 + \dot{E}x_7 + \dot{E}x_{dest} \quad (5.117)$$

The energy, entropy, and exergy flow rates of each stream entering and leaving Unit 2 is given in Table 5.7. In Table 5.7, electricity and heat energies are denoted as \dot{W} and \dot{Q} , respectively. Subscripts p and r indicate PV/T and the reactor.

Table 5.7 Summary of energy, entropy, and exergy flow rates of Streams 4–7.

Stream	Description	Energy rate	Entropy rate	Exergy rate
4	Electricity to the reactor	$\dot{E}_4 = \dot{W}_r$	-	$\dot{E}x_4 = \dot{W}_r$
5	Electricity product	$\dot{E}_5 = \dot{W}_p$	-	$\dot{E}x_5 = \dot{W}_p$
6	Heat to the reactor	$\dot{E}_6 = \dot{Q}_r$	$\dot{S}_6 = \frac{\dot{Q}_r}{T}$	$\dot{E}x_6 = \dot{Q}_r \left(1 - \frac{T_0}{T}\right)$
7	Heat product	$\dot{E}_7 = \dot{Q}_p$	$\dot{S}_7 = \frac{\dot{Q}_p}{T}$	$\dot{E}x_7 = \dot{Q}_p \left(1 - \frac{T_0}{T}\right)$

Unit III: Hybrid Reactor

Unit III, which is the hybrid reactor, is the core component of the integrated system where H₂ production takes place. The mass, energy, entropy, and exergy balance equations of the reactor are:

$$\dot{m}_8 + \dot{m}_9 = \dot{m}_{10} + \dot{m}_{11} + \dot{m}_{12} + \dot{m}_{13} \quad (5.118)$$

$$\dot{m}_8 h_8 + \dot{m}_9 h_9 + \dot{Q}_r + \dot{W}_r = \dot{m}_{10} h_{10} + \dot{m}_{11} h_{11} + \dot{m}_{12} h_{12} + \dot{m}_{13} h_{13} \quad (5.119)$$

$$\dot{m}_8 s_8 + \dot{m}_9 s_9 + \frac{\dot{Q}_r}{T} + \dot{S}_{gen} = \dot{m}_{10} s_{10} + \dot{m}_{11} s_{11} + \dot{m}_{12} s_{12} + \dot{m}_{13} s_{13} \quad (5.120)$$

$$\dot{m}_8 ex_8 + \dot{m}_9 ex_9 + \dot{Q}_r \left(1 - \frac{T_0}{T}\right) + \dot{W}_r = \dot{m}_{10} ex_{10} + \dot{m}_{11} ex_{11} + \dot{m}_{12} ex_{12} + \dot{m}_{13} ex_{13} + \dot{E}x_{dest} \quad (5.121)$$

Efficiencies

The integrated systems' energetic and exergetic performance can be evaluated based on the number of valuable products definition as presented in Table 5.8.

Table 5.8 Summary of energy and exergy efficiencies of integrated system.

	Valuable products	Energy efficiency	Exergy efficiency
1	H ₂	$\eta_1 = \frac{\dot{E}_{13}}{\dot{E}_1}$	$\psi_1 = \frac{\dot{E}x_{13}}{\dot{E}x_1}$
2	H ₂ , Cl ₂	$\eta_2 = \frac{\dot{E}_{12} + \dot{E}_{13}}{\dot{E}_1}$	$\psi_2 = \frac{\dot{E}x_{12} + \dot{E}x_{13}}{\dot{E}x_1}$
3	H ₂ , Cl ₂ , Electricity	$\eta_3 = \frac{\dot{E}_5 + \dot{E}_{12} + \dot{E}_{13}}{\dot{E}_1}$	$\psi_3 = \frac{\dot{E}x_5 + \dot{E}x_{12} + \dot{E}x_{13}}{\dot{E}x_1}$
4	H ₂ , Cl ₂ , Electricity, Heat	$\eta_4 = \frac{\dot{E}_5 + \dot{E}_7 + \dot{E}_{12} + \dot{E}_{13}}{\dot{E}_1}$	$\psi_3 = \frac{\dot{E}x_5 + \dot{E}x_7 + \dot{E}x_{12} + \dot{E}x_{13}}{\dot{E}x_1}$

5.5 Exergoeconomic Analysis

The common cost analysis methods do not take the effect of system irreversibilities into account. These irreversibilities are associated with the second law of thermodynamics, and an exergy analysis is required to identify them, as previously been discussed. Combined together, exergy and economic analyses represent a useful tool for energy systems' optimization. Exergoeconomics describes, at the system components level, the combination of the thermodynamic exergy based assessment and economic theories to deliver required information for a better design and operating of an efficient, affordable, and reliable system [183]. A combination of economic and exergetic analyses introduces a new approach, known as thermoeconomics, where the exergoeconomic analysis of each component is driven by the exergy model and cost calculations. In cost calculations, in addition to the cost of each component, capital, operating, and maintenance cost of the system components are also taken into account. The objectives of an exergoeconomic analysis can be listed as follows: (i) calculate the cost of each product of a system separately, (ii) determine system's cost flows by understanding how costs of flows are formed, (iii) optimize a particular variable in a specific component and optimize the performance of the complete system [184]. Exergy-centred economic assessment procedures have been comprehensively described in the literature [185–191].

A thorough exergoeconomic assessment of the integrated system includes (i) a thermodynamic (exergy) analysis, (ii) an economic (cost) analysis, (iii) exergetic cost analysis, and (iv) an exergoeconomic assessment and optimization. The exergy of all streams, exergy destruction rates, and the exergy efficiencies are evaluated in the exergy analysis. In an economic analysis, on the other hand, the annual values of carrying charges, fuel costs, raw water costs, and operating and maintenance expenses are the cost components. In economic analyses, annualized quantities for each and every cost component are used since cost components are subject to change over their economic lives. Among the exergoeconomic methods reported in literature SPECOC (specific exergy cost) is used in the analysis [192]. SPECOC methodology consists of three main steps [193]:

- Exergy stream identification and classification: Each exergy stream is properly identified and classified as thermal, mechanical, and chemical exergies. Then, the exergy values of associated streams are calculated.
- Input and output identification: In this step, the input (i.e., fuel) and the output (i.e., the desired product) of the system are clearly identified with associated exergy values.
- Cost evaluation: Since exergy is the reasonable base for the cost assessment, the equations for cost calculations are based on exergy streams.

For each flow stream in any system, a parameter \dot{C} (\$/s) is defined as cost flow. Using the exergoeconomic analysis, the cost rates are considered based on the exergy transfer rate, therefore, calculated as follows [184]:

$$\dot{C}_i = c_i \dot{E}x_i \quad (5.122)$$

where c and $\dot{E}x_i$ represent the cost per unit of exergy and associated exergy transfer rate of a stream, respectively. As mentioned earlier, each exergy stream's cost is calculated in exergy costing. Exergy cost rates related to matter, electricity, and heat flows can be described respectively as:

$$\dot{C}_{\text{matter}} = c_{\text{matter}} \dot{E}x_{\text{matter}} \quad (5.123)$$

$$\dot{C}_{\text{electricity}} = c_{\text{electricity}} \dot{E}x_{\text{electricity}} = c_{\text{electricity}} \dot{E}_{\text{electricity}} \quad (5.124)$$

$$\dot{C}_{\text{heat}} = c_{\text{heat}} \dot{E}x_{\text{heat}} = c_{\text{heat}} \dot{Q} \left(1 - \frac{T_0}{T}\right) \quad (5.125)$$

General cost rate balance can be written as

$$\sum(\dot{C}_i)_{in} + \dot{Z} = \sum(\dot{C}_i)_{out} \quad (5.126)$$

where *in* and *out* signify inputs and outputs, respectively. $\sum(\dot{C}_i)_{in}$ represents the total exergy cost of inlet flows, and heat/electricity if applicable. \dot{Z} is the capital and operation and maintenance costs of components. $\sum(\dot{C}_i)_{out}$ denotes the total exergy cost of outlet flows, and heat/electricity if applicable. Component related cost (\dot{Z}) includes life cycle phases of construction and operation of components and expressed as follows:

$$\dot{Z}_i = \frac{Z_i CRF \phi}{3600N} \quad (5.127)$$

where Z_i is the purchase cost of i^{th} component, CRF is capital recovery factor, φ is maintenance factor (~ 1.06) and N is the annual operating hours. Here, Z_i of a component is calculated from various correlations derived by considering the type of component by the study estimate method [194]. Given correlations for purchase cost are generally explained with a cost index, which should be updated using the chemical engineering plant cost index (CEPCI) [195]. The correlations are used as in Turton et al. [194], which are then updated to 2014 values using the following definition:

$$C_1 = C_2 \left(\frac{CEPCI_1}{CEPCI_2} \right) \quad (5.128)$$

Plant cost index for the year 2001 is 394, where this index is 575.7 for 2014 (December final) [191]. Thus, CEPCI factor is taken to be 0.684 to update the costs of components. CRF is dependent on interest rate (i) and total life time (n) of the system:

$$CRF = \frac{i(1-i)^n}{(1+i)^n - 1} \quad (5.129)$$

General cost rate balances for the integrated system for Unit I, II, and III are:

$$c_1 \dot{E}x_1 + \dot{Z}_I = c_2 \dot{E}x_2 + c_3 \dot{E}x_3 \quad (5.130)$$

$$c_3 \dot{E}x_3 + \dot{Z}_{II} = c_4 \dot{E}x_4 + c_5 \dot{E}x_5 + c_6 \dot{E}x_6 + c_7 \dot{E}x_7 \quad (5.131)$$

$$c_2 \dot{E}x_2 + c_4 \dot{E}x_4 + c_6 \dot{E}x_6 + c_8 \dot{E}x_8 + c_9 \dot{E}x_9 + \dot{Z}_{III} = c_{10} \dot{E}x_{10} + c_{11} \dot{E}x_{11} + c_{12} \dot{E}x_{12} + c_{13} \dot{E}x_{13} \quad (5.132)$$

To identify the most important components from the viewpoint of formation of cost, the sum of capital and operation and maintenance costs and cost of exergy destruction (\dot{C}_{dest}) is used and it is defined as:

$$\dot{C}_{dest} = c_{in} \dot{E}x_{dest} \quad (5.133)$$

It is necessary to derive auxiliary equations to calculate unknowns of a cost balance for a component, which requires additional exergy balances of the individual components by considering products and fuels of the component. These formulations can be made using input (I) and output (O) rule, in which it is possible to formulate ($n_e - I$) equations when there are (n_e) streams exiting from the individual component [193].

Principles of input and output should be interpreted to formulate auxiliary equations properly. The I principle dictates that specific cost of an exergy removal from a fuel stream

must be equal to average cost of the same stream entering to upstream components. It should be noted that auxiliary costing equation from I principle is not required when inlet-outlet exergy difference is not considered as fuel. As for the O rule, each exergy unit associated with the product is denoted as c_o . Thus, $(n_{e,p}-1)$ equations can be formulated with the P rule. Total formulated equations with fuel and product rules is equal to (n_e-1) equations to evaluate costs of components [193].

In SPECO method, component cost flow rates and exergy loss costs are used to calculate the exergoeconomic performance of a system. The exergoeconomic performance of a system depends on its exergoeconomic factor f which can be calculated as

$$f = \frac{\dot{Z}}{\dot{Z} + c_{in}\dot{E}x_{dest}} \quad (5.134)$$

Relative cost difference (RCD) is another helpful criteria for assessing and optimizing a system element in thermoeconomic evaluations. RCD determines the relative rise in the mean cost per exergy unit between fuel and product of the system component. The relative cost difference for the integrated system can be written as:

$$RCD = \frac{c_{out} - c_{in}}{c_{in}} \quad (5.135)$$

SPECO method [196] is dependent on specific exergies and costs per exergy unit, exergy efficiencies, and the supplementary costing equations for system elements. The procedure involves three steps: (i) classification of exergy streams, (ii) identification of fuel and product for each component within the system, and (iii) allocation of cost equations. SPECO approach could be utilized as an investigative method to improve the cost effectiveness of a system involving the following actions:

- Rank the components in decreasing order of cost significance using the total $(\dot{Z} + c_{in}\dot{E}x_{dest})$.
- Improve the design of the components starting from the ones with the highest $(\dot{Z} + c_{in}\dot{E}x_{dest})$ to the lowest.
- Give particular attention to components with a high relative cost difference (RCD), especially when the cost rates \dot{Z} and $c_{in}\dot{E}x_{dest}$ are high.

- Use the exergoeconomic factor f to identify the major cost source (capital investment or cost of exergy destruction):
 - if f is high, investigate whether it is cost effective to reduce the capital investment for the i^{th} component at the expense of component efficiency
 - if f is low, try to improve the component efficiency by increasing the capital investment
- Eliminate any sub-processes that increase the exergy destruction or exergy loss without contributing to the reduction of capital investment or of fuel costs for other components.
- Consider improving the exergy efficiency of a component if it has relatively low exergy efficiency or relatively large values of exergy destruction, exergy destruction ratio, or exergy loss ratio.

When performing economic assessment, the annual estimates of transporting charges, fuel prices, material resources' costs, and operating and maintenance expenses provided to the whole system are all essential inputs. On the other hand, these cost components might fluctuate considerably throughout their economic lifetimes. For that reason, levelized (annualized) quantities for each and every cost component are utilized when conducting economic examination and assessments.

It should be noted that the cost flow rate of H₂O and NaCl solution inlets to the integrated system (Streams 8 and 9) are taken to be zero, cost of electricity is assumed to be 0.09 USD/kWh, and cost of thermal energy is 0.032 USD/kWh [197] and normalized to 2014 values. Stream exergy values are taken from EES results.

Purchase equipment costs of the components are calculated based on Equation (5.127). In this equation Z_i is defined for the i^{th} component of the cycle, and it is calculated with various correlations which are defined in terms of their key parameters. Initially purchase equipment cost of the hybrid reactor (Unit III) can be defined as in [194]:

$$\log_{10} Z_{III} = 349.74 + 44.85 \log_{10}(0.05A_{III}^2) + 10.74(\log_{10}(0.05A_{III}^2))^2 \quad (5.136)$$

where V_{III} is the volume of the hybrid reactor.

Cost of the PV/T (II) and spectral splitter (I) are calculated as explained in [198]:

$$Z_I = 1500A_I \quad (5.137)$$

$$Z_{II} = 2500A_{II} \quad (5.138)$$

where A_I and A_{II} are the spectral splitter and PV/T area, respectively.

5.6 Exergoenvironmental Analysis

The environment is affected by the emissions and residuals of energy systems which can be in solid, liquid and/or gas phase. The amount of these emissions can be calculated through thermodynamic analyses and compared with similar conventional systems to assess their environmental impact.

An exergoenvironmental analysis consists of three steps which are: (i) evaluating exergy flow of each stream through the process, (ii) performing LCA of each component and input stream to the process, and (iii) assigning environmental impact of each stream by using LCA. Exergy analysis is an effective method for assessing the quality of a resource as well as the location, magnitude, and causes of thermodynamic inefficiencies. Combined with LCA, which evaluates a system's environmental impact during its entire life, exergoenvironmental analysis is a powerful tool to relate exergy analysis to environmental impacts. The most important components with the highest environmental impact can be identified with the aid of this method [199, 200]. Exergoenvironmental analysis is very similar to exergoeconomic analysis; instead of cost analysis in the exergoeconomic analysis LCA is performed. The exergoenvironmental analysis methodology is illustrated in Figure 5.2.

The method studied in this thesis for exergoenvironmental analysis is performed in analogy to the assignment of costs to exergy streams in exergoeconomics (SPECO method). An environmental impact rate \dot{B} is the environmental impact expressed in Eco-indicator points per time unit (Pts/s or mPts/s). Eco-indicator is a weighting method used in life cycle impact assessment phase, which converts overall environmental impacts of a system to a single value, and permits users to observe the environmental impacts of design alternatives. \dot{B} , for an inlet or outlet stream, can be defined as follows:

$$\dot{B} = b \dot{E}x \quad (5.139)$$

where b is the environmental impact per unit exergy. \dot{B} can be expressed as

$$\dot{B} = B^{ph} + B^{ch} = b \dot{E}x^{ph} + b \dot{E}x^{ch} = b \dot{E}x \quad (5.140)$$

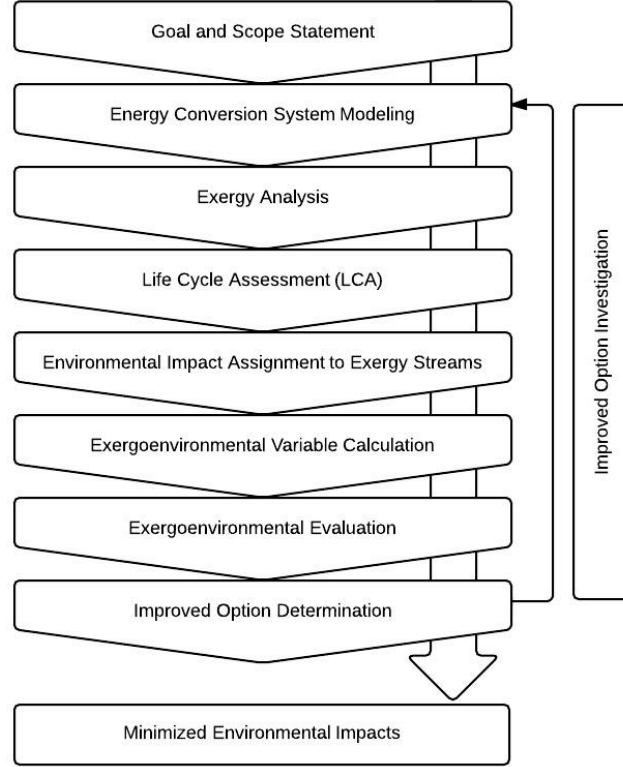


Figure 5.2 Exergoenvironmental analysis methodology (modified from [199]).

Environmental impact rates related to matter, electricity and heat flows can be expressed as

$$\dot{B}_{matter} = (b \dot{E}x)_{matter} \quad (5.141)$$

$$\dot{B}_{electricity} = (b \dot{E}x)_{electricity} = (b \dot{E})_{electricity} \quad (5.142)$$

$$\dot{B}_{heat} = (b \dot{E}x)_{heat} = b \dot{Q} \left(1 - \frac{T_0}{T_{reaction}}\right) \quad (5.143)$$

The component related environmental impact is shown as \dot{Y} (analogous to \dot{Z} in exergoeconomic analysis), which includes life cycle phases of construction, operating and maintenance, and disposal. To account for pollutant formation, a new variable should be

defined, which is \dot{B}^{PF} . Pollutant formation term can be neglected if there are no pollutants emitted during the process life cycle [199, 201]. \dot{B}^{PF} can be defined as

$$\dot{B}^{PF} = \sum [b(\dot{m}_{out} - \dot{m}_{in})]_i \quad (5.144)$$

It should be noted that only CO, CO₂, CH₄, N₂O, NO_x, and SO_x are taken into account as pollutants. Environmental impact rate can be rewritten as

$$\dot{B}_{out} = \dot{B}_{in} + (\dot{Y} + \dot{B}^{PF}) \quad (5.145)$$

If the process is assumed to emit zero pollutants:

$$\dot{B}_p = \dot{B}_{in} + \dot{Y} \quad (5.146)$$

Environmental impact as a result of exergy destruction is identified as

$$\dot{B}_{dest} = b_{in} \dot{E}x_{dest} \quad (5.147)$$

The exergoenvironmental factor is defined as

$$f_b = \frac{\dot{Y}}{\dot{Y} + b_{in} \dot{E}x_{dest}} \quad (5.148)$$

Relative difference of specific environmental impact is an indicator of the potential for reducing the environmental impact associated with a component which is defined as:

$$r_b = \frac{b_{out} - b_{in}}{b_{in}} \quad (5.149)$$

5.7 Optimization Study

Optimization of an energy system consists of modifying the system structure and component design parameters according to one or more specified design objectives. Since most of the problems depend on many parameters, optimization of these systems by considering a single objective does not provide precise results with respect to other objectives to be optimized [202]. Multiple objectives are generally involved in a design process: thermodynamic (e.g., maximum efficiency, minimum fuel consumption), economic (e.g., maximum profit, minimum cost) and environmental (e.g., minimum GHG emissions). A multi-objective optimization study allows finding the optimal set of design variables that satisfies the pre-set objectives [183, 202].

There are several considerations for performing an optimization study. The first step is to define the system boundary, including all important and effective parameters. For complex energy systems, the system can be broken down into subsystems. Specifying the optimization criteria is the next step. Economics, thermodynamics, and environment, each can be the basis of evaluation and optimization. Another essential element is to select the variables on which optimization is based on. They have to be independent and address the system or process characteristics in a well manner. These variables should be the important parameters that affect the performance and cost effectiveness of the system. Moreover, they should be distinguished from parameters with minor importance. The variables that are selected for an optimization study are subject to change and considered as decision variables, and should be distinguished from fixed value parameters of the system or the process. The next step is selection of a mathematical model for the analysis. The mathematical model related the variables and defines how the independent variables affect the system performance. The model consists of an optimization function and some technical constraints. For instance, the objective function can be the minimization of the product cost or maximizing the exergy efficiency of the system. Minimization of exergy loss or destruction could be another objective function.

Three objective functions considered in this study for the multi-objective optimization are the exergy efficiency (to be maximized), the total cost rate of product (to be minimized) and the total environmental impact rate (to be minimized). Genetic algorithm based multi-objective optimization study is performed using EES software. The first objective function, the exergy efficiency, is defined in Section 5.3. The second and third optimization functions, the total cost and environmental impact rates, are defined as follows:

$$\dot{C}_{total} = \dot{C}_{in} + \dot{C}_{dest} + \dot{Z} \quad (5.150)$$

$$\dot{B}_{total} = \dot{B}_{in} + \dot{B}_{dest} + \dot{Y} \quad (5.151)$$

One of the methods to implement this is the simplex method based on a subroutine given by Press [203]. Other sources and codes for other languages are available in versions of commercial packages (e.g., MATLAB). More efficient but more complicated, gradient-based methods are available from the same sources.

Curve fitting by optimization is one of the useful toolboxes in MATLAB software that is used during the course of this research. This toolbar can be used to fit an optional function to some data. The sub-routine code uses the `fminsearch` solver to minimize the sum of squares of errors between the data and selected function for varying parameters.

For a system to be optimized with multiple (K) objectives, minimization of the objectives is defined in [204]. In a solution space of X and for an n -dimensional decision variable:

$$x = \{x_1, x_2 \dots x_n\} \quad (5.152)$$

It is necessary to determine an x^* vector to minimize:

$$z(x^*) = \{z_1(x^*), \dots z_K(x^*)\} \quad (5.153)$$

The search space X is restricted with specified constraints of the system studied:

$$g(x^*) = b_j \text{ for } j = 1, \dots m \quad (5.154)$$

Decision for the optimization study can be made for both minimization and maximization. However, this selection should be at the same direction for all objective functions. Thus, if a minimization study is conducted and one of the objectives is to be maximized, these objective functions can be multiplied by negative one (-1). Among all feasible solutions, the most dominant solution is the Pareto optimal solution. For a determined Pareto optimal set, all corresponding objective function values are called the Pareto front.

There are several methods of optimization which can be adapted to solve multi-objective optimization problems. Genetic Algorithms (GA) are one of the most promising optimization methods, which is inspired by evolution theory of the nature [205]. In the GA, the solution vector (x) is defined as a chromosome, and collection of chromosomes form a population. Generation of new solutions are accomplished by crossover and mutation, where crossover is forming of new solutions from two chromosomes called 'parents'. It is expected that the offspring inherits the good genes from parents to optimize the population. Mutation is generally applied at gene level, which helps the population remain in the local optima by setting a mutation rate between 0 and 2, so that the offspring is not be very different than their parents. GA optimization can be accomplished with the following steps:

- Initiate a population
- Select random parents from the population
- Crossover
- Mutation
- Reproduction of new population from the children population
- Stop evolution

A multi-objective optimization study can be performed using GA by finding a set of non-dominated solutions in a single run [204]. Here, a general method can be defined as weight-based GA, where a user defined weight factor is used to minimize all objective functions in a single objective problem:

$$\min z = w_1 z'_1(x) + \dots + w_k z'_k(x) \quad (5.155)$$

Here, defining the weight factor is a challenging process through the optimization process. However, this is a simple and useful tool to solve multi-objective problems. There are several other modifications for multi-objective GA optimization, and can be found elsewhere [205]. Here, constraints are also taken into consideration for a feasible search space during optimization, which would lead to a more suitable solution space. The main performance influencing parameters in the cycle are the operating temperature, inlet mass flow rates to the hybrid reactor, PV/T and reactor active areas, and environmental temperature. Ranges of constraints are listed as follows:

- Operating temperature: $0^\circ\text{C} \leq T \leq 80^\circ\text{C}$
- Inlet mass flow rates: $0.0001 \leq \dot{m} \leq 1\text{kg/s}$
- PV/T area: $0.5 \leq A_{II} \leq 2\text{ m}^2$
- Reactor area: $0.5 \leq A_{III} \leq 2\text{ m}^2$
- Environmental temperature: $0^\circ\text{C} \leq T_0 \leq 40^\circ\text{C}$

The manipulated data have influence on the cycle performance characteristics as well as heating and cooling rates and size of the components which affect both cost and performance. Optimum values are obtained for minimized cost and environmental impact and maximized exergy efficiency.

CHAPTER 6: RESULTS AND DISCUSSION

This chapter consists of eight sections; in the first four sections, the experimental investigation and thermodynamic analysis results of Process 1, Process 2, Process 3, and Process 4 are presented and discussed in detail. These processes are electrolysis, PEC, chloralkali, and PEC-chloralkali. All processes are experimentally tested under four different temperatures (20, 40, 60, and 80°C) and three different inlet mass flow rates (0.25, 0.50, and 0.75 g/s). In addition, Processes 2 and 4 are tested under two different light settings: low (600 W/m²) and high (1200 W/m²). Each experimental run takes one hour and each run is repeated three times under the same input conditions to test the repeatability of the experiments. The effects of the operating temperature, inlet mass flow rate, and environmental temperature on the measured current, hydrogen production, energy and exergy efficiencies, and exergy destruction are investigated for each process type.

In addition, in Section 6.5, a performance assessment of the present integrated system is examined and the effects of the operating temperature, inlet mass flow rate, photoactive area, and the environmental temperature on the hydrogen, chlorine, heat and electricity production, exergy destruction, and the energy and exergy efficiencies are discussed in detail. The results of the exergoeconomic and exergoenvironmental analyses of the integrated system are presented in Sections 6.6 and 6.7, respectively. In exergoeconomic and exergoenvironmental analyses sections, the effects of the operating temperature, inlet mass flow rate, photoactive area, and the environmental temperature on the cost and emissions of hydrogen, chlorine, heat, and electricity production are investigated in detail. Finally, the optimization study results of the integrated system are presented in Section 6.8.

6.1 Process 1 – Electrolysis: Results and Discussion

In the electrolysis experiments, the hybrid reactor is tested under no simulated light conditions. H₂O is the only input to both anode and cathode of the reactor. In this section, the effects of the operating temperature, inlet mass flow rate, and environmental temperature on the measured current, H₂ production, energy and exergy efficiencies, and exergy destruction are discussed. The optimum operating temperature, inlet mass flow rate,

and environmental temperature are shown. In addition, the Cu₂O-coated membrane performance is presented by comparing the current generation before and after the coating process. In the end, the uncertainty and statistical analyses of Process 1 test results are provided.

6.1.1 Effect of Operating Temperature

The effect of the operating temperature is observed under 2.5 V voltage and 0.25 g/s inlet mass flow rate and the environmental temperature is 20°C. Under four different operating temperatures (20, 40, 60, and 80°C), measured current, H₂ production, energy and exergy efficiencies, and rate of exergy destruction are presented. In the end, the optimum operating temperature is calculated in order to determine the temperature where the H₂ production and energy and efficiencies are maximized and the exergy destruction is minimized.

a. Measured Current Results

The effect of the operating temperature on the current measurements during the electrolysis experiments is presented in Figure 6.1. The average standard deviation in the current measurements is 0.001 A. As can be seen in Figure 6.1, with increasing operating temperatures, the current measurements are increasing as well. The primary reason of this tendency is the increasing component conductivities. Since the voltage losses and electrical resistance of the reactor components are decreasing with the increasing operating temperatures, higher currents are measured at higher operating temperatures.

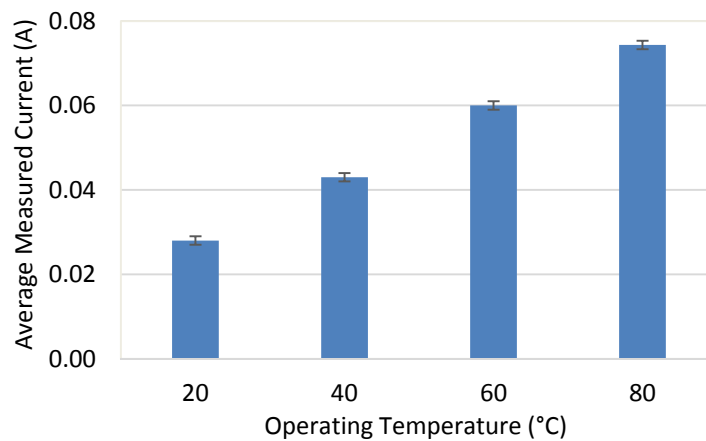


Figure 6.1 Effect of operating temperature on current measurement results (Process 1).

b. Hydrogen Production Results

The comparison of the experimental and model H₂ production outputs at different operating temperatures are presented in Figure 6.2. Each experimental run is repeated three times at each operating temperature resulting an average standard deviation of 0.1 g/h. As can be seen in Figure 6.2, the effect of the operating temperature on H₂ production is similar to the effect of operating temperature on the current generation presented in Figure 6.1. Because of the increasing conductivities and decreasing losses, the H₂ production increases with increasing operating temperatures.

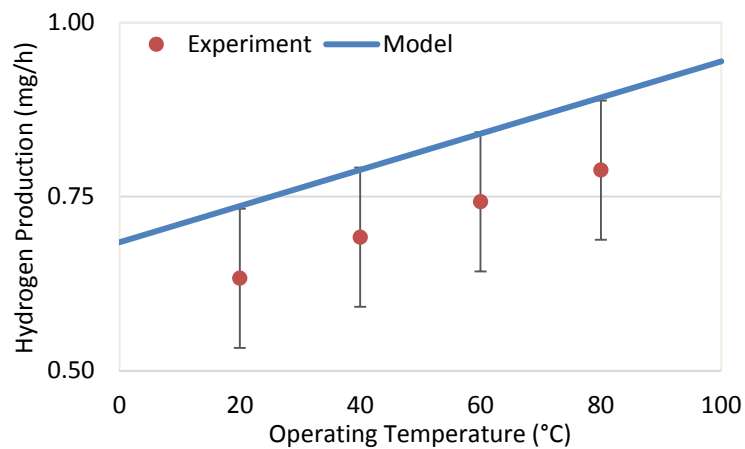


Figure 6.2 Effect of operating temperature on H₂ production with comparison of experimental and model outputs (Process 1).

Figure 6.2 also shows that the model outputs are in a good agreement with the experimental results. Within the selected operating temperature interval of 0-100°C, on average, the model predicts about 0.1 g/h more H₂ production which corresponds to an average difference of 14.2%. This difference might be caused from the following assumptions (i) steady-state steady-flow, (ii) changes in kinetic and potential energies, (iii) heat losses to the environment; and (iv) conductivity losses in auxiliary components.

c. Energy Efficiency Results

The effect of the operating temperature on the energy efficiency for Process 1 is presented in Figure 6.3. The experimental results show that when the operating temperature is increased from 20°C to 80°C, the energy efficiency decreases from about 36% to 17%. This decrease is due to the increasing heat input to the reactor in order to operate at higher

temperatures which lowers the efficiency despite the fact that H₂ production is increasing with increasing operating temperatures.

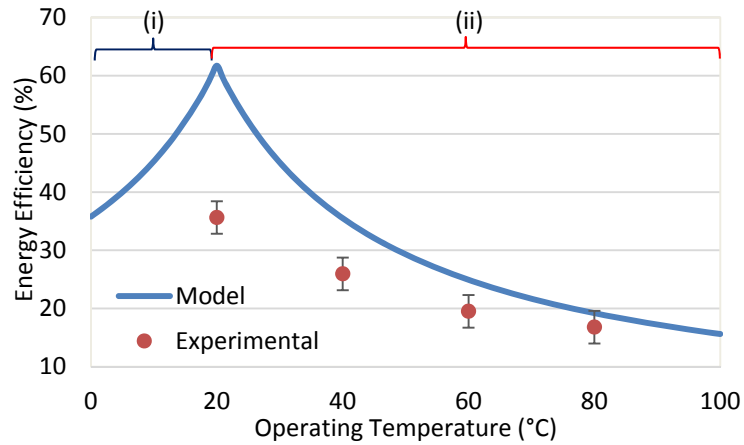


Figure 6.3 Effect of operating temperature on energy efficiency with comparison of experimental and model outputs (Process 1) – (i) cooling, (ii) heating.

From Figure 6.3, it can be seen that the energy efficiency shows different behaviors with respect to the operating temperature. The model states that the energy efficiency increases with increasing operating temperatures up to 20°C and then starts decreasing after 20°C. The reason of this change is the environmental temperature. Since the environmental temperature is set to 20°C, operating at temperatures lower than 20°C requires cooling and heating is required to operate at temperatures higher than 20°C. The experimental runs take place at 20, 40, 60, and 80°C and within the selected operating temperature interval, the experimental results and model outputs are in good agreement. On average, the model predicts about 11% higher energy efficiency. The primary reason for this difference is the assumptions used when developing the thermodynamic and electrochemical models, as discussed earlier in this section.

d. Exergy Efficiency Results

Figure 6.4 shows the effect of the operating temperature on the exergy efficiency of Process 1. The experimental results show that when the operating temperature is increased from 20°C to 80°C, the exergy efficiency decreases from about 32% to 27%. Similar to the energy efficiency results, higher heat input requirements lower the exergy efficiency at

increasing operating temperatures. Each experimental run is repeated three times at each operating temperature resulting an average standard deviation of around 5%.

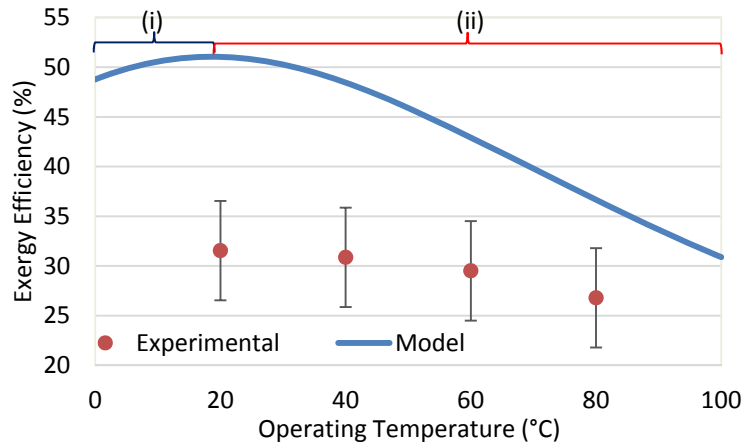


Figure 6.4 Effect of operating temperature on exergy efficiency with comparison of experimental and model outputs (Process 1) – (i) cooling, (ii) heating.

Similar to the energy efficiency results shown in Figure 6.3, the exergy efficiency increases with increasing operating temperatures up to 20°C and then starts decreasing after 20°C. The reason for this change is the environmental temperature. As the environmental temperature is set to 20°C, operating at temperatures lower than 20°C requires cooling and heating is needed to operate at temperatures higher than 20°C. The experimental runs take place at 20, 40, 60, and 80°C and within the selected operating temperature interval, the experimental results and model outputs are in good agreement. Within the selected operating temperature interval, on average, the model predicts about 15% higher exergy efficiency. The main cause of this variance is the assumptions taken into account when developing the thermodynamic and electrochemical models, which are discussed earlier in this section.

e. Exergy Destruction Results

The exergy destruction rate results of Process 1 within the selected operating temperature interval of 0°C - 100°C is presented in Figure 6.5. In the calculation of exergy destructions, the experimental results and the electrochemical and thermodynamic models are used together to evaluate the effect of the operating temperature on exergy destruction.

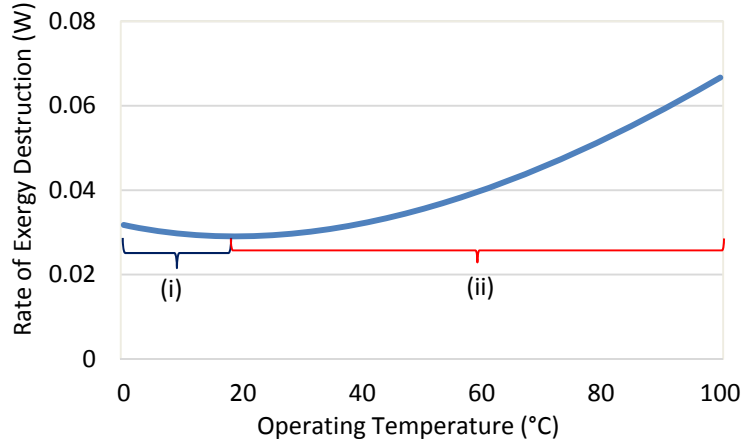


Figure 6.5 Effect of operating temperature on exergy destruction –model outputs (Process 1) – (i) cooling, (ii) heating.

Figure 6.5 shows that the lowest exergy destruction rate is observed at 20°C, which is about 0.03 W. At operating temperatures lower than 20°C, cooling is needed which increases the exergy destruction as the operating temperature is decreased. On the other hand, in order to operate at temperatures higher than 20°C, heating is required which also increases the exergy destruction with increasing operating temperatures.

f. Optimum Operating Temperature Results

In order to find the optimum operating temperature, the thermodynamic model results are normalized and ranked based on the following equations:

- For criteria that are desired to be maximized (e.g., energy and exergy efficiencies and H₂ production rate):

$$rank = \frac{i - minimum}{maximum - minimum} \times 10 \quad (6.1)$$

- For criteria that are desired to be minimized (e.g., exergy destruction rate):

$$rank = \frac{maximum - i}{maximum - minimum} \times 10 \quad (6.2)$$

Here *i* denotes the individual data point at a specific temperature and *maximum* and *minimum* correspond to the maximum and minimum values of a specific criteria (i.e., energy and exergy efficiencies, H₂ production rate, and exergy destruction rate) within the selected temperature operating temperature interval between 0-100°C. Normalized

rankings of H₂ production, energy and exergy efficiencies, and exergy destruction rates for Process 1 within based on the thermodynamic model results are given in Figure 6.6 along with their average rankings.

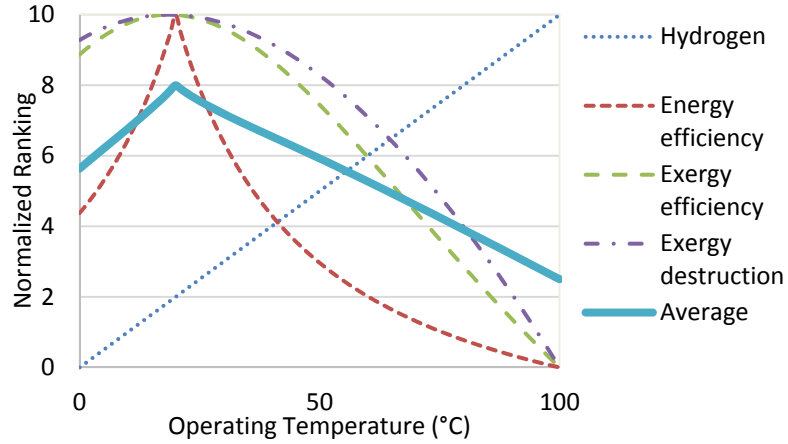


Figure 6.6 Normalized rankings of H₂ production, efficiencies, and exergy destruction at different operating temperatures (Process 1).

Figure 6.6 shows that the highest average ranking is observed at 20°C which is 8/10. This means, within the selected operating temperature interval, the highest possible H₂ production and efficiencies and the lowest possible exergy destruction occur at 20°C. Therefore, for the upcoming analyses, 20°C is chosen to be the operating temperature.

6.1.2 Effect of Inlet Mass Flow Rate

The effect of the inlet mass flow rate is monitored under 2.5 V applied voltage, and both the operating and environmental temperatures are set to 20°C. In this section, under three different inlet mass flow rates (0.25, 0.50, and 0.75 g/s), the measured current, H₂ production, energy and exergy efficiencies, and the rate of exergy destruction are presented. In the end, the optimum inlet mass flow rate is assessed to select the flow rate where the H₂ production and energy and efficiencies are maximized and the exergy destruction is minimized.

a. Measured Current Results

The average values of the current measurement results at selected inlet mass flow rates of 0.25, 0.50, and 0.75 g/s during the electrolysis experiments are presented in Figure 6.7

where the average standard deviation in current measurements is 0.002 A. Figure 6.7 shows that the current measurements increase with increasing inlet mass flow rates. The primary reason of this tendency is that with increasing mass flow rates, depleted ions are replaced more frequently and this prevents negative or positive ion accumulation. Positive or negative ion accumulation slows the redox reactions down and reduces the corresponding current generation due to ion replacement. Therefore, preventing and/or minimizing positive or negative ion replacement increases the current generation.

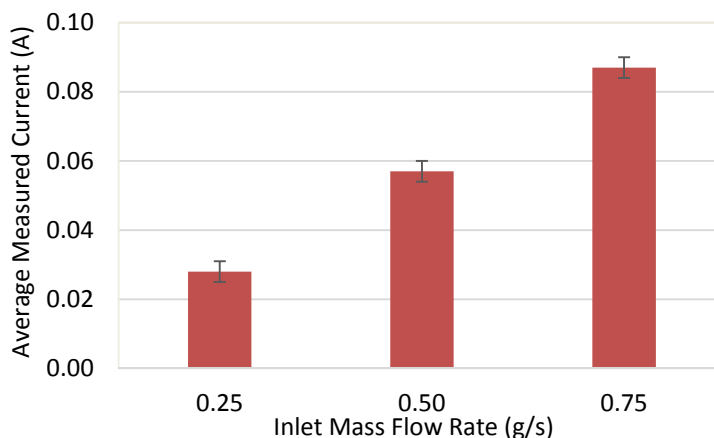


Figure 6.7 Effect of inlet mass flow rate on current measurements (Process 1).

b. Hydrogen Production Results

The experimental and model H₂ production outputs at different inlet mass flow rates are presented in Figure 6.8. Each experimental run is repeated three times at each inlet mass flow rate resulting an average standard deviation of 0.1 g/h. Figure 6.8 shows that the effect of the inlet mass flow rate on the H₂ production is similar to the current measurement results presented in Figure 6.7.

In addition, Figure 6.8 indicates that the model outputs are in a good agreement with the experimental results. On average, the model predicts about 0.3 g/h higher H₂ production resulting an average difference of 24.9%. This difference could potentially be caused from the assumptions of steady-state steady-flow, negligible kinetic and potential energy changes, heat losses to the environment; and conductivity losses.

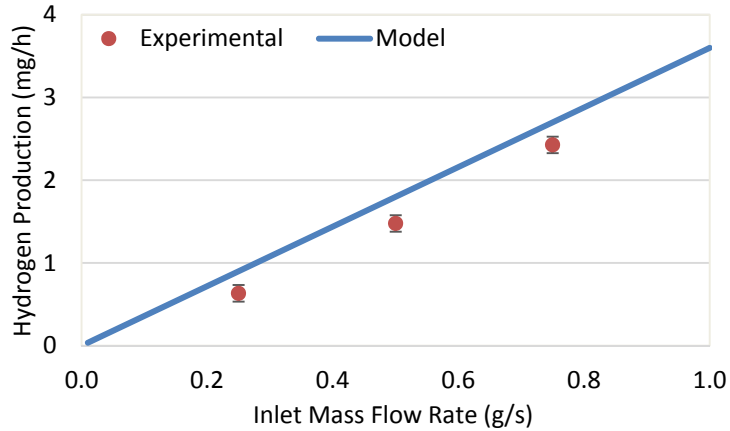


Figure 6.8 Effect of inlet mass flow rate on H₂ production with comparison of experimental and model outputs (Process 1).

c. Energy Efficiency Results

The effect of the inlet mass flow rate on the energy efficiency of Process 1 is presented in Figure 6.9. The experimental results show that when the inlet mass flow rate is increased from 0.25 to 0.75 g/s, the energy efficiency decreases from about 36% to 31%. The reason of this decrease is the increase in pump load and voltage requirements with increasing inlet mass flow rates. Each experimental run is repeated three times at each inlet mass flow rate resulting an average standard deviation of around 4%.

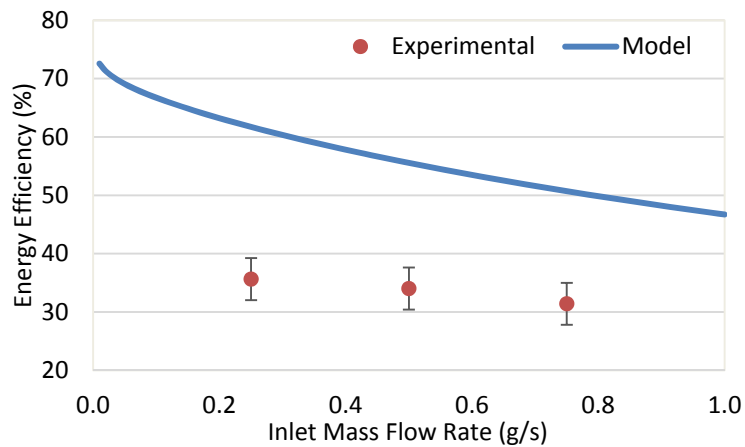


Figure 6.9 Effect of inlet mass flow rate on energy efficiency with comparison of experimental and model outputs (Process 1).

From Figure 6.9, it can be seen that the energy efficiency results of the experimental runs and model outputs have similar tendencies, which can be considered as an acceptable level of agreement. Within the selected inlet mass flow rate interval of 0.25 to 0.75 g/s, on average, the model predicts about 22% higher energy efficiency. The primary reason for this difference is the assumptions used when developing the thermodynamic and electrochemical models, as discussed earlier in this section.

d. Exergy Efficiency Results

Figure 6.10 shows the effect of the inlet mass flow rate on the exergy efficiency of Process 1. The experimental results show that when the inlet mass flow rate is increased from 0.25 to 0.75 g/s, the exergy efficiency decreases from about 32% to 27%. Similar to the energy efficiency results, increasing pump input and voltage requirements lowers the exergy efficiency at increasing inlet mass flow rates. Each experimental run is repeated three times at each inlet mass flow rate resulting an average standard deviation of around 3%.

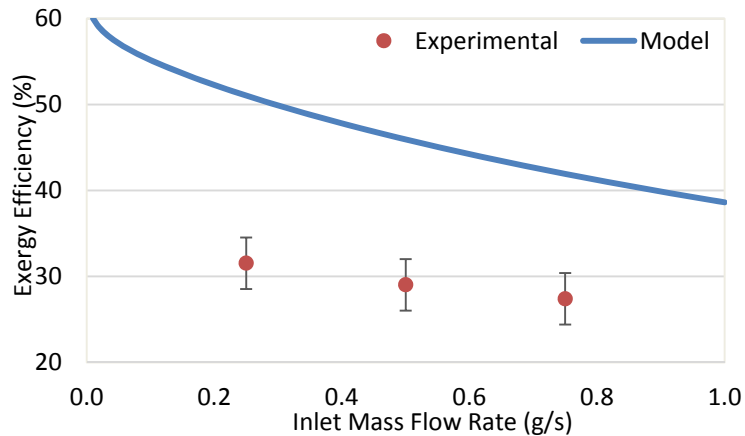


Figure 6.10 Effect of inlet mass flow rate on exergy efficiency with comparison of experimental and model outputs (Process 1).

The experimental runs take place at 0.25, 0.50, and 0.75 g/s inlet mass flow rates and within the selected inlet mass flow rate interval, the experimental results and model outputs have similar behaviors. Within the selected operating temperature interval, on average, the model predicts about 17% higher exergy efficiency. The main cause of this variance is the assumptions taken into account when developing the thermodynamic and electrochemical models, which are discussed earlier in this section.

e. Exergy Destruction Results

The effect of the inlet mass flow rate on the exergy destruction rate of Process 1 is presented in Figure 6.11. When evaluating the exergy destructions, the experimental results and the electrochemical and thermodynamic models are used together to evaluate the effect of the inlet mass flow rate on exergy destruction. Figure 6.11 shows that the lowest exergy destruction rate is observed at 0.1 g/s, which is about 0.003 W. With increasing inlet mass flow rates, the rate of exergy destruction increases due to increasing pump input and voltage requirements.

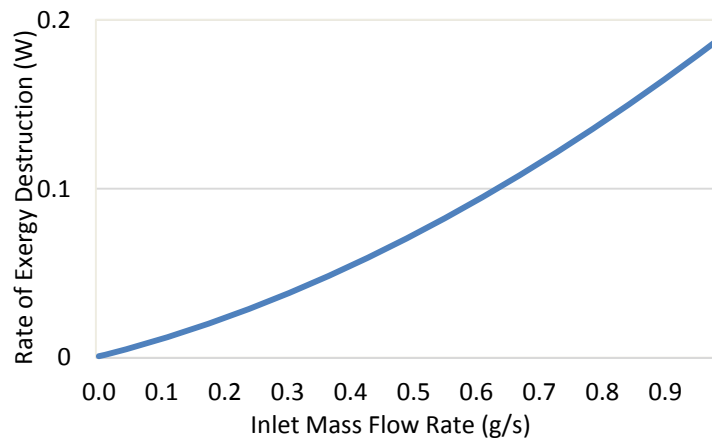


Figure 6.11 Effect of inlet mass flow rate on exergy destruction –model outputs (Process 1).

f. Optimum Inlet Mass Flow Rate Results

In order to find the optimum inlet mass flow rate, the thermodynamic model results are normalized and ranked using Equations (6.1) and (6.2). The normalized rankings of H₂ production, efficiencies, and exergy destruction rates for Process 1 based on the thermodynamic model results are given in Figure 6.12 along with their average rankings.

Figure 6.12 shows that except the H₂ production rate, all other performance criteria have decreasing rankings with increasing inlet mass flow rate. As a result, the average ranking is decreasing with increasing inlet mass flow rate, too. However, selecting 0 g/s inlet mass flow rate would mean zero H₂ production, and the aim is to produce H₂; therefore, 0.25 g/s is selected as the inlet mass flow rate which gives an average ranking of 6.5/10, which is high enough and acceptable within the given inlet mass flow rate interval.

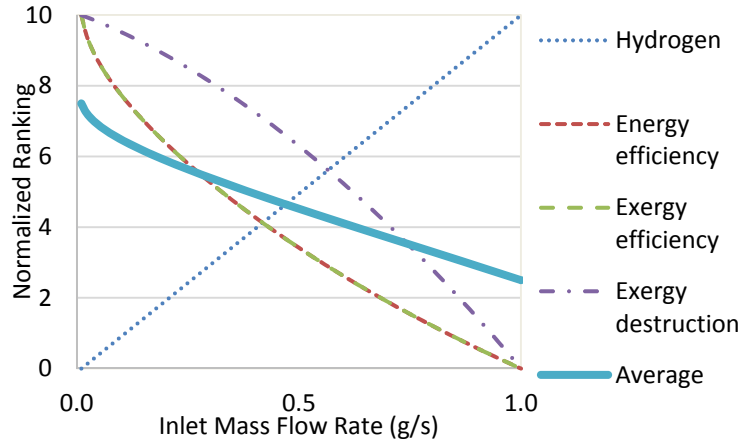


Figure 6.12 Normalized rankings of H₂ production, efficiencies, and exergy destruction at different inlet mass flow rates (Process 1).

6.1.3 Effect of Environmental Temperature

The effect of the environmental temperature is investigated based on the thermodynamic model under 2.5 V applied voltage, 0.25 g/s inlet mass flow rate, and the operating temperature is 20°C. Within the selected environmental temperature interval of 0-40°C, the efficiencies and exergy destruction results of Process 1 are presented in Figure 6.13. Since the operating temperature is 20°C, the system needs heating at environmental temperatures below 20°C. Conversely, the system needs cooling at environmental temperatures above 20°C. Thus, 20°C gives the highest efficiencies and lowest exergy destruction within the selected environmental temperature interval of 0-40°C.

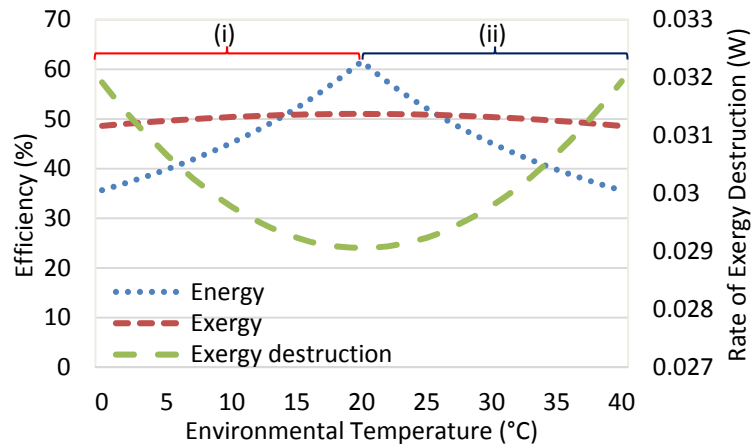


Figure 6.13 Effect of environmental temperature on exergy destruction and efficiencies (Process 1) – (i) heating, (ii) cooling.

6.1.4 Coated Membrane Results

In order to check the impact of the Cu_2O coating on the membrane's performance, the current readings of membrane before and after the coating process are recorded at three different applied potentials (2.5, 3, and 3.5 V) in Process 1 and the comparison results are presented in Figure 6.14. Figure 6.14 shows that the Cu_2O coating causes an increase in current generation. As a result, it is concluded that the Cu_2O coating increases the conductivity of the membrane, which gives higher current readings.

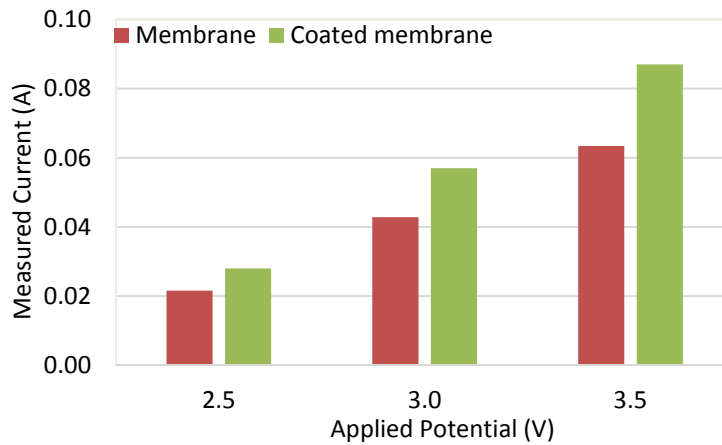


Figure 6.14 Effect of membrane coating on current measurements at different applied potentials.

6.1.5 Uncertainty Analysis Results

The average uncertainty analysis results of Process 1 experiments are presented in Table 6.1. The highest uncertainty is observed in exergy efficiency calculations, which is around ± 7.13 and this amount is followed by energy efficiency calculations (± 6.18). Uncertainty in hydrogen production results, on average, is calculated to be ± 1.10 . And the uncertainty in current measurements is less than ± 1.00 (± 0.52).

Table 6.1 Summary of uncertainties during the Process 1 experimental runs.

Type of result	Uncertainty (%)
Current	± 0.52
Hydrogen production	± 1.10
Energy efficiency	± 6.18
Exergy efficiency	± 7.13

6.1.6 Statistical Analysis Results

The statistical analysis of the Process 1 experimental results is conducted based on the Design of Experiments (DOE) approach. The agreement between the DOE model and the actual data points and leverage residuals plot for the current, hydrogen production, and energy and exergy efficiencies for Process 1 are presented in Figures 6.15–6.18. The F-test is conducted to evaluate the impact of the two key input parameters on the current generation, hydrogen production, and energy and exergy efficiencies in Process 1. These parameters are the operating temperature and the inlet mass flow rate.

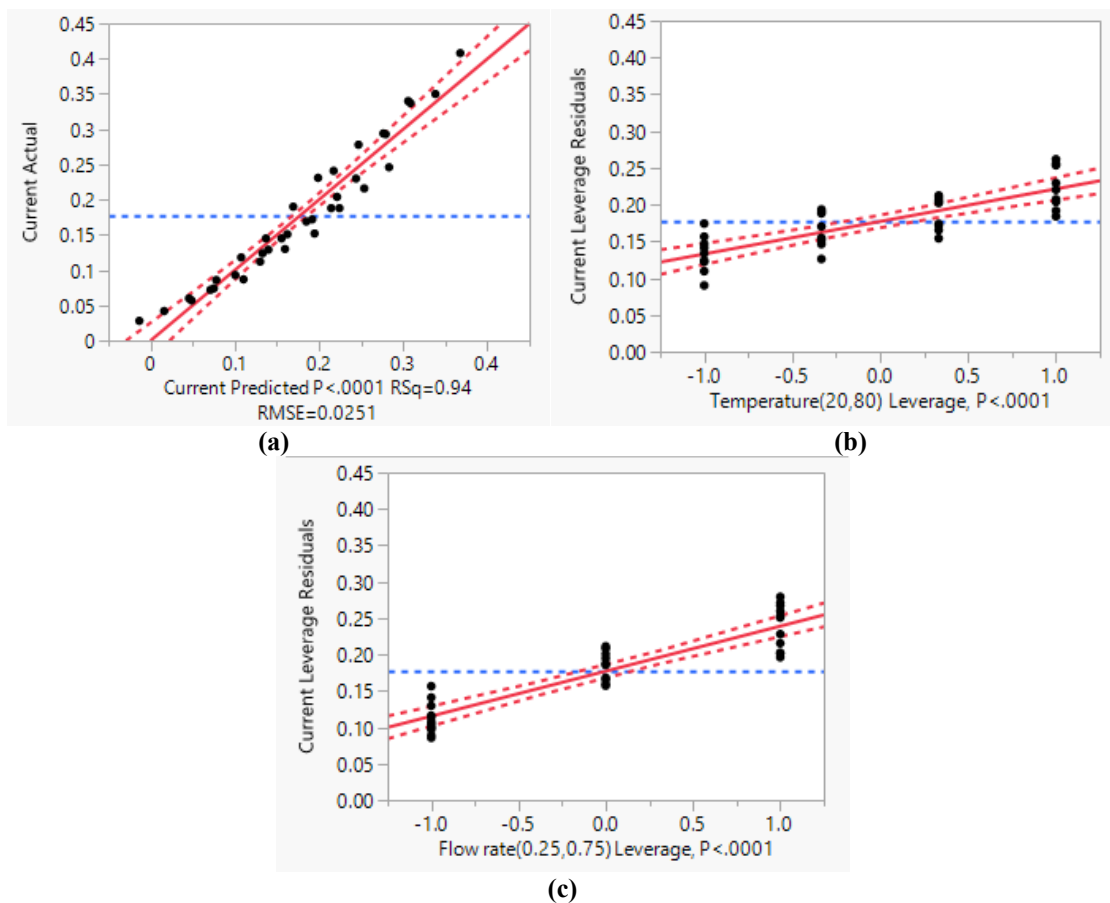


Figure 6.15 Results of (a) DOE model, (b) operating temperature leverage plot, and (c) inlet mass flow rate leverage plot of Process 1 experimental current measurements.

The detailed statistical analysis results of the current measurements of Process 1 is presented in Figure 6.15. The DOE model is in a good agreement with the actual experimental data with a root mean square error of 0.0251. The standard error in current

measurements is about 0.01. The F-test results show that the inlet mass flow rate has an F-ratio of 145.52 and the operating temperature has an F-ratio of 62.06. Therefore, it is concluded that the inlet mass flow rate has a higher impact on the current generation in Process 1 compared to the operating temperature.

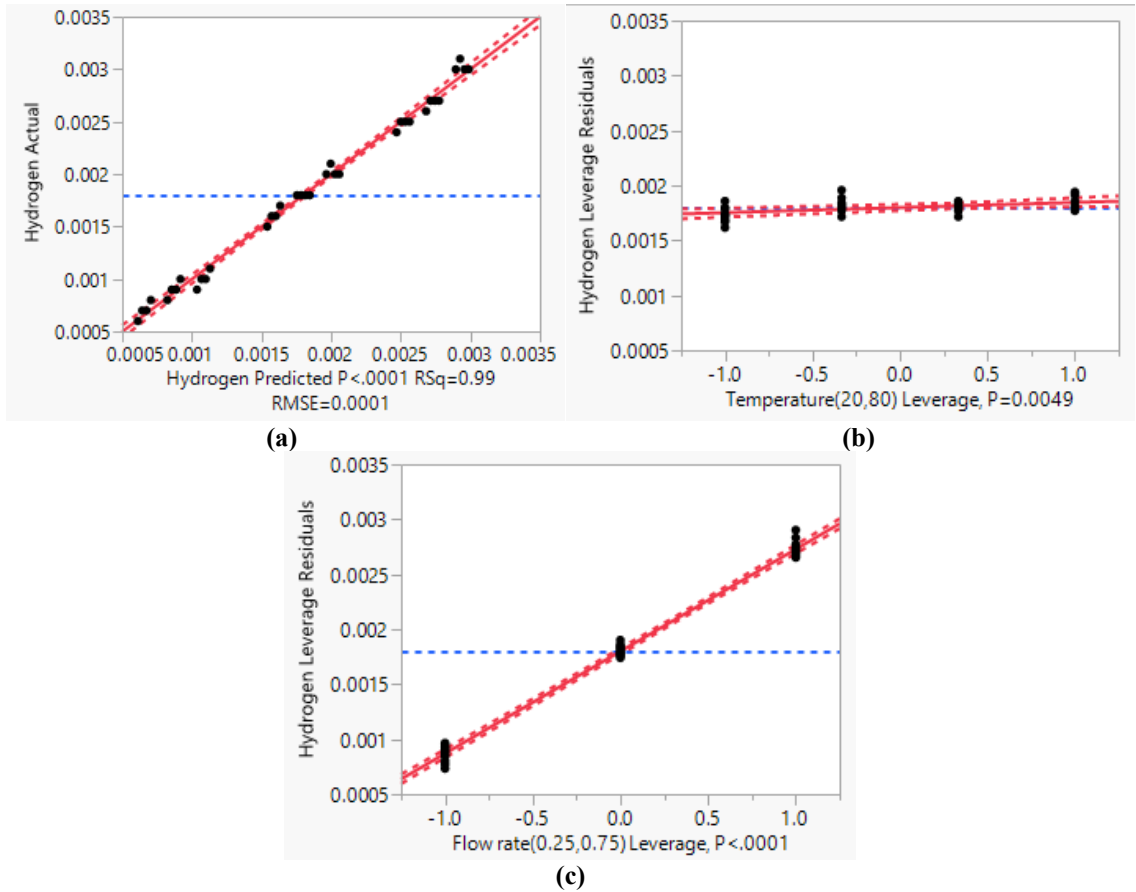


Figure 6.16 Results of (a) DOE model, (b) operating temperature leverage plot, and (c) inlet mass flow rate leverage plot of Process 1 experimental hydrogen production results.

The comparison of the present experimental hydrogen production and the DOE model results along with the leverage residuals of Process 1 are provided in Figure 6.16. The DOE model agrees with the actual experimental data with a root mean square error of 0.0001. The standard error in hydrogen production is less than 0.001, which is considered to be zero. The F-test results indicate that the inlet mass flow rate has an F-ratio of 4354.24 and the operating temperature has an F-ratio of 9.15. For that reason, it is determined that the inlet mass flow rate has a greater influence on the hydrogen production in Process 1 compared to the operating temperature.

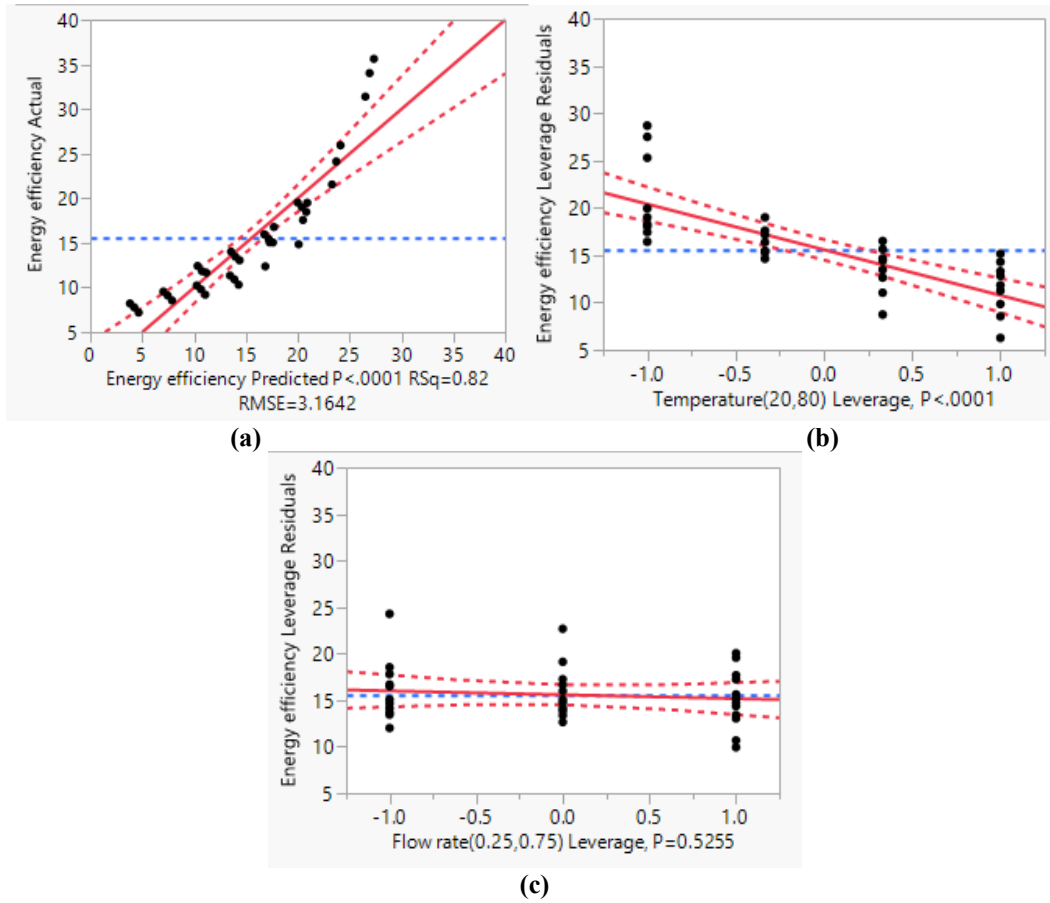


Figure 6.17 Results of (a) DOE model, (b) operating temperature leverage plot, and (c) inlet mass flow rate leverage plot of Process 1 experimental energy efficiency results.

Figure 6.17 shows the detailed statistical analysis of the energy efficiency results of Process 1. The DOE model has a satisfactory agreement with the actual experimental data with a root mean square error of 3.1642. The standard error in energy efficiency results is about 0.7. The F-test results present that the operating temperature has an F-ratio of 46.49 and the inlet mass flow rate has an F-ratio of 0.41. As a result, it is concluded that the operating temperature has a higher impact on the energy efficiency in Process 1 compared to the inlet mass flow rate.

Figure 6.18 shows the comparison of the present experimental exergy efficiency and the DOE model results along with the leverage residuals of Process 1. The DOE model agrees with the actual experimental data with a root mean square error of 2.9448. The standard error in exergy efficiency is about 0.60. The F-test results indicate that the operating temperature has an F-ratio of 51.18 and the inlet mass flow rate has an F-ratio of

0.27. For that reason, it is determined that the operating temperature has a greater influence on the exergy efficiency in Process 1 compared to the inlet mass flow rate.

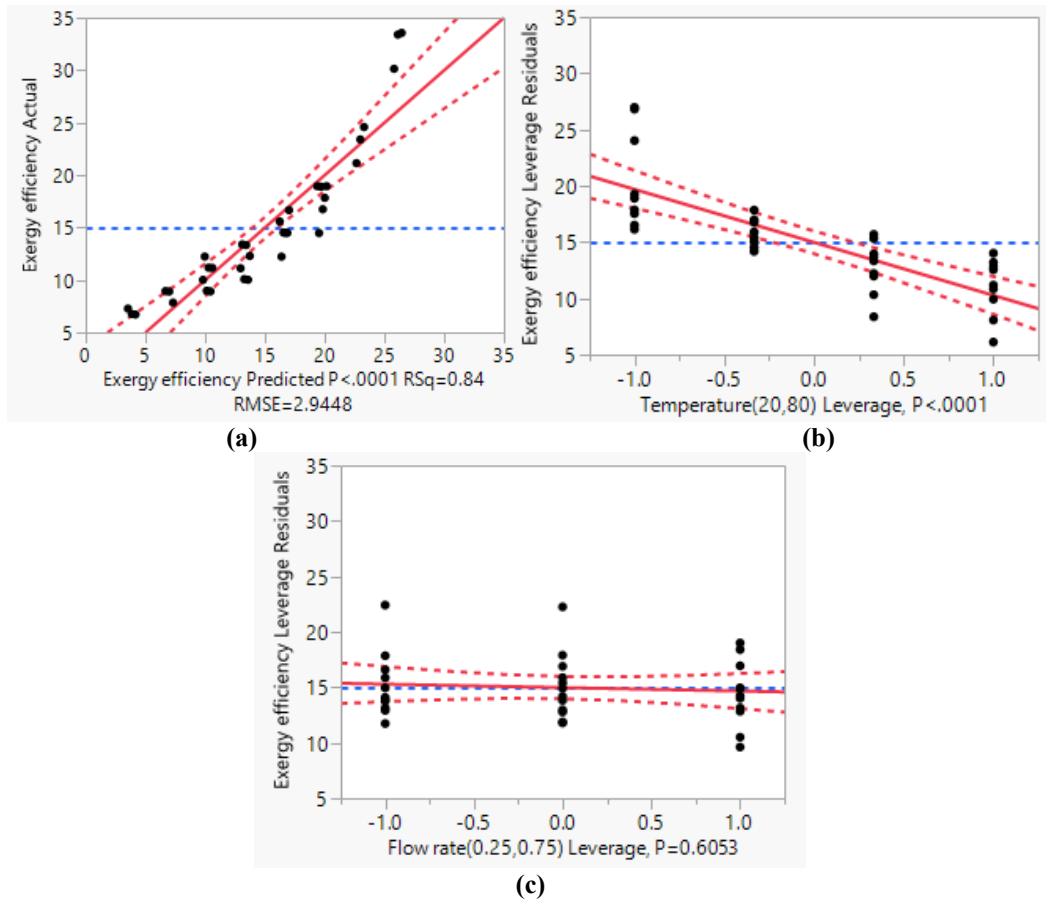


Figure 6.18 Results of (a) DOE model, (b) operating temperature leverage plot, and (c) inlet mass flow rate leverage plot of Process 1 experimental exergy efficiency results.

6.2 Process 2 – Photoelectrochemical: Results and Discussion

In the PEC experiments, the hybrid reactor is tested under two irradiation levels: 600 (low) and 1200 W/m² (high). H₂O is the only input to both anode and cathode. In this section, the effects of the operating temperature, inlet mass flow rate, and environmental temperature on the measured current, H₂ production, energy and exergy efficiencies, and exergy destruction are discussed in detail. The optimum operating temperature, inlet mass flow rate, and environmental temperature are also presented. In addition, the Cu₂O-coated membrane performance is given by comparing the current generation before and after the

coating process. And last but not least, the uncertainty and statistical analyses of Process 2 test results are provided.

6.2.1 Effect of Operating Temperature

The tests are run under 2.5 V applied voltage, 0.25 g/s inlet mass flow rate, and 20°C environmental temperature. Under four different operating temperatures (20, 40, 60, and 80°C), the measured current, H₂ production, energy and exergy efficiencies, and rate of exergy destruction are presented for both 600 (low) and 1200 W/m² (high) irradiation levels. The optimum operating temperature is calculated to find the temperature where the H₂ production and energy and efficiencies are maximized and the exergy destruction is minimized.

a. Measured Current Results

The average values of the current measurement results at selected operating temperatures (20, 40, 60, and 80 °C) are presented in Figure 6.19. The average standard deviation in the current measurements is 0.001. The measured current values are increasing with increasing operating temperatures and increasing irradiation level. Since the voltage losses and electrical resistance of the reactor components are decreasing with the increasing operating temperatures, higher currents are measured at higher operating temperatures. The increase in current measurements with increasing irradiation level confirms that the Cu₂O coated membrane is responding to light and generating photocurrent.

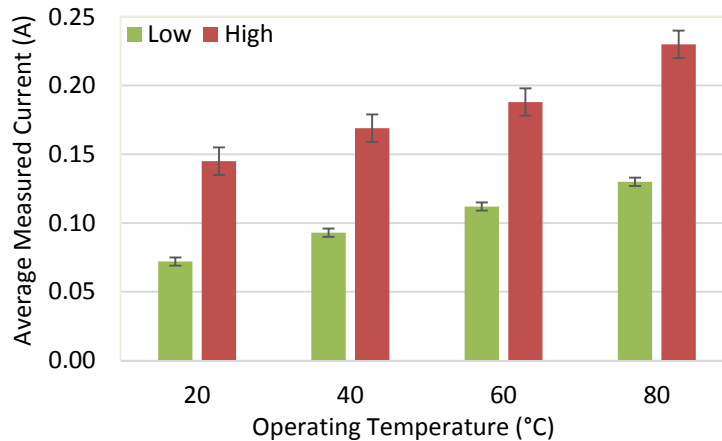


Figure 6.19 Effect of operating temperature on current measurement results (Process 2).

b. Hydrogen Production Results

The comparisons of the experimental and model H₂ production outputs at different operating temperatures and under two different light settings are presented in Figure 6.20. Each experimental run is repeated three times resulting an average standard deviation of 0.07 g/h for 600 W/m² irradiation and 0.10 g/h for 600 W/m² irradiation. As can be seen in Figure 6.20, the effect of the operating temperature on H₂ production is similar to the current measurement results presented in Figure 6.19. Because of the increasing conductivities and decreasing losses, the H₂ production increases at increasing operating temperatures. Also, the reactor is producing H₂ at higher rates with increasing irradiation.

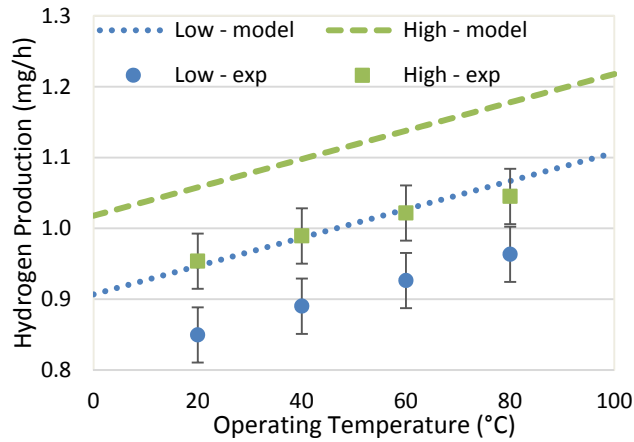


Figure 6.20 Effect of operating temperature on H₂ production with comparison of experimental and model outputs (Process 2).

Figure 6.20 also shows that the model outputs are showing a good agreement with the experimental results. Within the selected operating temperature interval, on average, the model predicts about 0.1 g/h higher H₂ production rate which corresponds to an average difference of 11%. This difference might be caused from the following assumptions (i) steady-state steady-flow, (ii) changes in kinetic and potential energies, (iii) heat losses to the environment; and (iv) conductivity losses in auxiliary components.

c. Energy Efficiency Results

The effect of the operating temperature on the energy efficiency of Process 2 is given in Figure 6.21. The experimental results show that when the operating temperature is increased from 20°C to 80°C, the energy efficiency decreases from about 18% to 12%

under 600 W/m^2 irradiation and from about 10% to 7% under 1200 W/m^2 irradiation. The reason of this decrease is the increasing heat input requirement with increasing operating temperatures which lowers the efficiency despite the fact that H_2 production is increasing with increasing operating temperatures. Each experimental run is repeated three times at each operating temperature and irradiation level resulting an average standard deviation of around 1%.

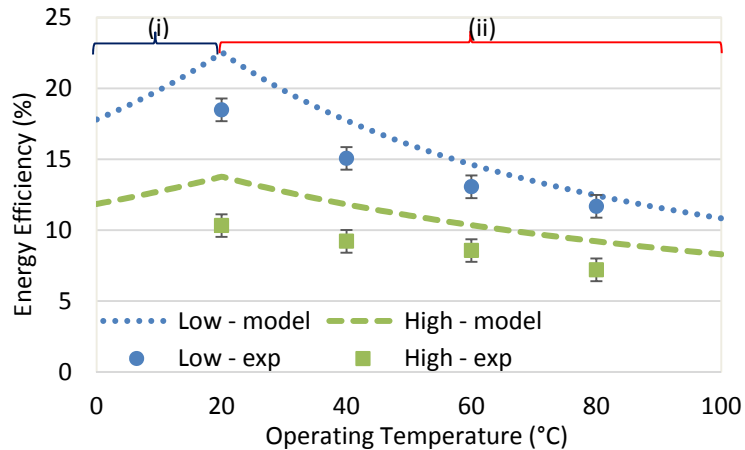


Figure 6.21 Effect of operating temperature on energy efficiency with comparison of experimental and model outputs (Process 2) – (i) cooling, (ii) heating.

From Figure 6.21, it can be seen that the energy efficiency shows different behaviors with respect to the operating temperature. The model states that the energy efficiency increases with operating temperatures up to 20°C and then starts decreasing. The reason of this change is the environmental temperature. As the environmental temperature is 20°C , operating at temperatures below 20°C requires cooling and heating is required to operate above 20°C . Within the selected operating temperature interval, the experimental results and model outputs are in good agreement. On average, the model predicts about 2% higher energy efficiency. The primary reason for this difference is the assumptions used when developing the thermodynamic and electrochemical models, as discussed earlier in this section.

d. Exergy Efficiency Results

Figure 6.22 shows the effect of the operating temperature on the exergy efficiency of Process 2. The experimental results show that when the operating temperature is increased

from 20°C to 80°C, the exergy efficiency decreases from 22% to 19% under 600 W/m² irradiation and from 13% to 10% under 1200 W/m² irradiation. Similar to the energy efficiency results, introduction and increase of the heat input lowers the exergy efficiency at increasing operating temperatures. Each experimental run is repeated three times at each operating temperature and irradiation level resulting an average standard deviation of around 1%.

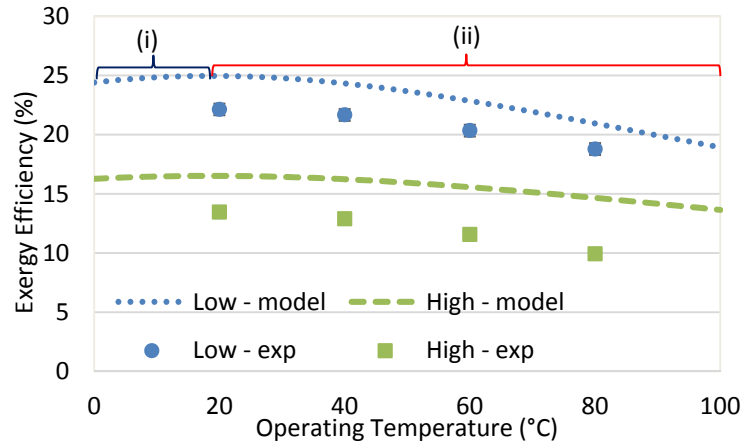


Figure 6.22 Effect of operating temperature on exergy efficiency with comparison of experimental and model outputs (Process 2) – (i) cooling, (ii) heating.

Similar to the energy efficiency results shown in Figure 6.21, the exergy efficiency increases with increasing operating temperatures up to 20°C and then starts decreasing after 20°C. As the environmental temperature is 20°C, operating below 20°C requires cooling and heating is needed to operate above 20°C. Within the selected operating temperature interval, the experimental results and the model outputs are in good agreement. Within the selected operating temperature interval, on average, the model predicts about 4% higher exergy efficiency. The main cause of this variance is the assumptions taken into account when developing the thermodynamic and electrochemical models, which are discussed earlier in this section.

e. Exergy Destruction Results

In addition to the current measurements, H₂ production, energy and exergy efficiencies; the rate of exergy destruction change within the selected operating temperature interval of 0°C - 100°C is presented in Figure 6.23. The lowest exergy destruction rate is observed at

20°C, which is about 0.03 W. The rate of exergy destruction under 1200 W/m² irradiation is slightly higher than that of under 600 W/m² irradiation, the difference in exergy destruction rates between two irradiation levels is around 0.005 W. At operating temperatures below 20°C, cooling is needed which increases the exergy destruction with decreasing operating temperatures. Conversely, to operate at temperatures above 20°C, heat input is required which also increases the exergy destruction with increasing operating temperatures.

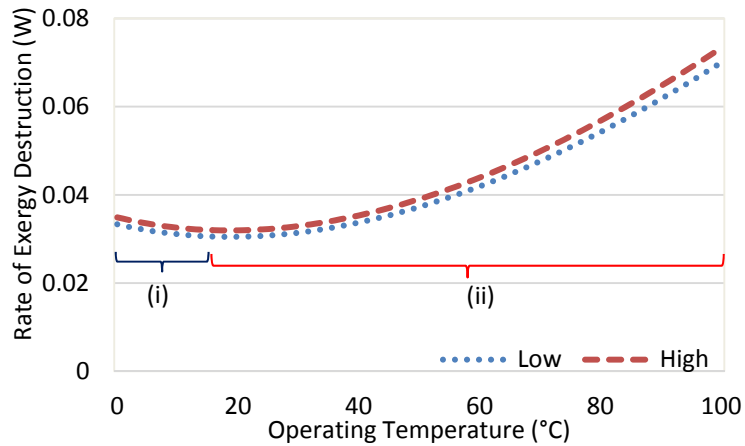


Figure 6.23 Effect of operating temperature on exergy destruction–model outputs (Process 2) – (i) cooling, (ii) heating.

f. Optimum Operating Temperature Results

In order to find the optimum operating temperature, the thermodynamic model results are normalized and ranked using Equations (6.1) and (6.2). The average normalized rankings of the H₂ production, energy and exergy efficiencies, and exergy destruction rates for Process 2 based on the thermodynamic model results are given in Figure 6.24. The selected operating temperature range for the optimum operating temperature investigation is 0-100°C. Figure 6.24 shows that the highest average rankings are observed at 20°C for both 600 W/m² and 1200 W/m² irradiation, which is 8/10. This means, within the selected operating temperature interval, the highest possible H₂ production and efficiencies and the lowest possible exergy destruction occur at 20°C. Therefore, for the upcoming analyses, 20°C is chosen to be the operating temperature.

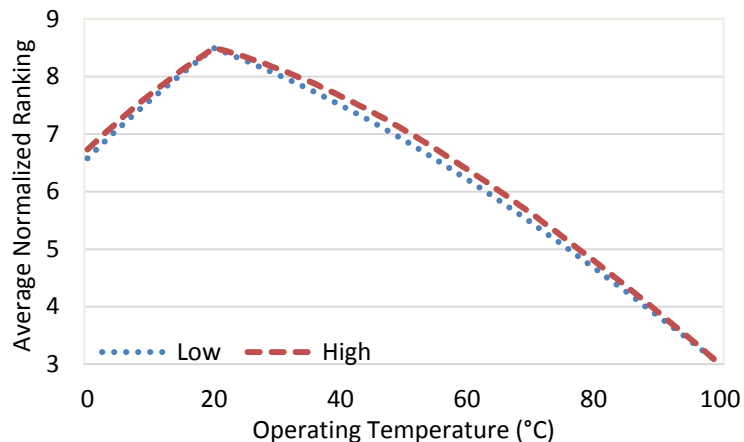


Figure 6.24 Average normalized rankings of H₂ production, efficiencies, and exergy destruction at different operating temperatures (Process 2).

6.2.2 Effect of Inlet Mass Flow Rate

The effect of the inlet mass flow rate is monitored under 2.5 V voltage and two different irradiation levels: 600 W/m² (low) and 1200 W/m² (high) and both the operating and environmental temperatures are set to 20°C. In this section, under three different inlet mass flow rates (0.25, 0.50, and 0.75 g/s), the measured current, H₂ production, energy and exergy efficiencies, and rate of exergy destruction are presented. In the end, optimum inlet mass flow rate is estimated to select the flow rate where the H₂ production and energy and efficiencies are maximized and the exergy destruction is minimized.

a. Measured Current Results

The average values of the current measurement results at selected inlet mass flow rates of 0.25, 0.50, and 0.75 g/s during the PEC experiments is presented in Figure 6.25. The average standard deviation in the current measurements is 0.001 A. Figure 6.21 shows that the current measurement increases with increasing inlet mass flow rates. The primary reason of this tendency is that with increasing flow rates, the consumed ions are replaced more frequently and this prevents from negative or positive ion accumulation. Positive or negative ion accumulation slows the redox reactions down and reduces the corresponding current generation due to ion replacement. Therefore, preventing and/or minimizing positive or negative ion replacement increases the current generation. Also, it can be seen

that the membrane is capable of generating photocurrent since the increase in irradiation causes an increase in the current measurement as well.

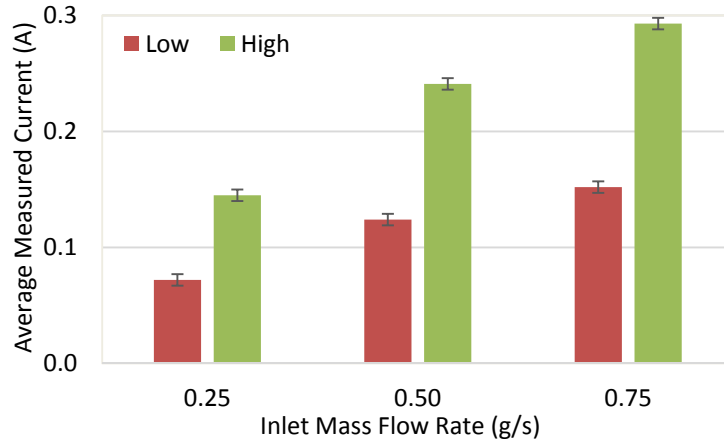


Figure 6.25 Effect of inlet mass flow rate on current measurements (Process 2).

b. Hydrogen Production Results

The experimental and model H₂ production outputs at different inlet mass flow rates are presented in Figure 6.26. Each experimental run is repeated three times at each inlet mass flow rate (0.25, 0.50, and 0.75 g/s) and irradiation level (600 and 1200 W/m²) resulting an average standard deviation of 0.1 g/h. Figure 6.26 shows that the effect of the inlet mass flow rate on the H₂ production is similar to the current measurement results presented in Figure 6.25.

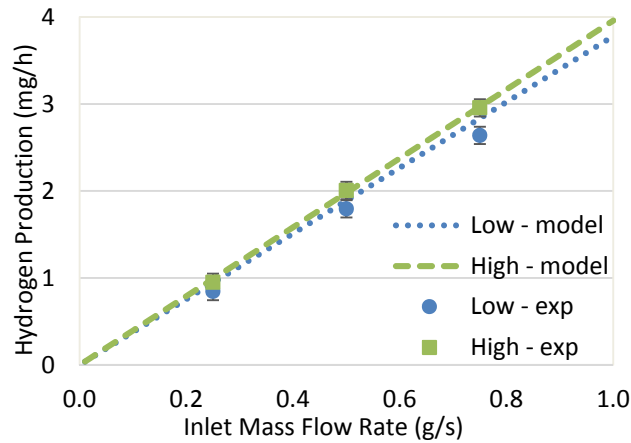


Figure 6.26 Effect of inlet mass flow rate on H₂ production with comparison of experimental and model outputs (Process 2).

In addition, Figure 6.26 points out that the model outputs are in a good agreement with the experimental results. Within the selected inlet mass flow rate interval, on average, the model predicts about 0.1 g/h more H₂ production which corresponds to an average difference of 5.5% for both 600 and 1200 W/m² irradiation. This difference might be caused by the assumptions of steady-state steady-flow, negligible kinetic and potential energy changes, heat losses to the environment; and conductivity losses in auxiliary components.

c. Energy Efficiency Results

The effect of the inlet mass flow rate on the energy efficiency of Process 2 is presented in Figure 6.27. The experimental results show that when the inlet mass flow rate is increased from 0.25 to 0.75 g/s, the energy efficiency increases from 18% to 20% under 600 W/m² irradiation and from 10% to 11% under 1200 W/m² irradiation. In contrast to Process 1 in which the energy efficiency decreases with increasing mass flow rates, in Process 2, the energy efficiency increases with flow rate. This could be because of the incoming photon energy reducing the load requirements by minimizing the losses. Each experimental run is repeated three times at each inlet mass flow rate (0.25, 0.50, and 0.75 g/s) and irradiation level (600 and 1200 W/m²) resulting an average standard deviation of around 0.7%.

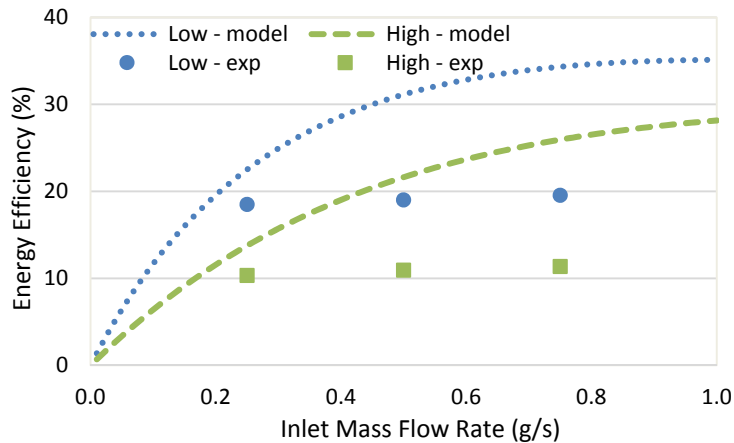


Figure 6.27 Effect of inlet mass flow rate on energy efficiency with comparison of experimental and model outputs (Process 2).

From Figure 6.27, it can be seen that the energy efficiency results of the experimental runs and model outputs have similar tendencies, which can be considered as

an acceptable level of agreement. Within the selected inlet mass flow rate interval, on average, the model predicts about 9% higher energy efficiency under 600 and 1200 W/m² irradiation. The primary reason for this difference is the assumptions used when developing the thermodynamic and electrochemical models, as discussed earlier in this section.

d. Exergy Efficiency Results

Figure 6.28 shows the effect of the inlet mass flow rate on the exergy efficiency in Process 2. The experimental findings show that when the inlet mass flow rate is increased from 0.25 to 0.75 g/s, the exergy efficiency increases from 20% to 22% under 600 W/m² irradiation and from 13% to 14% under 1200 W/m² irradiation. Similar to the energy efficiency results of Process 2, the incoming photon energy is reducing the load requirements by minimizing the losses. Each experimental run is repeated three times at each inlet mass flow rate (0.25, 0.50, and 0.75 g/s) and irradiation level (600 and 1200 W/m²) resulting an average standard deviation of around 1%.

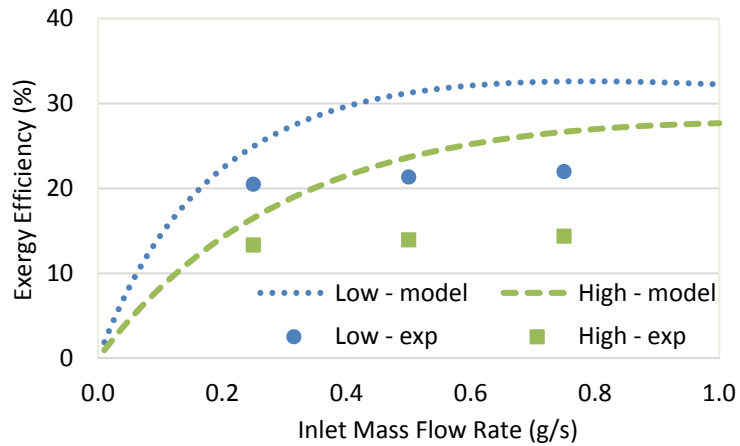


Figure 6.28 Effect of inlet mass flow rate on exergy efficiency with comparison of experimental and model outputs (Process 2).

The experimental runs take place at 0.25, 0.50, and 0.75 g/s inlet mass flow rates and within the selected inlet mass flow rate interval, the experimental results and model outputs have similar behaviors. Within the selected inlet mass flow rate interval, on average, the model predicts about 8% higher exergy efficiency. The main cause of this variance is the assumptions taken into account when developing the model, which are discussed earlier in this section.

e. Exergy Destruction Results

The effect of the inlet mass flow rate on the exergy destruction rate of Process 2 is presented in Figure 6.29. When evaluating the exergy destructions, the experimental results and the electrochemical and thermodynamic models are used together to evaluate the effect of the inlet mass flow rate on exergy destruction. Figure 6.29 shows that the lowest exergy destruction rate is observed at 0.1 g/s, which is about 0.003 W. With increasing inlet mass flow rates, the rate of exergy destruction increases due to increasing pump input and voltage requirements.

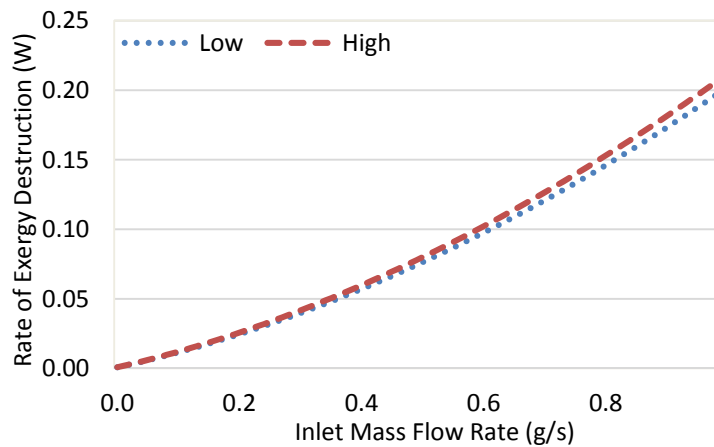


Figure 6.29 Effect of inlet mass flow rate on exergy destruction –model outputs (Process 2).

f. Optimum Inlet Mass Flow Rate Results

In order to find the optimum inlet flow rate, the thermodynamic model results are normalized and ranked using Equations (6.1) and (6.2). The average normalized rankings of H₂ production, energy and exergy efficiencies, and exergy destruction rates for Process 2 based on the thermodynamic model results are given in Figure 6.30. For the maximum possible H₂ production rate, energy and exergy efficiencies, and minimum possible exergy destruction, the optimum inlet mass flow rate is 0.70 g/s and 0.90 g/under 600 W/m² and 1200 W/m² irradiation, respectively.

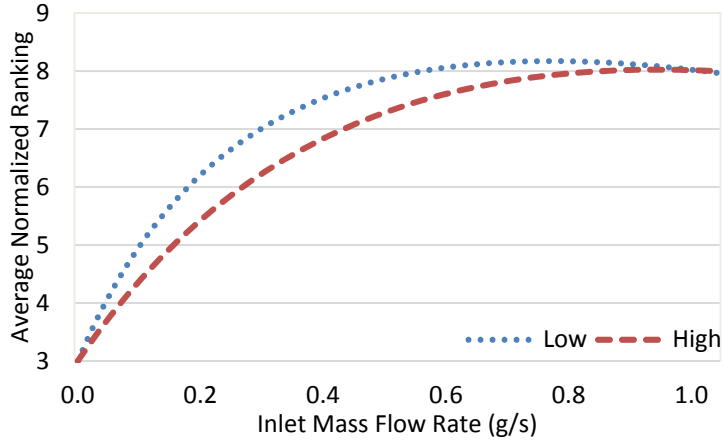


Figure 6.30 Average normalized rankings of H₂ production, efficiencies, and exergy destruction at different inlet mass flow rates (Process 2).

6.2.3 Effect of Environmental Temperature

The effect of the environmental temperature is investigated based on the thermodynamic model under 2.5 V applied voltage, 0.25 g/s inlet mass flow rate for both 600 and 1200 W/m² irradiation, and the operating temperature is 20°C. Within the selected environmental temperature interval of 0-40°C, the efficiencies and rate of exergy destruction of Process 2 under 600 W/m² irradiation are presented in Figure 6.31. Since the operating temperature is 20°C, the system needs heating at environmental temperatures below 20°C. Conversely, the system needs cooling at environmental temperatures above 20°C. Thus, 20°C gives the highest efficiencies and lowest exergy destruction.

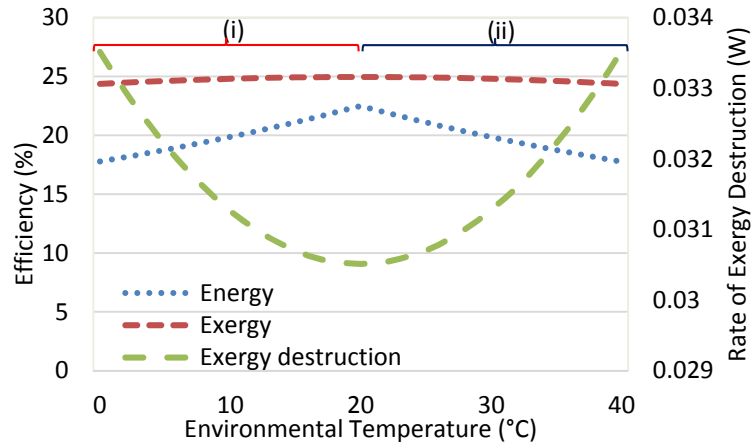


Figure 6.31 Effect of environmental temperature on exergy destruction and efficiencies under 600 W/m² irradiation (Process 2) – (i) heating, (ii) cooling.

Figure 6.32 demonstrates the energy and exergy efficiencies and rate of exergy destruction of Process 2 under 1200 W/m^2 irradiation. Since the operating temperature is 20°C , the system needs heating at environmental temperatures lower than 20°C . On the other hand, the system needs cooling at environmental temperatures higher than 20°C . As a result, 20°C gives the highest energy and exergy efficiencies and lowest exergy destruction within the selected environmental temperature interval. Therefore, the desired environmental temperature is 20°C for both 600 and 1200 W/m^2 irradiation.

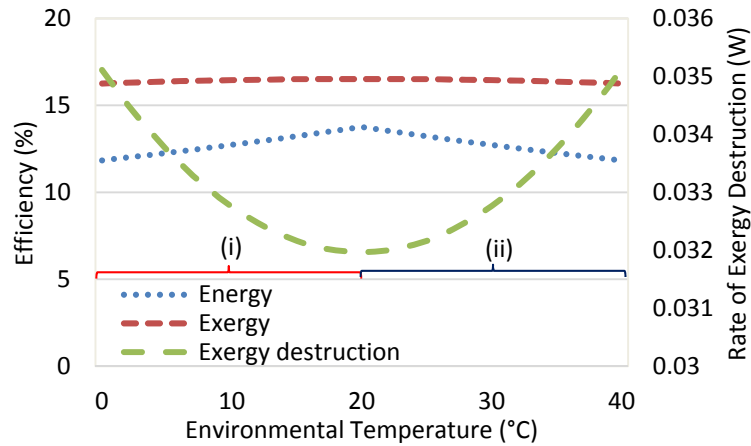


Figure 6.32 Effect of environmental temperature on exergy destruction and efficiencies under 1200 W/m^2 irradiation (Process 2) – (i) heating, (ii) cooling.

6.2.4 Coated Membrane Results

Figure 6.33 presents the current readings of the membrane before and after the Cu_2O coating process at three different potentials (2.5 , 3 , and 3.5 V) under 1200 W/m^2 irradiation in Process 2. From Figure 6.33, it can be seen that the Cu_2O coating causes an increase in current generation at selected applied potentials. As a result, it is concluded that the Cu_2O coating increases the light response (photocurrent generation) and the conductivity of the membrane, which gives higher current readings.

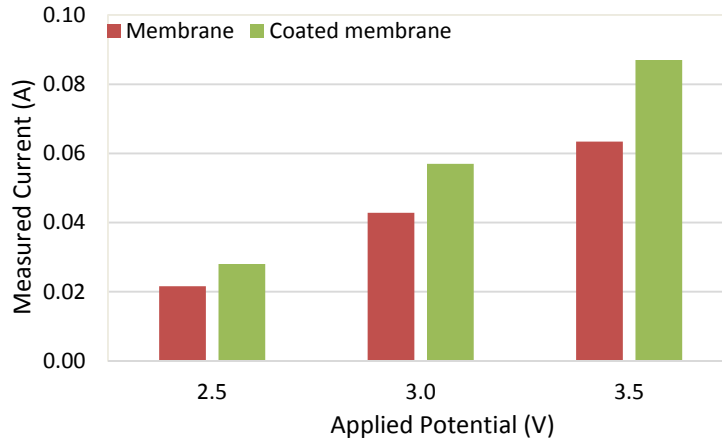


Figure 6.33 Effect of membrane coating on current measurements at different applied potentials under 1200 W/m² irradiation.

6.2.5 Uncertainty Analysis Results

The average uncertainty analysis results of Process 2 experiments are presented in Table 6.2. The highest uncertainty is observed in exergy efficiency calculations, which is around ± 7.98 and this amount is followed by energy efficiency calculations (± 6.46). Uncertainty in hydrogen production results, on average, is calculated to be ± 1.33 . And the uncertainty in current measurements is less than ± 1.00 (± 0.38).

Table 6.2 Summary of uncertainties during Process 2 experimental runs.

Type of result	Uncertainty (%)
Current	± 0.38
Hydrogen production	± 1.33
Energy efficiency	± 6.46
Exergy efficiency	± 7.98

6.2.6 Statistical Analysis Results

The statistical analysis of the Process 2 experimental results is conducted based on the Design of Experiments (DOE) approach. The agreement between DOE model and the actual data points and leverage residuals plot for the current, hydrogen production, and energy and exergy efficiencies for Process 2 are presented in Figures 6.34–6.37. The F-test is conducted to evaluate the impact of the three key input parameters on the current

generation, hydrogen production, and energy and exergy efficiencies in Process 2. These parameters are the operating temperature, inlet mass flow rate, and the irradiation level.

The detailed statistical analysis results of the current measurements of Process 2 is presented in Figure 6.34. The DOE model has a good agreement with the actual experimental data with a root mean square error of 0.0251. The standard error in current measurements is about 0.01. The F-test results show that the irradiation level has an F-ratio of 271.24, inlet mass flow rate has an F-ratio of 145.52, and the operating temperature has an F-ratio of 62.06. Therefore, it is concluded that the irradiation level has a higher impact on the current generation in Process 2 compared to the inlet mass flow rate and operating temperature.

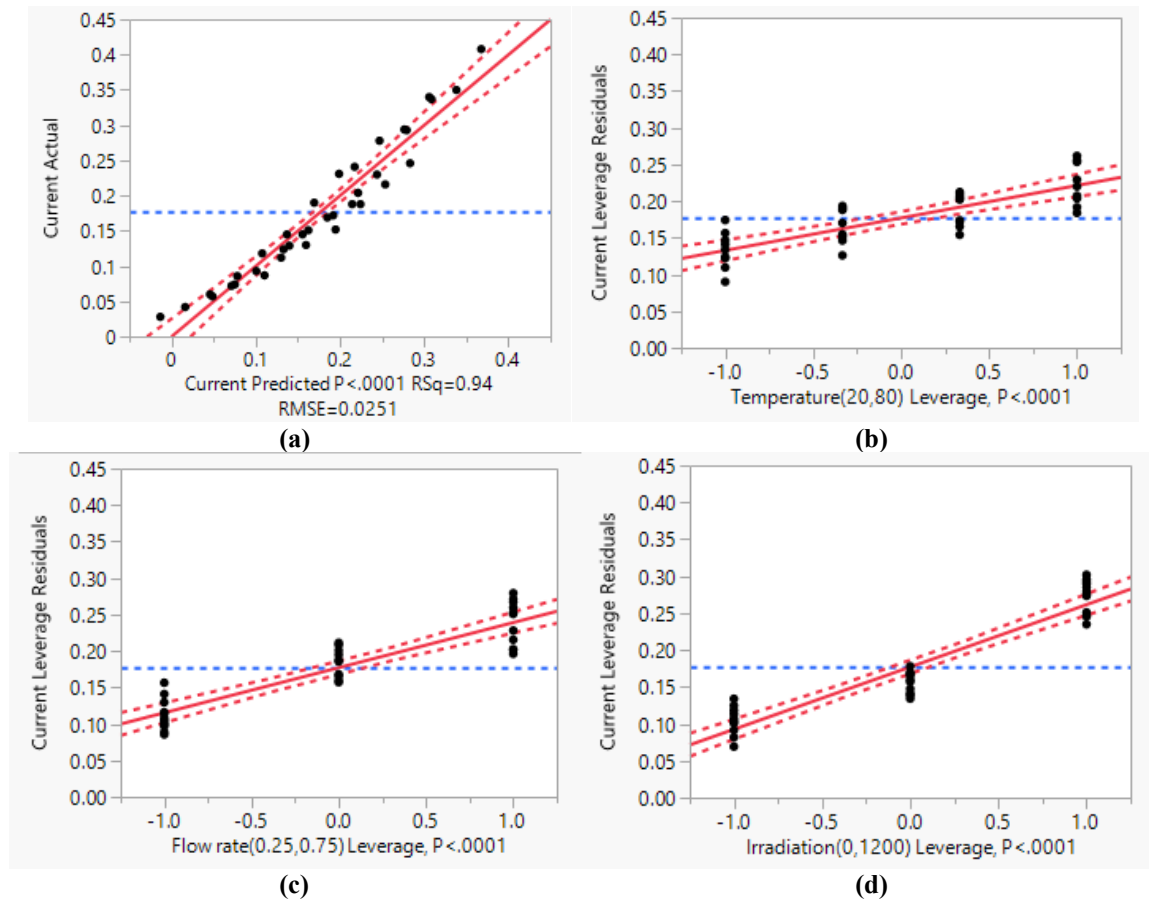


Figure 6.34 Results of (a) DOE model, (b) operating temperature leverage plot, (c) inlet mass flow rate leverage plot, and (d) irradiation level leverage plot of Process 2 experimental current measurements.

The comparison of the present experimental hydrogen production and the DOE model results along with the leverage residuals of Process 2 are provided in Figure 6.35.

The DOE model agrees with the actual experimental data with a root mean square error of 0.0001. The standard error in hydrogen production is less than 0.001, which is considered to be zero. The F-test results indicate that the inlet mass flow rate has an F-ratio of 4354.24, irradiation level has an F-ratio of 227.74, and the operating temperature has an F-ratio of 9.15. For that reason, it is determined that the inlet mass flow rate has a greater influence on the hydrogen production in Process 2 compared to the irradiation level and the operating temperature.

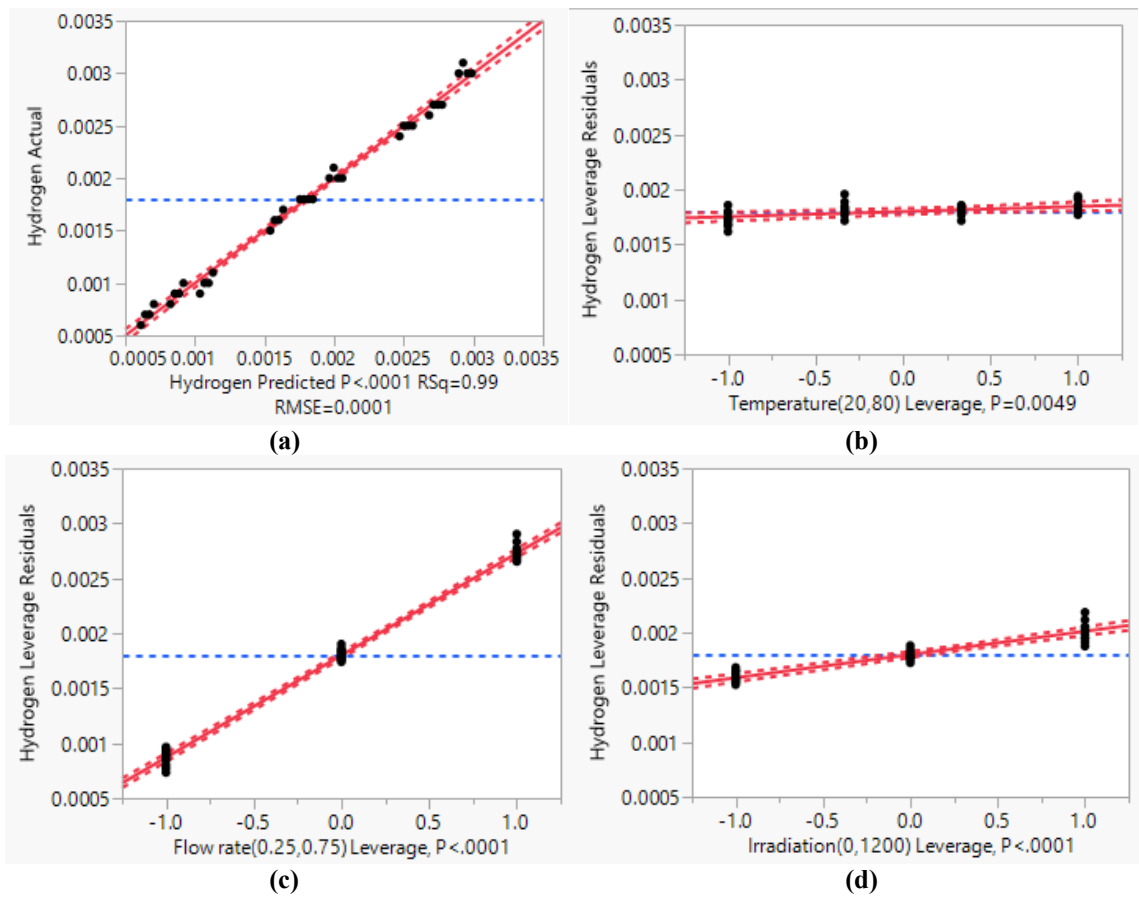


Figure 6.35 Results of (a) DOE model, (b) operating temperature leverage plot, (c) inlet mass flow rate leverage plot, and (d) irradiation level leverage plot of Process 2 experimental hydrogen production results.

Figure 6.36 shows the detailed statistical analysis of the energy efficiency results of Process 2. The DOE model has a satisfactory agreement with the actual experimental data with a root mean square error of 3.1642. The standard error in energy efficiency results is about 0.7. The F-test results present that the irradiation level has an F-ratio of 102.03, operating temperature has an F-ratio of 46.49, and the inlet mass flow rate has an F-ratio

of 0.41. As a result, it is concluded that the irradiation level has a higher impact on the energy efficiency in Process 2 compared to the operating temperature and inlet mass flow rate.

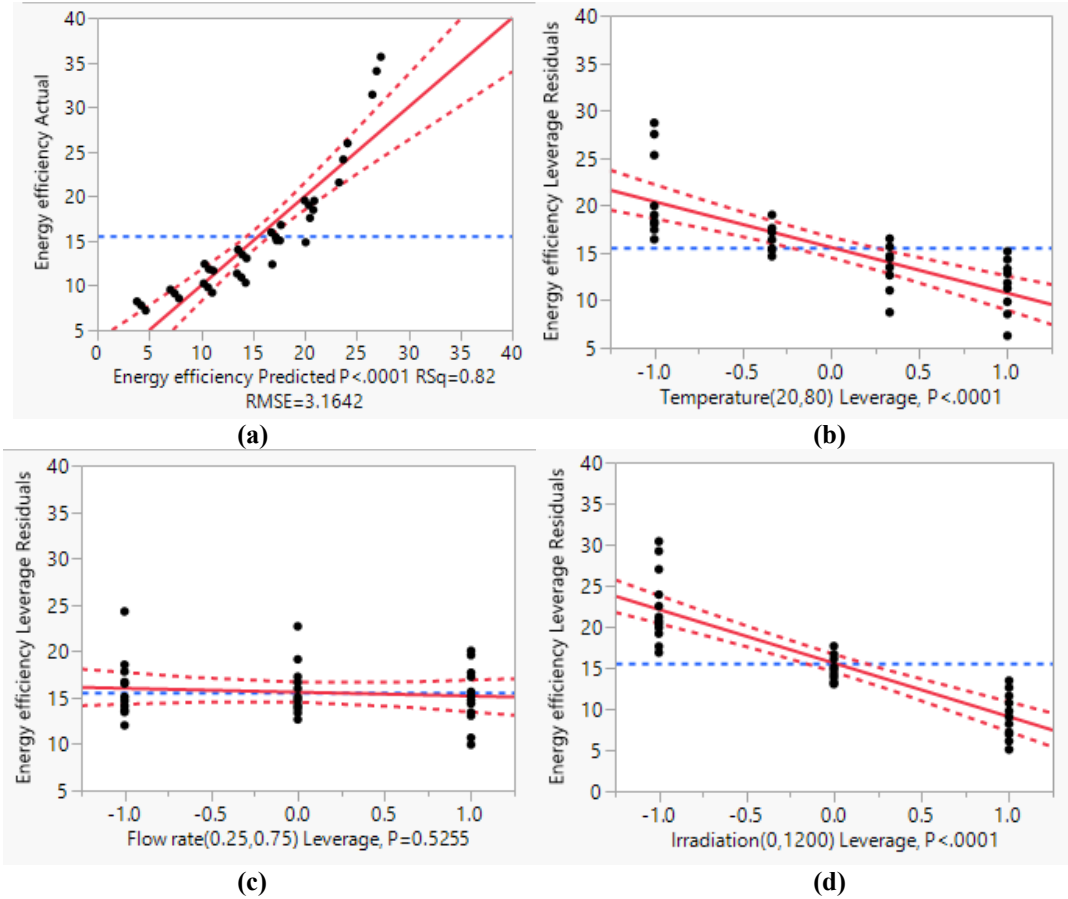


Figure 6.36 Results of (a) DOE model, (b) operating temperature leverage plot, (c) inlet mass flow rate leverage plot, and (d) irradiation level leverage plot of Process 2 experimental energy efficiency results.

Figure 6.37 shows the comparison of the present experimental exergy efficiency and the DOE model results along with the leverage residuals of Process 2. The DOE model agrees with the actual experimental data with a root mean square error of 2.9448. The standard error in exergy efficiency is about 0.60. The F-test results indicate that the irradiation level has an F-ratio of 114.21, operating temperature has an F-ratio of 51.18, and the inlet mass flow rate has an F-ratio of 0.27. For that reason, it is determined that the irradiation level has a greater influence on the exergy efficiency in Process 2 compared to the operating temperature and the inlet mass flow rate.

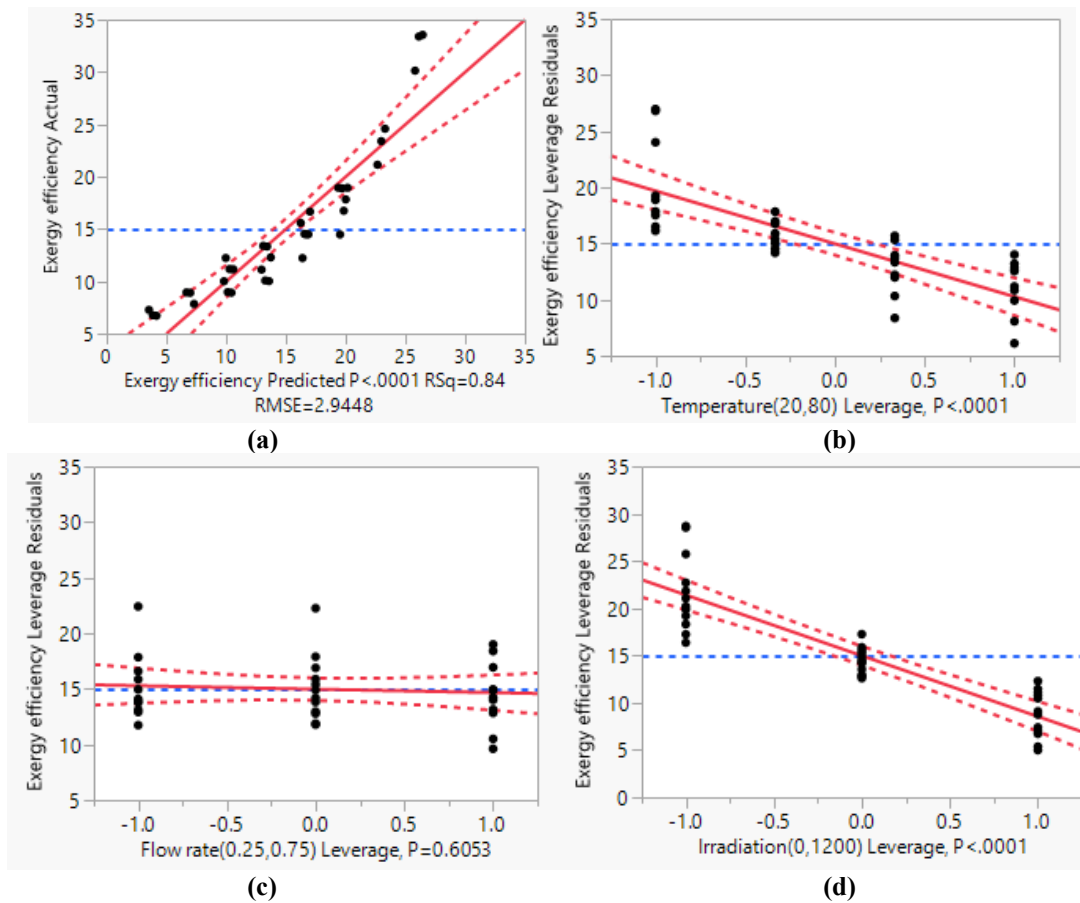


Figure 6.37 Results of (a) DOE model, (b) operating temperature leverage plot, (c) inlet mass flow rate leverage plot, and (d) irradiation level leverage plot of Process 2 experimental exergy efficiency results.

6.3 Process 3 – Chloralkali: Results and Discussion

In the chloralkali experiments, the hybrid reactor is tested under no simulated light conditions. Saturated NaCl solution and H₂O are fed to the anode and cathode, respectively. In this section, the effects of the operating temperature, inlet mass flow rate, and environmental temperature on the measured current, H₂ production, energy and exergy efficiencies, and exergy destruction are discussed. The optimum operating temperature, inlet mass flow rate, and environmental temperature are shown. In the end, the uncertainty and statistical analyses of Process 3 test results are provided.

6.3.1 Effect of Operating Temperature

The effect of the operating temperature is examined under 2.5 V applied voltage, 0.25 g/s inlet mass flow rate, and the environmental temperature is 20°C. Under four different operating temperatures (20, 40, 60, and 80°C), the measured current, H₂ production, energy and exergy efficiencies, and rate of exergy destruction are presented. In the end, the optimum operating temperature is assessed in order to find out the temperature where the H₂ production and energy and efficiencies are maximized and the exergy destruction is minimized.

a. Measured Current Results

The average current measurement results at the selected operating temperatures (20, 40, 60, and 80°C) during the chloralkali experiments is presented in Figure 6.38. The average standard deviation in the current measurements is 0.001 A. As can be seen in Figure 6.38, with increasing operating temperatures, the current measurements are increasing as well. The primary reason of this tendency is the increasing component conductivities. Since the voltage losses and electrical resistance of the reactor components are decreasing with the increasing operation temperature, higher currents are measured at higher temperatures.

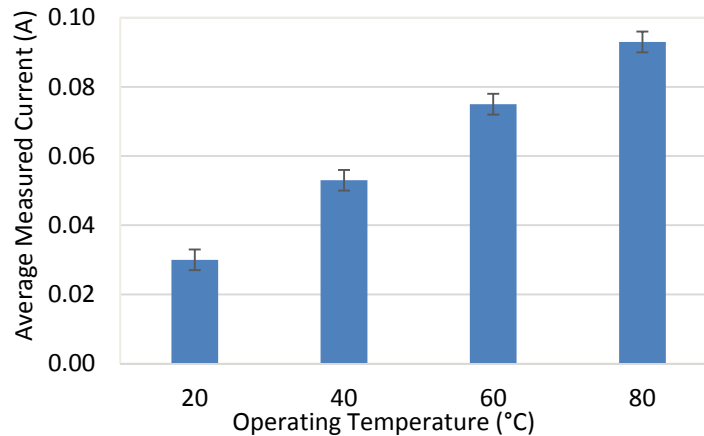


Figure 6.38 Effect of operating temperature on current measurement results (Process 3).

b. Hydrogen Production Results

The comparison of the experimental and model H₂ production outputs at different operating temperatures are presented in Figure 6.39. Each experimental run is repeated three times at

each temperature resulting an average standard deviation of 0.1 g/h. As can be seen in Figure 6.39, the effect of the operating temperature on H₂ production is similar to the effect of operating temperature on the current generation presented in Figure 6.30. With increasing conductivities and decreasing losses, the H₂ production increases with increasing temperatures.

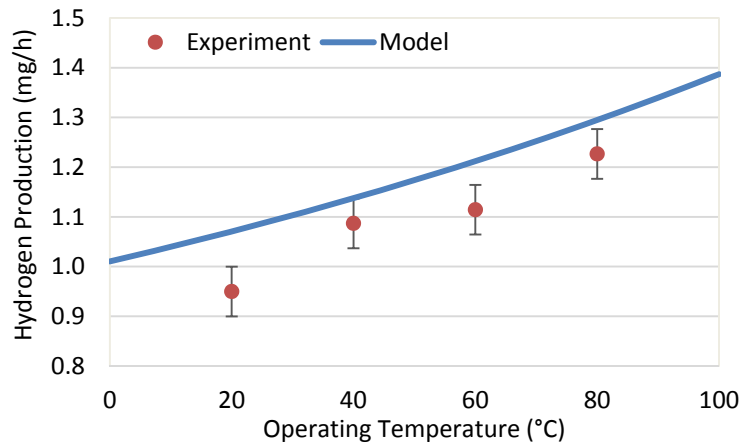


Figure 6.39 Effect of operating temperature on H₂ production with comparison of experimental and model outputs (Process 3).

Figure 6.39 also shows that the model outputs are in a good agreement with the experimental results. Within the selected operating temperature interval, on average, the model predicts about 0.1 g/h more H₂ production which corresponds to an average difference of 8%. This difference might be caused from the following assumptions (i) steady-state steady-flow, (ii) changes in kinetic and potential energies, (iii) heat losses to the environment; and (iv) conductivity losses in auxiliary components.

c. Energy Efficiency Results

The effect of the operating temperature on the energy efficiency for Process 3 is presented in Figure 6.40. The experimental results show that when the operating temperature is increased from 20°C to 80°C, the energy efficiency decreases from about 50 to 20%. The reason of this decrease is the introduction of heat input which lowers the efficiency despite the fact that H₂ production is increasing with increasing operating temperatures. Each experimental run is repeated three times at each temperature resulting an average standard deviation of around 2%.

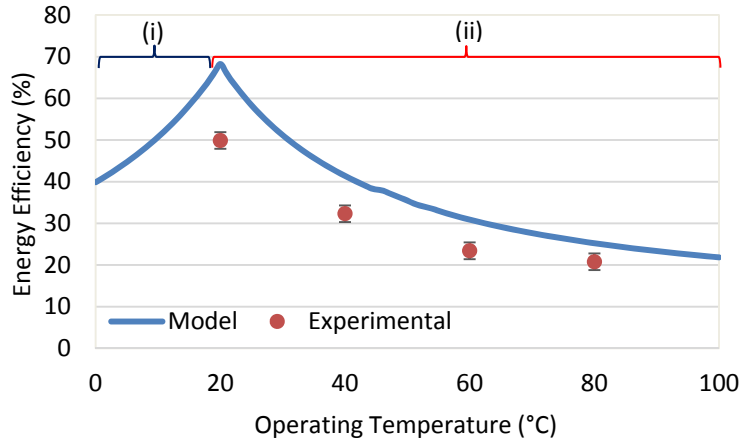


Figure 6.40 Effect of the operating temperature on energy efficiency with comparison of experimental and model outputs (Process 3) – (i) cooling, (ii) heating.

From Figure 6.40, it can be seen that the energy efficiency behaves differently with respect to the operating temperature. The model states that the energy efficiency increases with increasing operating temperatures up to 20°C and then starts decreasing after 20°C. The reason of this change is the environmental temperature. Since the environmental temperature is 20°C, operating at temperatures below 20°C require cooling and heating is required to operate at temperatures above 20°C. The experimental runs take place at 20, 40, 60, and 80°C and within the selected interval, the model outputs are in good agreement with the experiments. On average, the model predicts about 10% higher energy efficiency. The primary reason for this difference is the assumptions used when developing the thermodynamic and electrochemical models, as discussed earlier in this section.

d. Exergy Efficiency Results

Figure 6.41 shows the effect of the operating temperature on the exergy efficiency for Process 3. The experimental results show that when the operating temperature is increased from 20°C to 80°C, the exergy efficiency decreases from 38% to 29%. Similar to the energy efficiency results, higher heat input requirements lower the exergy efficiency at increasing operating temperatures. Each experimental run is repeated three times at each temperature resulting an average standard deviation of around 1%.

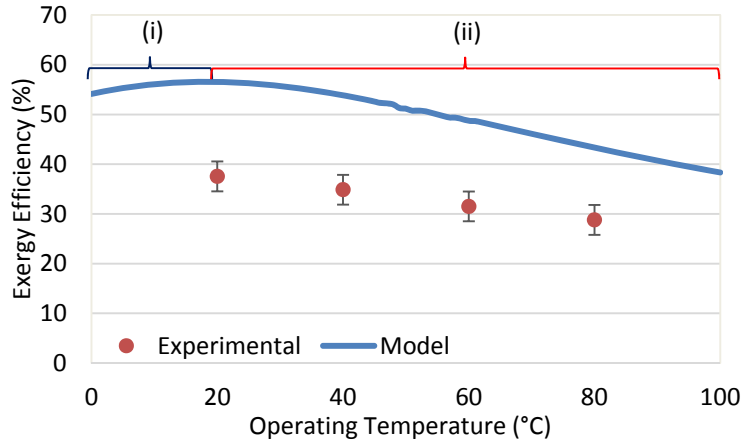


Figure 6.41 Effect of operating temperature on exergy efficiency with comparison of experimental and model outputs (Process 3) – (i) cooling, (ii) heating.

From Figure 6.41, it can be seen that the exergy efficiency increases with increasing operating temperatures up to 20°C and then starts decreasing after 20°C. The reason for this change is the environmental temperature. Since the environmental temperature is 20°C, operating at temperatures below 20°C requires cooling and heating is needed to operate at temperatures above 20°C. The experimental runs take place at 20, 40, 60, and 80°C and within the selected interval, the experimental results and the model outputs are in good agreement. On average, the model predicts about 17% higher exergy efficiency. The main cause of this variance is the assumptions taken into account when developing the thermodynamic and electrochemical models, which are discussed earlier in this section.

e. Exergy Destruction Results

The exergy destruction rate results of Process 3 within the operating temperature interval of 0°C - 100°C is presented in Figure 6.42. In the calculation of exergy destructions, the experimental results and the electrochemical and thermodynamic models are used together to evaluate the effect of the operating temperature on exergy destruction. Figure 6.42 shows that the lowest exergy destruction rate is observed at 0°C, which is about 0.03 W.

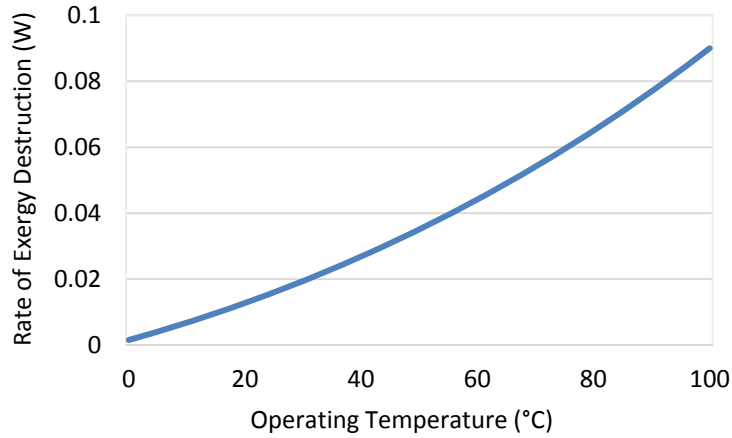


Figure 6.42 Effect of operating temperature on exergy destruction – model outputs (Process 3).

f. Optimum Operating Temperature Results

In order to find the optimum operating temperature, the thermodynamic model results are normalized and ranked using Equations (6.1) and (6.2). The normalized rankings of the H₂ production, energy and exergy efficiencies, and exergy destruction rates for Process 3 based on the thermodynamic model results are given in Figure 6.43 along with average rankings.

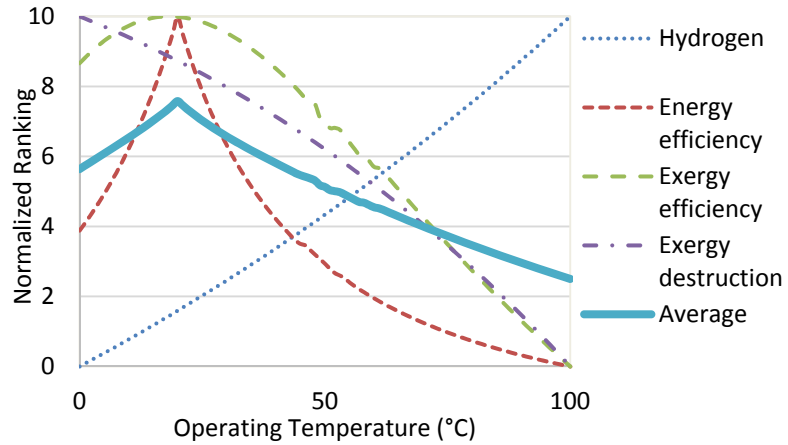


Figure 6.43 Normalized rankings of H₂ production, efficiencies, and exergy destruction at different operating temperatures (Process 3).

Figure 6.43 shows that the highest average ranking is observed at 20°C which is 7.58/10. This means that within the selected temperature interval, the highest possible H₂

production and efficiencies and the lowest possible exergy destruction occur at 20°C. Therefore, for the upcoming analyses, 20°C is chosen to be the operating temperature.

6.3.2 Effect of Inlet Mass Flow Rate

The effect of the inlet mass flow rate is monitored under 2.5 V applied voltage, and both the operating and environmental temperatures are 20°C. In this section, under three different inlet mass flow rates (0.25, 0.50, and 0.75 g/s), the measured current, H₂ production, energy and exergy efficiencies, and the rate of exergy destruction are presented. In the end, the optimum inlet mass flow rate is estimated to select the flow rate where the H₂ production and energy and efficiencies are maximized and the exergy destruction is minimized.

a. Measured Current Results

The average values of the measured current data results at selected inlet mass flow rates of 0.25, 0.50, and 0.75 g/s during the chloralkali experiments are presented in Figure 6.44. The average standard deviation in measured current is 0.003 A.

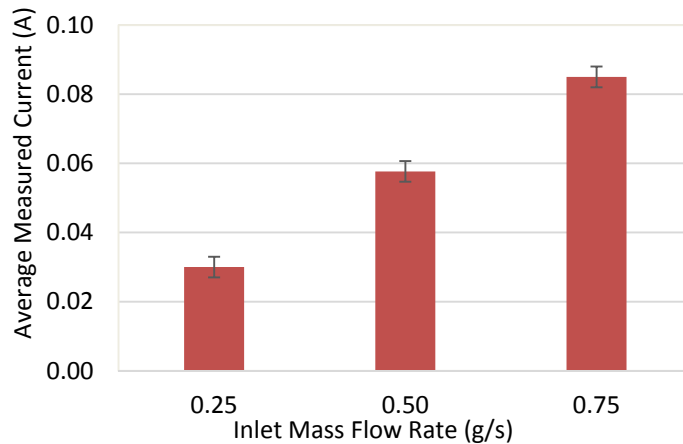


Figure 6.44 Effect of inlet mass flow rate on current measurement results (Process 3).

Figure 6.44 shows that the current measurements increase with increasing inlet mass flow rates. The primary reason of this tendency is that with increasing flow rates, the depleted ions are replaced more rapidly and this prevents from negative or positive ion accumulation. Positive or negative ion accumulation slows the redox reactions down and reduces the corresponding current generation due to ion replacement. Therefore,

preventing and/or minimizing positive or negative ion replacement increases the current generation.

b. Hydrogen Production Results

The experimental and model H₂ production outputs at different inlet mass flow rates are presented in Figure 6.45. Each experimental run is repeated three times at each inlet mass flow rate resulting an average standard deviation of 0.1 g/h. Figure 6.45 shows that the effect of the inlet mass flow rate on the H₂ production is similar to the current measurement results presented in Figure 6.44.

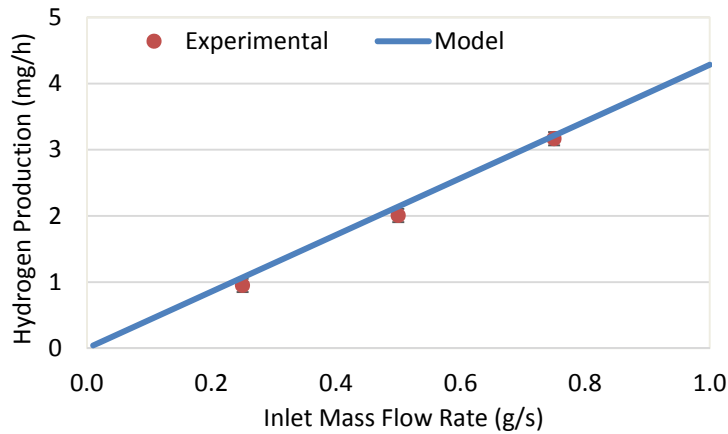


Figure 6.45 Effect of inlet mass flow rate on H₂ production with comparison of experimental and model outputs (Process 3).

In addition, Figure 6.45 indicates that the model outputs are in very good agreement with the experimental results. Within the selected inlet mass flow rate interval, on average, the model predicts about 0.1 g/h more H₂ production which corresponds to an average difference of 7%. This difference might be caused from the assumptions of steady-state steady-flow, negligible kinetic and potential energy changes, heat losses to the environment; and conductivity losses in auxiliary components.

c. Energy Efficiency Results

The effect of the inlet mass flow rate on the energy efficiency for Process 3 is presented in Figure 6.46. The experimental results show that when the inlet mass flow rate is increased from 0.25 to 0.75 g/s, the energy efficiency decreases from about 49% to 42%. The reason of this decrease is the increase in pump load and voltage requirements with increasing inlet

mass flow rates. Each experimental run is repeated three times at each inlet mass flow rate resulting an average standard deviation of around 1%.

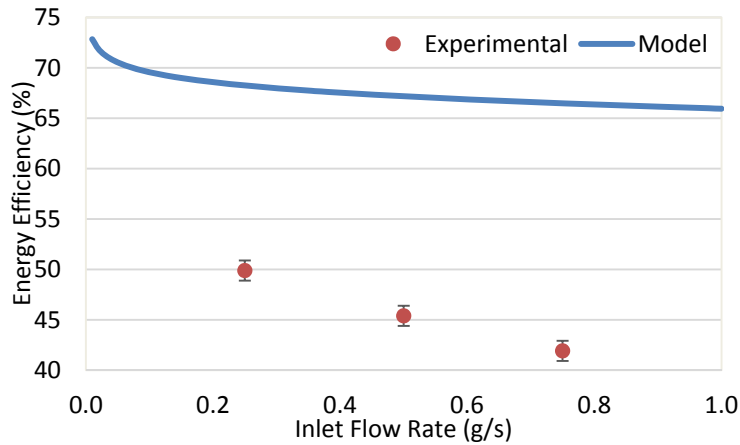


Figure 6.46 Effect of inlet mass flow rate on energy efficiency with comparison of experimental and model outputs (Process 3).

From Figure 6.46, it can be seen that the energy efficiency results of the experimental runs and the model outputs have similar tendencies, which can be considered as an acceptable level of agreement. Within the selected inlet mass flow rate interval of 0.25 to 0.75 g/s, on average, the model predicts about 22% higher energy efficiency. The primary reason for this difference is the assumptions used when developing the thermodynamic and electrochemical models, as discussed earlier in this section.

d. Exergy Efficiency Results

Figure 6.47 shows the effect of the inlet mass flow rate on the exergy efficiency of Process 3. The experimental results show that when the inlet mass flow rate is increased from 0.25 to 0.75 g/s, the exergy efficiency decreases from about 39% to 31%. Similar to the energy efficiency results, increasing pump input and voltage requirements lowers the exergy efficiency at increasing inlet mass flow rates. Each experimental run is repeated three times at each inlet mass flow rate resulting an average standard deviation of around 1%.

The experimental runs take place at 0.25, 0.50, and 0.75 g/s inlet mass flow rates and within the selected inlet mass flow rate interval, the experimental results and model outputs have similar behaviors. Within the selected interval, on average, the model predicts about 21% higher exergy efficiency. The main cause of this variance is the assumptions

taken into account when developing the thermodynamic and electrochemical models, which are discussed earlier in this section.

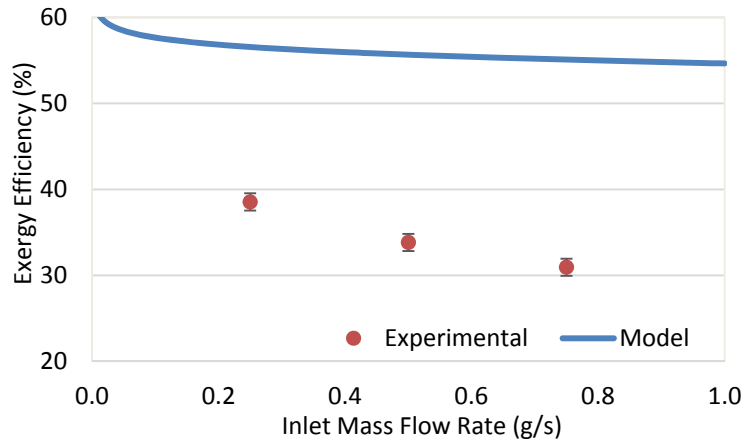


Figure 6.47 Effect of inlet mass flow rate on exergy efficiency with comparison of experimental and model outputs (Process 3).

e. Exergy Destruction Results

The effect of the inlet mass flow rate on the exergy destruction rate of Process 3 is presented in Figure 6.48. When evaluating the exergy destructions, the experimental results and the electrochemical and thermodynamic models are used together to evaluate the effect of the inlet mass flow rate on exergy destruction. Figure 6.48 shows that the lowest exergy destruction rate is observed at 0.1 g/s, which is about 0.003 W. With increasing inlet mass flow rates, the rate of exergy destruction increases due to increasing pump input and voltage requirements.

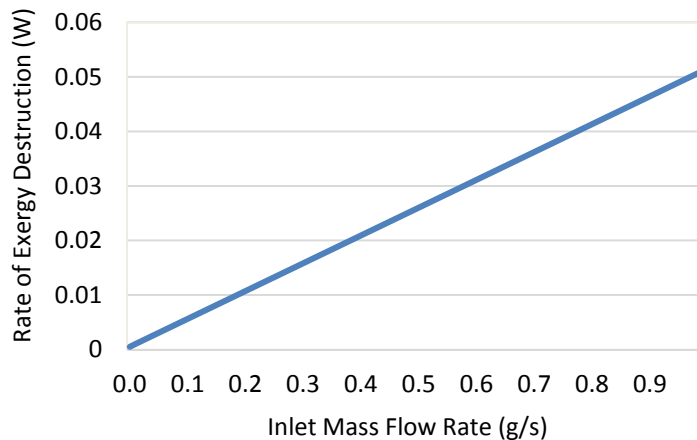


Figure 6.48 Effect of inlet mass flow rate on exergy destruction –model outputs (Process 3).

f. Optimum Inlet Mass Flow Rate Results

In order to find the optimum inlet mass flow rate, the thermodynamic model results are normalized and ranked using Equations (6.1) and (6.2). The normalized rankings of H₂ production, efficiencies, and exergy destruction rates for Process 3 based on the thermodynamic model results are given in Figure 6.49 along with their average rankings.

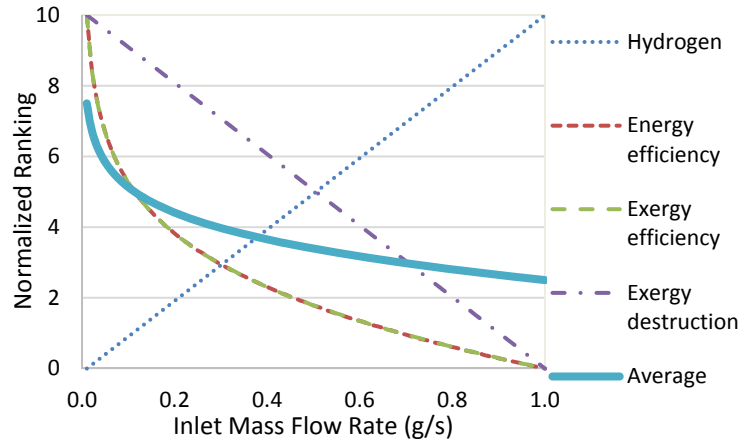


Figure 6.49 Normalized rankings of H₂ production, efficiencies, and exergy destruction at different inlet mass flow rates (Process 3).

Figure 6.49 shows that except the H₂ production rate, all other performance criteria have decreasing rankings with increasing inlet mass flow rates. As a result, the average ranking is decreasing with increasing inlet mass flow rates too. However, since 0 g/s inlet mass flow rate would mean zero H₂ production, and the aim is to produce H₂, an inlet mass flow rate of 0.25 g/s is selected and this flow rate provides an average ranking of 4.5/10, which is high enough and acceptable within the given inlet mass flow rate interval.

6.3.3 Effect of Environmental Temperature

The effect of the environmental temperature is investigated based on the thermodynamic model under 2.5 V applied voltage, 0.25 g/s inlet mass flow rate, and the operating temperature is 20°C. Within the selected environmental temperature interval of 0-40°C, the energy and exergy efficiencies and rate of exergy destruction of Process 3 are presented in Figure 6.50. Since the operating temperature is 20°C, the system needs heating at environmental temperatures below 20°C. On the other hand, the system needs cooling at

environmental temperatures above 20°C. As a result, 20°C gives the highest energy and exergy efficiencies and lowest exergy destruction within the selected environmental temperature interval of 0-40°C. Therefore, the desired environmental temperature is 20°C.

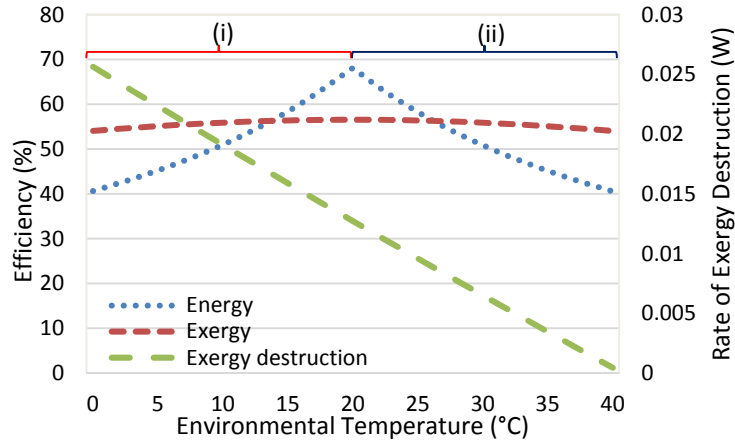


Figure 6.50 Effect of environmental temperature on exergy destruction and efficiencies (Process 3) – (i) heating, (ii) cooling.

6.3.4 Uncertainty Analysis Results

The average uncertainty analysis results of Process 3 experiments are presented in Table 6.3. The highest uncertainty is observed in exergy efficiency calculations, which is around ± 8.90 and this amount is followed by energy efficiency calculations (± 5.95). Uncertainty in hydrogen production results, on average, is calculated to be ± 1.25 . And the uncertainty in current measurements is less than ± 1.00 (± 0.81).

Table 6.3 Summary of uncertainties during Process 3 experimental runs.

Type of result	Uncertainty (%)
Current	± 0.81
Hydrogen production	± 1.25
Energy efficiency	± 5.95
Exergy efficiency	± 8.90

6.3.5 Statistical Analysis Results

The statistical analysis of the Process 3 experimental results is conducted based on the Design of Experiments (DOE) approach. The agreement between DOE model and the

actual data points and leverage residuals plot for the current, hydrogen production, and energy and exergy efficiencies for Process 3 are presented in Figures 6.51–6.54. The F-test is conducted to evaluate the impact of the two key input parameters on the current generation in Process 3. These parameters are the operating temperature and the inlet mass flow rate.

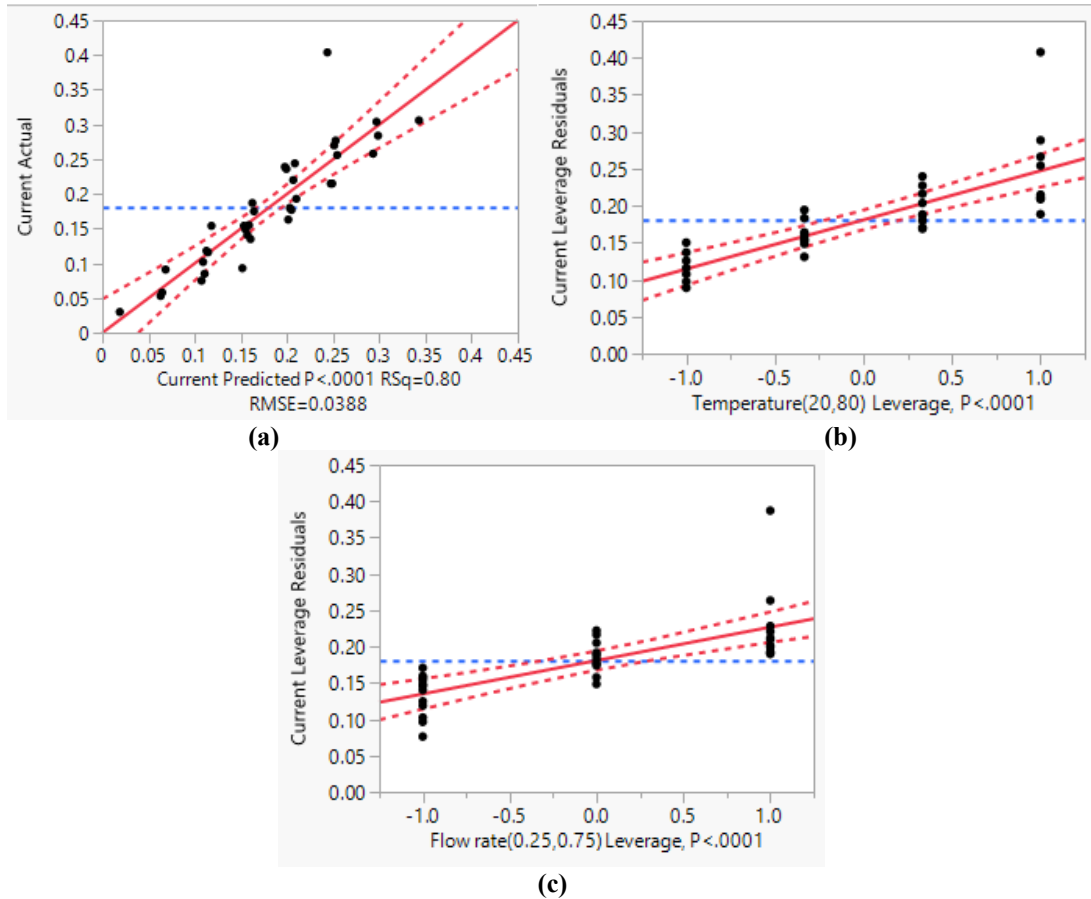


Figure 6.51 Results of (a) DOE model, (b) operating temperature leverage plot, and (c) inlet mass flow rate leverage plot of Process 3 experimental current measurements.

The detailed statistical analysis results of the current measurements of Process 3 is presented in Figure 6.51. The DOE model has a good agreement with the actual experimental data with a root mean square error of 0.0388. The standard error in current measurements is less than 0.001, which is considered as zero. The F-test results show that the operating temperature has an F-ratio of 58.50 and the inlet mass flow rate has an F-ratio of 33.09. Therefore, it is concluded that the operating temperature has a higher impact on the current generation in Process 3 compared to the inlet mass flow rate.

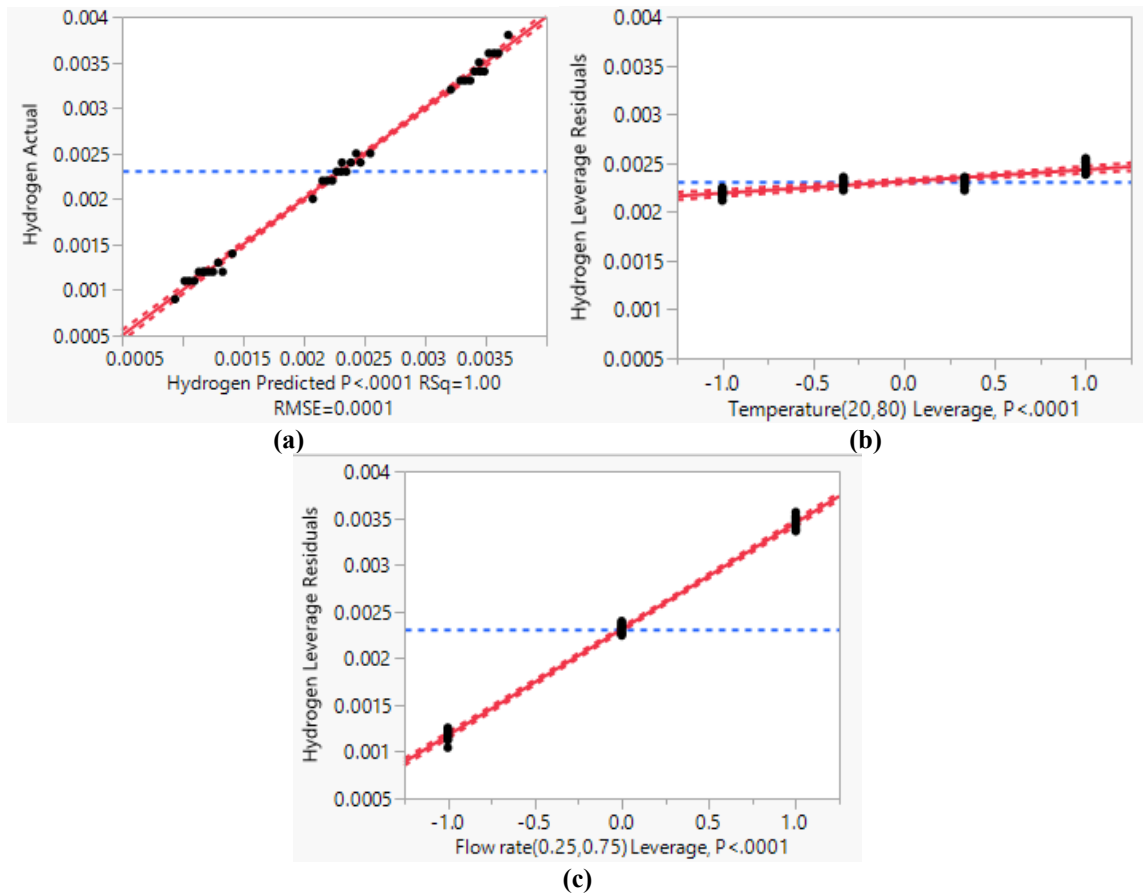


Figure 6.52 Results of (a) DOE model, (b) operating temperature leverage plot, and (c) inlet mass flow rate leverage plot of Process 3 experimental hydrogen production results.

The comparison of the present experimental hydrogen production and the DOE model results along with the leverage residuals of Process 3 are provided in Figure 6.52. The DOE model and experimental hydrogen production results comparison along with the leverage residuals of Process 3 are provided in Figure 6.52. The DOE model agrees with the actual experimental data with a root mean square error of 0.0001. The standard error in hydrogen production is less than 0.001, which is considered to be zero. The F-test results indicate that the inlet mass flow rate has an F-ratio of 9275.06 and the operating temperature has an F-ratio of 86.02. For that reason, it is determined that the inlet mass flow rate has a greater influence on the hydrogen production in Process 3 compared to the operating temperature.

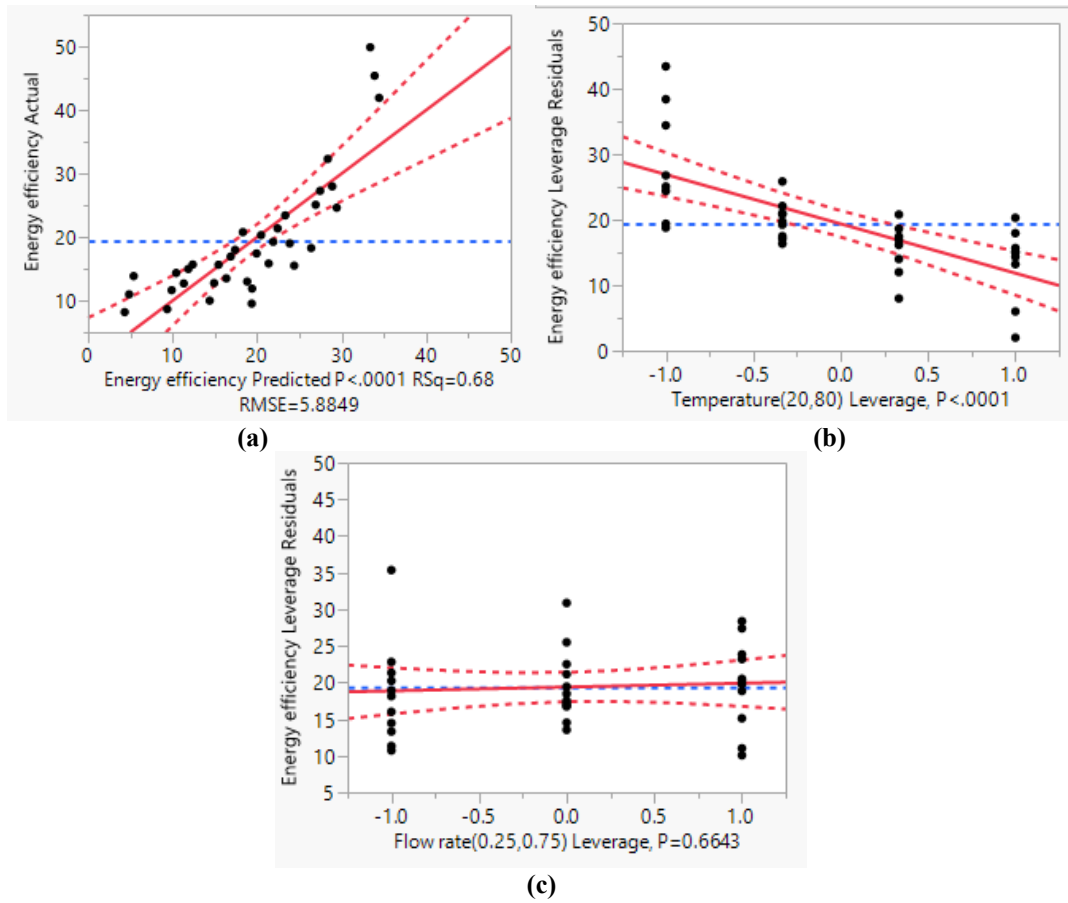


Figure 6.53 Results of (a) DOE model, (b) operating temperature leverage plot, and (c) inlet mass flow rate leverage plot of Process 3 experimental energy efficiency results.

Figure 6.53 shows the detailed statistical analysis of the energy efficiency results of Process 3. The DOE model has a satisfactory agreement with the actual experimental data with a root mean square error of 5.8849. The standard error in energy efficiency results is about 1.25. The F-test results present that the operating temperature has an F-ratio of 32.80 and the inlet mass flow rate has an F-ratio of 0.19. As a result, it is concluded that the operating temperature has a higher impact on the energy efficiency in Process 3 compared to the inlet mass flow rate.

Figure 6.54 shows the comparison of the present experimental exergy efficiency and the DOE model results along with the leverage residuals of Process 3. The DOE model and experimental exergy efficiency results comparison along with the leverage residuals of Process 3 are provided in Figure 6.54. The DOE model agrees with the actual experimental data with a root mean square error of 6.1182. The standard error in exergy efficiency is

about 1.30. The F-test results indicate that the operating temperature has an F-ratio of 28.21 and the inlet mass flow rate has an F-ratio of 0.34. For that reason, it is determined that the operating temperature has a greater influence on the exergy efficiency in Process 3 compared to the inlet mass flow rate.

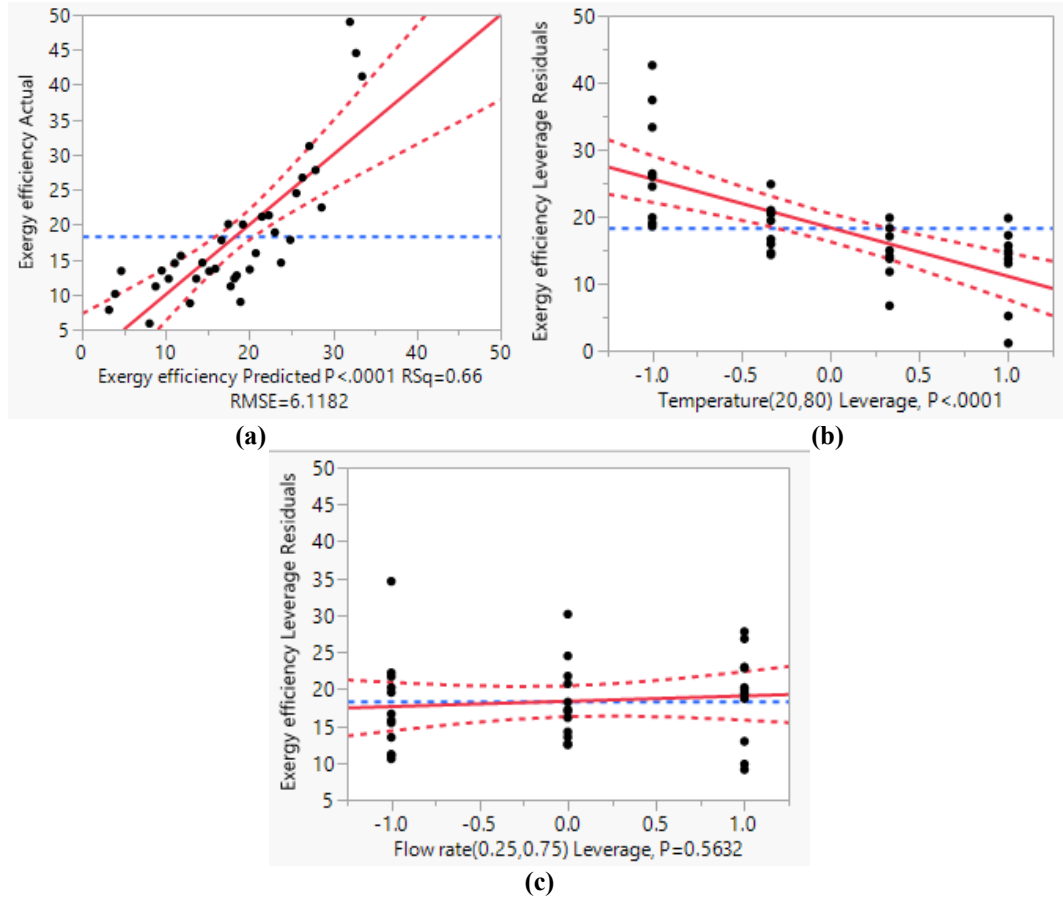


Figure 6.54 Results of (a) DOE model, (b) operating temperature leverage plot, and (c) inlet mass flow rate leverage plot of Process 3 experimental exergy efficiency results.

6.4 Process 4 – Photoelectrochemical-Chloralkali: Results and Discussion

In the PEC-chloralkali experiments, the hybrid reactor is investigated under two irradiation levels: 600 W/m² (low) and 1200 W/m² (high). Saturated NaCl solution and H₂O are fed to the anode and cathode, respectively. In this section, the effects of the operating temperature, inlet mass flow rate, and environmental temperature on the measured current, H₂ production, energy and exergy efficiencies, and exergy destruction are discussed in detail. The optimum operating temperature, inlet mass flow rate, and environmental

temperature are presented as well. And last but not least, the uncertainty and statistical analyses of Process 4 test results are provided.

6.4.1 Effect of Operating Temperature

The effect of the operating temperature is investigated under 2.5 V applied voltage, 0.25 g/s inlet mass flow rate, and the environmental temperature is 20°C. Under four different operating temperatures (20, 40, 60, and 80°C), the measured current, H₂ production, energy and exergy efficiencies, and rate of exergy destruction are presented for both 600 W/m² (low) and 1200 W/m² (high) irradiation levels. In the end, the optimum operating temperature is calculated in order to determine the temperature where the H₂ production and energy and efficiencies are maximized and the exergy destruction is minimized.

a. Measured Current Results

The average values of the current measurement results at operating temperatures (20, 40, 60, and 80 °C) during the during the PEC-chloralkali experiments is presented in Figure 6.55. The average standard deviation in the current measurements is 0.002 A. The current measurements are higher at elevated operating temperatures and irradiation levels. The voltage losses and electrical resistance of the reactor components are decreasing with the increasing operation temperatures, higher currents are measured at higher operating temperatures. The increase in current measurements with increasing irradiation level confirms that the Cu₂O coated membrane is responding generating photocurrent.

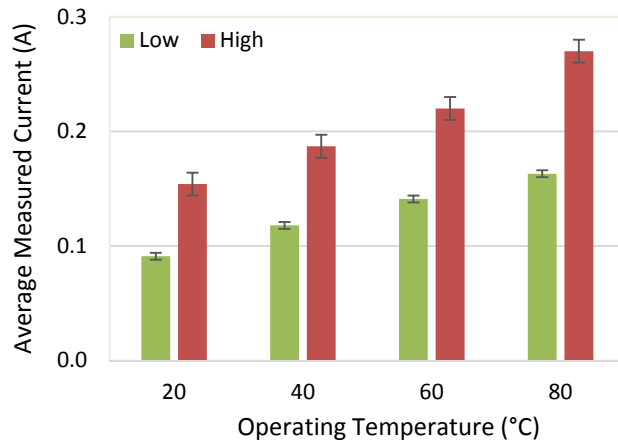


Figure 6.55 Effect of operating temperature on the current measurement results (Process 4).

b. Hydrogen Production Results

The comparisons of the experimental and model H₂ production outputs at different operating temperatures and under two different light settings are presented in Figure 6.56. Each experimental run is repeated three times at each operating temperature and each light setting resulting an average standard deviation of 0.09 g/h for 600 W/m² irradiation and 0.05 g/h for 600 W/m² irradiation. As can be seen from Figure 6.56, the effect of the operating temperature on H₂ production is similar to current measurement results presented in Figure 6.55. Because of the increasing conductivities and decreasing losses, the H₂ production increases with increasing operating temperatures. Also, the reactor is producing H₂ at higher rates with increasing irradiation.

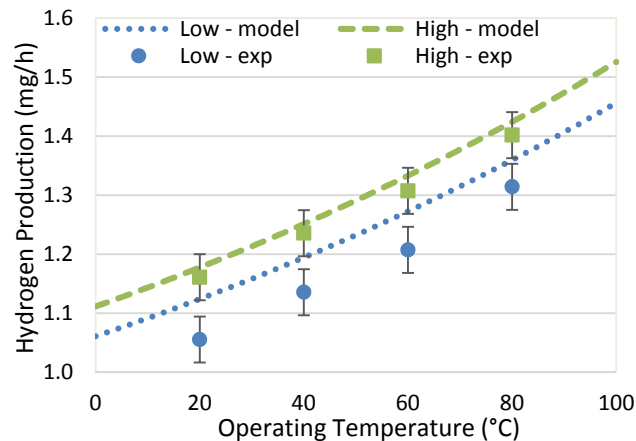


Figure 6.56 Effect of operating temperature on H₂ production with comparison of experimental and model outputs (Process 4).

Figure 6.56 also shows that the model outputs are showing a good agreement with the experimental results. Within the selected operating temperature interval, on average, the model predicts about 0.1 g/h more H₂ production which corresponds to an average difference of 3%. This difference might be caused by (i) transition state flows, (ii) changes in kinetic and potential energies, (iii) heat losses to the environment; and (iv) conductivity losses in auxiliary components.

c. Energy Efficiency Results

The effect of the operating temperature on the energy efficiency for Process 4 is given in Figure 6.57. The experimental results show that when the operating temperature is

increased from 20°C to 80°C, the energy efficiency decreases from about 18% to 13% under 600 W/m² irradiation and from about 12% to 8% under 1200 W/m² irradiation. The reason of this decrease is the increasing heat input requirement with increasing operating temperatures which lowers the efficiency despite the fact that H₂ production is increasing with increasing operating temperatures. Each experimental run is repeated three times at each operating temperature and irradiation level resulting an average standard deviation of around 1%.

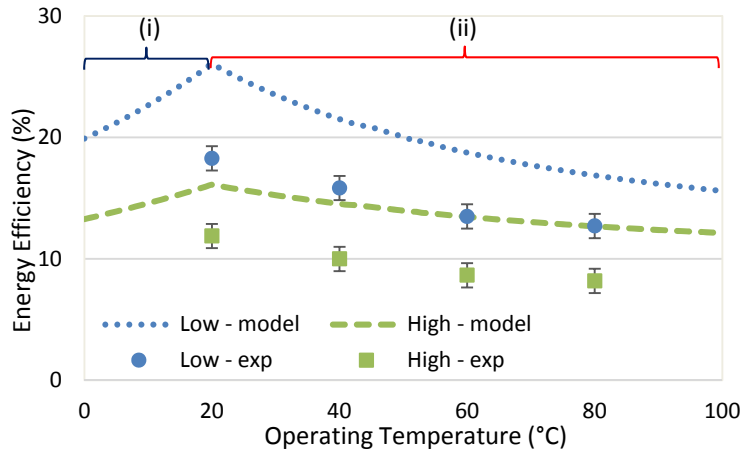


Figure 6.57 Effect of operating temperature on energy efficiency with comparison of experimental and model outputs (Process 4) – (i) cooling, (ii) heating.

From Figure 6.57, it can be seen that the energy efficiency shows different behaviors with respect to the operating temperature. The model states that the energy efficiency increases with increasing operating temperatures up to 20°C and then starts decreasing after 20°C. The reason for this change is the environmental temperature. As the environmental temperature is 20°C, operating at temperatures below 20°C requires cooling and heating is required to operate above 20°C. Within the selected temperature interval, the experimental results and model outputs are in good agreement. On average, the model predicts about 6% higher energy efficiency. The primary reason for this difference is the assumptions used when developing the thermodynamic and electrochemical models, as discussed earlier in this section.

d. Exergy Efficiency Results

Figure 6.58 shows the effect of the operating temperature on the exergy efficiency of Process 4. The experimental results show that when the operating temperature is increased from 20°C to 80°C, the exergy efficiency decreases from about 24% to 22% under 600 W/m² irradiation and from about 15% to 11% under 1200 W/m² irradiation. . Similar to the energy efficiency results, introduction and increase of the heat input lowers the exergy efficiency at increasing operating temperatures. Each experimental run is repeated three times at each operating temperature and irradiation level resulting an average standard deviation of around 1%.

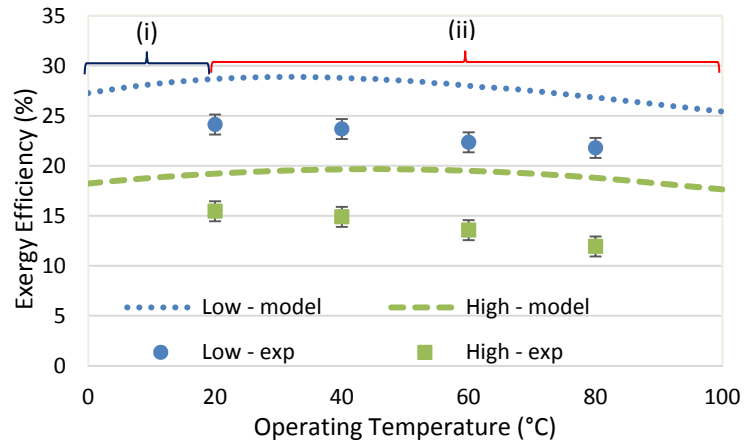


Figure 6.58 Effect of operating temperature on exergy efficiency with comparison of experimental and model outputs (Process 4) – (i) cooling, (ii) heating.

Similar to the energy efficiencies shown in Figure 6.58, the exergy efficiency increases with increasing operating temperatures up to 20°C and then starts decreasing after 20°C. As the environmental temperature is 20°C, operating below 20°C requires cooling and heating is needed to operate above 20°C. Within the selected operating temperature interval, the experimental results and model outputs are in good agreement. Within the selected operating temperature interval, on average, the model predicts about 5% higher exergy efficiency. The main cause of this variance is the assumptions taken into account when developing the thermodynamic and electrochemical models, which are discussed earlier in this section.

e. Exergy Destruction Results

The rate of exergy destruction change within the operating temperature interval of 0°C - 100°C is presented in Figure 6.59. The lowest exergy destruction rate is observed at 0°C, which is about 0.03 W. The rate of exergy destruction under 1200 W/m² irradiation is slightly higher than that of under 600 W/m² irradiation, the difference in exergy destruction rates between two irradiation levels is around 0.005 W.

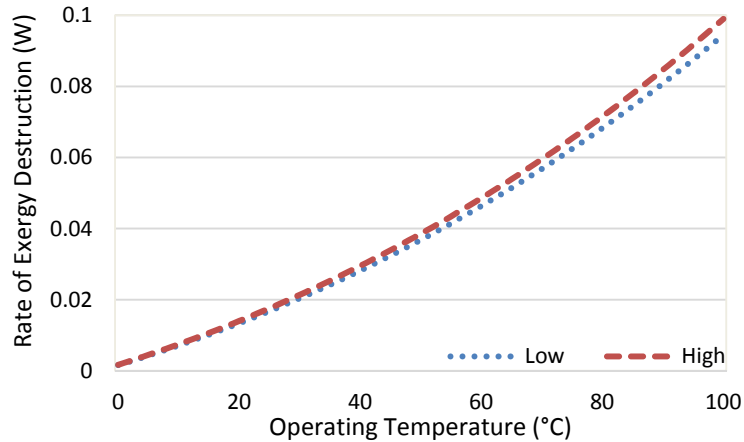


Figure 6.59 Effect of operating temperature on exergy destruction –model outputs (Process 4).

f. Optimum Operating Temperature Results

In order to find the optimum operating temperature, the thermodynamic model results are normalized and ranked using Equations (6.1) and (6.2). The average normalized rankings of the H₂ production, energy and exergy efficiencies, and exergy destruction rates for Process 4 based on the thermodynamic model results are given in Figure 6.60. The selected operating temperature range for the optimum operating temperature investigation is 0-100°C.

Figure 6.60 shows that the highest average rankings are observed at 20°C for both 600 and 1200 W/m² irradiation. The average normalized rankings at 20°C under 600 and 1200 W/m² irradiation are 7.44/10 and 7.02/10, respectively. Hence, within the selected interval, the highest possible H₂ production and efficiencies and lowest possible exergy destruction occur at 20°C. Therefore, 20°C is chosen to be the operating temperature.

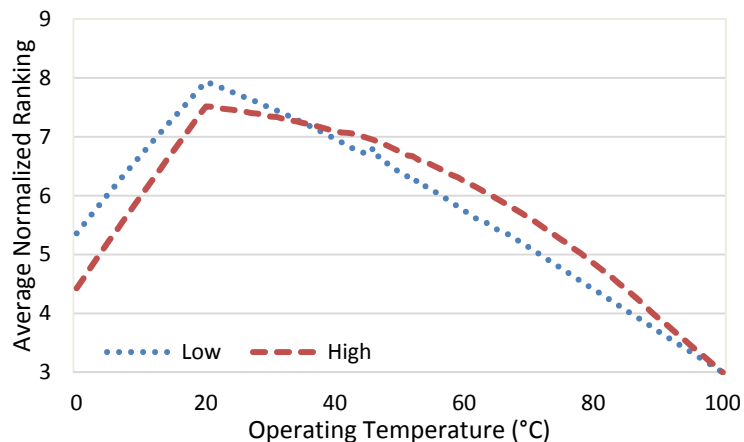


Figure 6.60 Average normalized rankings of H₂ production, efficiencies, and exergy destruction at different operating temperatures (Process 4).

6.4.2 Effect of Inlet Mass Flow Rate

The effect of the inlet mass flow rate is studied under 2.5 V applied voltage, and two different irradiation levels: 600 (low) and 1200 W/m² (high). Both the operating and environmental temperatures are 20°C. In this section, under three different mass flow rates, the measured current, H₂ production, energy and exergy efficiencies, and exergy destruction rates are presented. The optimum flow rate is estimated to find the flow rate where H₂ the production and energy and efficiencies are maximized and the exergy destruction is minimized.

a. Measured Current Results

Figure 6.61 shows the effect of the inlet mass flow rate on the current readings during Process 4 experiments. The average standard deviation in measured current is 0.001 A. Figure 6.61 shows that the current readings increase with increasing inlet mass flow rates. The primary reason of this tendency is that with increasing flow rates, the consumed ions are replaced more rapidly and this prevents from negative or positive ion accumulation. Positive or negative ion accumulation slows the redox reactions down and reduces the corresponding current generation due to ion replacement. Therefore, preventing and/or minimizing positive or negative ion replacement increases the current generation. Also, it can be seen that the membrane is capable of generating photocurrent since the increase in irradiation causes an increase in the current measurement as well.

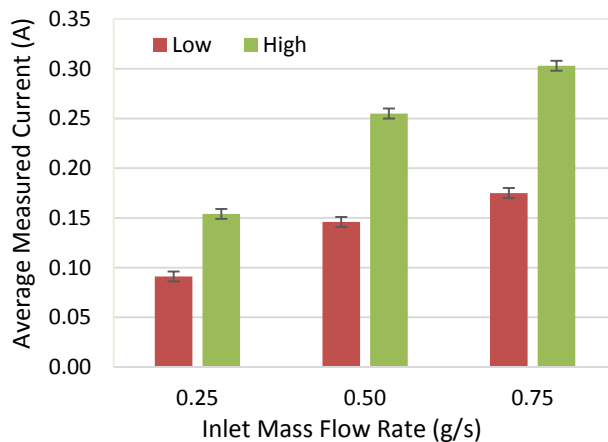


Figure 6.61 Effect of inlet mass flow rate on measured current (Process 4).

b. Hydrogen Production Results

The experimental and model H₂ production outputs at different inlet mass flow rates are presented in Figure 6.62. Each experimental run is repeated three times at each inlet mass flow rate (0.25, 0.50, and 0.75 g/s) and irradiation level (600 and 1200 W/m²) resulting an average standard deviation of 0.1 g/h. Figure 6.50 shows that the effect of the inlet mass flow rate on H₂ production is similar to the current measurement results presented in Figure 6.61.

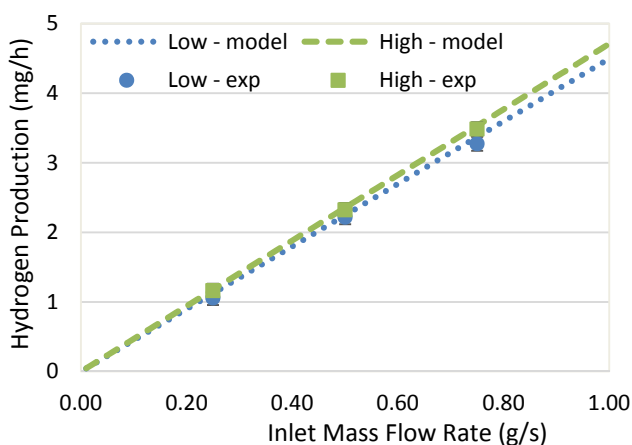


Figure 6.62 Effect of inlet mass flow rate on H₂ production with comparison of experimental and model outputs (Process 4).

Furthermore, Figure 6.62 points out that the model outputs are in a good agreement with the experimental results. Within the selected inlet mass flow rate interval, on average,

the model predicts about 0.1 g/h more H₂ production which corresponds to an average difference of 2.5% for both 600 and 1200 W/m² irradiation. This difference might be caused by the assumptions of steady-state steady-flow, negligible kinetic and potential energy changes, heat losses to environment; and conductivity losses in auxiliary components.

c. Energy Efficiency Results

The effect of the inlet mass flow rate on the energy efficiency of Process 4 is presented in Figure 6.63. The experimental results show when the inlet mass flow rate is increased from 0.25 to 0.75 g/s, the energy efficiency increases from 18% to 27% under 600 W/m² and from 12% to 20% under 1200 W/m² irradiation. Contrary to Process 3 in which the energy efficiency decreases with increasing flow rates, in Process 4, the energy efficiency increases with flow rate. Incoming photon energy could be reducing the load demand by minimizing the losses. Each experimental run is repeated three times at each inlet mass flow rate and irradiation level resulting an average standard deviation of around 1%.

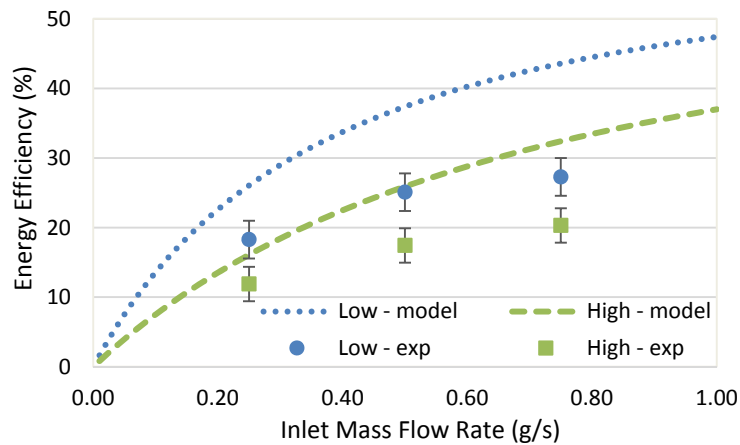


Figure 6.63 Effect of inlet mass flow rate on energy efficiency with comparison of experimental and model outputs (Process 4).

From Figure 6.63, it can be seen that the energy efficiency results of the experimental runs and model outputs have similar tendencies, which can be considered as an acceptable level of agreement. Within the selected inlet mass flow rate interval, on average, the model predicts about 10% higher energy efficiency under 600 and 1200 W/m²

irradiation. The primary reason for this difference is the assumptions used when developing the thermodynamic and electrochemical models, as discussed earlier in this section.

d. Exergy Efficiency Results

Figure 6.64 shows the effect of the inlet mass flow rate on the exergy efficiency in Process 4. The experimental results show that when the inlet mass flow rate is increased from 0.25 to 0.75 g/s, the exergy efficiency increases from 22% to 26% under 600 W/m² and from 14% to 21% under 1200 W/m² irradiation. Similar to the energy efficiency results, the incoming photon energy is reducing the load requirements by minimizing the losses. Each experimental run is repeated three times at each inlet mass flow rate and irradiation level resulting an average standard deviation of 1%.

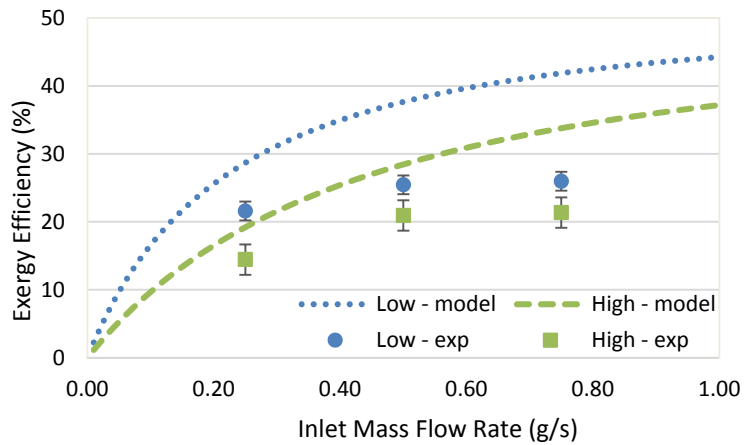


Figure 6.64 Effect of inlet mass flow rate on exergy efficiency with comparison of experimental and model outputs (Process 4).

The experimental runs take place at 0.25, 0.50, and 0.75 g/s inlet mass flow rates and within the selected inlet mass flow rate interval, the experimental results and model outputs have similar behaviors. Within the selected inlet mass flow rate interval, on average, the model predicts about 10% higher exergy efficiency. The main cause of this variance is the assumptions taken into account when developing the thermodynamic and electrochemical models, which are discussed earlier in this section.

e. Exergy Destruction Results

The effect of the inlet mass flow rate on the exergy destruction rate of Process 4 is presented in Figure 6.65. When evaluating the exergy destructions, the experimental results and the

electrochemical and thermodynamic models are used together to evaluate the effect of the inlet mass flow rate on exergy destruction. Figure 6.65 shows that the lowest exergy destruction rate is observed at 0.1 g/s, which is about 0.003 W. With increasing inlet mass flow rates, the rate of exergy destruction increases due to increasing pump input and voltage requirements.

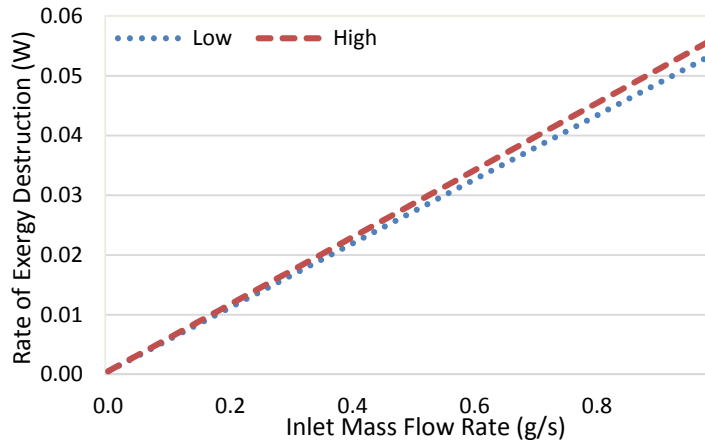


Figure 6.65 Effect of inlet mass flow rate on exergy destruction –model outputs (Process 4).

f. Optimum Inlet Mass Flow Rate Results

In order to find the optimum inlet mass flow rate, the thermodynamic model results are normalized and ranked based on Equations (6.1) and (6.2). The average normalized rankings of the H₂ production, energy and exergy efficiencies, and exergy destruction rates for Process 4 based on the thermodynamic model results are given in Figure 6.66.

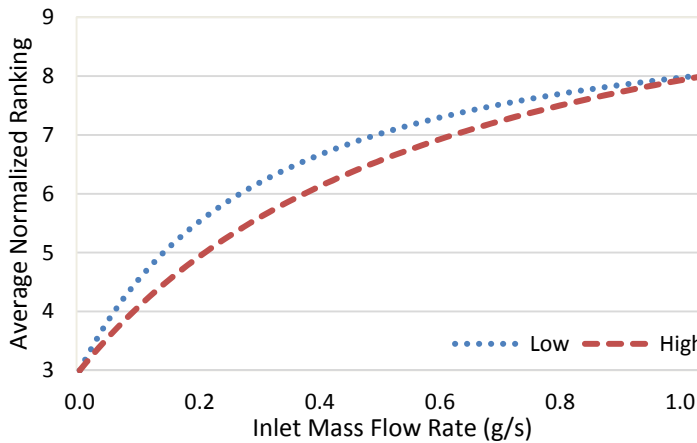


Figure 6.66 Average normalized rankings of H₂ production, efficiencies, and exergy destruction at different inlet mass flow rates (Process 4).

In order to have the maximum possible H₂ production rate, energy and exergy efficiencies, and minimum possible exergy destruction rate, the optimum inlet mass flow rate under 600 W/m² is about 0.90 g/s and this amount is 0.92 g/s for 1200 W/m² irradiation.

6.4.3 Effect of Environmental Temperature

The effect of the environmental temperature is investigated under 2.5 V applied voltage, 0.25 g/s inlet mass flow rate for both 600 and 1200 W/m² irradiation, and the operating temperature is 20°C. Within the selected environmental temperature interval of 0-40°C, the efficiencies and rate of exergy destruction of Process 4 under 600 W/m² irradiation are presented in Figure 6.67. Since the operating temperature is 20°C, the system needs heating at environmental temperatures below 20°C. Conversely, the system needs cooling at environmental temperatures above 20°C. Thus, 20°C gives the highest efficiencies and lowest exergy destruction.

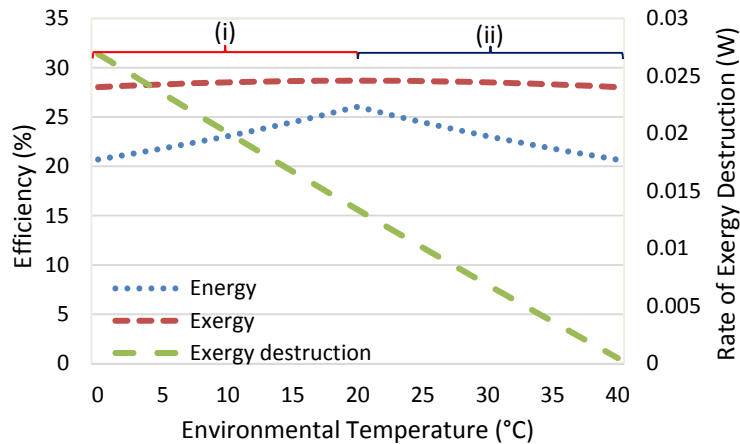


Figure 6.67 Effect of environmental temperature on exergy destruction and efficiencies under 600 W/m² irradiation (Process 4) – (i) heating, (ii) cooling.

Figure 6.68 shows the energy and exergy efficiencies and exergy destruction of Process 4 under 1200 W/m² irradiation. Since the operating temperature is 20°C, the system needs heating at environmental temperatures below 20°C. And it needs cooling at environmental temperatures above 20°C. As a result, 20°C gives the highest energy and exergy efficiencies and lowest exergy destruction within the selected interval. Therefore, the desired environmental temperature is 20°C for both 600 and 1200 W/m² irradiation.

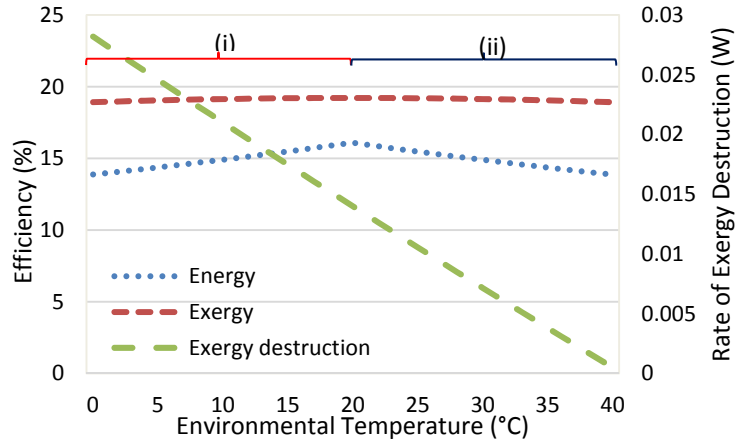


Figure 6.68 Effect of environmental temperature on exergy destruction and efficiencies under 1200 W/m² irradiation (Process 4) – (i) heating, (ii) cooling.

6.4.4 Uncertainty Analysis Results

The average uncertainty analysis results of Process 4 experiments are presented in Table 6.4. The highest uncertainty is observed in exergy efficiency calculations, which is around ± 8.51 and this amount is followed by energy efficiency calculations (± 6.78). Uncertainty in hydrogen production results, on average, is calculated to be ± 1.45 . And the uncertainty in current measurements is less than ± 1.00 (± 0.43).

Table 6.4 Summary of uncertainties during Process 4 experimental runs.

Type of result	Uncertainty (%)
Current	± 0.43
Hydrogen production	± 1.45
Energy efficiency	± 6.78
Exergy efficiency	± 8.51

6.4.5 Statistical Analysis Results

The statistical analysis of the Process 4 experimental results is conducted based on the Design of Experiments (DOE) approach. The agreement between DOE model and the actual data points and leverage residuals plot for the current, hydrogen production, and energy and exergy efficiencies for Process 4 are presented in Figures 6.69–6.72. The F-test is conducted to evaluate the impact of the three key input parameters on the current

generation in Process 4. These parameters are the operating temperature, inlet mass flow rate, and the irradiation level.

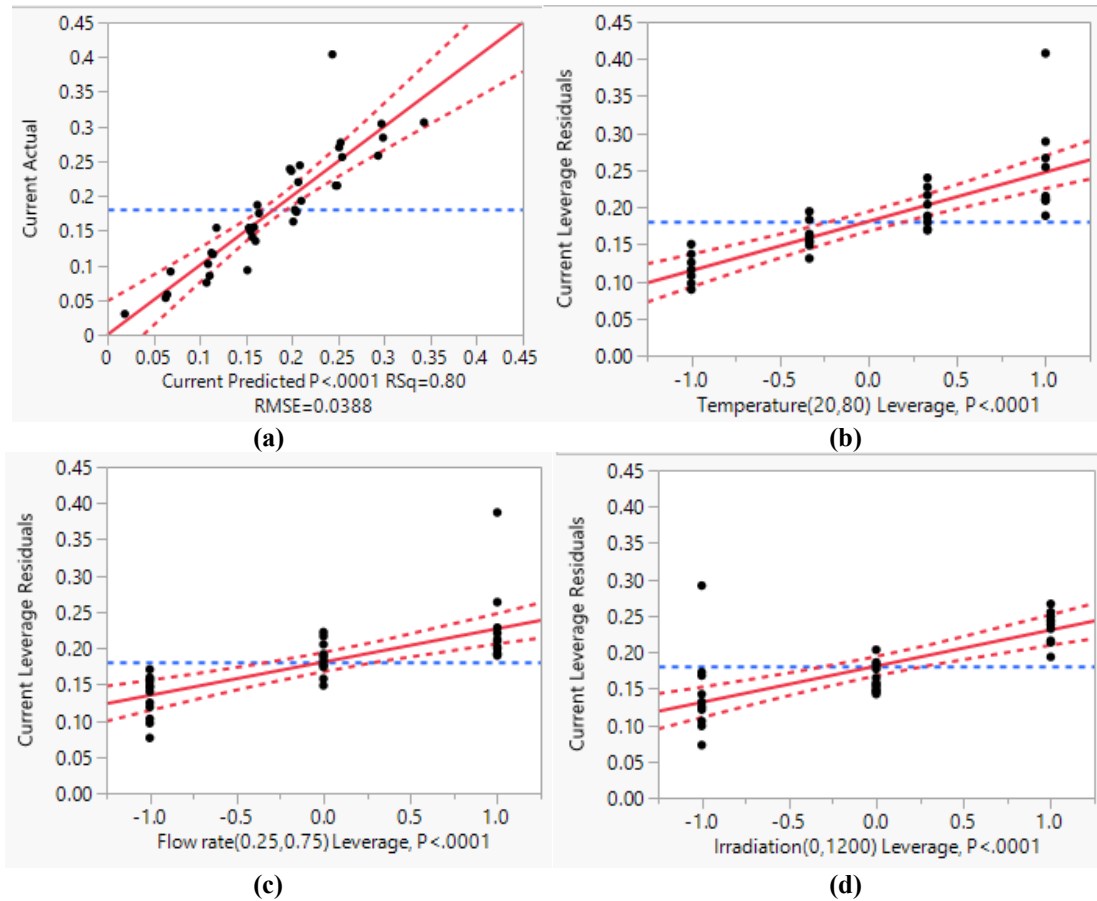


Figure 6.69 Results of (a) DOE model, (b) operating temperature leverage plot, (c) inlet mass flow rate leverage plot, and (d) irradiation level leverage plot of Process 4 experimental current measurements.

The detailed statistical analysis results of the current measurements of Process 4 is presented in Figure 6.69. The DOE model has a good agreement with the actual experimental data with a root mean square error of 0.0388. The standard error in current measurements is less than 0.001, which is considered as zero. The F-test results show that the operating temperature has an F-ratio of 58.50, irradiation level has an F-ratio of 39.23, and the inlet mass flow rate has an F-ratio of 33.59. Therefore, it is concluded that the operating temperature has a higher impact on the current generation in Process 4 compared to the inlet mass flow rate and irradiation level.

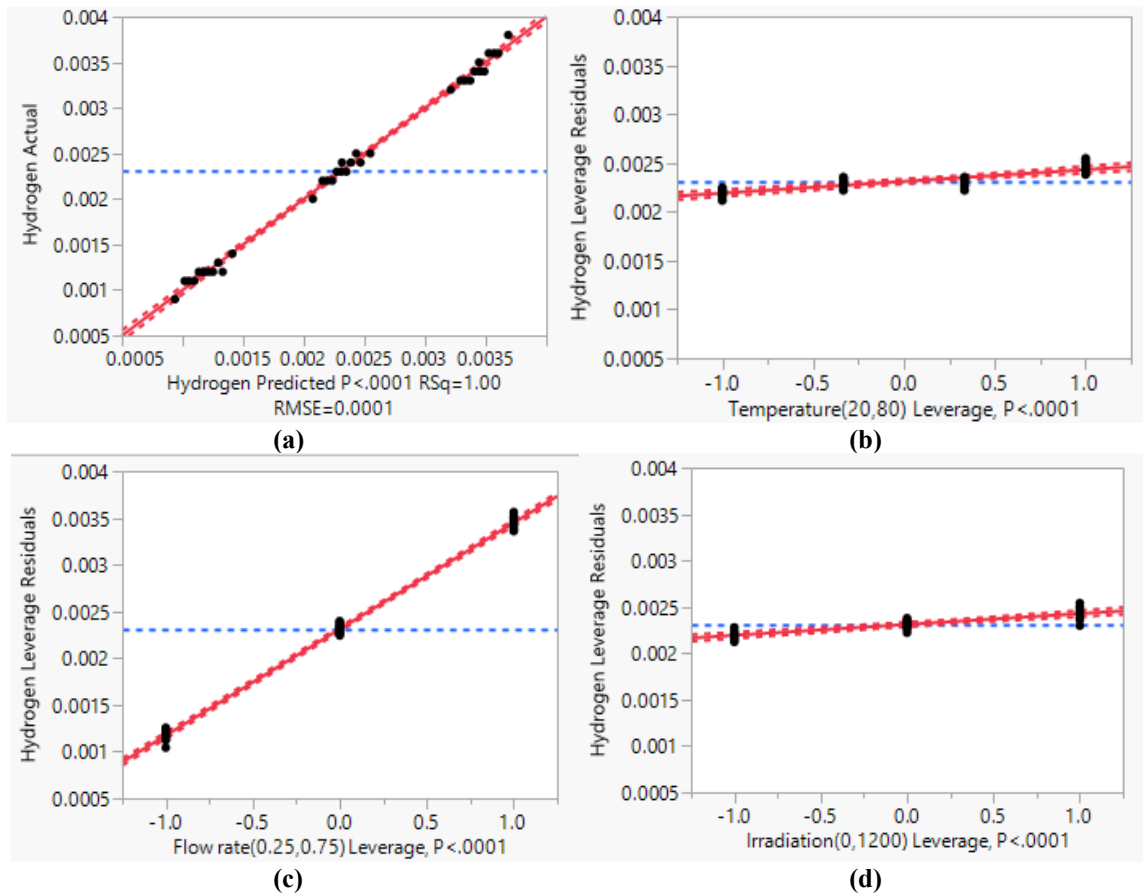


Figure 6.70 Results of (a) DOE model, (b) operating temperature leverage plot, (c) inlet mass flow rate leverage plot, and (d) irradiation level leverage plot of Process 4 experimental hydrogen production results.

The comparison of the present experimental hydrogen production and the DOE model results along with the leverage residuals of Process 4 are provided in Figure 6.70. The DOE model agrees with the actual experimental data with a root mean square error of 0.0001. The standard error in hydrogen production is less than 0.001, which is considered to be zero. The F-test results indicate that the inlet mass flow rate has an F-ratio of 9275.06, irradiation level has an F-ratio of 97.57, and the operating temperature has an F-ratio of 86.02. For that reason, it is determined that the inlet mass flow rate has a greater influence on the hydrogen production in Process 4 compared to the irradiation level and the operating temperature.

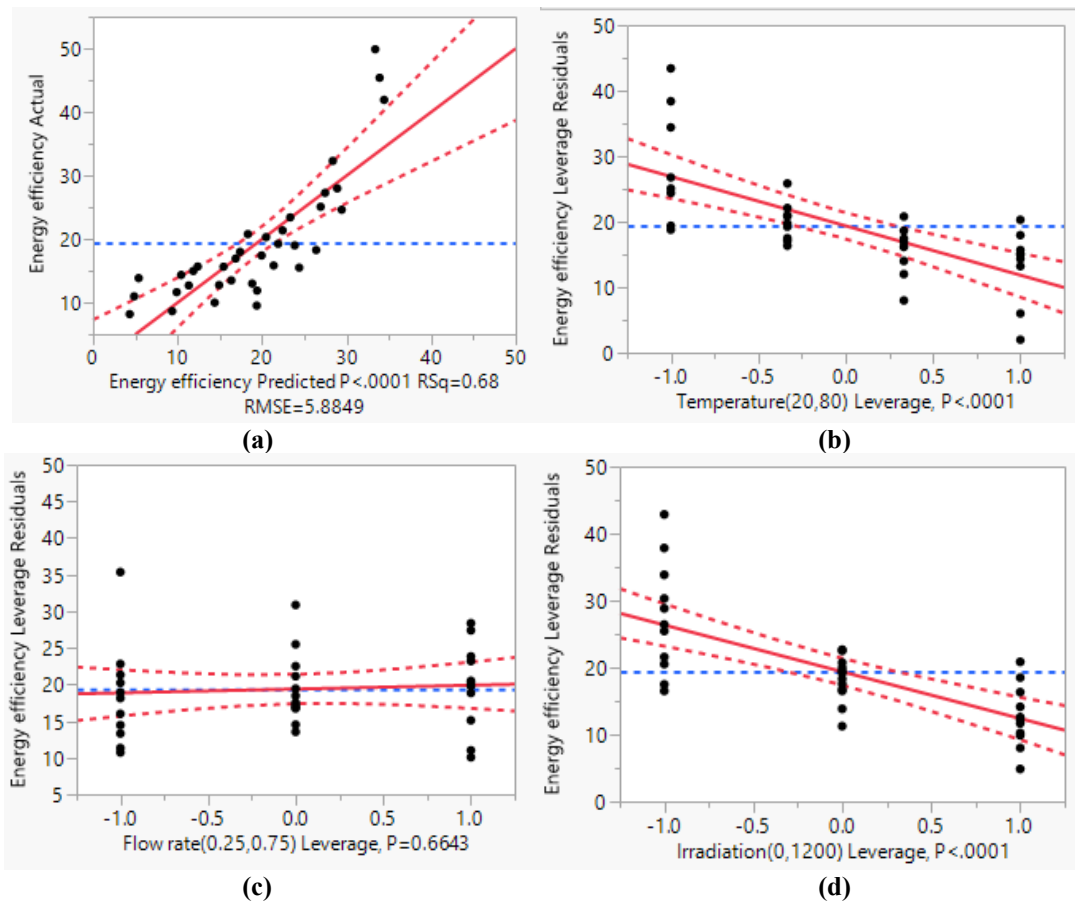


Figure 6.71 Results of (a) DOE model, (b) operating temperature leverage plot, (c) inlet mass flow rate leverage plot, and (d) irradiation level leverage plot of Process 4 experimental energy efficiency results.

Figure 6.71 shows the detailed statistical analysis of the energy efficiency results of Process 4. The DOE model has a satisfactory agreement with the actual experimental data with a root mean square error of 5.8849. The standard error in energy efficiency results is about 1.25. The F-test results present that the irradiation level has an F-ratio of 33.82, operating temperature has an F-ratio of 32.80, and the inlet mass flow rate has an F-ratio of 0.19. As a result, it is concluded that the irradiation level has a higher impact on the energy efficiency in Process 4 compared to the operating temperature and inlet mass flow rate.

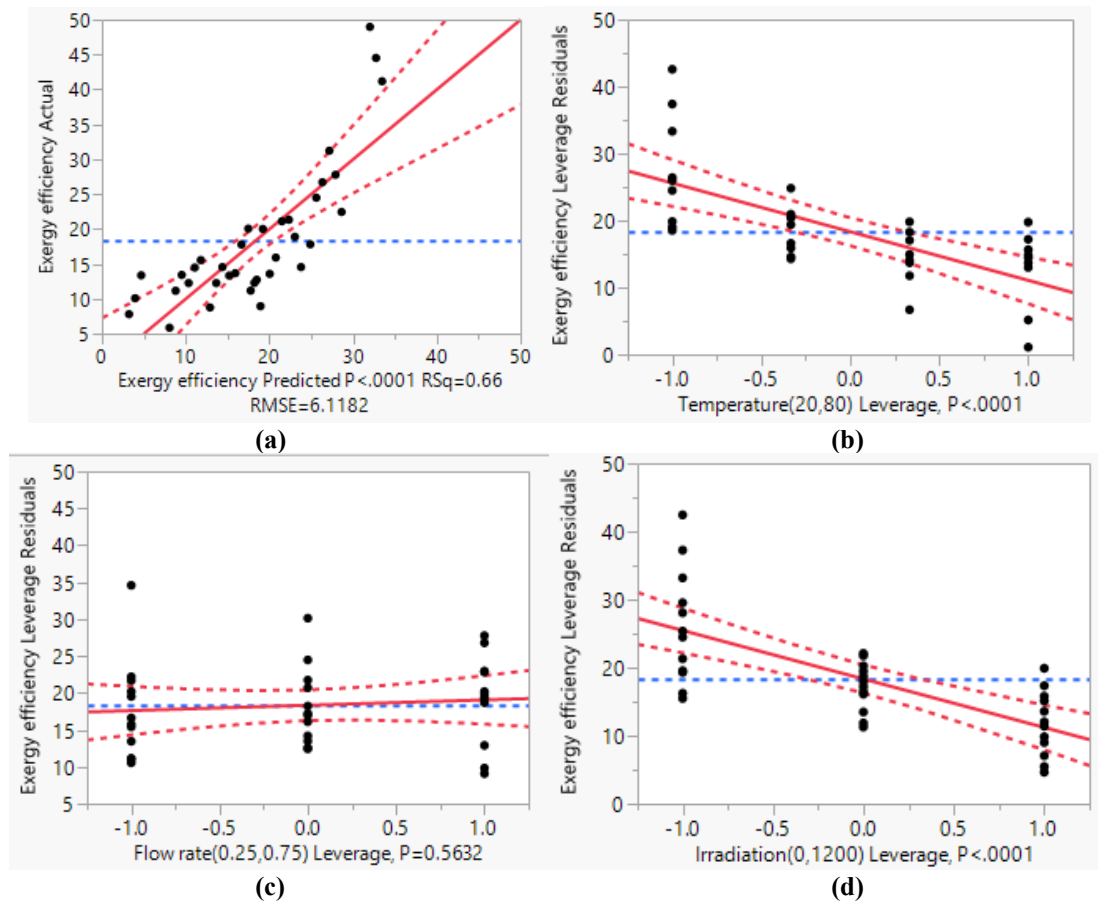


Figure 6.72 Results of (a) DOE model, (b) operating temperature leverage plot, (c) inlet mass flow rate leverage plot, and (d) irradiation level leverage plot of Process 4 experimental exergy efficiency results.

Figure 6.72 shows the comparison of the present experimental exergy efficiency and the DOE model results along with the leverage residuals of Process 4. The DOE model and experimental exergy efficiency results comparison along with the leverage residuals of Process 4 are provided in Figure 6.72. The DOE model agrees with the actual experimental data with a root mean square error of 6.1182. The standard error in exergy efficiency is about 1.30. The F-test results indicate that the irradiation level has an F-ratio of 32.55, operating temperature has an F-ratio of 28.21 and the inlet mass flow rate has an F-ratio of 0.34. For that reason, it is determined that the irradiation level has a greater influence on the exergy efficiency in Process 4 compared to the operating temperature and the inlet mass flow rate.

6.5 Integrated System Results

The integrated system performance is investigated based on varying the parameters as

- The operating temperature: between 20°C and 80°C
- The inlet mass flow rate: between 0.1 g/s and 15 g/s
- The total photoactive area: between 2.7 and 6 m²
- The environmental temperature: between 0°C and 40°C

The total photoactive area is the sum of the PV/T and reactor photocatalytic membrane area. Both PV/T and membrane areas are taken to be as half of the total photoactive area. The system performance is evaluated based on the H₂ and Cl₂ production, electricity and heat generation, rate of exergy destruction, and energy and exergy efficiencies criteria. Four different case studies are comparatively assessed based on these criteria. These case studies are (i) optimum operating temperature, (ii) optimum inlet mass flow rate, (iii) optimum photoactive area, and (iv) optimum environmental temperature. Each optimum case is designed to deliver the highest possible H₂, Cl₂, heat, and electricity production, energy and exergy efficiencies, and lowest possible exergy destruction. In the end, these case studies are compared to select the most suitable parameters for the integrated system.

6.5.1 Effect of Operating Temperature

When investigating the effects of the operating temperature on H₂, Cl₂, electricity, and heat production, exergy destruction, and energy and exergy efficiencies; the inlet mass flow rate is 1g/s NaCl and 1 g/s H₂O, the environmental temperature is 20°C, and the irradiation level is 1000 W/m². And the total photoactive area is 4 m² (2 m² PV/T, 2 m² PEC).

a. Hydrogen and Chlorine Production Results

The effect of the operating temperature on the integrated system's H₂ and Cl₂ production is presented in Figure 6.73. Figure 6.73 shows that both H₂ and Cl₂ production rates increase with increasing operating temperatures. At 20°C, the H₂ production rate is about 4.1 g/h (~ 48 L/h) and the Cl₂ production rate is around 124 g/h (~ 42 L/h). These amounts increase up to 4.9 g/h (70 L/h) for H₂ and 148 g/h (60 L/h) for Cl₂ at 80°C. The reason of

these increases is the enhanced conductivity of the system components and the membrane with increasing operating temperatures. With enhanced conductivities, potential losses are reduced, resulting an increased production from the same amount of input energy.

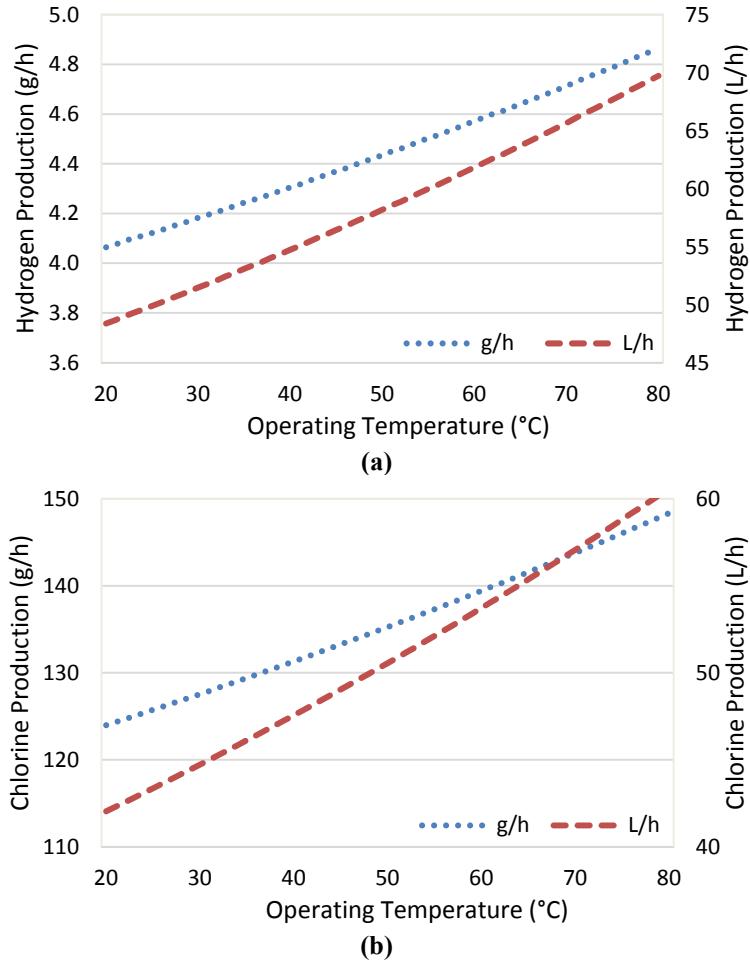


Figure 6.73 Effect of operating temperature on (a) H₂ and (b) Cl₂ production of integrated system.

b. Electricity and Heat Production Results

Figure 6.74 shows the effect of the operating temperature on the electricity and heat production in the integrated system. Figure 6.74 shows that with increasing operating temperatures, both electricity and heat production rate decreases. At 20°C, the electricity production is about 158 W and the heat production is around 792 W. These amounts decrease to 104 W for electricity and 296 W for heat at 80°C. The reason of these decreases is the increased electricity and heat consumption of the reactor with increasing operating temperatures. The solar irradiation is considered the only input to the integrated system

which is assumed to be set to 1000 W/m^2 and only excess electricity and heat are considered to be the products of the integrated system. Therefore, when the reactor electricity and heat demand increases, the electricity and heat productions decrease.

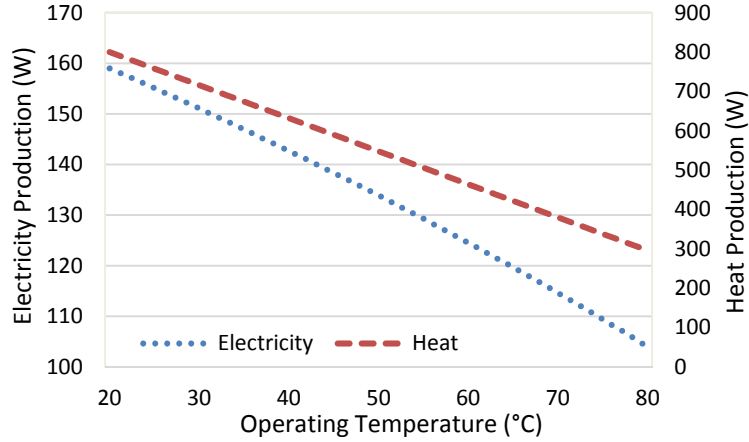


Figure 6.74 Effect of operating temperature on electricity and heat production of integrated system.

c. Exergy Destruction Results

When investigating the effect of the operating temperature on the exergy destruction rate, inlet flow rate is 1 g/s NaCl and $1 \text{ g/s H}_2\text{O}$, environmental temperature is 20°C , and irradiation level is 1000 W/m^2 . The total photoactive area is 4 m^2 . The effect of the operating temperature on the exergy destruction rate is presented in Figure 6.75(a). It can be seen that the exergy destruction rate increases with increasing operating temperatures. At 20°C , the exergy destruction rate is about 23 W . This amount increases to 348 W at 80°C . The primary reason of this trend is the increased heat consumption of the reactor.

d. Energy and Exergy Efficiencies Results

When investigating the effect of the operating temperature on the energy and exergy efficiencies, the inlet flow rate is 1 g/s NaCl and $1 \text{ g/s H}_2\text{O}$, environmental temperature is 20°C , and the irradiation level is 1000 W/m^2 . The total photoactive area is 4 m^2 . The results are presented in Figure 6.76. There are four different efficiency descriptions, each one is based on the number of useful products, which are explained in Table 5.8. In all cases, the input energy is constant since the irradiation level is fixed to 1000 W/m^2 and the photoactive area does not change.

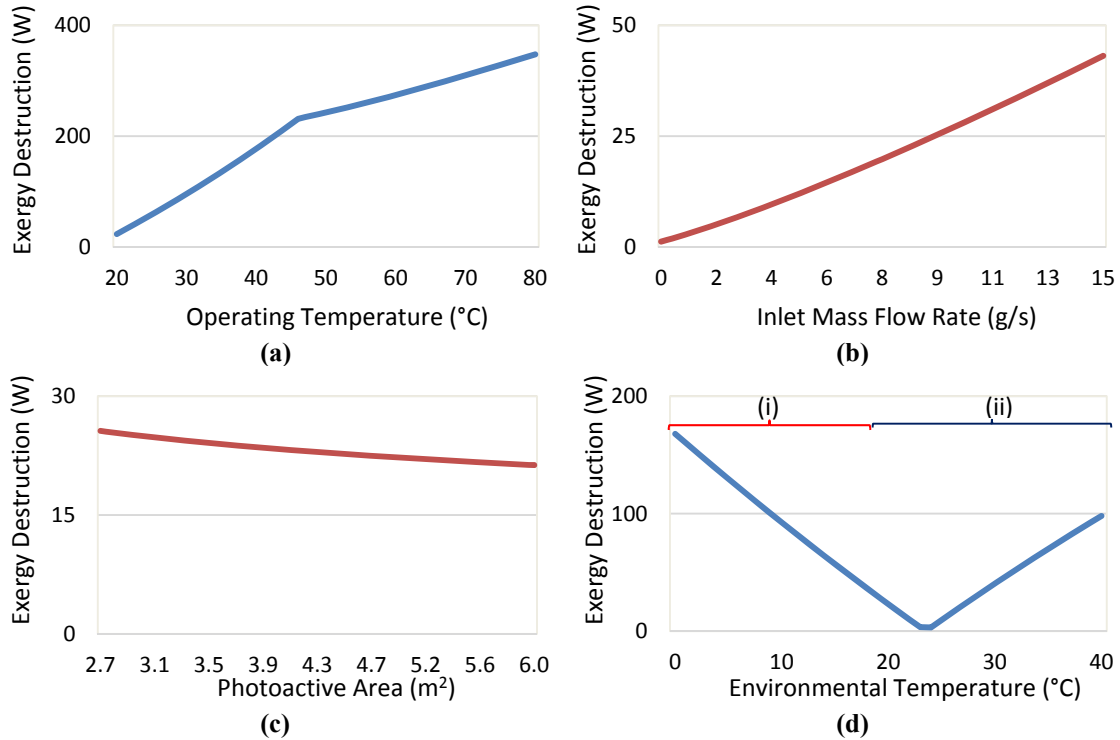


Figure 6.75 Effects of: (a) operating temperature, (b) inlet flow rate, (c) photoactive area, and (d) environmental temperature on exergy destruction of integrated system– (i) heating, (ii) cooling.

Figure 6.76 shows that the energy and exergy efficiencies of the H_2 ($\eta-1$ and $\psi-1$) and H_2-Cl_2 ($\eta-2$ and $\psi-2$) increase with increasing operating temperature since higher H_2 and Cl_2 production rates are observed at higher operating temperatures. At $20^\circ C$, $\eta-1$ and $\psi-1$ are 12% and 11%, respectively; and they increase to 14% and 13% at $80^\circ C$. Similarly, $\eta-2$ and $\psi-2$ are 13% and 15% at $20^\circ C$ and they are 23% and 18% at $80^\circ C$. When the electricity is considered as a useful amount as well, $\eta-3$ rises from 25% to 28% and $\psi-3$ decreases from 30% to 27% between $20^\circ C$ and $80^\circ C$. When H_2 , Cl_2 , electricity, and heat are considered all as useful outputs, the overall energy efficiency ($\eta-4$) decreases from 85% to 53% when operating temperature is increased from $20^\circ C$ to $80^\circ C$. However, within the same operating temperature interval, the overall exergy efficiency ($\psi-4$) increases from 28% to 31%. This is due to the increasing exergetic content of the heat with increasing operating temperatures as environmental temperature is fixed to $20^\circ C$.

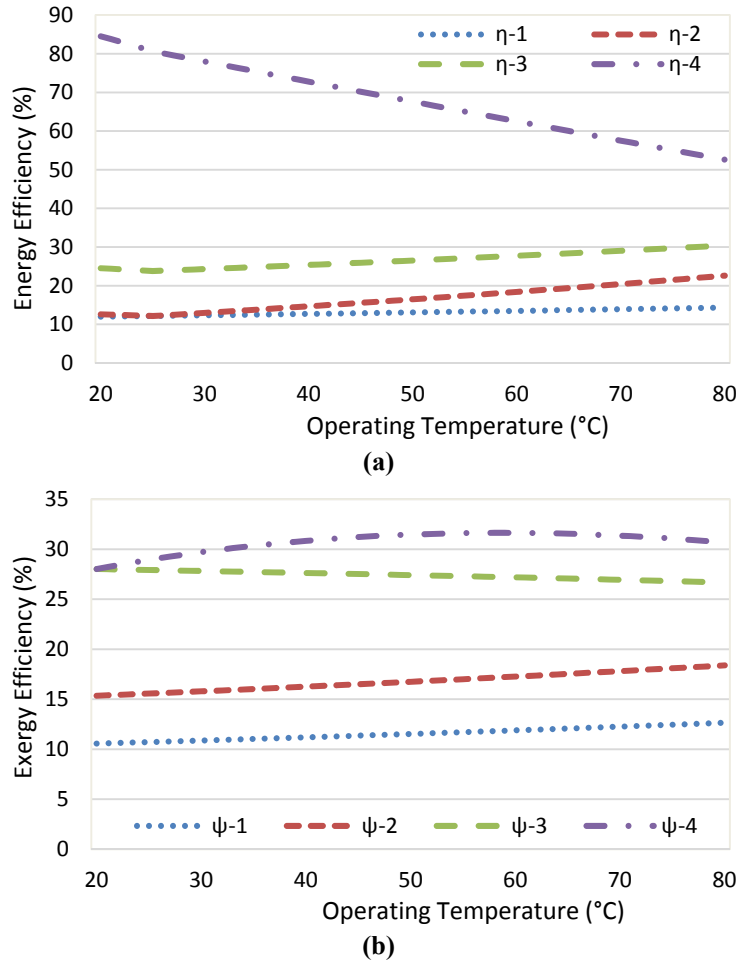


Figure 6.76 Effect of operating temperature on (a) energy and (b) exergy efficiencies of integrated system.

6.5.2 Effect of Inlet Mass Flow Rate

The effects of the inlet mass flow rate on the H₂, Cl₂, electricity, and heat production, exergy destruction, and energy and exergy efficiencies are investigated under the operating and environmental temperatures of 20°C, irradiation level of 1000 W/m², and a total photoactive area of 4 m² (2 m² PV/T, 2 m² PEC).

a. Hydrogen and Chlorine Production Results

Figure 6.77 shows that both H₂ and Cl₂ production rates increase with increasing inlet mass flow rates. When the inlet flow rate is 0.1 g/s, the H₂ production rate is about 0.4 g/h (~ 5 L/h) and the Cl₂ production rate is around 12 g/h (~ 4 L/h). These amounts increase up to 6.7 g/h (80 L/h) for H₂ and 205 g/h (70 L/h) for Cl₂ at 15 g/s inlet mass flow rate. The

reason of these increases is the rapid replacement of depleted ions with increasing inlet mass flow rates. With increasing mass flow rates, positive or negative ion accumulation within the system (which could potentially lower the H₂ and Cl₂ production rates) is reduced.

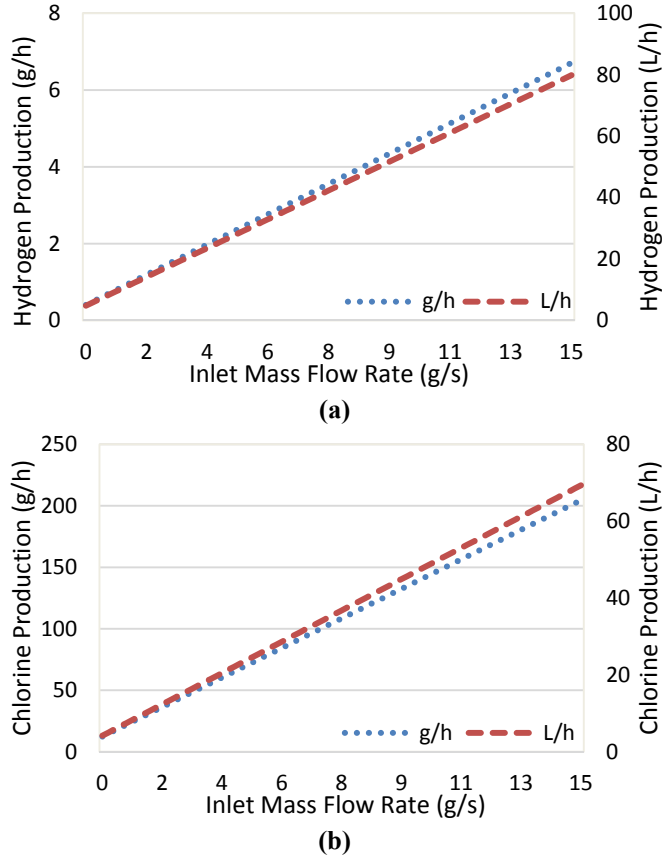


Figure 6.77 Effect of inlet mass flow rate on (a) H₂ and (b) Cl₂ production rate of integrated system.

b. Electricity and Heat Production Results

In Figure 6.78, the effect of the inlet mass flow rate on the electricity and heat production of the integrated system is presented. Here, it can be seen that the heat production is constant at 800 W. Since the operating and environmental temperatures are taken to be equal (20°C), the reactor is not using any heat so all of the heat recovered from the PV/T is considered to be the integrated system’s product, and this product is not affected by the inlet mass flow rate of the reactor. However, the electricity production decreases with increasing inlet mass flow rate. At 0.1 g/s, the electricity production is about 377 W and this amount decreases to 2 W when the inlet mass flow rate is 15 g/s. The electricity demand

of the reactor increases with increasing flow rates. In order to replace the depleted ions in a more rapid sense, the reactor needs higher currents which leads to increased electricity consumption. Because only excess electricity is considered as the product, when the reactor electricity demand increases, the electricity production decreases.

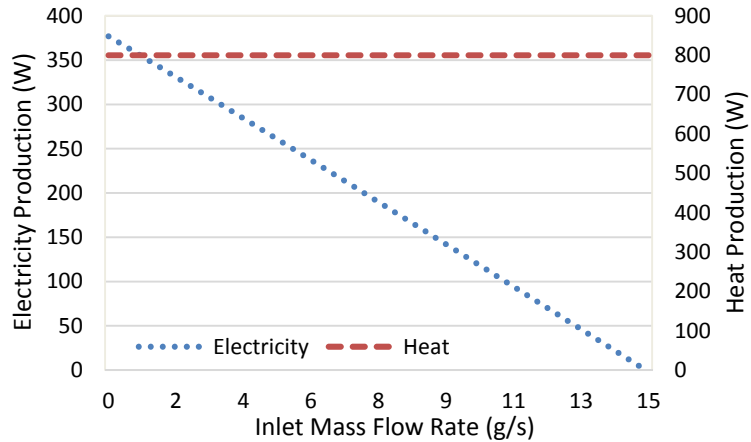


Figure 6.78 Effect of inlet mass flow rate on electricity and heat production of integrated system.

c. Exergy Destruction Results

The effect of the inlet mass flow rate on the exergy destruction rate is investigated under the operating and environmental temperatures of 20°C, irradiation level of 1000 W/m², and a total photoactive area of 4 m². Figure 6.75(b) presents the effect of the inlet mass flow rate on the exergy destruction in the integrated system. The exergy destruction increases with increasing inlet mass flow rates. When the inlet flow rate is 0.1 g/s, the exergy destruction is about 1 W and it increases to 43 W at 15 g/s inlet mass flow rate. Increasing flow rates amplifies the difference between inlet and exit streams' exergetic flow rates. The reactor is also using more electricity which also increases the exergy destruction rate.

d. Energy and Exergy Efficiencies Results

Figure 6.79 shows that the energy and exergy efficiencies of H₂ (η -1 and ψ -1) and H₂-Cl₂ (η -2 and ψ -2) increase with increasing inlet mass flow rates since higher H₂ and Cl₂ production rates are observed at higher flow rates. At 0.1 g/s, η -1 and ψ -1 are 1%; and they increase to 20% and 17%, respectively at 15 g/s. Similarly, η -2 and ψ -2 are 1% and 2% at 0.1 g/s and they are 21% and 25% at 15 g/s. When electricity is considered as a useful

output as well, η -3 decreases from 29% to 21% and ψ -3 decreases from 32% to 25% between 0.1 g/s and 15 g/s. When H₂, Cl₂, electricity, and heat are considered all as useful outputs, the overall energy efficiency (η -4) decreases from 90% to 81% when inlet mass flow rate is increased from 0.1 to 15 g/s. Within the same flow rate interval, the overall exergy efficiency (ψ -4) decreases from 32% to 25%. It should be noted that since the operating temperature is set to the environmental temperature (20°C), heat has no exergetic value within the selected mass flow rate interval, therefore ψ -3 and ψ -4 are equal.

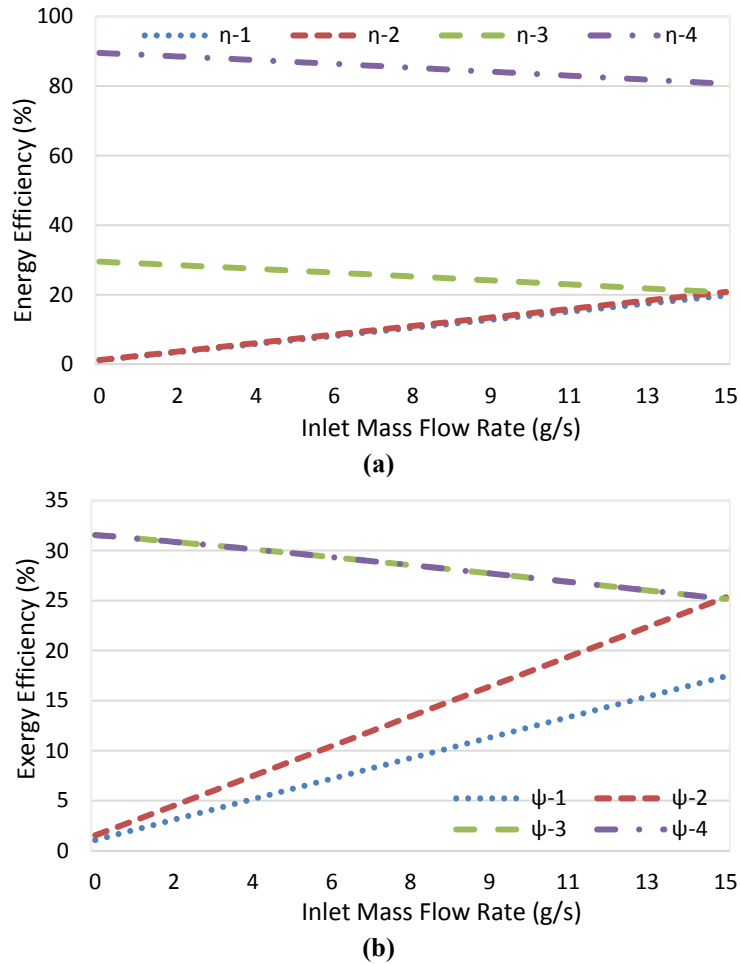


Figure 6.79 Effect of inlet mass flow rate on (a) energy and (b) exergy efficiencies of integrated system.

6.5.3 Effect of Photoactive Area

When investigating the effects of the photoactive area on the H₂, Cl₂, electricity, and heat production, exergy destruction, and energy and exergy efficiencies; the inlet flow rate is

1g/s NaCl and 1 g/s H₂O, both operating and environmental temperatures are 20°C, and the irradiation level is 1000 W/m². The photoactive area of PV/T and the reactor are half of the total photoactive area.

a. Hydrogen and Chlorine Production Results

The effect of the photoactive area on the H₂ and Cl₂ production is presented in Figure 6.80. Both H₂ and Cl₂ production increase when the total photoactive area is increased from 2.7 to 6 m².

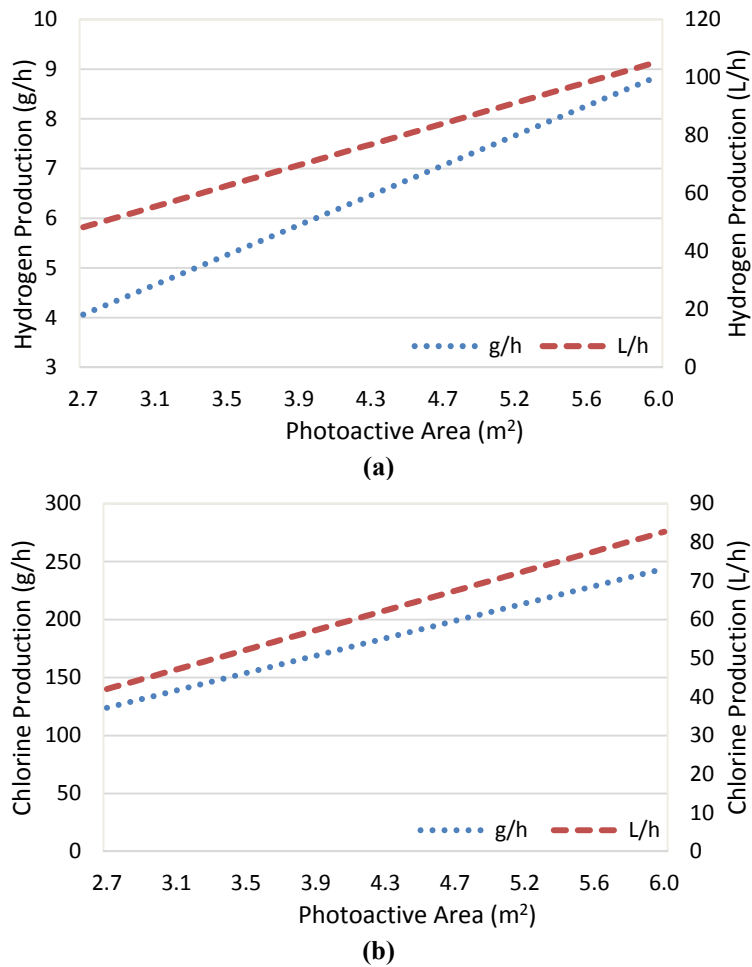


Figure 6.80 Effect of photoactive area on (a) H₂ and (b) Cl₂ production rate of integrated system.

When the total photoactive area is around 2.7 m², the H₂ production is about 4.1 g/h (~ 48 L/h) and the Cl₂ production is around 124 g/h (~ 42 L/h). These amounts increase to 8.9 g/h (105 L/h) for H₂ and 244 g/h (83 L/h) for Cl₂ when the total photoactive area is 6

m². The reason of these increases is the increased electricity generation due to increased PV/T area and the enhanced photocurrent generation of the reactor with increasing photoactive membrane area. With enhanced electrical supply and photocurrent, the H₂ and Cl₂ production rates increase.

b. Electricity and Heat Production Results

The effect of the photoactive area on the electricity and heat production is shown in Figure 6.81. Here, it can be seen that the electricity and heat production increase with increasing photoactive area. When the total photoactive area is 2.7 m², the electricity and heat production are about 22 W and 531 W, respectively. These amounts increase to 361 W electricity and 1200 W heat when the total photoactive area is 6 m². With increasing photoactive area, the electricity production and heat recovery from the Figure 6.81 also shows that the increase in heat production (669 W) is significantly higher than that of electricity (339 W). As the operating and environmental temperatures are equal (20°C), the reactor does not require heating, so all of the heat recovered from the PV/T is the system output. However, the reactor is still supported by the electricity from PV/T, and therefore, increase in electricity production with respect to photoactive area is less than that of heat production.

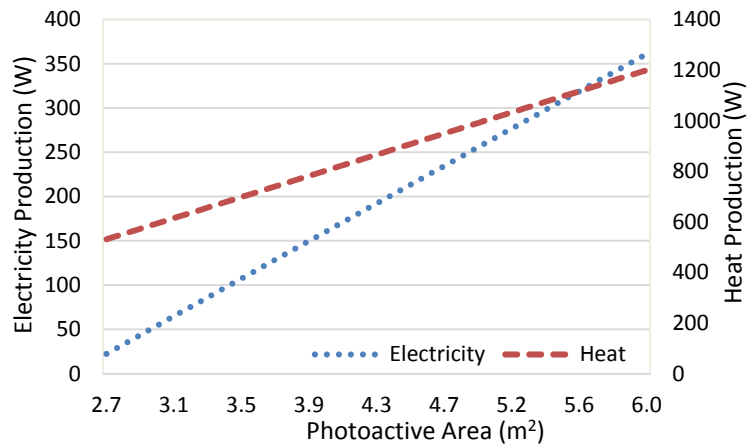


Figure 6.81 Effect of photoactive area on electricity and heat production of integrated system.

c. Exergy Destruction Results

When investigating the effect of the total photoactive area on the exergy destruction rate, the inlet mass flow rate is 1g/s NaCl and 1 g/s H₂O, both operating and environmental temperatures are 20°C, and the irradiation level is 1000 W/m². The photoactive areas of PV/T and the reactor are half of the total photoactive area. The effect of the total photoactive area on the exergy destruction rate is shown in Figure 6.75(c). From this figure, it can be seen that the exergy destruction rate decreases with increasing photoactive area. When the total photoactive area is 2.7 m², rate of exergy destruction is about 26 W and this amount decreases to 21 W when the total photoactive area is 6 m². With increasing photoactive area, all products (H₂, Cl₂, electricity, and heat) are generated at higher rates from the same source and amount of input energy. As a result, exergy destruction rate decreases.

d. Energy and Exergy Efficiencies Results

Figure 6.82 shows that the energy and exergy efficiencies of H₂ ($\eta-1$ and $\psi-1$) and H₂-Cl₂ ($\eta-2$ and $\psi-2$) decrease even though higher H₂ and Cl₂ production rates are observed at larger total photoactive areas. When the total photoactive area is 2.7 m², $\eta-1$ and $\psi-1$ are 18% and 16%; and they decrease to 8% and 7%, respectively at the total photoactive area of 6 m². Similarly, $\eta-2$ and $\psi-2$ are 19% and 23% at 2.7 m² and they are 8% and 10% at 6 m². When electricity is considered as a useful product as well, $\eta-3$ increases from 22% to 26% and $\psi-3$ increases from 26% to 29% from the total photoactive area of 2.7 to 6 m². When H₂, Cl₂, electricity, and heat are considered all as useful outputs, the overall energy efficiency ($\eta-4$) increases from 82% to 86% when the total photoactive area is increased from 2.7 to 6 m². Within the same total photoactive area interval, the overall exergy efficiency ($\psi-4$) increases from 26% to 29%. It should be noted that since operating temperature is set to the environmental temperature, heat has no exergetic value, therefore $\psi-3$ and $\psi-4$ are equal.

6.5.4 Effect of Environmental Temperature

The effects of the environmental temperature on the H₂, Cl₂, electricity, and heat production, exergy destruction, and energy and exergy efficiencies are investigated with

the inlet mass flow rate of 1g/s NaCl and 1 g/s H₂O. The operating temperature is 20°C, irradiation level is 1000 W/m², and the total photoactive area is 4 m² (2 m² PV/T, 2 m² PEC). Since the investigation is conducted under constant inlet flow rate, operating temperature, and photoactive area; H₂ and Cl₂ production are not affected by the change in environmental temperature.

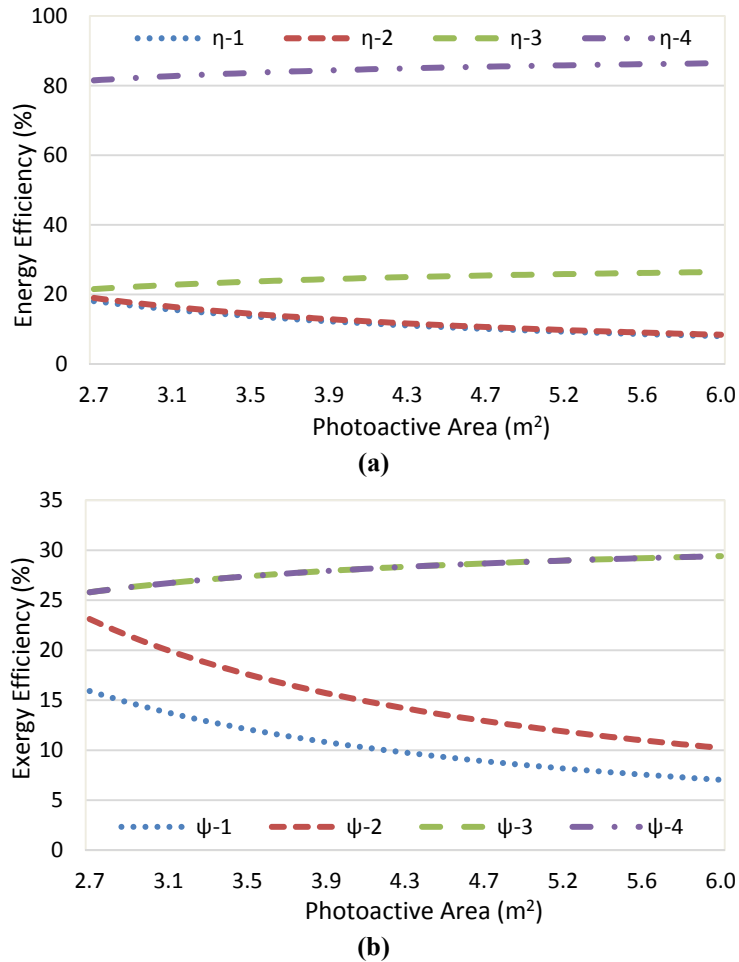


Figure 6.82 Effect of photoactive area on (a) energy and (b) exergy efficiencies of integrated system.

a. Electricity and Heat Production Results

In Figure 6.83, the effect of the environmental temperature on the electricity and heat production of the integrated system is presented. Here, it can be seen that the electricity production is constant at 159 W. Since the investigation is conducted under constant inlet flow rate, operating temperature, and photoactive area; the PV/T electricity generation and the reactor's electricity demand are constant as well. As a result, the electricity production

is not affected by the environmental temperature. However, the heat production first increases then decreases with increasing environmental temperature. At 0°C, heat production is about 632 W and this amount increases to 800 W at 20°C, then heat production decreases again and reaches to about 632 W at 40°C. The reason of this behavior is the operating temperature, which is 20°C. The reactor needs to be heated when the environmental temperature is below 20°C and it needs to be cooled down when the environmental temperature is 40°C. Because only excess heat is considered as the product, when the reactor's heating/cooling demand increases, the heat production decreases.

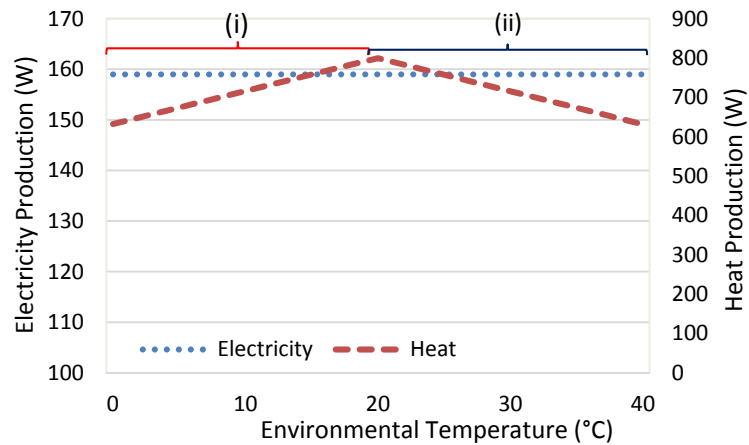


Figure 6.83 Effect of environmental temperature on electricity and heat production of integrated system – (i) heating, (ii) cooling.

b. Exergy Destruction Results

The effect of the environmental temperature on the exergy destruction rate is investigated with the inlet mass flow rate of 1g/s NaCl and 1 g/s H₂O. The operating temperature is 20°C, irradiation level is 1000 W/m², and the total photoactive area is 4 m². In Figure 6.75(d), the effect of the environmental temperature on the exergy destruction rate of the integrated system is presented. Here, it can be seen that the exergy destruction rate first decreases then increases with increasing environmental temperature. At 0°C, exergy destruction is about 168 W and this amount decreases to 3 W at 24°C, after that, it increases and reaches to about 98 W at 40°C. The reason of this behavior is the operating temperature of the reactor, which is 20°C. The reactor needs to be heated when the environmental

temperature is below 20°C and it needs to be cooled down when the environmental temperature is 40°C.

c. Energy and Exergy Efficiencies Results

The effect of the environmental temperature on the energy and exergy is presented in Figure 6.84. $\eta-1$, $\eta-2$, and $\eta-3$ are not affected by the change in environmental temperature. The change in $\psi-1$, $\psi-2$, and $\psi-3$ are negligible. They all increase by 0.1-0.2% within the selected environmental temperature interval. The overall energy efficiency first increases and then starts decreasing again after 20°C. At 0°C and 40°C, the overall energy efficiency is around 72% and the peak efficiency is 85% at 20°C. When the environmental temperature is increased from 0°C and 40°C, the overall exergy efficiency ($\psi-4$) decreases from 31% to 25%.

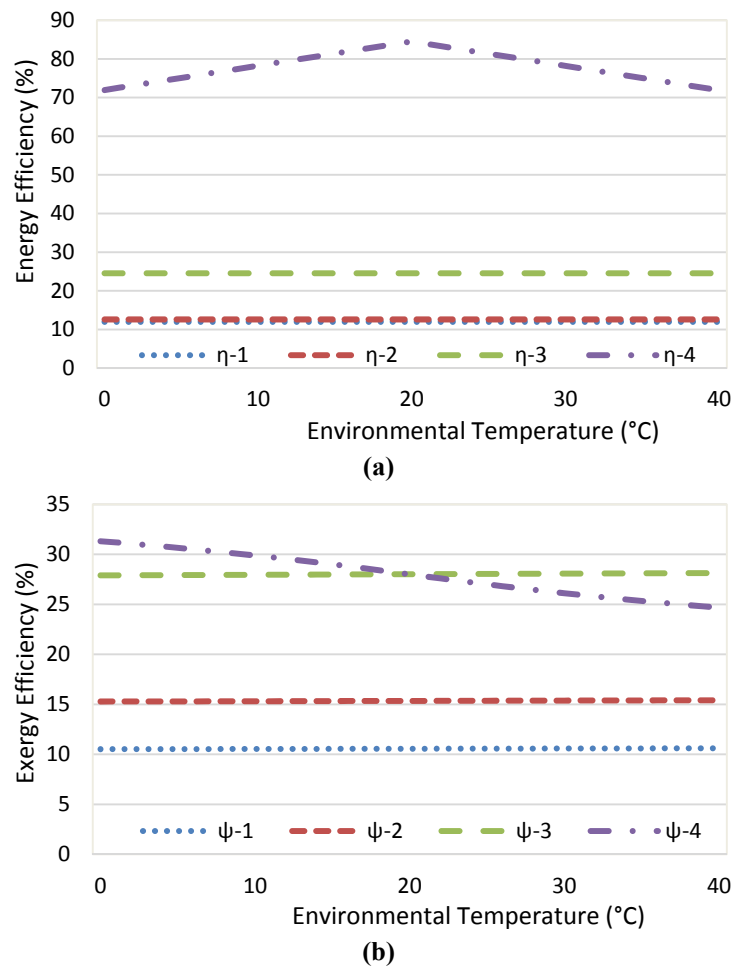


Figure 6.84 Effect of environmental temperature on (a) energy and (b) exergy efficiencies of integrated system.

6.5.5 Case Study Results

The aim of the case studies is to demonstrate the optimum operating temperature, inlet mass flow rate, total photoactive area, and the environmental temperature to reach the maximum achievable H₂, Cl₂, heat, and electricity production as well as energy and exergy efficiencies while keeping the exergy destruction as little as possible. In this section, there are four case studies and in each case study, one decision variable is optimized to get the desired performance results. Within the selected operating temperature, inlet mass flow rate, photoactive area, and the environmental temperature size intervals, all performance criteria (except exergy destruction) are normalized based on Equation (6.1). Exergy destruction is normalized based on Equation (6.2).

a. Case Study 1: Optimum Operating Temperature Results

In Case Study 1, it is aimed to find the optimum operating temperature to reach the highest possible production rates, efficiencies, and lowest possible exergy destruction. For that reason; the following criteria are normalized and ranked based on a 0-10 scale: H₂, Cl₂, electricity, heat production, overall energy and exergy efficiencies, and exergy destruction. Then the average ranking at each operating temperature is calculated. The operating temperature giving the highest possible average ranking is selected as the optimum operating temperature. Figure 6.85 shows that the optimum operating temperature is 30°C where the highest average ranking of 5.75/10 is reached.

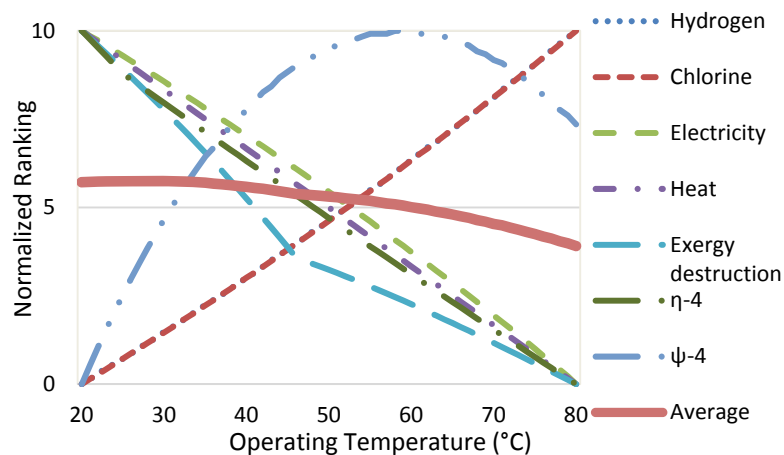


Figure 6.85 Operating temperature based normalized rankings of selected performance criteria of integrated system.

b. Case Study 2: Optimum Inlet Mass Flow Rate Results

In Case Study 2, ranking is done to find the inlet mass flow rate giving the highest possible production rates, efficiencies, and lowest possible exergy destruction. For that reason; the following criteria are normalized and ranked based on a 0-10 scale: H₂, Cl₂, electricity, heat production, overall energy and exergy efficiencies, and exergy destruction. Then the average ranking at each inlet mass flow rate is calculated. The inlet mass flow rate giving the highest possible average ranking is selected as the optimum inlet mass flow rate. Figure 6.86 shows that the optimum inlet mass flow rate is 0.1 g/s where the highest average ranking of 6.67/10 is reached.

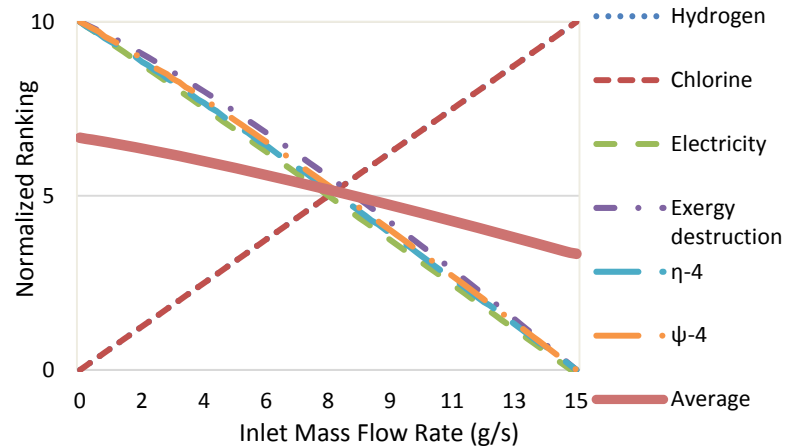


Figure 6.86 Inlet mass flow rate based normalized rankings of selected performance criteria of integrated system.

c. Case Study 3: Optimum Photoactive Area Results

In Case Study 3, ranking and normalization are performed to determine the photoactive area giving the highest possible production rates, efficiencies, and lowest possible exergy destruction. For that reason; the following criteria are normalized and ranked based on a 0-10 scale: H₂, Cl₂, electricity, heat production, overall energy and exergy efficiencies, and exergy destruction. Then the average ranking at each total photoactive area is calculated. The total photoactive area giving the highest possible average ranking is selected as the optimum total photoactive area. Figure 6.87 presents that optimum photoactive area is 6 m² g/s where the highest average ranking of 10/10 is reached.

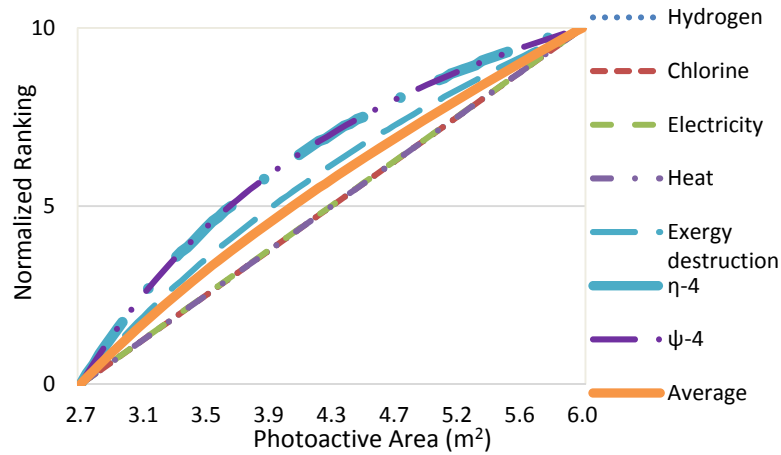


Figure 6.87 Photoactive area based normalized rankings of selected performance criteria of integrated system.

d. Case Study 4: Optimum Environmental Temperature Results

In Case Study 4, the following criteria are normalized and ranked based on a 0-10 scale: heat production, overall energy and exergy efficiencies, and exergy destruction. Then the average ranking at each environmental temperature is calculated. Figure 6.88 shows that the optimum environmental temperature is 20°C where the highest average ranking of 8.45/10 is reached.

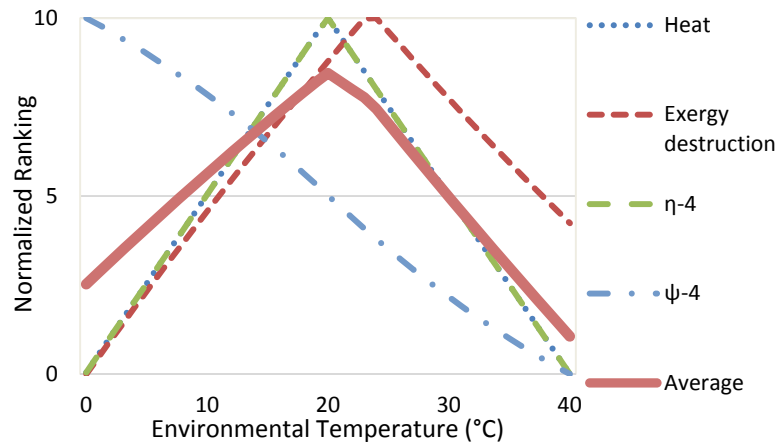


Figure 6.88 Environmental temperature based normalized rankings of selected performance criteria of integrated system.

e. Overall Comparison Results of the Case Studies

The overall comparison of the selected case studies is done by comparatively assessing the performance of these case studies which is summarized in Table 6.5. Case Study 1 has the lowest electricity and heat production and energy efficiency and the highest exergy destruction rate among the selected case studies. Case Study 2 has the lowest H₂ and Cl₂ production rates. On the other hand, this case has the highest electricity generation and energy and exergy efficiencies and lowest possible exergy destruction rate among the selected case studies. Case Study 3 has the highest H₂, Cl₂, and heat production rates. Case Study 4 has the lowest exergy efficiency among the selected case studies. The performance criteria of these case studies are normalized and ranked based on Equations (6.1) and (6.2) and the results are presented in Figure 6.89.

Table 6.5 Performance comparison of selected case studies.

	Case 1	Case 2	Case 3	Case 4
Temperature (°C)	30	20	20	20
Flow rate (g/s)	1	0.1	1	1
Area (m ²)	4	4	6	4
Environmental temperature (°C)	20	20	20	20
Hydrogen (g/h)	4.18	0.49	8.86	4.06
Chlorine (g/h)	127.45	12.4	243.98	123.98
Electricity (W)	151	377	361.1	159
Heat (W)	716	800	1200	799.6
Rate of exergy destruction (W)	95.74	1.25	21.29	28.03
Energy efficiency (%)	78.03	89.55	86.46	84.51
Exergy efficiency (%)	29.72	31.56	29.42	28.01

From Figure 6.89, it can be seen that Case Study 3 is the most desirable case since it has closest to ideal performance among selected options. The disadvantage of Case Study 3 is the low exergy efficiency compared to the other cases. Case Study 3 has an average normalized ranking of 8.35/10 followed by Case Study 2 which is 5.96/10. The reason why Case Study 2 has lower ranking is because it gives the lowest H₂ and Cl₂ production rates. Third highest average ranking is Case Study 4, 3.42/10. Case Study 4 has the lowest exergy efficiency, and relatively low H₂, Cl₂, electricity, and heat production. Overall, the lowest average ranking belongs to Case Study 1, which is 2.03/10. The reason of this poor performance is because it has the lowest electricity and heat production and energy efficiency and the highest exergy destruction rate among the selected case studies.

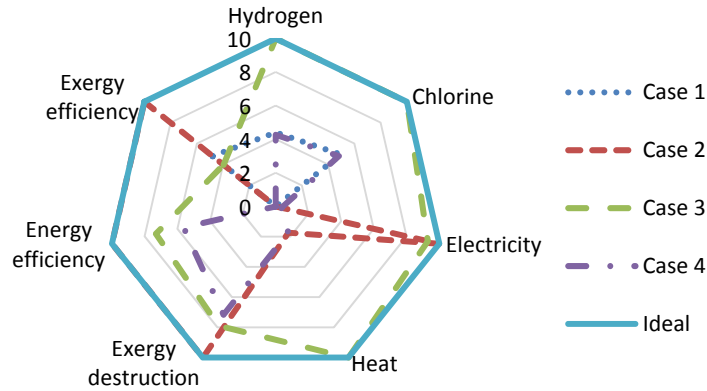


Figure 6.89 Overall performance comparison of case studies based on normalized rankings of selected performance criteria of integrated system.

6.6 Exergoeconomic Analysis Results

The exergoeconomic analysis is conducted based on varying the operating temperature, inlet mass flow rate, photoactive area, and the environmental temperature to assess how cost of H₂ and Cl₂ production are affected from these parameters. In the exergoeconomic analysis, lifetime of the solar spectral splitter (Unit I), PV/T (Unit II), and the hybrid reactor (Unit III) are assumed to be 20 years. During the lifetime of the reactor, photoactive membrane is assumed to be replaced once in six months, which is included in the cost equation of the reactor. The interest rate is assumed to be 10%.

The integrated system has solar irradiation as the only energy input which has no cost associated with the stream. Also, the inlet stream saturated NaCl solution is assumed to be taken from the waste stream of a desalination facility and similarly, water inlet is taken to be the waste coolant water stream of a plant. As a result of these assumptions, the integrated system's inlet streams has considered to have zero cost associated with them. Therefore, \dot{C}_{dest} is zero and the exergoeconomic factor (f) is equal to one. Also, RCD is not applicable to this case. The only cost factor of the integrated system is related to the equipment of the integrated system. In addition, cost of electricity is considered to be 0.09 USD/kWh and heat is 0.032 USD/kWh. Figure 6.90 shows the effect of the operating temperature on the cost of H₂ and Cl₂ productions.

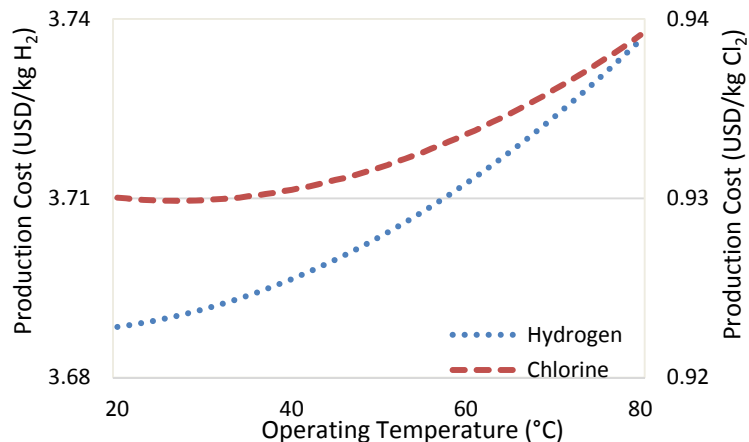


Figure 6.90 Effect of operating temperature on H₂ and Cl₂ production costs of integrated system.

From Figure 6.90, it can be seen that when operating temperature is increased from 20 to 80°C, the cost of H₂ production increases from 3.69 to 3.74 USD/kg H₂. This amount is higher than the reported electrolysis cost in the literature (2.5 USD/kg H₂) but lower than the cost of both PV-electrolysis (6 USD/kg H₂) and PEC (10 USD/kg H₂) based H₂ production [4]. Since the reactor recovers heat from PV/T and excess heat and electricity are considered to be useful products, the cost of H₂ production is lowered. And because heat and electricity production decreases with increasing operating temperature, cost of H₂ production increases with increasing operating temperature. Similarly, when operating temperature is increased from 20 to 80°C, the cost of Cl₂ production increases from 0.93 to 0.94 USD/kg Cl₂.

Figure 6.91 shows the effect of the inlet mass flow rate on the cost of H₂ and Cl₂ production. When the inlet mass flow rate is increased from 0.1 to 15 g/s, cost of H₂ production increases from 3.46 to 3.85 USD/kg H₂. This amount is higher than the reported electrolysis cost in the literature (2.5 USD/kg H₂) but lower than the cost of both PV-electrolysis (6 USD/kg H₂) and PEC (10 USD/kg H₂) based H₂ production [4]. Since the reactor recovers heat from PV/T and excess heat and electricity are considered to be useful products, the cost of H₂ production is lowered. And because the electricity production decreases with increasing inlet mass flow rate, the cost of H₂ production increases with increasing inlet mass flow rate. Similarly, when the inlet mass flow rate is increased from 0.1 to 15 g/s, the cost of Cl₂ production increases from 0.87 to 0.97 USD/kg Cl₂.

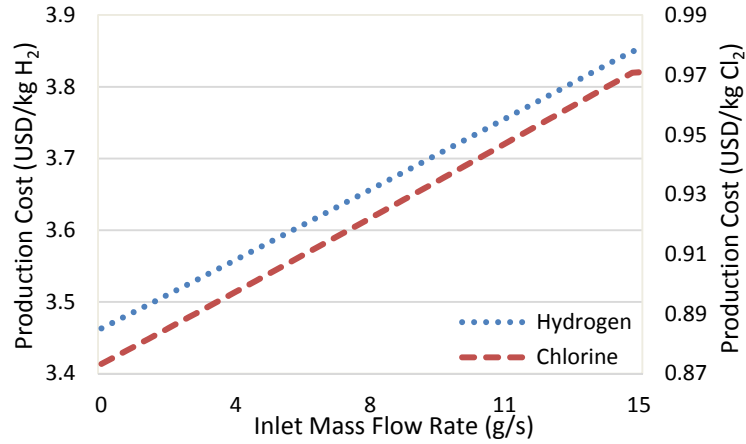


Figure 6.91 Effect of inlet mass flow rate on H₂ and Cl₂ production costs of integrated system.

The effect of the total photoactive area on the cost of H₂ and Cl₂ production is presented in Figure 6.92. When the total photoactive area is increased from 2.7 to 6 m², the cost of H₂ production increases from 1.94 to 9.91 USD/kg H₂. This amount is higher than the reported electrolysis cost in the literature (2.5 USD/kg H₂) but lower than the cost of PEC (10 USD/kg H₂) based H₂ production [4]. Since the reactor recovers heat from PV/T and excess heat and electricity are considered to be useful products, the cost of H₂ production is lowered. The reason of this cost increase is the increase in system equipment cost with increasing system area which is reflected on the increase in H₂ production cost. However, when the total photoactive area is increased from 2.7 to 6 m², the cost of Cl₂ production decreases from 0.97 to 0.88 USD/kg Cl₂.

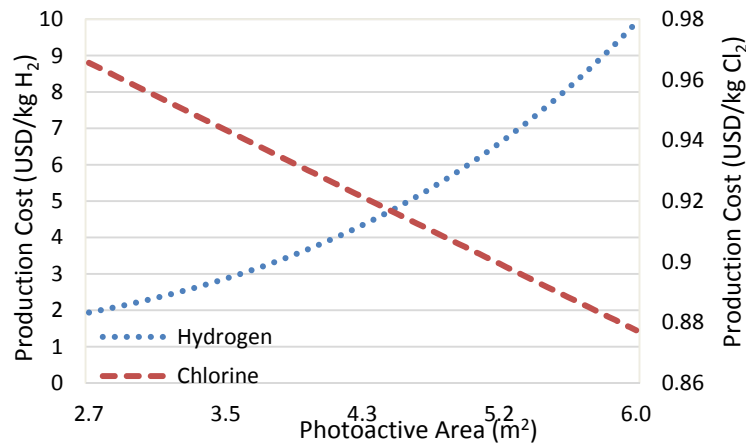


Figure 6.92 Effect of photoactive area on H₂ and Cl₂ production costs of integrated system.

Figure 6.93 shows the effect of the environmental temperature on the cost of H₂ and Cl₂ production. Here, it can be seen that the production costs are the highest when the environmental temperature is 20°C: 3.69 USD/kg H₂. This amount is higher than the reported electrolysis cost in the literature (2.5 USD/kg H₂) but lower than the cost of both PV-electrolysis (6 USD/kg H₂) and PEC (10 USD/kg H₂) based H₂ production [4]. This is because when environmental temperature is 20°C, the heat product has no exergetic value.

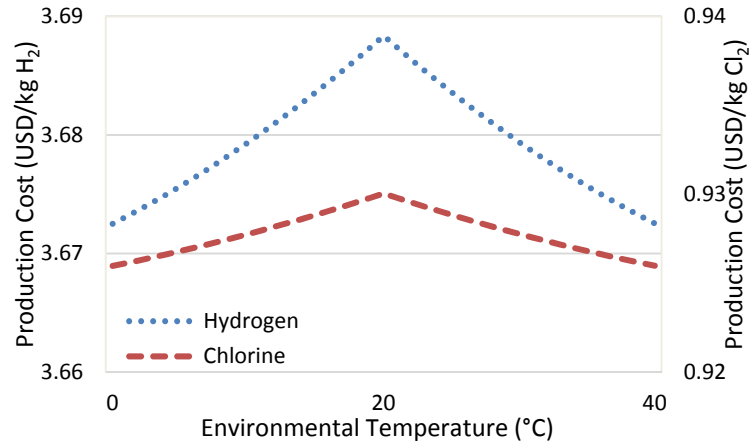


Figure 6.93 Effect of environmental temperature on H₂ and Cl₂ production costs of integrated system.

Furthermore, the overall comparison of the selected case studies presented in Section 6.5.5 is enhanced by including the cost of H₂ production as a performance criteria and the updated results are provided in Table 6.6. Table 6.6 shows that Case Study 3 has the highest H₂ production cost and Case Study 2 has the lowest production cost. The performance and cost criteria of these case studies are normalized and ranked based on Equations (6.1) and (6.2) and the results are presented in Figure 6.94.

From Figure 6.94, it can be seen that Case Study 3 is still the most desirable case since it has the closest to ideal performance among the selected case studies. Case Study 3 has an average normalized ranking of 8.35/10 followed by Case Study 2 which is 5.96/10. Third highest average ranking is Case Study 4, 3.42/10. Case Study 1 has the lowest average ranking which is 2.98/10. The detailed information is presented in Table 6.6.

Table 6.6 Performance and cost comparison of selected case studies.

	Case 1 <i>Optimum operating temperature</i>	Case 2 <i>Optimum inlet mass flow rate</i>	Case 3 <i>Optimum photoactive area</i>	Case 4 <i>Optimum environmental temperature</i>
Temperature (°C)	30	20	20	20
Flow rate (g/s)	1	0.1	1	1
Area (m ²)	4	4	6	4
Environmental temperature (°C)	20	20	20	20
Hydrogen (g/h)	4.18	0.49	8.86	4.06
Chlorine (g/h)	127.45	12.4	243.98	123.98
Electricity (W)	151	377	361.1	159
Heat (W)	716	800	1200	799.6
Rate of exergy destruction (W)	95.74	1.25	21.29	28.03
Energy efficiency (%)	78.03	89.55	86.46	84.51
Exergy efficiency (%)	29.72	31.56	29.42	28.01
Cost (USD/kg H ₂)	3.69	3.46	9.91	3.69

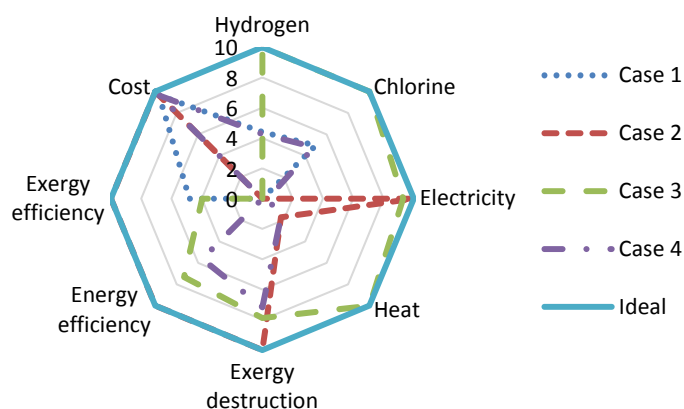


Figure 6.94 Overall performance and cost comparison of case studies based on normalized rankings.

6.7 Exergoenvironmental Analysis Results

The exergoenvironmental analysis is performed based on varying operating the operating temperature, inlet mass flow rate, total photoactive area, and the environmental temperature to assess how CO₂ emissions of H₂, Cl₂, electricity, and heat production are affected from these parameters. In the exergoenvironmental analysis, lifetime of the solar spectral splitter (Unit I), PV/T (Unit II), and the hybrid reactor (Unit III) are assumed to be 20 years. During the lifetime of the reactor, photoactive membrane is assumed to be replaced once in six months, which is included in the emissions equation of the reactor.

The integrated system has solar irradiation as the only energy input which has no emissions accompanying the stream. Also, the inlet stream saturated NaCl solution is assumed to be taken from the waste stream of a desalination facility and similarly, the water inlet is taken to be the waste coolant water stream of a plant. As a result of these assumptions, the integrated system's inlet streams has considered to have zero linked CO₂ emissions. The only source of CO₂ emissions of the integrated system is related to the equipment. Figure 6.95 shows the effect of the operating temperature on CO₂ emissions of H₂, Cl₂, electricity, and heat production.

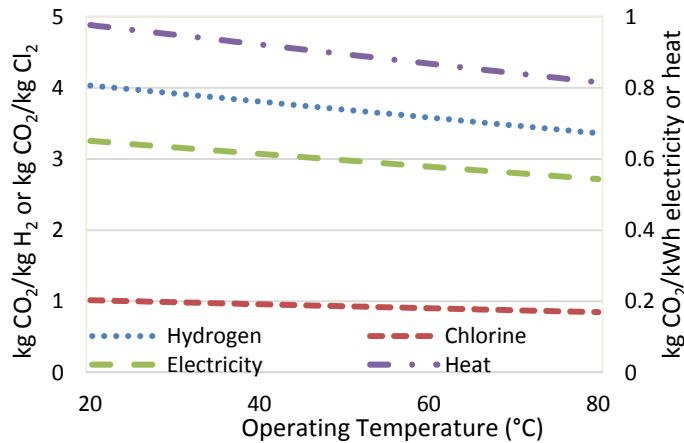


Figure 6.95 Effect of operating temperature on CO₂ emissions of integrated system.

From Figure 6.95, it can be seen that when the operating temperature is increased from 20 to 80°C, H₂ production emissions decrease from 4.03 to 3.36 kg CO₂/kg H₂. This amount is lower than the reported amounts of electrolysis (8 kg CO₂/kg H₂). However, it is higher than the reported data of PV-electrolysis (3 kg CO₂/kg H₂) and PEC (0.5 kg CO₂/kg H₂) in the literature [4]. This is due to the additional CO₂ emissions of the solar spectral splitter and reactor, especially the photoactive membrane which has an activated carbon layer. When operating temperature is increased from 20 to 80°C, CO₂ emissions of Cl₂ production decrease from 1.02 to 0.85 kg CO₂/kg Cl₂, electricity production decrease from 0.65 to 0.54 kg CO₂/kWh, and heat production emissions decrease from 0.98 to 0.82 kg CO₂/kWh. The reason of the decrease in CO₂ emissions of all products is due to the increase of H₂ and Cl₂ production with increasing operating temperatures. As the

equipment size remains constant, total amount of emissions does not change, and production emissions per kg H₂/Cl₂ and per kWh electricity/heat decrease.

Figure 6.96 shows the effect of the inlet mass flow rate on CO₂ emissions of H₂, Cl₂, electricity, and heat production. Here, it can be seen that when the inlet mass flow rate is increased from 0.1 to 15 g/s, H₂ production emissions decrease from 40.33 to 2.45 kg CO₂/kg H₂. Within the same interval, CO₂ emissions of Cl₂ production decrease from 10.17 to 0.62 kg CO₂/kg Cl₂, electricity production decrease from 6.51 to 0.39 kg CO₂/kWh, and heat production emissions decrease from 9.76 to 0.59 kg CO₂/kWh. The reason of the decrease in CO₂ emissions of all products is due to the increase of H₂ and Cl₂ production with increasing inlet mass flow rates. As the equipment size remains constant, total amount of emissions does not change, and production emissions per kg H₂/Cl₂ and per kWh electricity/heat decrease.

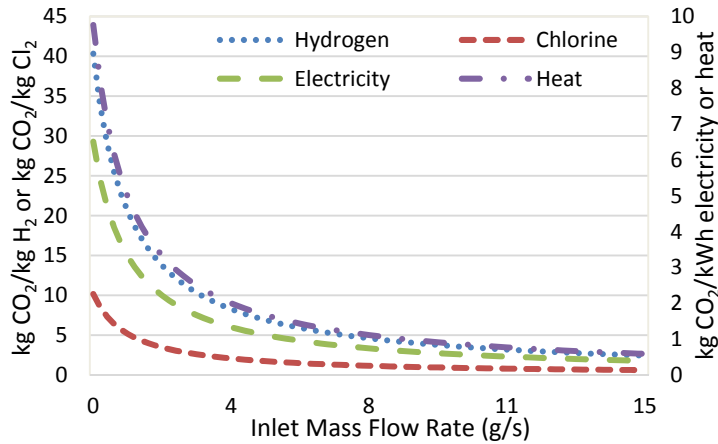


Figure 6.96 Effect of inlet mass flow rate on CO₂ emissions of integrated system.

Figure 6.97 shows the effect of the total photoactive area on CO₂ emissions of H₂, Cl₂, electricity, and heat production. Here, it can be seen that when the photoactive area is increased from 2.7 to 6 m², H₂ production emissions increase from 2.01 to 5.66 kg CO₂/kg H₂. This amount is lower than the reported amounts of electrolysis (8 kg CO₂/kg H₂). However, it is higher than the reported data of PEC (0.5 kg CO₂/kg H₂) in the literature [4]. This is due to the additional CO₂ emissions of the solar spectral splitter and reactor, especially the photoactive membrane which has an activated carbon layer.

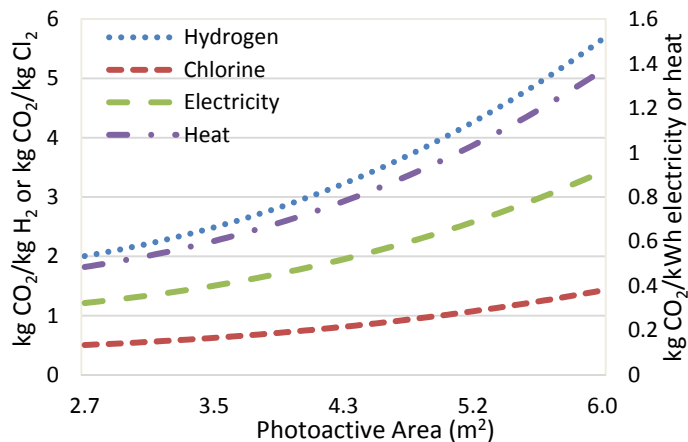


Figure 6.97 Effect of total photoactive area on CO₂ emissions of integrated system.

When the total photoactive area is increased from 2.7 to 6 m², CO₂ emissions of Cl₂ production increase from 0.51 to 1.43 kg CO₂/kg Cl₂, electricity production increase from 0.32 to 0.91 kg CO₂/kWh, and heat production emissions increase from 0.49 to 1.37 kg CO₂/kWh. The reason of the increase in the CO₂ emissions of all products despite the increase in H₂, Cl₂, electricity, and heat production is the equipment size increase with increasing photoactive area, which increases the total amount of emissions and production emissions per kg H₂/Cl₂ and per kWh electricity/heat decrease.

The integrated system's production emissions do not change with respect to the environmental temperature. The environmental temperature is increased from 0 to 40 °C, and the H₂ production emissions remain constant at 4.04 kg CO₂/kg H₂. Within the same interval, CO₂ emissions of the Cl₂ production is 0.48 kg CO₂/kg Cl₂, electricity production is 0.31 kg CO₂/kWh, and the heat production is 0.46 kg CO₂/kWh. The reason of the constant CO₂ emissions of all products is due to the constant equipment size. Also, the change in environmental temperature does not affect production amounts. Therefore, total amount of emissions does not change, and production emissions per kg H₂/Cl₂ and per kWh electricity/heat remain the same.

Furthermore, comparative assessment of the selected case studies presented in Section 6.6 is enhanced by including the emissions of H₂ production as a performance criteria and the updated results are provided in Table 6.7. Table 6.7 shows that Case Study

2 has the highest H₂ production emissions and Case Study 1 has the lowest production emissions.

Table 6.7 Performance, cost, and emissions comparison of selected case studies.

	Case 1 <i>Optimum operating temperature</i>	Case 2 <i>Optimum inlet mass flow rate</i>	Case 3 <i>Optimum photoactive area</i>	Case 4 <i>Optimum environmental temperature</i>
Temperature (°C)	30	20	20	20
Flow rate (g/s)	1	0.1	1	1
Area (m ²)	4	4	6	4
Environmental temperature (°C)	20	20	20	20
Hydrogen (g/h)	4.18	0.49	8.86	4.06
Chlorine (g/h)	127.45	12.4	243.98	123.98
Electricity (W)	151	377	361.1	159
Heat (W)	716	800	1200	799.6
Rate of exergy destruction (W)	95.74	1.25	21.29	28.03
Energy efficiency (%)	78.03	89.55	86.46	84.51
Exergy efficiency (%)	29.72	31.56	29.42	28.01
Cost (USD/kg H ₂)	3.69	3.46	9.91	3.69
Emissions (kg CO ₂ /kg H ₂)	3.92	40.33	5.66	4.04

The performance, cost, and emissions criteria of these case studies are normalized and ranked based on Equations (6.1) and (6.2) and the results are presented in Figure 6.98.

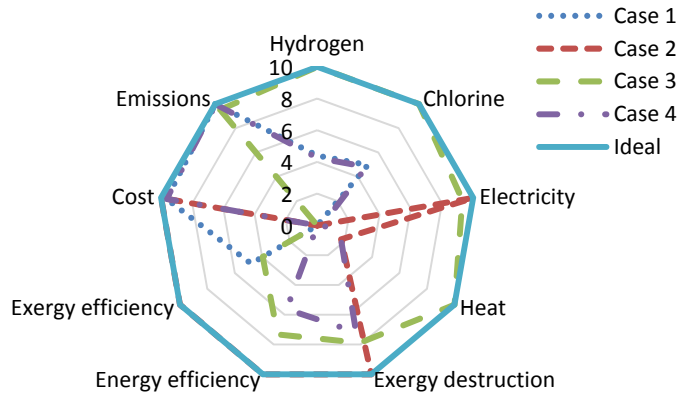


Figure 6.98 Overall performance, cost, and emissions comparison of case studies based on normalized rankings.

From Figure 6.98, it can be seen that Case Study 3 is still the most desirable case since it has closest to ideal performance among selected options. Case Study 3 has an average normalized ranking of 7.55/10 followed by Case Study 2 which is 5.75/10. Third

highest average ranking is Case Study 4, 4.84/10. Overall, the lowest average ranking belongs to Case Study 1, which is 3.76/10.

6.8 Optimization Study Results

The multi-objective optimization of the integrated system is performed by considering the following decision variables: the operating temperature, inlet mass flow rate, total photoactive area, and the environmental temperature. The aim of the optimization study is to maximize the production rates, efficiencies, and to minimize the exergy destruction, cost and emissions of the integrated system. The genetic algorithm application of the EES software is utilized to find the minimum and maximum values of the objective functions based on the selected decision variables. The relationship between the objective functions with decision variables are:

$$H_2 = 0.0133T + 0.4211F + 1.4354A - 2.8594 \quad (6.3)$$

$$Cl_2 = 0.4058T + 12.845F + 35.885A - 59.4899 \quad (6.4)$$

$$\dot{W} = -0.9129T - 25.363F + 101.26A - 151.5617 \quad (6.5)$$

$$\dot{Q} = -8.4T + 200.01A - 0.3847T_0^2 + 15.361T_0 + 341.8494 \quad (6.6)$$

$$\dot{E}x_{dest} = -0.0658T^2 + 11.984T + 2.8376F - 1.2571A + 0.287T_0^2 - 13.605T_0 - 39.4511 \quad (6.7)$$

$$\eta = -0.5175T - 0.5957F - 0.3442A^2 + 4.3582A - 0.0289T_0^2 + 1.152T_0 + 72.9507 \quad (6.8)$$

$$\psi = -0.0024T^2 + 0.2775T - 0.4315F - 0.2565A^2 + 3.2262A - 0.1763T_0 + 19.7978 \quad (6.9)$$

$$C = 10^{-5}T^2 + 0.002T + 0.0262F + 0.5632A^2 - 2.5734A - 4 \times 10^{-5}T_0^2 + 0.0014T_0 + 4.7932 \quad (6.10)$$

$$B = -0.0112T - 7.278\ln(F) + 1.0775A - 9 \times 10^{-7}T_0^2 + 4 \times 10^{-6}T_0 + 0.3832 \quad (6.11)$$

Equations (6.3–6.11) are set as the objective functions and decision variables are defined in matrix form with upper and lower bounds. Decision on the upper and lower

bounds are based on several constraints, such as commercial availability of the components and thermodynamic and material limits. It is now aimed to find out the best possible value of every decision variable for maximized production rates and efficiencies and minimized exergy destruction as well as minimized cost and emissions.

Six different case studies are investigated during the optimization study. The case study descriptions are provided in Table 6.8. The decision variable values maximizing the H₂ and Cl₂ production are the same. Therefore, these values are selected to be used in Case Study 1. Similarly, the decision variable values maximizing the electricity and heat production and the energy efficiency are the same, which are used in Case Study 2. Minimum exergy destruction and cost are attained with the same decision variable values, and they are assigned to Case Study 3. Finally, in Case Study 6, decision variables are selected to maximize the H₂, Cl₂, electricity, and heat production and energy and exergy efficiencies and minimize exergy destruction, cost, and emissions. The performance comparison of these cases are presented in Figures 6.99 – 6.102.

Table 6.8 Description of selected case studies used in optimization study.

Case 1	Maximum H ₂ and Cl ₂ production
Case 2	Maximum energy efficiency, electricity and heat production
Case 3	Minimum exergy destruction and cost
Case 4	Maximum exergy efficiency
Case 5	Minimum CO ₂ emissions
Case 6	Maximum H ₂ , Cl ₂ , electricity, and heat generation; maximum energy and exergy efficiencies, minimum exergy destruction, cost, and CO ₂ emissions

Figure 6.99 shows the H₂ and Cl₂ production comparison of the selected case studies. As expected, Case Study 1 has the highest H₂ (15.51 g/s) and Cl₂ (453.30 g/s) production rates. On the other hand, Case Study 3 has the lowest H₂ (0.05 g/s) and Cl₂ (13.56 g/s) production rates. Case Study 4 has the second highest H₂ (6.54 g/s) and Cl₂ (179.83 g/s) production rates. Third highest H₂ (6.36 g/s) and Cl₂ (174.21 g/s) production rates are achieved in Case Study 6.

The electricity and heat production comparison of the selected case studies are presented in Figure 6.100. In terms of electricity production, Case Study 2 has the highest rate (453.46 W), followed by Case Study 6 (419.58 W) and Case Study 4 (402.34 W). Case Study 1 has the lowest electricity production (9.01 W), followed by Case Study 5 (16.47

W) and Case Study 3 (48.42 W). Heat production comparison shows that Case Study 2 has the highest rate (1695.25 W), followed by Case Study 6 (1533.51 W) and Case Study 4 (1071.51 W). Case Study 3 has the lowest heat production (740.79 W), followed by Case Study 5 (773.01 W) and Case Study 1 (855.25 W).

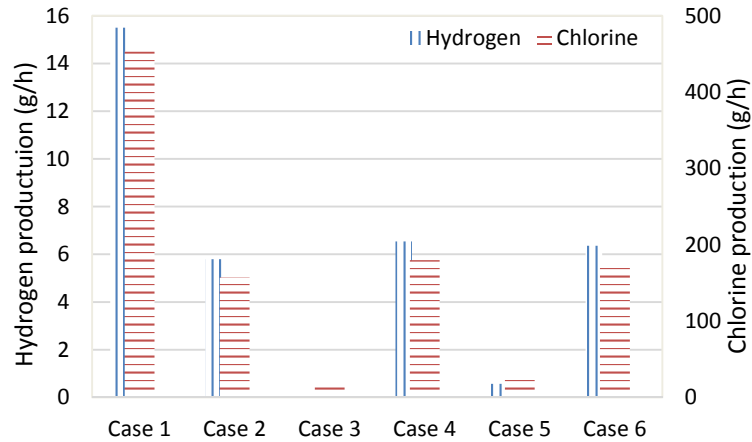


Figure 6.99 H₂ and Cl₂ production comparison of selected case studies used in optimization study.

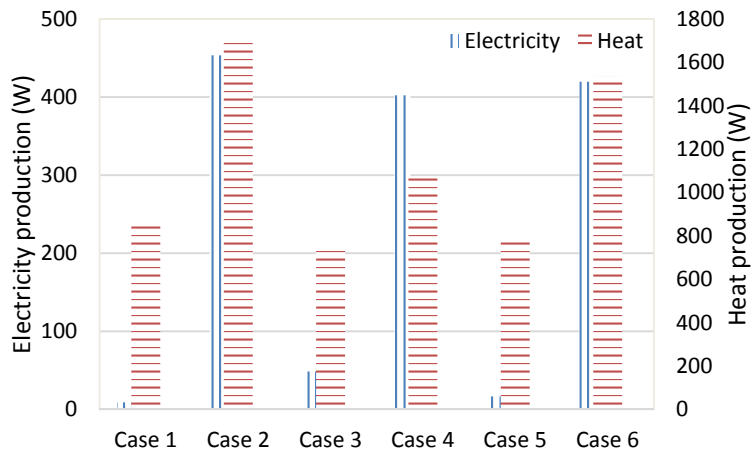


Figure 6.100 Heat and electricity production comparison of case studies used in optimization study.

Figure 6.101 shows the energy and exergy efficiencies comparison of the selected case studies. In terms of energy efficiencies, Case Study 2 has the highest rate (98.13%), followed by Case Study 6 (85.36%) and Case Study 5 (83.15%). Case Study 1 has the lowest energy efficiency (34.52%), followed by Case Study 4 (57.67%) and Case Study 3 (80.07%). The exergy efficiency comparison shows that Case Study 4 has the highest efficiency (37.89%), followed by Case Study 6 (29.59%) and Case Study 2 (26.45%). Case

Study 3 has the lowest exergy efficiency (18.13%), followed by Case Study 1 (21.52%) and Case Study 5 (25.56%).

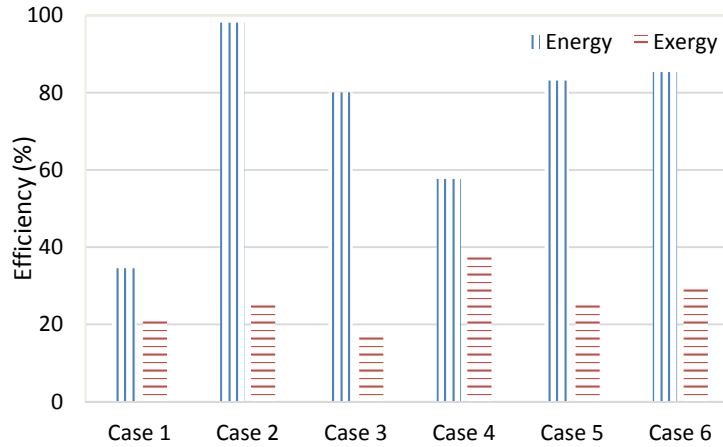


Figure 6.101 Energy and exergy efficiencies comparison of case studies used in optimization study.

Cost and emissions comparison of the selected case studies are presented in Figure 6.102. Case Study 1 has the highest cost (10.46 USD/kg H₂), followed by Case Study 4 (9.77 USD/kg H₂) and Case Study 6 (9.67 USD/kg H₂). Case Study 3 has the lowest cost (1.89 USD/kg H₂), followed by Case Study 5 (1.96 USD/kg H₂) and Case Study 2 (9.64 USD/kg H₂). H₂ production emissions comparison shows that Case Study 2 has the highest emissions (23.61 kg CO₂/kg H₂), followed by Case Study 4 (22.98 kg CO₂/kg H₂) and Case Study 3 (19.30 kg CO₂/kg H₂). Case Study 5 has the lowest emissions (2.43 kg CO₂/kg H₂), followed by Case Study 6 (7.39 kg CO₂/kg H₂) and Case Study 1 (16.08 kg CO₂/kg H₂).

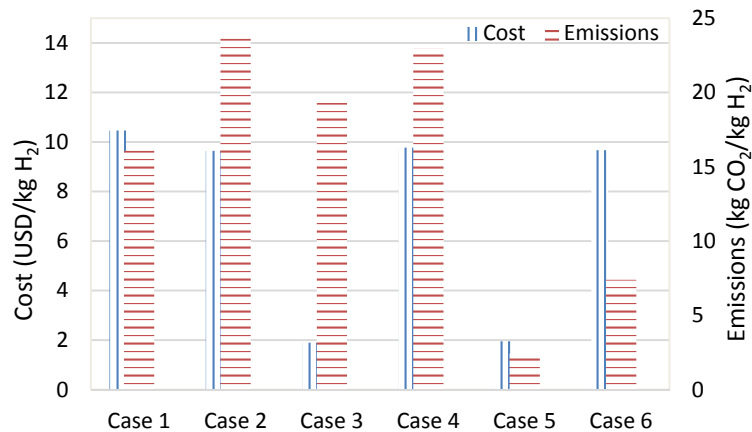


Figure 6.102 Cost and emissions comparison of selected case studies used in optimization study.

The findings presented in Figures 6.99 – 6.102 are summarized and given in Table 6.9. In addition to the data presented in the figures, Table 6.9 provide information on exergy destruction as well. Here, it can be seen that Case 3 has the lowest and Case 4 has the highest exergy destruction.

Table 6.9 Overall performance, cost, and emissions comparison of selected case studies used in optimization study.

	Case 1	Case 2	Case 3	Case 4	Case 5	Case 6
T (°C)	100	0	0	56	10	1
F (g/s)	20.0	0.1	0.1	0.1	1.0	1.4
A (m ²)	6	6	2	6	2	6
T ₀ (°C)	20	20	40	0	10	0
H ₂ (g/h)	15.51	5.80	0.05	6.54	0.57	6.36
C ₂ (g/h)	453.30	157.10	13.56	179.83	29.18	174.21
W (W)	9.01	453.46	48.42	402.34	16.47	419.58
Q (W)	855.25	1695.25	740.79	1071.51	773.01	1533.51
Ex _{dest} (W)	392.86	204.01	126.68	418.05	145.68	147.80
η (%)	34.52	98.13	80.07	57.67	83.15	85.36
ψ (%)	21.52	26.35	18.13	37.89	25.56	29.59
C (USD/kg H ₂)	10.46	9.64	1.89	9.77	1.96	9.67
B (kg CO ₂ /kg H ₂)	16.08	23.61	19.30	22.98	2.43	7.39

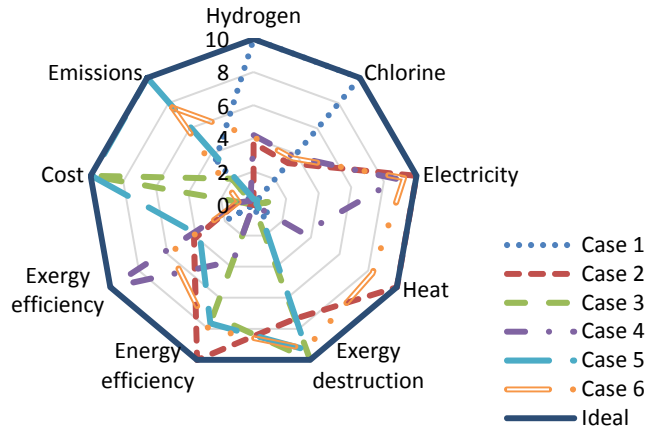


Figure 6.103 Overall performance, cost, and emissions comparison of optimization case studies based on normalized rankings.

When the data presented in Table 6.9 are normalized and ranked based on Equations (6.1) and (6.2), it can be seen that Case Study 6 is the most advantageous one with highest possible production rates and efficiencies and lowest possible exergy destruction, cost, and emissions. Overall ranking of Case Study 6 is 6.33/10, followed by Case Study 2 (5.49/10),

Case Study 5 (4.65/10), Case Study 4 (3.89/10), Case Study 3 (3.34/10), and Case Study 1 (3.04/10). Detailed rankings are presented in Figure 6.103.

Finally, the efficiency, cost, and emissions results of Case Study 6 are compared to the available data in the literature [6, 9, 15]. The energy and exergy efficiencies are compared in Figure 6.104 and cost and emissions comparison is presented in Figure 6.105.

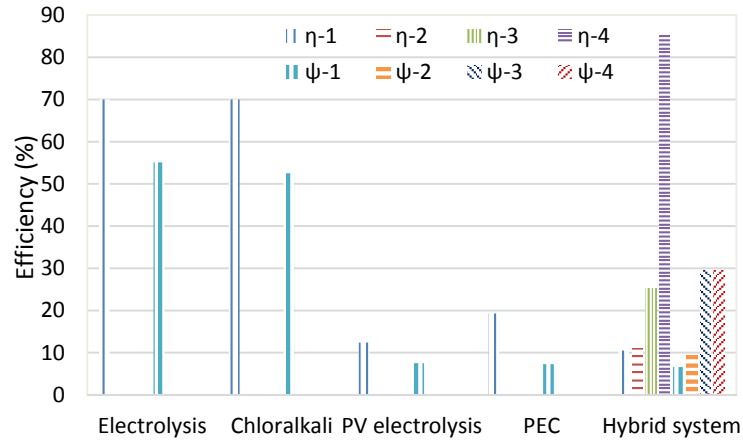


Figure 6.104 Energy and exergy efficiencies of present hybrid system compared to available data in literature.

From Figure 6.104, it can be seen that only first efficiencies (H_2 as the only product) of electrolysis, chloralkali, PV-electrolysis, and PEC are presented. The present integrated system developed in this study has lower $\eta-1$ and $\psi-1$ compared to the other methods in Figure 6.88. However, when Cl_2 and electricity are taken into account, $\eta-3$ and $\psi-3$ are higher than the energy and exergy efficiencies of PV-electrolysis and PEC. And when all four products are taken into account, it can be seen that $\eta-4$ is higher than all of the energy efficiencies presented in Table 6.88. Because operating and environmental temperatures are nearly equal in Case Study 6, heat product has no exergetic value and $\psi-4$ is equal to $\psi-3$.

Cost and emissions comparison presented in Figure 6.105 indicate that electrolysis has the lowest production cost and PEC has the lowest emissions. The present integrated system has the second highest production cost and emissions. This provides an insight on the trade-off between system efficiencies, cost, and emissions. Case Study 6 is selected for literature comparison as it gives the optimized values for all of the objective functions.

When cost is the only objective function, the present integrated system has lower production cost (1.89 USD/kg H₂) than even the conventional electrolysis (2.5 USD/kg H₂). Similarly, when emissions is the only objective function, the present integrated system has lower emissions (2.43 kg CO₂/kg H₂) than all of the options in Figure 6.89 except PEC (1 kg CO₂/kg H₂). Material development on more efficient solar harvesting and lowering emissions related to PV/T and photoreactor (especially membrane) manufacturing would greatly improve the present integrated system's overall production, efficiency, cost, and emissions performance.

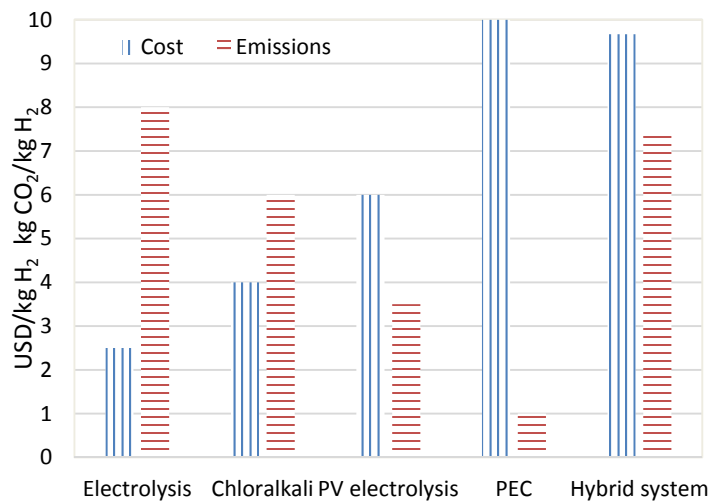


Figure 6.105 Cost and emissions of present hybrid system compared to the available data in literature.

CHAPTER 7: CONCLUSIONS AND RECOMMENDATIONS

The aim of this study is to experimentally and thermodynamically investigate an integrated system to convert solar energy in H₂ form which has a potential to be an energy supply that is as cheap as existing conventional supplies, as convenient in use, less environmentally damaging, and reasonably safe in use.

PEC-based H₂ production is not yet a commercial solution. Each element of the PEC process has a bearing on the cost of H₂ production, and impacting the overall economic viability. The issues related to PEC H₂ production can be summarized as: cost, efficiency, system losses, by-product accumulation, and durability. Furthermore, efficient harvesting of the full solar spectrum is an issue that directly affects cost and efficiency. Thus, for PEC systems to be considered as a commercial H₂ production method, basic material improvements together with robust system implementation are required. Therefore, in this study, it is aimed to develop and integrate a continuous type PEC-based H₂ production system with chloralkali process in order to maximize the harvested solar spectrum range and convert system by-products into commercially viable commodities. The existing literature reports no studies on characteristics and comprehensive analysis of continuous type hybrid PEC with chloralkali process. Also, the thesis study develops models for the exergoeconomic and exergoenvironmental analyses and assessments, along with an optimization study, which were not done elsewhere before for the integrated and hybrid systems developed here, while there were some studies on conventional electrolysis, photoelectrolysis, photocatalysis and chloralkali processes only.

In this study, after a literature review on H₂ production methods and background information, the present experimental setup and integrated system are introduced. Experiments are performed at CERL under various temperatures and inlet mass flow rates. Four different processes are tested experimentally: electrolysis, photochemical, chloralkali, and hybrid PEC-chloralkali. Next, the present integrated system is thermodynamically analyzed to investigate how H₂, Cl₂, electricity, and heat production, exergy destruction, and energy and exergy efficiencies are affected by the operating temperature, inlet mass flow rate, photoactive area, and environmental temperature. In the exergoeconomic and exergoenvironmental analyses, the changes in cost and emissions with respect to operating

temperature, inlet mass flow rate, photoactive area, and environmental temperature are presented. In the final step, a multi-objective optimization study is used to determine the optimum decision variables to deliver the highest possible production rates and efficiencies, and lowest possible exergy destruction, cost, and emissions of the present integrated system.

7.1 Conclusions

First, Process 1 (electrolysis), Process 2 (PEC), Process 3 (chloralkali), and Process 4 (hybrid PEC-chloralkali) are tested experimentally. The effect of the operating temperature and inlet mass flow rate on H₂ production rate and energy and exergy efficiencies are investigated experimentally. The experimental results are compared to the thermodynamic model outputs. Also, the thermodynamic model calculations are carried out using the EES software to investigate the effect of the operating temperature, inlet mass flow rate, and environmental temperature on H₂ production, energy and exergy efficiencies, and exergy destruction. The following are the summary of findings from the present experimental studies.

- The highest H₂ production rates of Processes 1 and 3 are observed experimentally at 80°C, which are 2.43 and 3.17 mg/h, respectively. 2.96 and 3.48 mg/h H₂ are produced experimentally at 80°C and under 1200 W/m² irradiation in Processes 2 and 4, respectively.
- The highest energy and exergy efficiencies of Process 1 are obtained at 20°C, which are 36% and 32%, respectively. In Process 2, these amounts are 20% and 22% at 20°C and 600 W/m² irradiation. The highest energy and exergy efficiencies of Process 3 are observed at 20°C, which are 50% and 39%, respectively. The highest energy and exergy efficiencies of Process 4 are obtained at 20°C and 600 W/m² irradiation, which are 27% and 26%, respectively.

Following the experimental tests, the present integrated system is thermodynamically investigated under various operating and environmental temperatures, inlet mass flow rates, and photoactive areas. The effects of these selected parameters on the present integrated system's performance can be summarized as

- The highest possible production rates, energy and exergy efficiencies, and exergy destruction are observed at the operating temperature of 30°C within the selected interval of 20°C to 80°C. At 30°C, 4.18 g/h H₂, 127.55 g/h Cl₂, 151 W electricity, and 716 W heat are produced. Exergy destruction rate is 95.74W. Overall energy and exergy efficiencies are 78% and 30%, respectively.
- 0.1 g/s is the optimum inlet mass flow rate within the selected interval of 0.1 to 15 g/s. At 0.1 g/s; 0.41 g/h H₂, 12.40 g/h Cl₂, 377 W electricity, and 800 W heat are produced. Exergy destruction rate is 1.25W. Overall energy and exergy efficiencies are 90% and 32%, respectively.
- Within the selected overall photoactive area interval of 2.7–6 m², the optimum size is 6 m². When this optimum size is used in the present integrated system, the production results are 8.86 g/h H₂, 243.98 g/h Cl₂, 361 W electricity, and 1200 W heat. Exergy destruction rate is 21.29 W. Overall energy and exergy efficiencies are 86% and 29%, respectively.
- The optimum environmental temperature is 20°C within the selected interval of 0°C to 40°C. At 20°C, 4.06 g/h H₂, 123.98 g/h Cl₂, 159 W electricity, and 800 W heat are produced. Exergy destruction rate is 23 W. Overall energy and exergy efficiencies are 85% and 28%, respectively.

The exergoeconomic analysis results show that the lowest H₂ production cost is 1.94 USD/kg H₂ when the photoactive area is 2.7 m², environmental and operating temperatures are 20°C and the inlet mass flow rate is 1 g/s. The exergoenvironmental analysis results suggest that the lowest H₂ production emissions is 2.01 kg CO₂/kg H₂ when the photoactive area is 2.7 m², environmental and operating temperatures are 20°C and the inlet mass flow rate is 1 g/s. The findings of the multi-objective optimization study of the present integrated system can be summarized as

- The highest H₂ and Cl₂ rates are 16 g/h and 453 g/h which are achieved at 100°C, 20 g/s inlet flow rate, 6 m² photoactive area, and 20°C environmental temperature. Under these conditions, the overall exergy efficiency is 22%, and H₂ production cost and emissions are 10.46 USD/kg H₂ and 16.08 kg CO₂/kg H₂.

- The highest electricity and heat production amounts are 453 W and 1695 W at 0°C operating temperature, 0.1 g/s inlet flow rate, 6 m² photoactive area, and 20°C environmental temperature. In this case, the overall exergy efficiency is 26%, and H₂ production cost and emissions are 9.64 USD/kg H₂ and 23.61 kg CO₂/kg H₂. Also, the highest overall energy efficiency of 98.13% is obtained in this case.
- The highest possible exergy efficiency of 38% is reached under 56°C operating temperature, 0.1 g/s inlet flow rate, 6 m² total photoactive area, and 0°C environmental temperature. Under the same conditions, H₂ production cost and emissions are 9.77 USD/kg H₂ and 22.98 kg CO₂/kg H₂.
- The minimum possible CO₂ emissions, 2.43 kg CO₂/kg H₂, is reached under 10°C operating temperature, 1 g/s inlet flow rate, 2 m² total photoactive area, and 10°C environmental temperature. Under the same conditions, the exergy efficiency is 26% and cost of H₂ production is 1.96 USD/kg H₂.
- A multi-objective optimization study is conducted to find the decision variables for highest possible production rates, energy and exergy efficiencies and lowest possible exergy destruction, cost, and emissions. These parameters are 1°C operating temperature, 1.4 g/s inlet flow rate, 6 m² total photoactive area, and 0°C environmental temperature. Under these conditions, the overall exergy efficiency is 30%, and cost and emissions are 9.67 USD/kg H₂ and 7.39 kg CO₂/kg H₂.

In this study, a hybrid reactor is built, experimentally tested, and thermodynamically assessed. It is shown that the hybrid reactor can operate under different conditions and in different processes. Based on the environmental conditions (e.g., day/night, cloudy days, lack of clean water, excess salty water, etc.), the hybrid reactor can be used in different process types and deliver end users' needs. Also, when the reactor is integrated with a solar spectral splitter and PV/T, it can provide multiple products, such as H₂, Cl₂, NaOH, heat, and electricity. In the literature, there is no other example of an integrated photoelectrochemical-chloralkali system with solar spectral splitter and PV/T. The novelty of this study is that the system is stand alone and it does not take any energy input other than the solar irradiation. The present integrated system's thermodynamic assessment shows that the system can operate in day/night cycles and in cloudy days.

7.2 Recommendations

There are many original contributions made by this thesis work on the PEC-based H₂ production. A detailed investigation is performed by experimental testing and system integration for sustainable H₂ production. However, there are several other issues to be considered as future studies for the PEC-based H₂ production. Several recommendations can be made for future research on PEC-based H₂ production are as follows:

- The photoactive membrane should be improved by testing new photoactive materials that have stability, low cost, abundance, efficiency, minimum losses, appropriate band gap, corrosion resistance, and stability for large scale production.
- Different photocatalyst deposition techniques, such as vapor deposition, spin coating, sol-gel, spray pyrolysis, etc. should be tested to determine if electrodeposition is the most suitable method on the membrane.
- The complete photocurrent spectrometer and semiconductor characterisation of the photoactive materials should be studied in order to fully understand the effective working regions of these materials in the solar spectrum. Also, different photoactive materials can be used together based on their semiconductor characteristics in order to increase the utilized portion of the solar spectrum.
- A large scale integrated system capable of providing above 1 kW energy should be tested experimentally. This system should employ the hybrid PEC integrated with solar spectral splitter and PV/T.
- The possibilities of system integration to various energy systems, such as bioreactors and desalination units should be investigated.
- A comprehensive three-dimensional transport phenomena modeling should be conducted numerically by taking temperature and concentration gradients into account.
- The prospect of synthetic fuel integration to the PEC-chloralkali system should be explored.

REFERENCES

- [1] International Energy Agency (IEA) Technical Report. 2015 Key World Energy Statistics. (2015). *Website*, [accessed on 06.02.2016] https://www.iea.org/publications/freepublications/publication/KeyWorld_Statistics_2015.pdf.
- [2] Friedlingstein, P., Andrew, R. M., Rogelj, J., Peters, G. P., Canadell, J. G., Knutti, R., Luderer, G., Raupach, M. R., Schaeffer, M., Van Vuuren, D. P., Le Quéré, C. (2014). Persistent growth of CO₂ emissions and implications for reaching climate targets. *Nature Geoscience*, 7(10), 709–715.
- [3] Gillett, N. P., Arora, V. K., Matthews, D., Allen, M. R. (2013). Constraining the ratio of global warming to cumulative CO₂ emissions using CMIP5 simulations. *Journal of Climate*, 26(18), 6844–6858.
- [4] Dincer, I., Acar, C. (2015). A review on clean energy solutions for better sustainability. *International Journal of Energy Research*, 39(5), 585–606.
- [5] Dincer, I. (2012). Green methods for hydrogen production. *International Journal of Hydrogen Energy*, 37(2), 1954–1971.
- [6] Dincer, I., Acar, C. (2015). Review and evaluation of hydrogen production methods for better sustainability. *International Journal of Hydrogen Energy*, 40(34), 11094–11111.
- [7] Acar, C., Dincer, I. (2015). Impact assessment and efficiency evaluation of hydrogen production methods. *International Journal of Energy Research*, 39(13), 1757–1768.
- [8] Acar, C., Dincer, I. (2014). Comparative assessment of hydrogen production methods from renewable and non-renewable sources. *International Journal of Hydrogen Energy*, 39(1), 1–12.
- [9] Hosseini, S. E., Wahid, M. A. (2016). Hydrogen production from renewable and sustainable energy resources: Promising green energy carrier for clean development. *Renewable and Sustainable Energy Reviews*, 57, 850–866.
- [10] Acar, C., Dincer, I. (2013). Comparative environmental impact evaluation of hydrogen production methods from renewable and nonrenewable sources. In *Causes, Impacts and Solutions to Global Warming* (493–514). Springer: New York.
- [11] Naterer, G. F., Suppiah, S., Stolberg, L., Lewis, M., Wang, Z., Dincer, I., Rosen, M. A., Gabriel, K., Secnik, E., Easton, E. B., Pioro, I. (2013). Progress of international hydrogen production network for the thermochemical Cu–Cl cycle. *International Journal of Hydrogen Energy*, 38(2), 740–759.
- [12] Naterer, G. F., Dincer, I., Zamfirescu, C. (2013). *Hydrogen Production from Nuclear Energy*. Springer: New York.
- [13] Naterer, G. F., Suppiah, S., Stolberg, L., Lewis, M., Ferrandon, M., Wang, Z., Dincer, I., Gabriel, K., Rosen, M. A., Secnik, E., Easton, E. B., Trevani, L., Pioro, I., Tremaine, P., Lvov, S., Jiang, J., Rizvi, G., Ikeda, B. M., Lu, L., Kaye, M., Smith,

- W. R., Mostaghimi, J., Spekkens, P., Fowler, M., Avsec, J. (2011) Clean hydrogen production with the Cu-Cl cycle – Progress of International Consortium, I: Experimental Unit Operations” *International Journal of Hydrogen Energy*, 36(24), 15472–15485.
- [14] Zhang, Y., Wang, R., Lin, X., Wang, Z., Liu, J., Zhou, J., Cen, K. (2015). Catalytic performance of different carbon materials for hydrogen production in sulfur–iodine thermochemical cycle. *Applied Catalysis B: Environmental*, 166, 413–422.
- [15] Basile, A., Iulianelli, A. (2014). *Advances in Hydrogen Production, Storage and Distribution*. Elsevier: New York.
- [16] Sharma, S., Ghoshal, S. K. (2015). Hydrogen the future transportation fuel: From production to applications. *Renewable and Sustainable Energy Reviews*, 43, 1151–1158.
- [17] Giraldi, M. R., François, J. L., Martin-del-Campo, C. (2015). Life cycle assessment of hydrogen production from a high temperature electrolysis process coupled to a high temperature gas nuclear reactor. *International Journal of Hydrogen Energy*, 40(10), 4019–4033.
- [18] Clark, J. H., Deswarte, F. (2015). *Introduction to Chemicals from Biomass*. John Wiley and Sons: New York.
- [19] Acar, C., Dincer, I., Zamfirescu, C. (2014). A review on selected heterogeneous photocatalysts for hydrogen production. *International Journal of Energy Research*, 38(15), 1903–1920.
- [20] Dincer, I., Zamfirescu, C. (2012). Sustainable hydrogen production options and the role of IAHE. *International Journal of Hydrogen Energy*, 37(21), 16266–16286.
- [21] Lewis, N. S., Nocera, D. G. (2006). Powering the planet: Chemical challenges in solar energy utilization. *Proceedings of the National Academy of Sciences*, 103(43), 15729–15735.
- [22] Keohane, R. O. (2015). The global politics of climate change: Challenge for political science. *PS: Political Science and Politics*, 48(1), 19–26.
- [23] Hoffert, M. I. (2010). Farewell to fossil fuels? *Science*, 329(5997), 1292–1294.
- [24] Van de Krol, R., Grätzel, M. (2012). *Photoelectrochemical Hydrogen Production* (Vol. 90). Springer: New York.
- [25] Dincer I., Zamfirescu, C. (2011). *Sustainable Energy Systems and Applications* Springer: New York.
- [26] Zamfirescu, C., Dincer, I., Naterer, G. F. (2011). Analysis of a photochemical water splitting reactor with supramolecular catalysts and a proton exchange membrane. *International Journal of Hydrogen Energy*, 36(17), 11273–11281.
- [27] Zamfirescu, C., Dincer, I., Naterer, G. F., Banica, R. (2013). Quantum efficiency modeling and system scaling-up analysis of water splitting with Cd_{1-x}Zn_xS solid-solution photocatalyst. *Chemical Engineering Science*, 97, 235–255.

- [28] Chen, Z., Dinh, H. N., Miller, E. (2013). *Photoelectrochemical Water Splitting*. Springer Briefs in Energy: New York.
- [29] Joshi, A. S., Dincer, I., Reddy, B. V. (2011). Solar hydrogen production: A comparative performance assessment. *International Journal of Hydrogen Energy*, 36(17), 11246–11257.
- [30] Fujishima, A., Honda, K. (1972). Electrochemical photolysis of water at a semiconductor electrode. *Nature*, 238, 37–38.
- [31] Luo, J., Im, J. H., Mayer, M. T., Schreier, M., Nazeeruddin, M. K., Park, N. G., Tilley, S. D., Fan, H. J., Grätzel, M. (2014). Water photolysis at 12.3% efficiency via perovskite photovoltaics and Earth-abundant catalysts. *Science*, 345(6204), 1593–1596.
- [32] Memming, R., Bahnemann, D. (2015). *Semiconductor Electrochemistry*. John Wiley and Sons: New York.
- [33] Minggu, L. J., Daud, W. R. W., Kassim, M. B. (2010). An overview of photocells and photoreactors for photoelectrochemical water splitting. *International Journal of Hydrogen Energy*, 35(11), 5233–5244.
- [34] Xing, Z., Zong, X., Pan, J., Wang, L. (2013). On the engineering part of solar hydrogen production from water splitting: photoreactor design. *Chemical Engineering Science*, 104, 125–146.
- [35] Molinari, R., Marino, T., Argurio, P. (2014). Photocatalytic membrane reactors for hydrogen production from water. *International Journal of Hydrogen Energy*, 39(14), 7247–7261.
- [36] Polman, A., Atwater, H. A. (2012). Photonic design principles for ultrahigh-efficiency photovoltaics. *Nature Materials*, 11(3), 174–177.
- [37] Dincer, I., Rosen, M. A. (2011). Sustainability aspects of hydrogen and fuel cell systems. *Energy for Sustainable Development*, 15(2), 137–146.
- [38] Gibson, T. L., Kelly, N. A. (2010). Predicting efficiency of solar powered hydrogen generation using photovoltaic-electrolysis devices. *International Journal of Hydrogen Energy*, 35(3), 900–911.
- [39] Dincer, I. (2007). Environmental and sustainability aspects of hydrogen and fuel cell systems. *International Journal of Energy Research*, 31(1), 29–55.
- [40] Novak, P. (2015). Sustainable energy system with zero emissions of GHG for cities and countries. *Energy and Buildings*, 98, 27–33.
- [41] Peter, L. M. (2015). Photoelectrochemical water splitting. A status assessment. *Electroanalysis*, 27(4), 864–871.
- [42] Schiavello, M. (2013). *Photoelectrochemistry, Photocatalysis and Photoreactors Fundamentals and Developments* (Vol. 146). Springer Science and Business Media: New York.

- [43] Schulze, T. F., Schmidt, T. W. (2015). Photochemical upconversion: present status and prospects for its application to solar energy conversion. *Energy and Environmental Science*, 8(1), 103–125.
- [44] Pinaud, B.A., Benck, J.D., Seitz, L.C., Forman, A.J., Chen, Z., Deutsch, T.G., James, B.D., Baum, K.N., Baum, G.N., Ardo, S. Wang, H. (2013). Technical and economic feasibility of centralized facilities for solar hydrogen production via photocatalysis and photoelectrochemistry. *Energy and Environmental Science*, 6(7), 1983–2002.
- [45] Kamat, P. V., Bisquert, J. (2013). Solar fuels. Photocatalytic hydrogen generation. *The Journal of Physical Chemistry C*, 117(29), 14873–14875.
- [46] Zamfirescu, C., Naterer, G. F., Dincer, I. (2012). Solar light based hydrogen production systems. *Encyclopedia of Energy Engineering and Technology*, Taylor and Francis: New York.
- [47] Seger, B., Pedersen, T., Laursen, A. B., Vesborg, P. C., Hansen, O., Chorkendorff, I. (2013). Using TiO₂ as a conductive protective layer for photocathodic H₂ evolution. *Journal of the American Chemical Society*, 135(3), 1057–1064.
- [48] Nowotny, J., Bak, T., Chu, D., Fiechter, S., Murch, G. E., Veziroglu, T. N. (2014). Sustainable practices: Solar hydrogen fuel and education program on sustainable energy systems. *International Journal of Hydrogen Energy*, 39(9), 4151–4157.
- [49] Li, Z., Luo, W., Zhang, M., Feng, J., Zou, Z. (2013). Photoelectrochemical cells for solar hydrogen production: current state of promising photoelectrodes, methods to improve their properties, and outlook. *Energy and Environmental Science*, 6(2), 347–370.
- [50] Liu, B., Wu, C. H., Miao, J., Yang, P. (2014). All inorganic semiconductor nanowire mesh for direct solar water splitting. *ACS Nano*, 8(11), 11739–11744.
- [51] Prévot, M. S., Sivula, K. (2013). Photoelectrochemical tandem cells for solar water splitting. *The Journal of Physical Chemistry C*, 117(35), 17879–17893.
- [52] Lin, Y., Battaglia, C., Boccard, M., Hettick, M., Yu, Z., Ballif, C., Ager, J. W., Javey, A. (2013). Amorphous Si thin film based photocathodes with high photovoltage for efficient hydrogen production. *Nano Letters*, 13(11), 5615–5618.
- [53] Ohta, T. (2013). *Solar-hydrogen Energy Systems: An Authoritative Review of Water-splitting Systems by Solar Beam and Solar Heat: Hydrogen Production, Storage and Utilization*. Elsevier: New York.
- [54] Abe, R., Shinmei, K., Koumura, N., Hara, K., Ohtani, B. (2013). Visible-light-induced water splitting based on two-step photoexcitation between dye-sensitized layered niobate and tungsten oxide photocatalysts in the presence of a triiodide/iodide shuttle redox mediator. *Journal of the American Chemical Society*, 135(45), 16872–16884.
- [55] Liao, C. H., Huang, C. W., Wu, J. (2012). Hydrogen production from semiconductor-based photocatalysis via water splitting. *Catalysts*, 2(4), 490–516.

- [56] Liu, C., Tang, J., Chen, H. M., Liu, B., Yang, P. (2013). A fully integrated nanosystem of semiconductor nanowires for direct solar water splitting. *Nano Letters*, 13(6), 2989–2992.
- [57] Liu, C., Hwang, Y. J., Jeong, H. E., Yang, P. (2011). Light-induced charge transport within a single asymmetric nanowire. *Nano Letters*, 11(9), 3755–3758.
- [58] Gao, Y., Ding, X., Liu, J., Wang, L., Lu, Z., Li, L., Sun, L. (2013). Visible light driven water splitting in a molecular device with unprecedentedly high photocurrent density. *Journal of the American Chemical Society*, 135(11), 4219–4222.
- [59] Lai, C. W., Sreekantan, S. (2013). Preparation of hybrid WO₃–TiO₂ nanotube photoelectrodes using anodization and wet impregnation: Improved water-splitting hydrogen generation performance. *International Journal of Hydrogen Energy*, 38(5), 2156–2166.
- [60] Georgieva, J., Valova, E., Armyanov, S., Philippidis, N., Poullos, I., Sotiropoulos, S. (2012). Bi-component semiconductor oxide photoanodes for the photoelectrocatalytic oxidation of organic solutes and vapours: a short review with emphasis to TiO₂–WO₃ photoanodes. *Journal of Hazardous Materials*, 211, 30–46.
- [61] ThanhThuy, T. T., Feng, H., Cai, Q. (2013). Photocatalytic degradation of pentachlorophenol on ZnSe/TiO₂ supported by photo-Fenton system. *Chemical Engineering Journal*, 223, 379–387.
- [62] Meshram, S. P., Adhyapak, P. V., Mulik, U. P., Amalnerkar, D. P. (2012). Facile synthesis of CuO nanomorphs and their morphology dependent sunlight driven photocatalytic properties. *Chemical Engineering Journal*, 204, 158–168.
- [63] Le, T. T., Akhtar, M. S., Park, D. M., Lee, J. C., Yang, O. B. (2012). Water splitting on rhodamine-B dye sensitized Co-doped TiO₂ catalyst under visible light. *Applied Catalysis B: Environmental*, 111, 397–401.
- [64] Nouri, J., Nouri, N., Moeeni, M. (2012). Development of industrial waste disposal scenarios using life-cycle assessment approach. *International Journal of Environmental Science and Technology*, 9(3), 417–424.
- [65] Hosseini, M. G., Momeni, M. M. (2012). UV-cleaning properties of Pt nanoparticle-decorated Titania nanotubes in the electro-oxidation of methanol: An anti-poisoning and refreshable electrode. *Electrochimica Acta*, 70, 1–9.
- [66] Dong, X., Li, Y., Lin, Z., Ge, J., Qiu, J. (2013). Oriented TiO₂ nanowire array grown on curved surface of Ti wire with superior photoelectrochemical properties. *Applied Surface Science*, 270, 457–461.
- [67] Chang, W., Xu, F., Mu, X., Ji, L., Ma, G., Nie, J. (2013). Fabrication of nanostructured hollow TiO₂ nanofibers with enhanced photocatalytic activity by coaxial electrospinning. *Materials Research Bulletin*, 48(7), 2661–2668.
- [68] Petronella, F., Diomede, S., Fanizza, E., Mascolo, G., Sibillano, T., Agostiano, A., Curri, M. L., Comparelli, R. (2013). Photodegradation of nalidixic acid assisted by TiO₂ nanorods/Ag nanoparticles based catalyst. *Chemosphere*, 91(7), 941–947.

- [69] Xiao, Q., Ouyang, L., Gao, L., Yao, C. (2011). Preparation and visible light photocatalytic activity of mesoporous N, S-codoped TiO₂ (B) nanobelts. *Applied Surface Science*, 257(8), 3652–3656.
- [70] Jang, J. S., Kim, H. G., Lee, J. S. (2012). Heterojunction semiconductors: A strategy to develop efficient photocatalytic materials for visible light water splitting. *Catalysis Today*, 185(1), 270–277.
- [71] Rabbani, M., Dincer, I., Naterer, G. F. (2014). Efficiency assessment of a photo electrochemical chloralkali process for hydrogen and sodium hydroxide production. *International Journal of Hydrogen Energy*, 39(5), 1941–1956.
- [72] Acar, C., Dincer, I. (2014). Analysis and assessment of a continuous-type hybrid photoelectrochemical system for hydrogen production. *International Journal of Hydrogen Energy*, 39(28), 15362–15372.
- [73] Acar, C., Ghosh, S., Dincer, I., Zamfirescu, C. (2015). Evaluation of a new continuous type hybrid photo-electrochemical system. *International Journal of Hydrogen Energy*, 40(34), 11112–11124.
- [74] Carver, C., Ulissi, Z., Ong, C. K., Dennison, S., Kelsall, G. H., Hellgardt, K. (2012). Modelling and development of photoelectrochemical reactor for H₂ production. *International Journal of Hydrogen Energy*, 37(3), 2911–2923.
- [75] Higashi, M., Domen, K., Abe, R. (2012). Highly stable water splitting on oxynitride TaON photoanode system under visible light irradiation. *Journal of the American Chemical Society*, 134(16), 6968–6971.
- [76] Karuturi, S. K., Luo, J., Cheng, C., Liu, L., Su, L. T., Tok, A. I. Y., Fan, H. J. (2012). A novel photoanode with three-dimensionally, hierarchically ordered nanobushes for highly efficient photoelectrochemical cells. *Advanced Materials*, 24(30), 4157–4162.
- [77] Luo, J., Ma, L., He, T., Ng, C. F., Wang, S., Sun, H., Fan, H. J. (2012). TiO₂/(CdS, CdSe, CdSeS) nanorod heterostructures and photoelectrochemical properties. *The Journal of Physical Chemistry C*, 116(22), 11956–11963.
- [78] Maeda, K., Higashi, M., Siritanaratkul, B., Abe, R., Domen, K. (2011). SrNbO₂N as a water-splitting photoanode with a wide visible-light absorption band. *Journal of the American Chemical Society*, 133(32), 12334–12337.
- [79] Ida, S., Yamada, K., Matsunaga, T., Hagiwara, H., Matsumoto, Y., Ishihara, T. (2010). Preparation of p-type CaFe₂O₄ photocathodes for producing hydrogen from water. *Journal of the American Chemical Society*, 132(49), 17343–17345.
- [80] Li, Y., Yu, H., Song, W., Li, G., Yi, B., Shao, Z. (2011). A novel photoelectrochemical cell with self-organized TiO₂ nanotubes as photoanodes for hydrogen generation. *International Journal of Hydrogen Energy*, 36(22), 14374–14380.
- [81] Karuturi, S. K., Luo, J., Cheng, C., Liu, L., Su, L. T., Tok, A. I. Y., Fan, H. J. (2012). A novel photoanode with three-dimensionally, hierarchically ordered nanobushes

- for highly efficient photoelectrochemical cells. *Advanced Materials*, 24(30), 4157–4162.
- [82] Paracchino, A., Laporte, V., Sivula, K., Grätzel, M., Thimsen, E. (2011). Highly active oxide photocathode for photoelectrochemical water reduction. *Nature Materials*, 10(6), 456–461.
- [83] Tétreault, N., Arsenault, É., Heiniger, L. P., Soheilnia, N., Brillet, J., Moehl, T., Zakeeruddin, S., Ozin, G. A., Grätzel, M. (2011) High-efficiency dye-sensitized solar cell with three-dimensional photoanode. *Nano Letters*, 11(11), 4579–4584.
- [84] Vidyarthi, V. S., Hofmann, M., Savan, A., Sliozberg, K., König, D., Beranek, R., Schuhmann, W., Ludwig, A. (2011). Enhanced photoelectrochemical properties of WO₃ thin films fabricated by reactive magnetron sputtering. *International Journal of Hydrogen Energy*, 36(8), 4724–4731.
- [85] Tseng, C. J., Wang, C. H., Cheng, K. W. (2012). Photoelectrochemical performance of gallium-doped AgInS₂ photoelectrodes prepared by electrodeposition process. *Solar Energy Materials and Solar Cells*, 96, 33–42.
- [86] Acar, C., Dincer, I. (2016). A review and evaluation of photoelectrode coating materials and methods for photoelectrochemical hydrogen production. *International Journal of Hydrogen Energy*, 41(19), 7950–7959.
- [87] Lo, C. C., Huang, C. W., Liao, C. H., Wu, J. C. (2010). Novel twin reactor for separate evolution of hydrogen and oxygen in photocatalytic water splitting. *International Journal of Hydrogen Energy*, 35(4), 1523–1529.
- [88] Yu, S. C., Huang, C. W., Liao, C. H., Wu, J. C., Chang, S. T., Chen, K. H. (2011). A novel membrane reactor for separating hydrogen and oxygen in photocatalytic water splitting. *Journal of Membrane Science*, 382(1), 291–299.
- [89] Tsydenov, D. E., Parmon, V. N., Vorontsov, A. V. (2012). Toward the design of asymmetric photocatalytic membranes for hydrogen production: preparation of TiO₂-based membranes and their properties. *International Journal of Hydrogen Energy*, 37(15), 11046–11060.
- [90] Liao, C. H., Huang, C. W., Wu, J. C. (2012). Novel dual-layer photoelectrode prepared by RF magnetron sputtering for photocatalytic water splitting. *International Journal of Hydrogen Energy*, 37(16), 11632–11639.
- [91] Marschall, R., Klaysom, C., Mukherji, A., Wark, M., Lu, G. Q. M., Wang, L. (2012). Composite proton-conducting polymer membranes for clean hydrogen production with solar light in a simple photoelectrochemical compartment cell. *International Journal of Hydrogen Energy*, 37(5), 4012–4017.
- [92] Klaysom, C., Marschall, R., Wang, L., Ladewig, B. P., Lu, G. M. (2010). Synthesis of composite ion-exchange membranes and their electrochemical properties for desalination applications. *Journal of Materials Chemistry*, 20(22), 4669–4674.
- [93] Ohta, T., Kamiya, N., Yamaguchi, M., Gotoh, N., Otagawa, T., Asakura, S. (1978). System efficiency of a water-splitting system synthesized by photochemical and

- thermoelectric conversion of solar energy. *International Journal of Hydrogen Energy*, 3(2), 203–208.
- [94] Abdin, Z., Webb, C. J., Gray, E. M. (2015). Solar hydrogen hybrid energy systems for off-grid electricity supply: A critical review. *Renewable and Sustainable Energy Reviews*, 52, 1791–1808.
- [95] Shabani, B., Andrews, J. (2015). Standalone solar-hydrogen systems powering fire contingency networks. *International Journal of Hydrogen Energy*, 40(15), 5509–5517.
- [96] Belmili, H., Haddadi, M., Bacha, S., Almi, M. F., Bendib, B. (2014). Sizing stand-alone photovoltaic–wind hybrid system: Techno-economic analysis and optimization. *Renewable and Sustainable Energy Reviews*, 30, 821–832.
- [97] Baniasadi, E., Dincer, I., Naterer, G. F. (2012). Performance analysis of a water splitting reactor with hybrid photochemical conversion of solar energy. *International Journal of Hydrogen Energy*, 37(9), 7464–7472.
- [98] Baniasadi, E., Dincer, I., Naterer, G. F. (2012). Radiative heat transfer and catalyst performance in a large-scale continuous flow photoreactor for hydrogen production. *Chemical Engineering Science*, 84, 638–645.
- [99] Zamfirescu, C., Dincer, I., Naterer, G. F. (2012). Molecular charge transfer and quantum efficiency analyses of a photochemical reactor for hydrogen production. *International Journal of Hydrogen Energy*, 37(12), 9537–9549.
- [100] Zamfirescu, C., Naterer, G. F., Dincer, I. (2013). Water splitting with a dual photo-electrochemical cell and hybrid catalysis for enhanced solar energy utilization. *International Journal of Energy Research*, 37(10), 1175–1186.
- [101] Huang, C. W., Liao, C. H., Wu, C. H., Wu, J. C. (2012). Photocatalytic water splitting to produce hydrogen using multi-junction solar cell with different deposited thin films. *Solar Energy Materials and Solar Cells*, 107, 322–328.
- [102] Fuentes, M., Vivar, M., Scott, J., Srithar, K., Skryabin, I. (2012). Results from a first autonomous optically adapted photocatalytic–photovoltaic module for water purification. *Solar Energy Materials and Solar Cells*, 100, 216–225.
- [103] Baniasadi, E., Dincer, I., Naterer, G. F. (2013). Measured effects of light intensity and catalyst concentration on photocatalytic hydrogen and oxygen production with zinc sulfide suspensions. *International Journal of Hydrogen Energy*, 38(22), 9158–9168.
- [104] Zamfirescu, C., Dincer, I. (2014). Assessment of a new integrated solar energy system for hydrogen production. *Solar Energy*, 107, 700–713.
- [105] Rabbani, M., Dincer, I., Naterer, G. F. (2014). Electrochemical analysis of a photoelectrochemical chloralkali reactor. *Chemical Engineering and Processing: Process Intensification*, 82, 42–53.
- [106] Baniasadi, E., Dincer, I., Naterer, G. F. (2014). Scale-up analysis and exergoeconomic assessment of large scale photo-catalytic hydrogen production plants. *Solar Energy*, 107, 475–488.

- [107] Dincer, I., Naterer, G. F. (2014). Overview of hydrogen production research in the Clean Energy Research Laboratory (CERL) at UOIT. *International Journal of Hydrogen Energy*, 39(35), 20592–20613.
- [108] Dincer, I., Zamfirescu, C. (2012). Renewable-energy-based multigeneration systems. *International Journal of Energy Research*, 36(15), 1403–1415.
- [109] Cetin, E., Yilanci, A., Oner, Y., Colak, M., Kasikci, I., Ozturk, H. K. (2009). Electrical analysis of a hybrid photovoltaic-hydrogen/fuel cell energy system in Denizli, Turkey. *Energy and Buildings*, 41(9), 975–981.
- [110] Zamfirescu, C., Naterer, G. F., Dincer, I. (2012). Photo-electro-chemical chlorination of cuprous chloride with hydrochloric acid for hydrogen production. *International Journal of Hydrogen Energy*, 37(12), 9529–9536.
- [111] Baniasadi, E., Dincer, I., Naterer, G. F. (2013). Oxygen evolving reactor overpotentials and ion diffusion in photo-catalytic and electro-catalytic hydrogen production. *International Journal of Hydrogen Energy*, 38(14), 6112–6119.
- [112] Joya, K. S., Joya, Y. F., Ocakoglu, K., van de Krol, R. (2013). Water-splitting catalysis and solar fuel devices: Artificial leaves on the move. *Angewandte Chemie International Edition*, 52(40), 10426–10437.
- [113] Abdi, F. F., Firet, N., van de Krol, R. (2013). Efficient BiVO₄ thin film photoanodes modified with Cobalt Phosphate catalyst and W-doping. *ChemCatChem*, 5(2), 490–496.
- [114] Bornoz, P., Abdi, F. F., Tilley, S. D., Dam, B., Van De Krol, R., Graetzel, M., Sivula, K. (2014). A bismuth vanadate–cuprous oxide tandem cell for overall solar water splitting. *The Journal of Physical Chemistry C*, 118(30), 16959–16966.
- [115] Dabirian, A., Van De Krol, R. (2015). High-temperature ammonolysis of thin film Ta₂O₅ photoanodes: Evolution of structural, optical, and photoelectrochemical properties. *Chemistry of Materials*, 27(3), 708–715.
- [116] Proot, J. P., Delerue, C., Allan, G. (1992). Electronic structure and optical properties of silicon crystallites: application to porous silicon. *Applied Physics Letters*, 61(16), 1948–1950.
- [117] Ismail, A. A., Bahnemann, D. W. (2014). Photochemical splitting of water for hydrogen production by photocatalysis: A review. *Solar Energy Materials and Solar Cells*, 128, 85–101.
- [118] Kreibig, U., Vollmer, M. (2013). *Optical Properties of Metal Clusters* (Vol. 25). Springer Science and Business Media: New York.
- [119] Raman, A. (2013). *Physics of Semiconductor Devices*. Shree Publishers and Distributors: India.
- [120] Kittel, C. (2005). *Introduction to Solid State Physics*. John Wiley and Sons: New York.
- [121] Deskins, N. A., Dupuis, M. (2008). Intrinsic hole migration rates in TiO₂ from density functional theory. *The Journal of Physical Chemistry C*, 113(1), 346–358.

- [122] Nozik, A. J. (2001). Spectroscopy and hot electron relaxation dynamics in semiconductor quantum wells and quantum dots. *Annual Review of Physical Chemistry*, 52(1), 193–231.
- [123] Takeda, H., Adachi, K. (2007). Near infrared absorption of tungsten oxide nanoparticle dispersions. *Journal of the American Ceramic Society*, 90(12), 4059–4061.
- [124] Tsuda, N., Nasu, K., Fujimori, A., Siratori, K. (2013). *Electronic Conduction in Oxides* (Vol. 94). Springer Science and Business Media: New York.
- [125] Matsuzaki, K., Nomura, K., Yanagi, H., Kamiya, T., Hirano, M., Hosono, H. (2008). Epitaxial growth of high mobility Cu₂O thin films and application to p-channel thin film transistor. *Applied Physics Letters*, 93(20), 210–217.
- [126] Asahi, R., Morikawa, T., Ohwaki, T., Aoki, K., Taga, Y. (2002). Photocatalysts sensitive to visible light-response. *Science*, 295(5555), 627–627.
- [127] Di Paola, A., Marci, G., Palmisano, L., Schiavello, M., Uosaki, K., Ikeda, S., Ohtani, B. (2002). Preparation of polycrystalline TiO₂ photocatalysts impregnated with various transition metal ions: characterization and photocatalytic activity for the degradation of 4-nitrophenol. *The Journal of Physical Chemistry B*, 106(3), 637–645.
- [128] Tsujiko, A., Itoh, H., Kisumi, T., Shiga, A., Murakoshi, K., Nakato, Y. (2002). Observation of cathodic photocurrents at nanocrystalline TiO₂ film electrodes, caused by enhanced oxygen reduction in alkaline solutions. *The Journal of Physical Chemistry B*, 106(23), 5878–5885.
- [129] Diebold, U. (2003). The surface science of titanium dioxide. *Surface Science Reports*, 48(5), 53–229.
- [130] Kato, H., Kudo, A. (2002). Visible-light-response and photocatalytic activities of TiO₂ and SrTiO₃ photocatalysts codoped with antimony and chromium. *The Journal of Physical Chemistry B*, 106(19), 5029–5034.
- [131] Kay, A., Grätzel, M. (2002). Dye-sensitized core-shell nanocrystals: improved efficiency of mesoporous tin oxide electrodes coated with a thin layer of an insulating oxide. *Chemistry of Materials*, 14(7), 2930–2935.
- [132] Rajeshwar, K., McConnell, R. D., Licht, S. (Eds.). (2008). *Solar Hydrogen Generation*. Springer: New York.
- [133] Kudo, A., Miseki, Y. (2009). Heterogeneous photocatalyst materials for water splitting. *Chemical Society Reviews*, 38(1), 253–278.
- [134] Ritterskamp, P., Kuklya, A., Wüstkamp, M. A., Kerpen, K., Weidenthaler, C., Demuth, M. (2007). A titanium disilicide derived semiconducting catalyst for water splitting under solar radiation—reversible storage of oxygen and hydrogen. *Angewandte Chemie International Edition*, 46(41), 7770–7774.
- [135] National Renewable Energy Laboratory (NREL). Reference Solar Spectral Irradiance: Air Mass 1.5. *Website*, [accessed on 10.02.2016] <http://rredc.nrel.gov/solar/spectra/am1.5/>.

- [136] Santato, C., Ulmann, M., Augustynski, J. (2001). Enhanced visible light conversion efficiency using nanocrystalline WO₃ films. *Advanced Materials*, 13(7), 511–514.
- [137] Cho, I. S., Chen, Z., Forman, A. J., Kim, D. R., Rao, P. M., Jaramillo, T. F., Zheng, X. (2011). Branched TiO₂ nanorods for photoelectrochemical hydrogen production. *Nano Letters*, 11(11), 4978–4984.
- [138] Park, N. G., Van de Lagemaat, J., Frank, A. J. (2000). Comparison of dye-sensitized rutile-and anatase-based TiO₂ solar cells. *The Journal of Physical Chemistry B*, 104(38), 8989–8994.
- [139] van de Krol, R., Liang, Y., Schoonman, J. (2008). Solar hydrogen production with nanostructured metal oxides. *Journal of Materials Chemistry*, 18(20), 2311–2320.
- [140] Licht, S., Wang, B., Mukerji, S., Soga, T., Umeno, M., Tributsch, H. (2000). Efficient solar water splitting, exemplified by RuO₂-catalyzed AlGaAs/Si photoelectrolysis. *The Journal of Physical Chemistry B*, 104(38), 8920–8924.
- [141] Murphy, A. B., Barnes, P. R. F., Randeniya, L. K., Plumb, I. C., Grey, I. E., Horne, M. D., Glasscock, J. A. (2006). Efficiency of solar water splitting using semiconductor electrodes. *International Journal of Hydrogen Energy*, 31(14), 1999–2017.
- [142] Youngblood, W. J., Lee, S. H. A., Kobayashi, Y., Hernandez-Pagan, E. A., Hoertz, P. G., Moore, T. A., Moore, A. L., Gust, D., Mallouk, T. E. (2009). Photoassisted overall water splitting in a visible light-absorbing dye-sensitized photoelectrochemical cell. *Journal of the American Chemical Society*, 131(3), 926–927.
- [143] Kanan, M. W., Nocera, D. G. (2008). In situ formation of an oxygen-evolving catalyst in neutral water containing phosphate and Co²⁺. *Science*, 321(5892), 1072–1075.
- [144] Maeda, K., Teramura, K., Lu, D., Takata, T., Saito, N., Inoue, Y., Domen, K. (2006). Photocatalyst releasing hydrogen from water. *Nature*, 440(7082), 295–295.
- [145] Alexander, B. D., Kulesza, P. J., Rutkowska, I., Solarska, R., Augustynski, J. (2008). Metal oxide photoanodes for solar hydrogen production. *Journal of Materials Chemistry*, 18(20), 2298–2303.
- [146] Kay, A., Cesar, I., Grätzel, M. (2006). New benchmark for water photooxidation by nanostructured α -Fe₂O₃ films. *Journal of the American Chemical Society*, 128(49), 15714–15721.
- [147] Sayama, K., Nomura, A., Arai, T., Sugita, T., Abe, R., Yanagida, M., Oi, T., Iwasaki, Y., Abe, Y., Sugihara, H. (2006). Photoelectrochemical decomposition of water into H₂ and O₂ on porous BiVO₄ thin-film electrodes under visible light and significant effect of Ag ion treatment. *The Journal of Physical Chemistry B*, 110(23), 11352–11360.
- [148] Kharton, V. V. (Ed.). (2009). *Solid State Electrochemistry I: Fundamentals, Materials and Their Applications*. John Wiley and Sons: New York.

- [149] Oldham, K., Myland, J., Bond, A. (2011). *Electrochemical Science and Technology: Fundamentals and Applications*. John Wiley and Sons: New York.
- [150] Nian, J. N., Hu, C. C., Teng, H. (2008). Electrodeposited p-type Cu₂O for H₂ evolution from photoelectrolysis of water under visible light illumination. *International Journal of Hydrogen Energy*, 33(12), 2897–2903.
- [151] Hu, C. C., Nian, J. N., Teng, H. (2008). Electrodeposited p-type Cu₂O as photocatalyst for H₂ evolution from water reduction in the presence of WO₃. *Solar Energy Materials and Solar Cells*, 92(9), 1071–1076.
- [152] Zhu, H., Zhang, J., Li, C., Pan, F., Wang, T., Huang, B. (2009). Cu₂O thin films deposited by reactive direct current magnetron sputtering. *Thin Solid Films*, 517(19), 5700–5704.
- [153] Yang, W. Y., Kim, W. G., Rhee, S. W. (2008). Radio frequency sputter deposition of single phase cuprous oxide using Cu₂O as a target material and its resistive switching properties. *Thin Solid Films*, 517(2), 967–971.
- [154] Eisermann, S., Kronenberger, A., Laufer, A., Bieber, J., Haas, G., Lautenschläger, S., Homm, G., Klar, P.J. Meyer, B.K. (2012). Copper oxide thin films by chemical vapor deposition: Synthesis, characterization and electrical properties. *Physica Status Solidi (A)*, 209(3), 531–536.
- [155] Liang, J., Kishi, N., Soga, T., Jimbo, T., Ahmed, M. (2012). Thin cuprous oxide films prepared by thermal oxidation of copper foils with water vapor. *Thin Solid Films*, 520(7), 2679–2682.
- [156] Ahirrao, P. B., Sankapal, B. R., Patil, R. S. (2011). Nanocrystalline p-type-cuprous oxide thin films by room temperature chemical bath deposition method. *Journal of Alloys and Compounds*, 509(18), 5551–5554.
- [157] Izaki, M., Shinagawa, T., Mizuno, K. T., Ida, Y., Inaba, M., Tasaka, A. (2007). Electrochemically constructed p-Cu₂O/n-ZnO heterojunction diode for photovoltaic device. *Journal of Physics D: Applied Physics*, 40(11), 3326–3329.
- [158] Xi, Z., Zeng, H., Liao, N., Shi, L., Huang, H., Guo, S., Wang, N., Jin, D. Wang, L., 2012. Study on the effect of annealing on the electrical properties of n-type cuprous oxide. *Thin Solid Films*, 520(7), 2708–2710.
- [159] Paracchino, A., Laporte, V., Sivula, K., Grätzel, M., Thimsen, E. (2011). Highly active oxide photocathode for photoelectrochemical water reduction. *Nature Materials*, 10(6), 456–461.
- [160] Wang, P., Wu, H., Tang, Y., Amal, R., Ng, Y. H. (2015). Electrodeposited Cu₂O as photoelectrodes with controllable conductivity type for solar energy conversion. *The Journal of Physical Chemistry C*, 119(47), 26275–26282.
- [161] Webster, J. G., Eren, H. (Eds.). (2014). *Measurement, Instrumentation, and Sensors Handbook: Spatial, Mechanical, Thermal, and Radiation Measurement (Vol. 1)*. CRC press: New York.
- [162] Northrop, R. B. (1997). *Introduction to Instrumentation and Measurements*. CRC Press: Boca Raton, FL.

- [163] Pope, K. (2012). *Multiphase Flow and Chemical Reactor Thermodynamics for Hydrolysis and Thermochemical Hydrogen Production*. (Doctoral dissertation, University of Ontario Institute of Technology).
- [164] Jianu, O. A. (2013). *Mass Transfer and Particle Dissolution in Liquid-gas and Solid-liquid Flows: Application to Hydrogen Production Processes*. (Doctoral dissertation, University of Ontario Institute of Technology).
- [165] Annual book of ASTM standards. (2008). *G173, Standard Tables for Reference Solar Spectral Irradiances: Direct Normal and Hemispherical on 37 Tilted Surface*.
- [166] Cengel, Y. A., Boles M. A. (2015). *Thermodynamics: An Engineering Approach*. McGraw-Hill Education: New York.
- [167] Annamalai, K., Puri, I. K., Jog, M. A. (2010). *Advanced Thermodynamics Engineering*. CRC Press: New York.
- [168] Sparrow, B. S. (2003). Empirical equations for the thermodynamic properties of aqueous sodium chloride. *Desalination*, 159(2), 161–170.
- [169] Dincer, I., Rosen, M. A. (2012). *Energy, Environment, and Sustainable Development*. Elsevier: Oxford.
- [170] BoroumandJazi, G., Rismanchi, B., Saidur, R. (2013). A review on exergy analysis of industrial sector. *Renewable and Sustainable Energy Reviews*, 27, 198–203.
- [171] Kotas, T. J. (2013). *The Exergy Method of Thermal Plant Analysis*. Elsevier: Oxford.
- [172] Moran, M. J., Shapiro, H., Boettner, D. D., Bailey, M. B. (2011). *Fundamentals of Engineering Thermodynamics*. John Wiley and Sons: New York.
- [173] Nauman, E. B. (2008). *Chemical Reactor Design, Optimization, and Scale-up*. John Wiley and Sons: New York.
- [174] Ulleberg, Ø. (2003). Modeling of advanced alkaline electrolyzers: a system simulation approach. *International Journal of Hydrogen Energy*, 28(1), 21–33.
- [175] Jalali, A. A., Mohammadi, F., Ashrafizadeh, S. N. (2009). Effects of process conditions on cell voltage, current efficiency and voltage balance of a chlor-alkali membrane cell. *Desalination*, 237(1), 126–139.
- [176] Pourbaix, M. (1966). *Atlas of Electrochemical Equilibria in Aqueous Solutions*. Pergamon Press: Oxford.
- [177] Downs, A. J., Adams, C. J. (1975). *Chemistry of Chlorine, Bromine, Iodine and Astatine*. Pergamon Press: Oxford.
- [178] Bard, A. J., Parsons, R., Jordan, J. (1985). *Standard Potentials in Aqueous Solutions* (Vol. 6). CRC Press: New York.
- [179] Bratsch, S. G. (1989). Standard electrode potentials and temperature coefficients in water at 298.15 K. *Journal of Physical and Chemical Reference Data*, 18(1), 1–21.
- [180] Song, G., Atrens, A., Stjohn, D., Nairn, J., Li, Y. (1997). The electrochemical corrosion of pure magnesium in 1 N NaCl. *Corrosion Science*, 39(5), 855–875.

- [181] Shock, E. L., Sassani, D. C., Willis, M., Sverjensky, D. A. (1997). Inorganic species in geologic fluids: correlations among standard molal thermodynamic properties of aqueous ions and hydroxide complexes. *Geochimica et Cosmochimica Acta*, 61(5), 907–950.
- [182] Moussallem, I., Jörissen, J., Kunz, U., Pinnow, S., Turek, T. (2008). Chlor-alkali electrolysis with oxygen depolarized cathodes: history, present status and future prospects. *Journal of Applied Electrochemistry*, 38(9), 1177–1194.
- [183] Ahmadi, P., Dincer, I., Rosen, M. A. (2011). Exergy, exergoeconomic and environmental analyses and evolutionary algorithm based multi-objective optimization of combined cycle power plants. *Energy*, 36(10), 5886–5898.
- [184] Bejan, A., Tsatsaronis, G., Moran, M. (1996). *Thermal Design and Optimization*. John Wiley and Sons: New York.
- [185] Rosen, M. A., Dincer, I. (2003). Exergoeconomic analysis of power plants operating on various fuels. *Applied Thermal Engineering*, 23(6), 643–658.
- [186] Ozgener, L., Hepbasli, A., Dincer, I., Rosen, M. A. (2007). Exergoeconomic analysis of geothermal district heating systems: a case study. *Applied Thermal Engineering*, 27(8), 1303–1310.
- [187] Lior, N. (2012). *Advances in Water Desalination* (Vol. 1). John Wiley and Sons: New York.
- [188] El-Sayed, Y. M. (2013). *The Thermoconomics of Energy Conversions*. Elsevier: New York.
- [189] Naterer, G. F., Dincer, I., Zamfirescu, C. (2013). *Hydrogen Production from Nuclear Energy*. Springer: New York.
- [190] Enteria, N., Yoshino, H., Mochida, A., Satake, A., Takaki, R. (2015). Exergoeconomic performances of the desiccant-evaporative air-conditioning system at different regeneration and reference temperatures. *International Journal of Refrigeration*, 56, 81–98.
- [191] Ozcan, H. (2015). *Experimental and Theoretical Investigations of Magnesium-Chlorine Cycle and Its Integrated Systems*. (Doctoral dissertation, University of Ontario Institute of Technology).
- [192] Orhan, M. F., Dincer, I., Rosen, M. A. (2010). Exergoeconomic analysis of a thermochemical copper–chlorine cycle for hydrogen production using specific exergy cost (SPECOC) method. *Thermochimica Acta*, 497(1), 60–66.
- [193] Lazzaretto, A., Tsatsaronis, G. (2006). SPECOC: a systematic and general methodology for calculating efficiencies and costs in thermal systems. *Energy*, 31(8), 1257–1289.
- [194] Turton, R., Bailie, R. C., Whiting, W. B., Shaeiwitz, J. A. (2008). *Analysis, Synthesis and Design of Chemical Processes*. Pearson Education: New York.
- [195] Vataavuk, W. M. (2002). Updating the CE plant cost index. *Chemical Engineering*, 109(1), 62–75.

- [196] Tsatsaronis, G., Moran, M. J. (1997). Exergy-aided cost minimization. *Energy Conversion and Management*, 38(15), 1535–1542.
- [197] U.S. Energy Information Administration (EIA) Annual Energy Outlook. (2015). *Website*, [accessed on 13.02.2016]
[http://www.eia.gov/forecasts/aeo/pdf/0383\(2015\).pdf](http://www.eia.gov/forecasts/aeo/pdf/0383(2015).pdf).
- [198] Smestad, G. P. (2008). *Solar Energy: New Materials and Nanostructured Devices for High Efficiency*. Optical Society of America.
- [199] Meyer, L., Tsatsaronis, G., Buchgeister, J., Schebek, L. (2009). Exergoenvironmental analysis for evaluation of the environmental impact of energy conversion systems. *Energy*, 34(1), 75–89.
- [200] Buchgeister, J. (2010). Exergoenvironmental Analysis—A New Approach to Support the Design for Environment of Chemical Processes? *Chemical Engineering and Technology*, 33(4), 593–602.
- [201] Boyano, A., Blanco-Marigorta, A. M., Morosuk, T., Tsatsaronis, G. (2011). Exergoenvironmental analysis of a steam methane reforming process for hydrogen production. *Energy*, 36(4), 2202–2214.
- [202] Toffolo, A., Lazzaretto, A. (2002). Evolutionary algorithms for multi-objective energetic and economic optimization in thermal system design. *Energy*, 27(6), 549–567.
- [203] Press, W. H. (2007). *Numerical Recipes 3rd Edition: The Art of Scientific Computing*. Cambridge University Press: New York.
- [204] Konak, A., Coit, D. W., Smith, A. E. (2006). Multi-objective optimization using genetic algorithms: A tutorial. *Reliability Engineering and System Safety*, 91(9), 992–1007.
- [205] Bonabeau, E., Dorigo, M., Theraulaz, G. (1999). *Swarm Intelligence: from Natural to Artificial Systems* (No. 1). Oxford University Press.